Fakultät für Informatik
Technische Universität München

Accelerating Quantitative Magnetic Resonance Imaging

Pedro A. Gómez Damián

Vollständiger Abdruck der von der Fakultät für Informatik der Technischen Universität München zur Erlangung des akademischen Grades eines

Doktors der Naturwissenschaften (Dr. rer. nat.)

genehmigten Dissertation.

Vorsitzender:
    Prof. Dr.-Ing. Darius Burschka

Prüfende der Dissertation:
    Prof. Dr. rer. nat. Bjoern H. Menze
    Priv.-Doz. Dr. rer. nat. Marion I. Menzel

Die Dissertation wurde am 26.06.2017 bei der Technischen Universität München eingereicht und durch die Fakultät für Informatik am 22.08.2017 angenommen.

ACCELERATING QUANTITATIVE MAGNETIC RESONANCE IMAGING

PEDRO A. GÓMEZ DAMIÁN

ABSTRACT

Magnetic Resonance Imaging (MRI) has become one of the most essential diagnostic imaging techniques, as it is capable of non-invasively providing highly detailed anatomical and physiological information of the human body. In clinical centers worldwide, MRI is the modality of choice when it comes to diagnosing tumors, neurodegenerative disorders, and cardiac diseases, amongst others. Although MRI has matured significantly since it was first developed, it still faces a fundamental challenge: the acquisition time. The nature of how MRI signals are encoded for image formation, especially if designed to encode quantitative parametric maps, leads to exceedingly long acquisitions — sometimes beyond the scope for clinical acceptance.

This work focuses on developing novel methods to accelerate quantitative MRI. It builds on recent technological advances in image acquisition and reconstruction, including Magnetic Resonance Fingerprinting (MRF), Compressed Sensing (CS), and Parallel Imaging (PI); and combines them with machine learning techniques to achieve outcomes in speed and accuracy previously unattainable with MRI. Improved outcomes are demonstrated with scientific contributions in three areas of quantitative MRI: hyperpolarized ^{13}C metabolic imaging in preclinical rodent models of cancer, motion encoding methods to map diffusion and flow *in vivo*, and multiparametric mapping techniques for fast, quantitative neuroimaging in the human brain.

ZUSAMMENFASSUNG

Die Magnetresonanztomographie (MRT) hat sich zu einer der wichtigsten diagnostischen Bildgebungstechniken entwickelt, da sie in der Lage ist, sehr detaillierte anatomische und physiologische Informationen des menschlichen Körpers nicht invasiv darzustellen. In klinischen Zentren weltweit ist die MRT die Modalität der Wahl, wenn es u.a. um die Diagnose von Tumoren, neurodegenerativen Erkrankungen und Herzerkrankungen geht. Obwohl die MRT seit ihrer ersten Entwicklung deutlich gereift ist, steht sie immer noch vor einer grundsätzlichen Herausforderung: der Messzeit. Die Art, wie MRT-Signale zur Bildgebung kodiert werden, insbesondere wenn sie für quantitative parametrische Karten konzipiert sind, führt zu langen Messzeiten, die oft über den Umfang der klinischen Akzeptanz hinausgehen.

Diese Arbeit konzentriert sich auf die Entwicklung neuer Methoden zur Beschleunigung der quantitativen MRT. Sie baut auf den neuesten technologischen Fortschritten in Bildgebung und Rekonstruktion auf, wie Magnetic Resonance Fingerprinting, Compressed Sensing und parallele Bildgebung, und kombiniert sie mit Machine Learning Techniken, um Ergebnisse in Geschwindigkeit und Genauigkeit zu erreichen, die bisher mit MRT unerreichbar waren. Verbesserte Ergebnisse werden mit wissenschaftlichen Beiträgen in drei Bereichen der quantitativen MRT präsentiert: hyperpolarisierte ^{13}C metabolische Bildgebung im Kleintiermodell von Tumoren, Methoden zur Kodierung von Bewegung, um Diffusion und Blutfluss *in vivo* zu messen, sowie multiparametrische Quantifizierungstechniken für die Neurobildgebung im menschlichen Gehirn.

PUBLICATIONS

This publication-based thesis contains the following publications in their original form:

STUDYING METABOLISM WITH HYPERPOLARIZED ^{13}C NMR

1. **PA. Gómez**, JI. Sperl, MA. Janich, O. Khegai, F. Wiesinger, SJ. Glaser, A. Haase, M. Schwaiger, R. Schulte, MI. Menzel. Multisite Kinetic Modeling of ^{13}C Metabolic MR Using [1-13C]Pyruvate. In: *Radiology Research and Practice* 871619 (2014), p. 10 [32].

2. E. Kubala, KA. Muñoz-Álvarez, G. Topping, C. Hundshammer, B. Feuerecker, **PA. Gómez**, G. Pariani, F. Schilling, SJ. Glaser, MI. Menzel, M. Schwaiger. Hyperpolarized ^{13}C Metabolic Magnetic Resonance Spectroscopy and Imaging. In: *Journal of Visualized Experiments* 118 (2016), e54751 [50].

ENCODING FOR MOTION: DIFFUSION AND PERFUSION

3. C. Ulas, **PA. Gómez**, JI. Sperl, C. Preibisch, BH. Menze. Spatiotemporal MRI Reconstruction by Enforcing Local and Global Regularity via Dynamic Total Variation and Nuclear Norm Minimization. In: *Proceedings of International Symposium on Biomedical Imaging (ISBI)* (2016), pp. 306–309 [83].

4. C. Ulas, **PA. Gómez**, F. Krahmer, JI. Sperl, MI. Menzel, BH. Menze. Robust Reconstruction of Accelerated Perfusion MRI Using Local and Nonlocal Constraints. In: *International Workshop on Reconstruction and Analysis of Moving Body Organs* LNCS 10129 (2017), pp. 37–47 [85].

MULTIPARAMETRIC MAPPING: MR FINGERPRINTING AND BEYOND

5. **PA. Gómez**, JI. Sperl, T. Sprenger, C. Metzler-Baddeley, DK. Jones, P. Saemann, M. Czisch, MI. Menzel, BH. Menze. Joint Reconstruction of Multi-Contrast MRI for Multiple Sclerosis Lesion Segmentation. In: *Bildverarbeitung für die Medizin 2015* (2015). [34].

6. **PA. Gómez**, C. Ulas, JI. Sperl, T. Sprenger, M. Molina-Romero, MI. Menzel, BH. Menze. Learning a Spatiotemporal Dictionary for Magnetic Resonance Fingerprinting with Compressed Sensing. In: *MICCAI Patch-MI Workshop* LNCS 9467 (2015), pp. 112–119 [35].

7. **PA. Gómez**, M. Molina-Romero, C. Ulas, G. Buonincontri, JI. Sperl, DK. Jones, MI. Menzel, BH. Menze. Simultaneous Parameter Mapping, Modality Synthesis, and Anatomical Labeling of the Brain with MR Fingerprinting. In: *MICCAI: International Conference on Medical Image Computing and Computer-Assisted Intervention* LNCS 9902 (2016), pp. 579 – 586 [38].

The following works relevant to this dissertation were published as Peer-reviewed abstracts at the annual conference of the International Society for Magnetic Resonance in Medicine:

ENCODING FOR MOTION: DIFFUSION AND PERFUSION

1. **PA. Gómez**, T. Sprenger, MI. Menzel, JI. Sperl. Fitting the Diffusional Kurtosis Tensor to Rotated Diffusion MR Images. In: *Proc Intl Soc Mag Reson Med* (2015) [33].

2. M. Molina-Romero, **PA. Gómez**, JI. Sperl, AJ. Stewart, DK. Jones, MI. Menzel, BH. Menze. Theory, Validation and Aplication of Blind Source Separation to Diffusion MRI for Tissue Characterisation and Partial Volume Correction. In: *Proc Intl Soc Mag Reson Med* (2017) [60].

3. C. Ulas, **PA. Gómez** JI. Sperl, C. Preibisch, MI. Menzel, A. Haase, BH. Menze. A Robust Reconstruction Method for Quantitative Perfusion MRI: Application to Brain Dynamic Susceptibility Contrast (DSC) Imaging. In: *Proc Intl Soc Mag Reson Med* (2017) [84].

MULTIPARAMETRIC MAPPING: MR FINGERPRINTING AND BEYOND

4. **PA. Gómez**, G. Buonincontri, M. Molina-Romero, C. Ulas, JI. Sperl, MI. Menzel, BH. Menze. 3D Magnetic Resonance Fingerprinting with a Clustered Spatiotemporal Dictionary. In: *Proc Intl Soc Mag Reson Med* (2016) [37].

5. G. Buonincontri, L. Biagi, **PA. Gómez**, R. Schulte, M. Tosetti. Spiral Keyhole Imaging for MR Fingerprinting. In: *Proc Intl Soc Mag Reson Med* (2017) [14].

6. X. Liu, **PA. Gómez**, T. Sprenger, AB. Solana, F. Wiesinger, MI. Menzel, JI. Sperl, BH. Menze. Fast, Volumetric and Silent Multicontrast Zero Echo Time Imaging. In: *Proc Intl Soc Mag Reson Med* (2017) [54].

7. **PA. Gómez**, G. Buonincontri, M. Molina-Romero, JI. Sperl, MI. Menzel, BH. Menze. Accelerated Parameter Mapping with Compressed Sensing: an Alternative to MR Fingerprinting. In: *Proc Intl Soc Mag Reson Med* (2017) [39].

The annex of thesis contains the following manuscripts currently under preparation or review for publication:

MANUSCRIPTS IN PREPARATION OR UNDER REVIEW

1. **PA. Gómez**, M. Molina-Romero, P. Orihuela, G. Buonincontri, T. Rincón-Domíngez, MI. Menzel, BH. Menze. Ultrafast Magnetic Resonance Imaging and Parametric Mapping with Optimal Transient-state Encoding. Under review (2017).

2. M. Molina-Romero, **PA. Gómez**, JI. Sperl, DK. Jones, MI. Menzel, BH. Menze. A Diffusion Model-free Framework with Echo Time Dependence for Brain Tissue Microstructure Characterization. Under review (2017).

ACKNOWLEDGMENTS

CONTENTS

ACRONYMS

ADMM Alternating Direction Method of Multipliers

AD   Axial Diffusivity

BSS   Blind Source Separation

BV   Blood Vessels

CBF   Cerebral Blood Flow

CBV   Cerebral Blood Volume

CSF   Cerebrospinal Fluid

CS   Compressed Sensing

DKI   Diffusion Kurtosis Imaging

DSI   Diffusion Spectrum Imaging

DTI   Diffusion Tensor Imaging

DWI   Diffusion Weighted Imaging

dMRI Dynamic Magnetic Resonance Imaging

DNP   Dynamic Nuclear Polarization

DSC   Dynamic Susceptibility Contrast

EPI   Echo-planar Imaging

EPG   Extended Phase Graphs

FLASH Fast Low-Angle Shot Imaging

FA   Fractional Anisotropy

GM   Gray Matter

LR   Low Rank

ILT   Inverse Laplace Transform

MRI   Magnetic Resonance Imaging

MRF   Magnetic Resonance Fingerprinting

MRSI Magnetic Resonance Spectroscopic Imaging

ML   Maximum Likelihood

MD   Mean Diffusivity

MTT   Mean Transit Time

MS   Multiple Sclerosis

NMR   Nuclear Magnetic Resonance

NLLS   Non-Linear Least Squares

NN   Nuclear Norm

PI   Parallel Imaging

PCA   Principal Component Analysis

PDF   Probability Density Function

PD   Proton Density

QTI   Quantitative Transient-state Imaging

RD   Radial Diffusivity

RF   Radiofrequency

SNR   Signal to Noise Ratio

SVD   Singular Value Decomposition

TMCMC   Transitional Markov Chain Monte Carlo

SSFP   Steady-state Free Precession

WM   White Matter

ZTE   Zero Echo Time

Part I

INTRODUCTION AND SUMMARY OF
CONTRIBUTIONS

INTRODUCTION

Magnetic Resonance Imaging (MRI) is a non-invasive imaging modality that enables the *in vivo* study of the structure and function of biological systems. MRI is made possible by the NMR effect, where its use for imaging was introduced in 1973 by Lauterbur [52] and Mansfield [57]. Since its inception, MRI has evolved into an unparalleled imaging modality, with the ability of providing detailed and versatile information of a tissue's anatomy and physiology. The versatility behind MRI can be attributed to the wide range of physical phenomena that interact with resonant nuclei to affect the NMR signal. Among these, the most commonly investigated interactions are chemical shift [2], motion, such as molecular self-diffusion [76], and relaxation [10, 61]. Therefore, through precise calibration of Radiofrequency (RF) pulses and magnetic gradients, one can manipulate spins of resonant nuclei to produce signals *weighted* by one or more of these interactions. Thus, different experiments with distinct acquisition parameters allow one to create unique contrasts, providing critical information in clinical settings [21].

Moreover, modern parameter mapping techniques enable one to progress from qualitative images — i.e. the use of these physical interactions to create imaging contrast — to quantitative maps, where the phenomena themselves can be quantified. In this way, chemical shifts can be taken advantage of to monitor metabolic activity in biological tissues [11], motion encoding methods create information on the three dimensional incoherent motion of water molecules [7], blood perfusion [53], or blood flow [64], and relaxometry techniques provide quantitative maps of the Proton Density (PD), the longitudinal relaxation time (T_1) and the transverse relaxation time (T_2) [23]. All of these quantitative MRI techniques share a common goal: they aim at generating quantitative image biomarkers that are both specific and sensitive to pathology, increasing the accuracy and reproducibility of diagnostic information [79].

As they share a common goal, quantitative MRI techniques also share a common drawback: they are inherently slow techniques, for they require multiple samples along different encoding dimensions to resolve and accurately estimate quantitative metrics. With increasing acquisition times, these techniques become more susceptible to motion-related artifacts, including voluntary (e.g. head movement) and involuntary (e.g. cardiac pulsations, breathing, brain pulsations) motion. Also, mapping methods generally need to sacrifice Signal to Noise Ratio (SNR) or resolution in favor of faster measurements to re-

main within the scope of clinical usability. Therefore, as accelerating MRI in general has long been a research objective of the field [42, 75]; accelerating *quantitative* MRI is the specific goal of this work.

1.1   INTRODUCTION TO NMR IMAGING

The NMR effect, which was first observed by Rabi in gases in 1938 [69], and later shown for solids independently by Bloch [10] and Purcell [68] in 1946, is the fundamental principle that makes MRI possible. The NMR effect states that atomic nuclei that have a non-zero spin (^{1}H, for example), when exposed to a strong magnetic field, will precess at a frequency ω_0 that is directly proportional to the applied magnetic field $\mathbf{B}_0$ and a known constant unique to every nucleus, called the gyromagnetic ratio γ [17]. The resonance frequency, also called the Larmor precession frequency, is defined as[1]:

$$\omega_0 = \gamma \mathbf{B}_0. \tag{1}$$

When a biological sample is exposed to a magnetic field, its precessing nuclei will with a Boltzmann distribution, where the spins with parallel alignment will exceed the spins in anti-parallel alignment only by a small fraction [12]. Nonetheless, a biological sample contains millions of precessing nuclei, allowing for the formation of a bulk magnetization vector $\mathbf{M} = [M_x \ M_y \ M_z]^\top$ that behaves according to the Bloch equations:

$$\frac{\partial \mathbf{M}}{\partial t} = \gamma \mathbf{M} \times \mathbf{B} - \frac{\left(M_x \hat{\mathbf{i}} + M_z \hat{\mathbf{j}}\right)}{T_2} - \frac{(M_z - M_{0,z}) \hat{\mathbf{k}}}{T_1}. \tag{2}$$

In Eq. 2, $\mathbf{B}$ is the total magnetic field, $M_{0,z}$ is the longitudinal component of the equilibrium magnetization vector $\mathbf{M}_0$, $\hat{\mathbf{i}}$, $\hat{\mathbf{j}}$, $\hat{\mathbf{k}}$ are unit directional vectors in the x, y, and z direction, and T_1 and T_2 are the longitudinal and transversal relaxation times, respectively. The amplitude of $\mathbf{M}_0$ is related to the PD of a sample, while T_1 and T_2 relaxation times are tissue specific. Therefore, these three properties currently constitute the main imaging contrasts for structural MRI.

If $\mathbf{B} = \mathbf{B}_0$, the bulk magnetization will remain in its equilibrium value oriented along the longitudinal direction $\hat{\mathbf{k}}$. However, by applying a second magnetic field $\mathbf{B}_1$ in the form of a RF pulse such that

$$\mathbf{B}(t) = \mathbf{B}_0 + \mathbf{B}_1(t) \tag{3}$$

---

1 This section follows the notation, and is a brief account of the concepts introduced in Chapters 1,9, and 10 of [12]. For a more comprehensive introduction to NMR imaging, see [12, 15, 89].

the bulk magnetization vector can be excited and tipped into the transversal $x_i - y_j$ plane. To achieve this excitation, the $\mathbf{B}_1$ pulse must have a frequency equal to the Larmor frequency defined in Eq. 1. After excitation, the magnetization in the transversal plane will exponentially decay according to:

$$M_\perp(t) = M_{xy}(0)e^{-i\omega_0 t}e^{-\frac{t}{T_2}},$$ (4)

while the magnetization in the longitudinal plane will gradually return to its thermal equilibrium:

$$M_z(t) = M_z(0)e^{-\frac{t}{T_1}} + M_{0,z}(1 - e^{-\frac{t}{T_1}}).$$ (5)

By introducing RF receiving coils in the perpendicular $x_i - y_j$ plane, and as the magnetization returns to thermal equilibrium, changes in the magnetic flux will induce a current through the receiving coils. The measurement of this current is the principal behind the NMR experiment, where serial applications of $\mathbf{B}_1$ pulses (generally referred to as a pulse sequence), produce signals that are a function of different parameters, including PD, T_1, and T_2. Hence, the only ingredient missing to create images from NMR measurements is the ability to spatially resolve different signals. This can be achieved by the use of magnetic gradients, as described in Lauterbur's seminal paper [52].

Let $G_z = \partial B_z / \partial z$ represent a spatially constant gradient in the z-direction. It follows, that the z-component of the field is

$$B_z(z,t) = B_{0,z} + zG(t)$$ (6)

and per Eq. 1, the variation of the angular frequency of the spins

$$\omega(z,t) = \omega_0 + \omega_G(z,t),$$ (7)

where

$$\omega_G(z,t) = \gamma z G(t).$$ (8)

From Eq. 8, one can derive that spins will deviate from the Larmor frequency linearly in both z and G. That is, it is possible to use a gradient to establish a link between the *spatial position* of spins with their *precessional frequency*, a term referred to as frequency encoding.

The applied gradient will also introduce a phase accumulation of the spins

$$\phi_G(z,t) = -\gamma z \int_0^t dt\, G(t).$$ (9)

Let

$$\rho(z) \propto M_\perp(z, T_E) \tag{10}$$

be a factor proportional the spatially varying transverse magnetization $M_\perp(z, T_E)$ at the time of data collection, or echo time, T_E. This factor, depending on the pulse sequence, can also be a proxy for the spatially varying spin density of the samples $\rho(z)$. Thereafter, the signal acquired by the RF coils, once the ω_0 frequency has been demodulated, is determined by

$$y(t) = \int dz \rho(z) e^{i\phi_G(z, t)}, \tag{11}$$

where the phase $\phi_G(z, t)$ is determined by the introduced gradient field. It is also possible to rewrite the spatial dependence on the accumulated phase (Eq. 9) as a function of a *spatial frequency* $k = k(t)$, with

$$k(t) = -\gamma \int_0^t dt G(t). \tag{12}$$

Equation 11 now becomes

$$y(k) = \int dz \rho(z) e^{-i2\pi kz}, \tag{13}$$

where it can be seen that the measured signal $y(k)$ is the Fourier Transform of the spatial distribution $\rho(z)$. Therefore, $\rho(z)$ of any sample can be determined by taking the inverse Fourier transform of the acquired signal:

$$\rho(z) = \int dk y(k) e^{+i2\pi kz}. \tag{14}$$

The Fourier relationship between the acquired signal and the spatial spin distribution introduced by magnetic gradients is the key principle that enables imaging (i.e. the reconstruction of 2D and 3D signals). To create an image, the concept of the spatial frequency, also called k-space, needs to be extended into higher dimensions $\mathbf{k} = [k_x \ k_y \ k_z]^\top$. Thereafter, the spatial spin distribution in a three-dimensional position space $\mathbf{r} = [r_x \ r_y \ r_z]^\top$ is given by

$$\rho(\mathbf{r}) = \int_\mathbf{k} y(\mathbf{k}) e^{+i2\pi \mathbf{kr}}, \tag{15}$$

and likewise, the acquired k-space signal determined by the Fourier pair

$$y(\mathbf{k}) = \int_\mathbf{r} \rho(\mathbf{r}) e^{-i2\pi \mathbf{kr}}. \tag{16}$$

An important point in the above equations is that the spatial function $\rho(\mathbf{r})$, as described in Eq. 10, is *not* a measure of the density of the protons in the classical sense (number of protons per unit volume), but rather a measure of the transverse magnetization $M_\perp(\mathbf{r})$, which in its simplest form depends on the T_2 decay and the amount of initial transverse magnetization available after RF excitation (Eq. 4) — a factor that in turn is a function of the actual PD and T_1 recovery (Eq. 5). In its more complex form, any physical phenomenon that directly or indirectly affects the magnetization vector will manifest itself in the resulting reconstructed image $\rho(\mathbf{r})$.

Consequently, MRI pulse sequences generally have two purposes: to manipulate the magnetization vector at the time of signal collection to produce contrasts that are a function of different parameters, and to collect enough samples in k-space to reconstruct uncorrupted images. The first purpose, contrast weighting, can be extended to parameter quantification within the field of quantitative MRI (Sect. 1.2). The second purpose, k-space sampling, is related to the Nyquist limit, and is one of the most limiting factors behind scanning speed. Relevant acceleration techniques and their applications in quantitative MRI are discussed in Sect. 2.2.

1.2 QUANTITATIVE MRI

Quantitative MRI refers to the collection of techniques used to quantify physical phenomena that affect the NMR signal. Quantitative MRI techniques rely on the same image encoding principles introduced in Sect. 1.1, and can be generalized by modifying Eq. 16 to incorporate a temporal dependence to the k-space samples

$$y(\mathbf{k}, t) = \int_{\mathbf{r}} \rho(\mathbf{r}) f_t(\mathbf{r}) e^{-i2\pi \mathbf{k}(t) \cdot \mathbf{r}}. \tag{17}$$

Here, the observed signal in k-t space is described as the combination of the spatial distribution of spin densities $\rho(\mathbf{r})$ with a temporally varying function $f_t(\mathbf{r})$, which in turn is a function of two parameter sets:

$$f_t(\mathbf{r}) = g(\eta(t); \theta(\mathbf{r})). \tag{18}$$

In Eq. 18, $\eta(t)$ refers to temporally varying acquisition parameters, such as flip angle or repetition time, which can be manipulated to encode for $\theta(\mathbf{r})$, the spatially varying tissue-specific parameters of interest, including $T_1(\mathbf{r})$ and $T_2(\mathbf{r})$. Finally, $g(\cdot)$ is the encoding function which links η with θ. Therefore the task of quantitative MRI is threefold:

1. Create the encoding function $g(\cdot)$ and design the corresponding acquisition parameters η such that observed NMR signals are sensitive to relevant quantitative parameters θ.

2. Develop and implement k-t sampling schemes that efficiently sample the measurement space.

3. Reconstruct signals to produce voxel-wise estimates of θ, and hence, quantitative parametric maps.

In the following, a brief overview of three quantitative MRI techniques will be given: hyperpolarized ^{13}C metabolic NMR, motion encoding techniques, and multiparametric mapping techniques, such as Magnetic Resonance Fingerprinting (MRF). An extensive treatment of other quantitative MRI techniques can be found in [79].

1.2.1 *Hyperpolarized ^{13}C metabolic NMR*

Hyperpolarized ^{13}C metabolic NMR is a spectroscopic imaging method that relies on the chemical shift of compounds to study the metabolism of tissue *in vivo*. Whereas most NMR techniques measure the magnetic moment produced by protons (^{1}H), hyperpolarization techniques enable imaging of multiple nuclei, such as ^{15}N and ^{13}C [31]. This was only made possible by the development of Dynamic Nuclear Polarization (DNP), which lead to a $10,000$-fold increase in sensitivity of nuclear spins [1]. By combining DNP with subsequent fast encoding techniques, studies of e.g. cancer metabolism [51], how now become feasible *in vivo*.

The experimental design of hyperpolarized ^{13}C measurements starts with the DNP of a particular substance, for example $[1-^{13}$C]pyruvate, subsequent rapid dissolution, and injection into a biological specimen [50]. After injection, efficient spectro-spatial encoding techniques [93] allow for the collection of 5-dimensional signals: 3D spatial, 1D spectroscopic, and 1D temporal. The kinetics of the temporal signals for every metabolite seen in the spectrum can be quantified to yield metabolic exchange rates, as investigated in [32]. The modeling of these temporal signals is determined by the system of differential equations

$$
\begin{aligned}
\frac{dM_p(t)}{dt} &= -r_p M_p(t) - \sum_x k_{p\rightarrow x} M_p(t) \\
&\quad + \sum_x k_{x\rightarrow p} M_x(t) + I_p(t)
\end{aligned}
\tag{19}
$$

$$
\frac{dM_x(t)}{dt} = -r_x M_x(t) + k_{p\rightarrow x} M_p(t) - k_{x\rightarrow p} M_x(t),
$$

where $M_p(t)$ refers to the magnetization signal over time of the injected substance with an injection function over time determined by

$I_p(t)$, $M_x(t)$ is the magnetization over time of downstream metabolites, $k_{p \to x}$ and $k_{x \to p}$ are forward and backward exchange rates, and r_x refers to signal a decay term

$$r_x = \frac{1}{T_{1,x}} + k_{x \to p} + f(\alpha) \tag{20}$$

with

$$f(\alpha) = \frac{1 - \cos(\alpha)}{T_R}. \tag{21}$$

Here, α is the flip angle and T_R the repetition time. Hence, following the notation introduced in Sect. 1.2, Eq. 19 is the encoding function $g(\cdot)$, and the acquisition parameters $\eta = \{I_p(t), \alpha, T_R\}$ need to be selected such that they enable the quantification of the parameters $\theta = \{T_{1,x}, k_{p \to x}, k_{x \to p}\}$.

1.2.2 *Motion encoding techniques*

Spins inside a biological tissue are not static: they diffuse with Brownian motion, flow inside blood vessels, disperse with brain pulsation or move rigidly with the rest of the body. Since motion results in spatial shifts of the spin distribution, it directly affects the NMR signal. This also means that appropriate acquisition schemes are capable of encoding for and quantifying motion and motion-related properties. This work focuses on two motion encoding techniques: diffusion and perfusion.

1.2.2.1 *Diffusion*

Diffusion Weighted Imaging (DWI) is made possible by incorporating magnetic field gradients into a spin echo experiment, as demonstrated by Stejskal and Tanner [76]. The presence of these gradients will cause signal loss with respect to a baseline signal proportional to the amount of diffusion of a particular tissue. Since the Stejskal-Tanner experiment, modeling the signal loss caused by diffusion has been a relevant subject of study: Diffusion Tensor Imaging (DTI) was the first attempt to capture the spatial diffusion anisotropy via a tensor model [7], followed by multiple acquisition techniques — such as Diffusion Kurtosis Imaging (DKI) [47] and Diffusion Spectrum Imaging (DSI) [81] — and biophysical models that attempt to reflect the underlying tissue architecture. Examples of choices for biophysical models for diffusion are collected elswhere [3, 4, 63, 80].

All of these techniques rely on an exponential signal loss caused by diffusion. Using the tensor as an example, the signal loss is given by

$$E(b) = \frac{S(b)}{S(0)} = e^{-b\mathbf{D}}, \tag{22}$$

where $S(0)$ denotes the baseline signal acquired with no diffusion weighting, $\mathbf{D} \in \mathbb{R}^{3 \times 3}$ is a second order diffusion tensor

$$\mathbf{D} = \begin{bmatrix} D_{xx} & D_{yx} & D_{zx} \\ D_{xy} & D_{yy} & D_{zy} \\ D_{xz} & D_{yz} & D_{zz} \end{bmatrix} \tag{23}$$

and the b-value groups all of the relevant terms to the diffusion experiment:

$$b = (2\pi)^2 \left(\Delta - \frac{\delta}{3}\right) \|\mathbf{q}\|^2. \tag{24}$$

In Eq. 24, δ is the duration of the gradient, Δ is the mixing time, and $\mathbf{q}$ is as a wave vector

$$\mathbf{q} = \frac{\gamma}{2\pi}\mathbf{g}\delta \tag{25}$$

that is a function of the directional gradient $\mathbf{g} = [g_x \ g_y \ g_z]^\top$. After computing the diffusion tensor, it can an be decomposed into its Eigenvectors and Eigenvalues

$$\mathbf{D} = \mathbf{E}\mathbf{\Lambda}\mathbf{E}^\mathrm{T}, \tag{26}$$

where $\mathbf{E}$ are the Eigenvectors in matrix form and the i-th Eigenvalue λ_i is in the i-th element of the diagonal of the matrix $\mathbf{\Lambda}$:

$$\boldsymbol{\lambda} = \mathrm{diag}\left(\mathbf{\Lambda}\right). \tag{27}$$

From the Eigenvalue decomposition of the diffusion tensor, multiple scalar metrics can be computed. For instance, the Mean Diffusivity (MD)

$$MD = \bar{D} = \bar{\lambda} = \frac{1}{3}\sum_{i=1}^{3} \lambda_i, \tag{28}$$

the Axial Diffusivity (AD)

$$AD = D_\| = \lambda_\| = \lambda_1, \tag{29}$$

the Radial Diffusivity (RD)

$$RD = D_\perp = \lambda_\perp = \frac{\lambda_2 + \lambda_3}{2} \tag{30}$$

or the Fractional Anisotropy (FA)

$$FA = \sqrt{\frac{3}{2}} \sqrt{\frac{\sum_{i=1}^{3} (\lambda_i - \bar{\lambda})^2}{\sum_{i=1}^{3} \lambda_i^2}}. \tag{31}$$

As before, diffusion techniques share a common framework with the presented quantitative MRI notation from Sect. 1.2. Equation 22 acts as an encoding function $g(\cdot)$, where the acquisition parameters collected in the b-value $\eta = b$ are manipulated to quantify the tensor $\theta = \mathbf{D}$ and its derived metrics. This notation also holds for different acquisition schemes and more complex diffusion models.

1.2.2.2 *Perfusion*

Perfusion imaging in the form of Dynamic Susceptibility Contrast (DSC) relies on the magnetic susceptibility effects caused by the injection of a bolus of paramagnetic agents [20, 88]. In a similar manner to the DNP experiments previously described, accelerated acquisition schemes combined with advanced reconstruction techniques create a 4-dimensional signal (3D spatial plus 1D temporal) over which the kinetics of the injected bolus can be modeled. From the kinetic modeling, quantitative metrics such as the Cerebral Blood Flow (CBF), Cerebral Blood Volume (CBV), or the Mean Transit Time (MTT) can be computed.

1.2.3 *Multiparametric mapping*

Parameter mapping techniques offer quantitative measurements of intrinsic tissue properties, such as the relaxation times T_1 and T_2. These techniques suffer also from the main limitation of quantitative MRI: long acquisition times.

To overcome this limitation, multiple rapid parameter mapping techniques have been proposed. These techniques generally make use of sparse sampling with iterative reconstructions [8, 9, 26, 46, 65, 77, 99, 100], fast imaging protocols [24, 28, 56, 73, 90], or a combination of both [65, 86]. The first class of methods aims at reconstructing undersampled measurements by using lower dimensional signal or image models as constraints. Typical constraints include the incorporation of simulations of expected signal evolutions for model-based reconstructions [8, 77]; sparsity in a transform domain, e.g. wavelets [86], finite differences [97], or data-driven transforms [9, 26]; and Low Rank (LR) constraints [46, 100].

The second class of methods uses pulse sequences to accelerate data acquisition. Interestingly, most of these methods rely on variations of the Steady-state Free Precession (SSFP) sequence, which precedes the imaging era [17]. One alternative is to use an unbalanced SSFP for T_1 mapping and then combine it with a balanced SSFP for T_2 estimation [24]. Another alternative is to prepare the magnetization to sensitize the SSFP train to multiple contrasts. For example, one could combine an unbalanced SSFP with a saturation recovery experiment for estimation of T_1,T_2^*, and PD [90], or use an inversion recovery balanced SSFP for quantification T_1, T_2, and PD [28, 73].

One of the most novel mapping methods, MRF [56], also relies on an inversion recovery SSFP-like sequence structure (in both its balanced [5, 56] and unbalanced [48] versions) for multiparametric mapping, but with two important distinctions: 1) it avoids the steady-state by pseudorandom variations of the acquisition parameters and 2) it subsequently estimates parameter maps by matching the acquired transient-state signals, or so-called fingerprints, to a precomputed dictionary of all foreseeable parameter combinations. With these two differences, pseudorandom acquisitions and dictionary matching, MRF achieves efficient relaxation mapping and sets itself apart from the rest of the methods.

Moreover, it is possible to incorporate iterative reconstruction algorithms to MRF acquisitions. Davies *et al.* proposed the use of iterative projections [22], which can be extended to multiscale reconstructions [66], accelerated with data compression and fast parameter searches [18], or coupled with a spatiotemporal dictionary learnt from data [35]. Zhao *et al.* made use of the Alternating Direction Method of Multipliers (ADMM) to estimate parameters in a statistical framework [99]. The ADMM algorithm is also suitable to incorporate additional low dimensional constraints, for example, LR constraints [6] or LR with spatial regularization [98]. By incorporating iterative reconstructions to MRF one can reduce acquisition times, increasing scan efficiency. Additionally, it has been demonstrated that MRF acquisitions can be used to eliminate artifacts caused by RF field inhomogeneities through an estimation of B_1 maps together with relaxation maps [13, 19]. Based on the above, MRF has become a highly appealing method, with the potential to enable robust, fully quantitative parametric mapping within clinical settings.

Despite its potential, MRF could still benefit from methodological improvements in both its key ideas. First, although incoherent sampling schemes are a requirement for Compressed Sensing (CS) [55], there is no theoretical justification to extend this concept to pseudorandom acquisitions. In fact, there is a whole body of literature on the subject of transient-state signal response characterization and modification to fulfill certain criteria [25, 29, 44, 74, 94]. Second, creating a dictionary for all possible parameter combinations and matching by

searching over the simulated space has certain drawbacks: 1) an exhaustive search over the entire parameter space is suboptimal; 2) the number of combinations in the dictionary scales exponentially with the dimensionality of the parameter space, which could result in infeasible dictionary sizes even for modest spaces; 3) pattern matching with cross product requires vector normalization, leading to the loss of magnitude information and possible confounding between fingerprints; and 4) the estimated parametric maps will always be subject to the discretization of the dictionary. The last point implies, on the one hand, that a coarsely sampled dictionary is subject to estimation errors of up to half the distance between dictionary atoms, and on the other hand, that a densely sampled dictionary will increase memory requirements and search times.

This thesis proposes methodological improvements to MRF through various works concerning learning a spatiotemporal dictionary (Sect. 5.1.2), creating novel parameter maps (Sect. 5.1.3), and proposing a robust and efficient alternative, termed Quantitative Transient-state Imaging (QTI) (Appendix A.1.1). The methodology behind these works is covered in Sect. 2.

1.3   OUTLINE AND CONTRIBUTION OF THIS THESIS

The rest of this thesis is structured as follows. Chapter 2 covers the most relevant methodology to the presented publications, beginning with signal encoding and modeling for image formation (Sect. 2.3), followed by data acquisition (Sect. 2.2), image reconstruction (Sect. 2.3), parameter estimation (Sect. 2.4) and anatomical labeling (Sect. 2.5). Subsequently, a chapter with a summary and each of the relevant publications — the main contribution of this thesis — is dedicated for each of the quantitative MRI categories that have just been introduced: hyperpolarized ^{13}C metabolic NMR (Chapter 3), motion encoding techniques (Chapter 4), and multiparametric mapping techniques (Chapter 5). Chapter 6 provides a discussion of the presented methods, whereas Chapter 7 offers conclusions and an outlook to the future. Finally, Appendix A contains manuscripts in preparation or peer-review at the moment of submission of this dissertation.

METHODOLOGY

2.1 SIGNAL ENCODING AND MODELING

As introduced in Sect. 1.2, in an MRI acquisition spanning multiple repetitions the observed signal $y(\mathbf{k}, t)$ at a given time t can be described by a mixture of a spatial spin distribution, usually referred to as spin density, with a temporally varying function:

$$y(\mathbf{k}, t) = \int_{\mathbf{r}} \rho(\mathbf{r}) f_t(\mathbf{r}) e^{-i2\pi \mathbf{k}(t) \cdot \mathbf{r}}, \tag{32}$$

where $\rho(\mathbf{r})$ is the complex-valued spatial distribution of spins, i.e. the PD, at position $\mathbf{r}$, $\mathbf{k}(t)$ is the k-space trajectory, and $f_t(\cdot)$ is the temporal signal, which cab be modified from Eq. 18 to create the recursion:

$$f_t(\mathbf{r}) = f_{t-1} g(\eta(t); \theta(\mathbf{r})). \tag{33}$$

In Eq. 33, the value of the function at time t is determined by the value of the function at time $t-1$ modulated by the operator $g(\cdot)$, which in turn depends on two sets of parameters: the temporally varying acquisition parameters $\eta(t)$, such as the flip angle $\alpha(t)$, repetition time $T_R(t)$, and echo time $T_E(t)$; and the spatially dependent biophysical parameters of interest $\theta(\mathbf{r})$, including the relaxation times $T_1(\mathbf{r})$ and $T_2(\mathbf{r})$. The operator $g(\cdot)$ captures alterations to the spin dynamics given by phenomena such as RF excitation, relaxation, or gradient dephasing and can be simulated with Bloch simulators or Extended Phase Graphs (EPG) [45, 91, 92]. Furthermore, the formulation of Eq. 33 allows for the incorporation of system imperfections, such as B_1 inhomogeneities, by either including a spatial dependence in the acquisition parameters $\eta(t, \mathbf{r})$ or by modeling them as an additional spatial parameter in $\theta(\mathbf{r})$.

Traditionally, SSFP experiments maintain acquisition parameters constant through time to reach a steady-state. In these experiments, the transient-state signal is discarded, and is only characterized in an effort to minimize it [44]. Once in the steady-state, $f_t(\cdot)$ can be reduced to a well-described, time invariant analytical expression [17], resulting in simplified signal modeling with consistent signal intensity in all of the imaging encoding steps. In the transient-state, as the name suggests, the signal changes with every repetition. And while this introduces an extra degree of complexity, full analytical descriptions have been demonstrated for multiple transient-state signals [29, 44,

71]. Also, one could define an initial magnetization at $t = 0$ (one generally assumes the entire magnetization is in longitudinal thermal equilibrium prior to the first RF excitation) and follow Eq. 33 recursively to derive a simulated signal evolution for any given set of acquisition parameters. The ability to make use of simulations to predict different signal evolutions removes constraints on the choice of acquisition parameters, creating ample possibilities for sequence design.

Amongst these possibilities, MRF originally proposed arbitrary and random patterns of $\eta(t)$ to create $f_t(\cdot)$ [56]. Subsequently, Jiang *et al.* replaced random flip angles with a sinusoidally varying pattern to create smooth transient responses [48]. More elaborate choices of $\eta(t)$ can include rapid flip angle variations [13] or orthogonal coil configurations [19] to incorporate B_1 mapping into parameter estimation. Simpler alternatives for $\eta(t)$ include constant repetition times with variable flip angles [94] or linear ramps [25]. The latter idea, acquiring data during a linear ramp-up, results in smooth transient-state signals with an accelerated acquisition. Alternative methods for finding the optimal acquisition parameters include the use of design frameworks, such as Bayesian experimental design [40, 62, 87].

Irrespective of the final form of $f_t(\cdot)$, image encoding can be formulated to account for both the temporal spin dynamics and the Fourier relationship of the spatial signal [78]. Let

$$\mathbf{x}_t(\mathbf{r}) = \rho(\mathbf{r})f_t(\mathbf{r};\eta(t);\theta(\mathbf{r})) \tag{34}$$

represent the acquired image at the t-th time point at voxel $\mathbf{r}$. The entire image $\mathbf{x}_t \in \mathbb{C}^N$ for N voxels is related to the acquired data

$$\mathbf{y}_t \in \mathbb{C}^M$$

with M measurements by

$$\mathbf{y}_t = \mathbf{E}_t\mathbf{x}_t \tag{35}$$

with the encoding operator

$$\mathbf{E}_t = \mathbf{U}_t\mathbf{F}\mathbf{S} \in \mathbb{C}^{M \times N}. \tag{36}$$

The encoding operator acts on every temporal image independently, where $\mathbf{x}_t$ is multiplied by the coil sensitivities $\mathbf{S}$, Fourier transformed with $\mathbf{F}$, and masked by the sampling trajectory $\mathbf{U}_t$ of the t-th time point. This model can be extended into k-t space encoding by taking the entire image series $\mathbf{X} \in \mathbb{C}^{T \times N}$ for T time points and N voxels. In this representation, the encoding operator in k-t space is $\mathbf{E}_t = \mathbf{U}\mathbf{F}\mathbf{S}$, with $\mathbf{X}$ now determined by

$$\mathbf{Y} = \mathbf{E}\mathbf{X}. \tag{37}$$

Image reconstruction can now be formulated as in inverse problem

$$\hat{\mathbf{X}} = \mathbf{E}^*\mathbf{Y}, \tag{38}$$

where $\mathbf{E}^*$ represents the Hermitian encoding operator. This inverse problem can also be solved with iterative algorithms that incorporate lower dimensional constraints, as is described in Sect. 2.3

2.2 ACCELERATED DATA ACQUISITION

Data acquisition refers to the strategies for exciting spins and collecting k-space samples in k-t space. Amongst these, fast pulse sequences such as Fast Low-Angle Shot Imaging (FLASH) [42] and SSFP [17], alongside fast readout schemes, including Echo-planar Imaging (EPI) [75], were crucial to the development and widespread commercialization of MRI scanners. Nonetheless, fast pulse sequences and readout schemes still need to collect samples at the Nyquist frequency in order to reconstruct images with no artifacts.

With the introduction of the modern acceleration techniques Parallel Imaging (PI) and CS, it is possible to overcome the Nyquist limit. PI is built on the observation that receiver coils have a spatial encoding effect, yielding speed-up factors proportional to the number of additional coils incorporated into the scanner [41, 67, 82]. CS exploits structure and redundancy present in NMR images to further accelerated scans [16, 27, 55]. Both of these techniques can be used in conjunction to recover full images from highly undersampled measurements, as shown in Eq. 41: PI considers data from multiple coils in the coil sensitivity operator $\mathbf{S}$ and the number of measurements is generally far less than the number of voxels $M \ll N$, thus requiring iterative reconstruction algorithms that incorporate prior information to regularize the ill-posed problem.

2.3 IMAGE RECONSTRUCTION WITH PRIOR INFORMATION

Let

$$\mathbf{d}_l = \rho_l f(\eta; \theta_l) \in \mathbb{C}^T, \tag{39}$$

represent the mapping of known acquisition parameters η and a set of biological parameters $\theta_l = \{T_1, T_2\}$ to a T-dimensional transient-state signal $\mathbf{d}_l \in \mathbb{C}^T$, where ρ_l represents a complex scaling factor. By considering an ensemble of L parameter combinations, it is possible to use Eq. 39 to compute a dictionary $\mathbf{D} \in \mathbb{C}^{T \times L}$ of multiple signal evolutions.

The exponential nature of the Bloch equations, which govern the dynamics of transient-state signals, indicate that there is a smooth

dependence of the signals in **D** with respect to θ. That is, small variations over θ will result in smooth signal changes of $f(\cdot)$. This signifies that signal evolutions of continuously sampled parameter combinations exhibit a high level of correlation. While this high level of correlation may be prohibitive to denoting each signal evolution in the dictionary as unique, one could still exploit it to create a low-dimensional temporal subspace. In the context of MRF, this idea has previously been used to compress the dictionary to less temporal coefficients via Singular Value Decomposition (SVD) [58] and recently paired with iterative reconstructions to constrain signal evolutions to a lower-dimensional subspace [6, 98]. Reconstruction with a temporal subspace can be achieved as follows.

Let $\mathbf{\Phi} \in \mathbb{C}^{T \times T}$ denote an orthonormal temporal basis obtained with Principal Component Analysis (PCA) such that $\mathbf{D} = \mathbf{\Phi}\mathbf{\Phi}^{*}\mathbf{D}$. A LR approximation of the temporal basis $\mathbf{\Phi}_K \in \mathbb{C}^{T \times K}$ can be obtained by truncating $\mathbf{\Phi}$ to its first K temporal coefficients, with $K \ll T$. One can project the image series **X** onto the temporal subspace by

$$\mathbf{Z} = \mathbf{\Phi}_K^{*}\mathbf{X} \in \mathbb{C}^{K \times N}. \tag{40}$$

Thus, by incorporating $\mathbf{\Phi}_K$ into the encoding operator

$$\mathbf{E}_K = \mathbf{UFS}\mathbf{\Phi}_K \tag{41}$$

it is possible to rewrite Eq. 37 as a function of **Z**

$$\mathbf{Y} = \mathbf{E}_K\mathbf{Z}. \tag{42}$$

It follows, that Eq. 38 can be re-formulated as a standard regularized reconstruction

$$\hat{\mathbf{Z}} = \arg\min_{\mathbf{Z}} \|\mathbf{E}_K\mathbf{Z} - \mathbf{Y}\| + R(\mathbf{Z}), \tag{43}$$

where the first term is the data fidelity term and the second term $R(\cdot)$ is the regularization term, corresponding to a local LR operator that acts on spatiotemporal image patches [35, 78, 83]. Equation 43 is readily solved with multiple iterative algorithms, such as the ADMM. In fact, most iterative reconstruction algorithms presented in this thesis present a similar two-term formulation, with the choice of regularization term and solver being the key difference amongst them. After solving for $\hat{\mathbf{Z}}$, one can estimate the image series by projecting back into the full temporal domain:

$$\hat{\mathbf{X}} = \mathbf{\Phi}_K\hat{\mathbf{Z}}. \tag{44}$$

2.4   PARAMETER ESTIMATION

The final goal of quantitative MRI is to provide a voxel-wise estimate of the parameters θ_n $n = 1,..,N$. As Eq. 33 establishes a forward model that predicts potential signal evolutions, a cost function can be defined and for every voxel in the reconstructed image series, solve Eq. 39 in a Non-Linear Least Squares (NLLS) sense

$$\{\hat{\rho}_n, \hat{\theta}_n\} = \arg\min_{\{\rho_n, \theta_n\}} \|\hat{\mathbf{x}}_n - \rho_n f(\eta; \theta_n)\|_2^2 . \tag{45}$$

Note that this departs from the dictionary matching approach proposed by MRF. In dictionary matching, a closest matching dictionary entry $\hat{l}$ is found by correlation

$$\hat{l} = \arg\max_l \frac{<\hat{\mathbf{x}}_n, \mathbf{d}_l>}{\|\hat{\mathbf{x}}_n\|_2 \|\mathbf{d}_l\|_2} \tag{46}$$

where the parametric maps of the corresponding entry are directly assigned to the voxel in question $\hat{\theta}_n = \theta_{\hat{l}}$ and the density ρ_n is determined by the scaling factor between $\hat{\mathbf{x}}_n$ and $\mathbf{d}_l$. This means that the resulting maps will necessarily be one of the L dictionary samples. Furthermore, the denominator in Eq. 46 shows that matching by correlation requires vector normalization. By doing so, magnitude information is lost, left only with directionality. Thus, if parameters in θ_n are encoded into the vectors magnitude, this encoding will be lost in the process of matching to the dictionary. This could signify that the selected entry might be confounded with other signals, affecting the matching procedure. Conversely, Eq. 45 is not subject to the discretization of and does not require vector normalization for parameter estimation.

Another alternative to parameter estimation is to rely on Bayesian inference methods to compute the posterior Probability Density Function (PDF) of the parameters θ_n given the data and the model. For instance, the high-performance computing framework Π4U [43] uses Transitional Markov Chain Monte Carlo (TMCMC) sampling to achieve this. The posterior PDF $p(\theta_n|\mathbf{x}_n, f_t(\cdot))$ of the parameters given the reconstructed data $\mathbf{x}_n$ and our signal model $f_t(\cdot)$:

$$p(\theta_n|\mathbf{x}_n, f_t(\cdot)) = \frac{p(\mathbf{x}_n,|\theta_n, f_t(\cdot))\pi(\theta_n)}{p(\mathbf{x}_n|f_t(\cdot)} . \tag{47}$$

In Eq. 47, $p(\mathbf{x}_n,|\theta_n, f_t(\cdot))$ is the likelihood of observing the data from the model, $\pi(\theta_n)$ is the prior, and $p(\mathbf{x}_n|f_t(\cdot)$ is the evidence of the model. From the posterior PDF, it is possible to compute the Maximum Likelihood (ML) of each of the parameters in the model, leading again to a voxel-wise parameter estimation and, consequently, parametric maps.

2.5   ANATOMICAL LABELING

Thus far, all shown examples have presented an encoding function to link acquisition parameters with quantitative parameters of interest. However, multiple medical imaging applications do not rely on the quantification of physical parameters, but on the discrete labeling of different tissue classes. For instance, one might be interested in segmenting the brain into typically observed healthy tissue, such as: Gray Matter (GM), White Matter (WM), Cerebrospinal Fluid (CSF), and Blood Vessels (BV); or into segmenting brain tumors into important regions [59].

In a way, anatomical labels are also quantitative maps — they are voxel-wise estimates that provide information on the underlying tissue characteristics. However, anatomical labels generally lack an encoding function that links the acquired data to the corresponding label. Therefore, machine learning based approaches acquire importance to *learn* the mapping from input data to output labels. Throughout the next chapters, multiple examples are shown on how machine learning techniques can be incorporated into quantitative MRI pipelines to simultaneously produce quantitative maps *and* anatomical labels from the same dataset.

Part II

PUBLICATIONS

STUDYING METABOLISM WITH HYPERPOLARIZED ^{13}C NMR

3

3.1 PEER-REVIEWED PUBLICATIONS

This chapter contains two publications in the area of hyperpolarized ^{13}C NMR. In Multisite Kinetic Modeling of ^{13}C Metabolic MR Using [1-13C]Pyruvate we develop, compare and validate an alternative model to evaluate dynamic time curves of spectroscopic data. Hyperpolarized ^{13}C Metabolic Magnetic Resonance Spectroscopy and Imaging provides a scientific overview of the methodology required to accurately conduct ^{13}C Magnetic Resonance Spectroscopic Imaging (MRSI) experiments with DNP, including the kinetic modeling of the injection bolus and its downstream metabolites.

3.1.1   *Multisite Kinetic Modeling of ^{13}C Metabolic MR Using [1-13C]Pyruvate*

Peer-reviewed Journal Paper

Authors: PA. Gómez, JI. Sperl, MA. Janich, O. Khegai, F. Wiesinger, SJ. Glaser, A. Haase, M. Schwaiger, R. Schulte, MI. Menzel

Abstract: Hyperpolarized ^{13}C imaging allows real-time *in vivo* measurements of metabolite levels. Quantification of metabolite conversion between $[1-^{13}$C]pyruvate and its downstream metabolites $[1-^{13}$C]alanine, $[1-^{13}$C]lactate, and $[^{13}$C]bicarbonate can be achieved with kinetic modeling. Since pyruvate interacts dynamically and simultaneously with its downstream metabolites, the purpose of this work is the determination of parameter values through a multisite, dynamic model involving possible biochemical pathways present in MR spectroscopy. Kinetic modeling parameters were determined by fitting the multisite model to time-domain dynamic metabolite data. The results for different pyruvate doses were compared with those of different two-site models to evaluate the hypothesis that for identical data the uncertainty of a model and the signal-to-noise ratio determine the sensitivity in detecting small physiological differences in the target metabolism. In comparison to the two-site exchange models, the multisite model yielded metabolic conversion rates with smaller bias and smaller standard deviation, as demonstrated in simulations with different signal-to-noise ratio. Pyruvate dose effects observed previously were confirmed and quantified through metabolic conversion rate values. Parameter interdependency allowed an accurate quantification and can therefore be useful for monitoring metabolic activity in different tissues.

Contribution of thesis author: Model development and implementation, experimental analysis, manuscript preparation and editing.

Research Article

Multisite Kinetic Modeling of ^{13}C Metabolic MR Using [1-^{13}C]Pyruvate

Pedro A. Gómez Damián,[1,2,3] **Jonathan I. Sperl,**[1] **Martin A. Janich,**[1,4,5]
Oleksandr Khegai,[1,5] **Florian Wiesinger,**[1] **Steffen J. Glaser,**[5] **Axel Haase,**[3]
Markus Schwaiger,[4] **Rolf F. Schulte,**[1] **and Marion I. Menzel**[1]

[1]*GE Global Research, 85748 Garching bei München, Germany*
[2]*Medical Engineering, Tecnológico de Monterrey, 64849 Monterrey, NL, Mexico*
[3]*Medical Engineering, Technische Universität München, 85748 Garching bei München, Germany*
[4]*Nuclear Medicine, Technische Universität München, 81675 Munich, Germany*
[5]*Chemistry, Technische Universität München, 85748 Garching bei München, Germany*

Correspondence should be addressed to Marion I. Menzel; menzel@ge.com

Hyperpolarized ^{13}C imaging allows real-time *in vivo* measurements of metabolite levels. Quantification of metabolite conversion between [1-^{13}C]pyruvate and downstream metabolites [1-^{13}C]alanine, [1-^{13}C]lactate, and [^{13}C]bicarbonate can be achieved through kinetic modeling. Since pyruvate interacts dynamically and simultaneously with its downstream metabolites, the purpose of this work is the determination of parameter values through a multisite, dynamic model involving possible biochemical pathways present in MR spectroscopy. Kinetic modeling parameters were determined by fitting the multisite model to time-domain dynamic metabolite data. The results for different pyruvate doses were compared with those of different two-site models to evaluate the hypothesis that for identical data the uncertainty of a model and the signal-to-noise ratio determine the sensitivity in detecting small physiological differences in the target metabolism. In comparison to the two-site exchange models, the multisite model yielded metabolic conversion rates with smaller bias and smaller standard deviation, as demonstrated in simulations with different signal-to-noise ratio. Pyruvate dose effects observed previously were confirmed and quantified through metabolic conversion rate values. Parameter interdependency allowed an accurate quantification and can therefore be useful for monitoring metabolic activity in different tissues.

1. Introduction

While ^{13}C magnetic resonance spectroscopy (MRS) has been utilized for *in vivo* imaging and spectroscopy of metabolism [1] for a long time, only the development of dynamic nuclear polarization (DNP) helped to overcome the inherent sensitivity limit; as through hyperpolarization using DNP followed by rapid dissolution, the ^{13}C MR signal can be amplified by more than 10,000-fold [2].

One of the most common and viable agents for *in vivo* use is [1-^{13}C]pyruvate (PYR) [3]. After intravenous injection, it is transported to the observed tissue or organ under observation, where it is enzymatically metabolized to its downstream metabolites [1-^{13}C]alanine (ALA) by alanine transaminase (ALT), [1-^{13}C]lactate (LAC) by lactate dehydrogenase (LDH), and [^{13}C]bicarbonate (BC) by pyruvate dehydrogenase (PDH) to varying extent, depending on tissue type and predominant metabolic activity. At the same time PYR is in chemical exchange with [1-^{13}C]pyruvate-hydrate (PYRH). As part of gluconeogenesis, PYR may also be carboxylated to oxaloacetate [4].

In order to quantify the metabolic exchange between PYR and its downstream metabolites, MRS data acquired over a certain time period after injection first require assignment of

spectral peaks [5] in the spectral domain and second require quantification of these peaks over time. Several different methods have been used for this time-domain analysis, and among these the most simple and robust method is the determination of metabolite signal ratios. These ratios are usually obtained from the peak metabolite signals [6] or through integrating over time [5]. The latter approach has been employed in our previous study, conducted by Janich et al. [5], where hyperpolarized PYR spectra were quantified for different PYR doses and subsequently used to determine the dose effects on Wistar rats based on time integrated metabolite signal ratios.

Although the approach of obtaining relative metabolite signal ratios, LAC to PYR or ALA to PYR, is straightforward and robust, independently if obtained from peak signal or time integrals, the results suffer from an increasingly strong T_1 weighting of the integral, which skews the resulting ratios. Furthermore, although time-domain visualization and signal ratio determination is an effective tool for assessing the effect of different PYR doses, it provides no quantitative kinetic data of metabolic exchange.

In order to achieve this quantification, different methods for kinetic modeling of hyperpolarized ^{13}C MR data have been reported. Most approaches, derived from the modified Bloch equations, represent a two-site interaction between PYR and one specific downstream metabolite, for example, either LAC or ALA [7–14]. Modeling can be extended to include more sites (intra- and extracellular) or more metabolites [9, 12] (for a comprehensive comparison, see [15]). Even so, presumably for robustness, previous work focuses primarily on fitting data with just one downstream metabolite, keeping most parameters fixed, or even model free, based on signal ratios [5, 16, 17]. When PYR is injected and the corresponding metabolic reactions begin to take place, PYR is not metabolized exclusively into ALA (or LAC), but it changes dynamically into all of the aforementioned downstream metabolites [18]. There is furthermore some skepticism, if the implicit assumption of rate constant stability holds in all applications [17] and there are few analyses on model parameter dependence on SNR [19]. In particular, metabolic conversion in the heart predominantly follows the PDH path producing BC [6, 20]. We therefore hypothesize that the simultaneous consideration of various metabolic pathways is necessary to obtain an accurate evaluation of *in vivo* metabolic conversion rates. On this basis, we propose using a mathematical framework for multisite modeling (similar to [8, 21, 22]) by simultaneously fitting different possible ^{13}C metabolic pathways for PYR, which can typically be observed after injection of pyruvate labeled in the [1-^{13}C] position.

Additionally, although our prior work [5] evaluates quantification of spectra and employed a semiquantitative method to investigate metabolic conversion under different PYR doses (based on metabolite to PYR ratios), it does not provide fully quantitative kinetic data. Therefore, in this subsequent work we employ the experimental data obtained in [5] and implement the proposed multisite, dynamic model to determine metabolic conversion and signal decay rates for full

quantification of the kinetics of metabolic conversion. Furthermore, the proposed model gives access to effective longitudinal relaxation times ($T_{1\mathrm{eff}}$), both for PYR and for the downstream metabolites.

Using the identical biological data, the kinetic parameters estimated by the multisite model are then compared to the parameters obtained using the two-site models proposed both in [8] and in [23]. The estimated parameters of all models are also compared between the three different doses utilized in [5], that is, 20, 40, and 80 mM (corresponding to 0.1, 0.2, and 0.4 mmol/kg bodyweight) of PYR, in order to evaluate the capability of the model for the assessment of dose response. As identical data is used, the evaluation allows for direct assessment of kinetic model stability and quality. Ideally, a successful kinetic model would allow the reduction of data variability due to modeling to a minimum, allowing the visualization of biological variability (i.e., as a response to dose treatment, etc.). In addition, using simulated metabolic data based on exemplary conversion rates, we assessed the variability and stability of the kinetic models under the influence of noise. Here, the expectation towards a model is that both systematic bias and standard deviation of the resulting metabolic conversion rates should be as low as possible over a large range of signal-to-noise ratio (SNR).

2. Theory

In our previous study [5], MRS spectral data after injection of pyruvate was acquired and analyzed utilizing time-domain fitting with AMARES [24], resulting in a time course of metabolite levels. To quantify the metabolic conversion, this previous study employed integrated metabolite signal ratios. In the following paragraphs, we will compare this simple integrative approach to kinetic modeling using three different approaches, which are two-site exchange differential model, two-site exchange integral model, and multisite exchange integral model.

2.1. Two-Site Exchange Differential Model. Using a two-site exchange differential model (2SDM) allows computing metabolic exchange rates $k_{\mathrm{pyr} \to x}$ and the respective metabolite's effective signal decay rates r_x by solving a system of linear equations given in differential form

$$\frac{dM_x(t)}{dt} = -r_x M_x(t) + k_{\mathrm{pyr} \to x} M_{\mathrm{pyr}}(t). \qquad (1)$$

The effective metabolite signal decay rate r_x is dominated by T_1 relaxation, the respective backward metabolic exchange rate $k_{x \to \mathrm{pyr}}$, and a flip angle (FA) term, which also depends on the repetition time (TR), accounting for the irreversible consumption of signal after successive excitations:

$$r_x = \frac{1}{T_x} + k_{x \to \mathrm{pyr}} + f(\mathrm{FA}) \qquad (2)$$

with

$$f(\mathrm{FA}) = \frac{1 - \cos(\mathrm{FA})}{\mathrm{TR}}. \qquad (3)$$

Hence, r_x results in a single, inseparable term of signal decay. However, FA and TR are known from experimentation and

can be corrected for. In case the backward exchange rate $k_{x \to \mathrm{pyr}}$ is assumed to be negligible, true T_1 relaxation times can be quantified; however, it remains unclear whether this assumption holds true in all physiological states of the animal.

2SDM does not assume a PYR input function and for that reason the first order differential equation (1) can be solved as a linear system. This approach is independent of the time course of PYR administration and is therefore straightforward to apply.

2.2. Two-Site Exchange Integral Model. Another approach in kinetic modeling, the two-site exchange integral model (2SIM), assumes a PYR input function that represents the PYR signal in time ($M_{\mathrm{pyr}}(t)$). In Zierhut et al. [8] a series of piecewise defined exponential equations were presented:

$$M_{\mathrm{pyr}}(t) = \begin{cases} \dfrac{I_{\mathrm{pyr}}}{r_{\mathrm{pyr}}}\left[1 - e^{-r_{\mathrm{pyr}}(t-t_{\mathrm{arrival}})}\right], & t_{\mathrm{arrival}} \leq t < t_{\mathrm{end}}, \\ M_{\mathrm{pyr}}(t_{\mathrm{end}})\, e^{-r_{\mathrm{pyr}}(t-t_{\mathrm{end}})}, & t \geq t_{\mathrm{end}}. \end{cases}$$
(4)

The first part of the equation takes into account PYR signal loss due to r_{pyr} and the injection of PYR with a constant rate I_{pyr} from the arrival time t_{arrival} until t_{end}. It nevertheless assumes that no conversion of PYR takes place during injection. The second part, for all time measurements later than t_{end}, is characterized only by the PYR signal loss. In a similar manner, an assumption on the initial PYR concentration can be made instead of an assumption on the input function, leading to the modeling of only the exponential decay, as shown in [25]. Explicit modeling of M_{pyr} allows for (1) to be solved yielding metabolite signals in time [8]:

$M_x(t)$

$$= \begin{cases} \dfrac{k_{\mathrm{pyr} \to x} I_{\mathrm{pyr}}}{r_{\mathrm{pyr}} - r_x}\left[\dfrac{1 - e^{-r_x(t-t_{\mathrm{arrival}})}}{r_x} - \dfrac{1 - e^{-r_{\mathrm{pyr}}(t-t_{\mathrm{arrival}})}}{r_{\mathrm{pyr}}}\right], \\ \qquad\qquad\qquad\qquad\qquad t_{\mathrm{arrival}} \leq t < t_{\mathrm{end}}, \\ \dfrac{M_{\mathrm{pyr}}(t_{\mathrm{end}}) * k_{\mathrm{pyr} \to x}}{r_{\mathrm{pyr}} - r_x}\left[e^{-r_x(t-t_{\mathrm{end}})} - e^{-r_{\mathrm{pyr}}(t-t_{\mathrm{end}})}\right] \\ \quad + M_x(t_{\mathrm{end}})\, e^{-r_x(t-t_{\mathrm{end}})}, \\ \qquad\qquad\qquad\qquad\qquad t \geq t_{\mathrm{end}}. \end{cases}$$
(5)

Alongside the parameters characterizing the PYR input function, these equations contain the same parameters ($k_{\mathrm{pyr} \to x}$ and r_x) that were solved for using 2SDM.

2SIM can be considered as a two-step approach. First, t_{arrival}, r_{pyr}, and I_{pyr} are determined by fitting (4) to the measured PYR signal. t_{end} is simply calculated by summing t_{arrival} and the known injection duration. These parameters are then utilized to fit (5) to the LAC and ALA signals. In [6], this model is also utilized to fit the BC signal. Finally the computed metabolic exchange rates $k_{\mathrm{pyr} \to x}$, the decay rate r_{pyr}, and the flip angle correction (3) can be used to estimate apparent T_1 relaxation of PYR.

2.3. Multisite Exchange Integral Model. As described above, the metabolite signal decay rate r_x depends on T_1 relaxation, backward metabolic exchange rates $k_{x \to \mathrm{pyr}}$, and signal loss from flip angle variations. On the other hand, the PYR signal decay r_{pyr} does not depend on backward metabolic exchange, but on forward metabolic exchange rates $k_{\mathrm{pyr} \to x}$. This signifies that the rate of PYR decay is also proportional to the rate of PYR downstream conversion.

Hence, when passing from 2SIM to a multisite exchange integral model (MSIM), the PYR input function (4)—represented in its differential form—needs to include all of the metabolic exchange rates:

$$\frac{dM_{\mathrm{pyr}}(t)}{dt} = \begin{cases} -r_{\mathrm{pyr}} M_{\mathrm{pyr}}(t) - \displaystyle\sum_x k_{\mathrm{pyr} \to x} M_{\mathrm{pyr}}(t) + I_{\mathrm{pyr}}, \\ \quad t_{\mathrm{arrival}} \leq t < t_{\mathrm{end}}, \\ -r_{\mathrm{pyr}} M_{\mathrm{pyr}}(t) - \displaystyle\sum_x k_{\mathrm{pyr} \to x} M_{\mathrm{pyr}}(t), \\ \quad t \geq t_{\mathrm{end}}. \end{cases}$$
(6)

Note that both the PYR signal decay rate r_{pyr} and the sum of all the metabolic exchange rates $\sum_x k_{\mathrm{pyr} \to x}$ are multiplied by the same term $M_{\mathrm{pyr}}(t)$ and can therefore be grouped into a total PYR signal decay rate:

$$R_{\mathrm{pyr}} = r_{\mathrm{pyr}} + \sum_x k_{\mathrm{pyr} \to x}.$$
(7)

By replacing (7) in (6), the integral form of the new PYR input function reads

$$M_{\mathrm{pyr}}(t) = \begin{cases} \dfrac{I_{\mathrm{pyr}}}{R_{\mathrm{pyr}}}\left[1 - e^{-R_{\mathrm{pyr}}(t-t_{\mathrm{arrival}})}\right], & t_{\mathrm{arrival}} \leq t < t_{\mathrm{end}}, \\ M_{\mathrm{pyr}}(t_{\mathrm{end}})\, e^{-R_{\mathrm{pyr}}(t-t_{\mathrm{end}})}, & t \geq t_{\mathrm{end}}. \end{cases}$$
(8)

The representation of the total PYR relaxation rate R_{pyr} as the sum of the PYR relaxation rate and the metabolic conversion rates allows for a simultaneous fitting process, where the conversion rates are taken into account also in the PYR input function, creating dependent curves and a parameter interdependency. In addition, the estimation of T_1 values for PYR can be achieved directly using

$$\frac{1}{T_{1\mathrm{pyr}}} = r_{\mathrm{pyr}} - f(\mathrm{FA}).$$
(9)

Utilizing the same R_{pyr} term for the metabolite signals, (5) becomes

$M_x(t)$

$$= \begin{cases} \dfrac{k_{\mathrm{pyr} \to x} I_{\mathrm{pyr}}}{R_{\mathrm{pyr}} - r_x}\left[\dfrac{1 - e^{-r_x(t-t_{\mathrm{arrival}})}}{r_x} - \dfrac{1 - e^{-R_{\mathrm{pyr}}(t-t_{\mathrm{arrival}})}}{R_{\mathrm{pyr}}}\right], \\ \qquad\qquad\qquad\qquad\qquad t_{\mathrm{arrival}} \leq t < t_{\mathrm{end}}, \\ \dfrac{M_{\mathrm{pyr}}(t_{\mathrm{end}}) * k_{\mathrm{pyr} \to x}}{R_{\mathrm{pyr}} - r_x}\left[e^{-r_x(t-t_{\mathrm{end}})} - e^{-R_{\mathrm{pyr}}(t-t_{\mathrm{end}})}\right] \\ \quad + M_x(t_{\mathrm{end}})\, e^{-r_x(t-t_{\mathrm{end}})}, \\ \qquad\qquad\qquad\qquad\qquad t \geq t_{\mathrm{end}}. \end{cases}$$
(10)

As seen in (2), the backward exchange rates are inseparably confounded with T_1 in the respective signal decay rate r_x of each metabolite. A nonnegligible backward reaction thus leads to an overestimation of the true T_1 values for all of the downstream metabolites. For LAC, the overestimation might be considered negligible since the backward reaction was reported to have only a very small effect on kinetics [26], although earlier work indicates upregulated gluconeogenesis in liver-metabolism of tumor-bearing rats [27]. The assumption of negligible backward reactions might also not hold for ALA. There is no need to apply a backward exchange to BC; however, depending on pH, it is breathed out as $^{13}CO_2$ and this could lead to an apparent shortening in T_1. This signifies that the T_1 values for ALA and BC obtained utilizing this model can only be considered bounds for the true value.

3. Methods

3.1. Experimental Data. The experimental data was obtained from healthy male Wistar rats through the acquisition of slice-selective FID signals in heart, liver, and kidney tissue. Three different hyperpolarized PYR concentrations (20, 40, and 80 mM, which correspond to an injected dose of 0.1, 0.2, and 0.4 mmol/kg bodyweight) were utilized to measure a total of 15 animals. Each dose was injected into five different animals twice, resulting in a total of 10 measurements for each dose. A flip angle of 5° was utilized and TR was triggered to animal breathing yielding an average value of ~1 s. SNR was calculated by dividing the maximum PYR signal by the average noise for all time steps. More experimental details can be directly found in [5].

Further exemplary data to evaluate modeling performance at presence of pathology were obtained from adult female Fischer 344 rats (Charles River, Sulzfeld, Germany) beating subcutaneous mammary adenocarcinomas. The animals' anesthesia was maintained with 1–3% isoflurane in oxygen starting about 1 h before the first injection. During the experiment, the heart rate, temperature, and breathing signal were monitored using an animal monitoring system (SA Instruments, Stony Brook, NY, USA). All ^{13}C animal experiments were approved by the regional governmental commission for animal protection (Regierung von Oberbayern, Munich, Germany). Two injections were performed using an 80 mM concentration, allowing for direct comparison. For this set of experiments, a flip angle of 10° was utilized and TR was fixed to 1 s.

3.2. Data Processing. The experimental data $y_{m,i}$ with $m \in$ {lac, ala, pyr, bc} acquired at time steps t_i was fitted to MSIM in a constrained least-squares sense; that is,

$$\min_\beta f(\beta) \qquad \text{s.t. } \text{lb} \leq \beta \leq \text{ub}, \qquad (11)$$

with cost function

$$f(\beta) = \sum_m \sum_i \left(y_{m,i} - M_m(t_i, \beta)\right)^2, \qquad (12)$$

parameters $\beta = [r_{\text{lac}}, \ldots, r_{\text{bc}}, k_{\text{pyr} \to \text{lac}}, \ldots, k_{\text{pyr} \to \text{bc}}, I_{\text{pyr}}, t_{\text{end}}]$, and lower and upper bounds lb and ub, respectively. While

t_{arrival} was fixed to the time when the PYR signal reached 10% of its maximum peak value, t_{end} was set as a fitting parameter accounting for various injection times. On the contrary, the implementation in [8] kept t_{end} fixed while fitting for t_{arrival}. Even though the duration of the injection was known, fixing t_{arrival} in function of its peak value and calculating t_{end} as a parameter allowed for different delivery and perfusion times. Delivery, perfusion, and export are however not implicitly included in the model. To improve the convergence properties of the optimization, the gradient of the cost function was calculated analytically. The optimization was carried out using the MATLAB function *fmincon* (MathWorks, Natick, MA, USA) employing the *Trust Region Reflective Algorithm* and a function tolerance of $1E - 10$. The utilized bound constraints were set to physically relevant limits: upper bounds of $0.1 \, \text{s}^{-1}$ for metabolic conversion rates $k_{\text{pyr} \to x}$, since they have been reported to be of a smaller order [8, 23], and of $0.005 \, \text{s}^{-1}$ for the decay rates r_x (equivalent to a 200 s inverse effective signal decay rate) and lower bounds establishing the positivity of all parameters. Note that the optimization always converged far away from the bounds and they were only implemented for numerical improvement. After optimization, T_1 values were estimated for all metabolites from the effective signal decay rate (see (2) and (9)). Initial conditions were fixed to expected normal parameters; however, randomizing the starting guess in between bounds and performing various iterations yielded comparable results.

Pyruvate-hydrate (PYRH), which is also present in spectroscopy, was not included in the minimization process. The reason for this is that conversion between PYR and PYRH is not enzymatic and we are interested in quantifying metabolic rates that lead to a better understanding of enzymatic activity. Additionally, since chemical exchange with PYRH is instantaneous and almost in equilibrium, including PYR would require adding three extra parameters to the minimization without providing additional information regarding metabolic activity. In fact, if PYRH were to be included, the immediate conversion of PYR to PYRH would lead to an overestimation of the apparent metabolic rate, which in turn would decrease all other parameters intrinsic in R_{pyr} leading to an overestimation of T_1 values for PYR.

The same reasoning holds for the exclusion of additional pools. Although the MSIM model can be further extended to include multiple pools [15, 22], including them only adds variables to the minimization with no direct benefit to the determination of enzymatic conversion rates.

4. Results

4.1. Convergence and Quality of Fit. Parameter fitting with MSIM was shown to converge to an optimal point for every set of experimental data. Figures 1(a)–1(c) show the fitted curves of all metabolites for all models. The residuals for every metabolite and every measurement in the time domain were analyzed (Figures 1(d)–1(f)), and the error of the fitted curves and computed parameters was determined based on the parameter covariance matrix [28]. This error was utilized to determine 95% confidence intervals on the fitted data (see Figures 1(a)–1(c)).
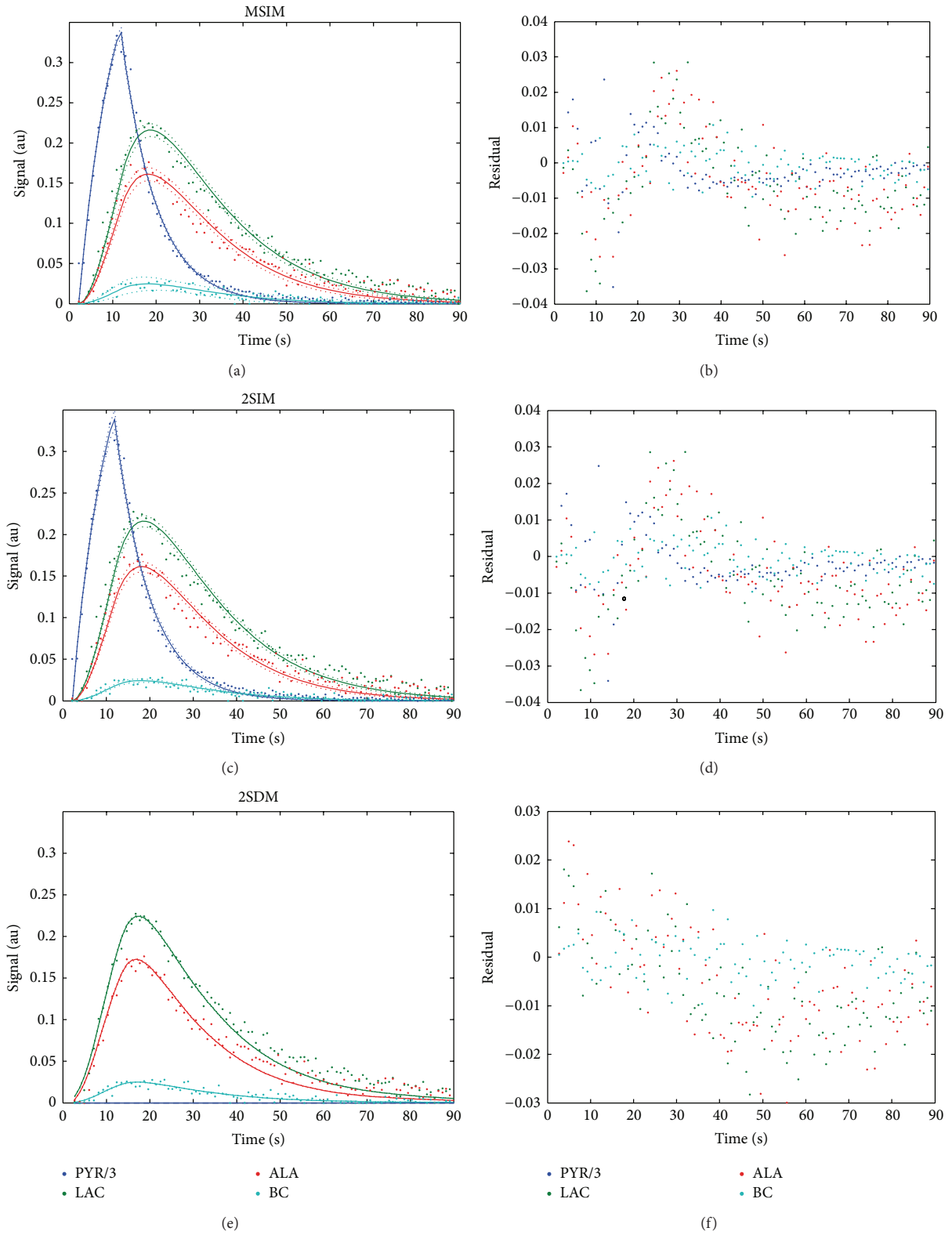
FIGURE 1: Example of metabolic data acquired for a 40 mM (0.2 mmol/kg) dose in kidney predominant tissue, fitted curves (solid lines) using (a) MSIM, (b) 2SIM, and (c) 2SDM and 95% confidence intervals (dotted lines). (d–f) Residuals of fit.

TABLE 1: Exemplary parameter estimates (± standard error) obtained from three different kinetic modeling methods for a 40 mM (0.2 mmol/kg) dose of kidney predominant tissue.

Model	MSIM	2SIM	2SDM
$k_{\mathrm{pyr}\to\mathrm{lac}}$ [s^{-1}]	$0.03194 \pm 9.71E-04$	$0.03202 \pm 7.75E-04$	$0.03448 \pm 1.15E-03$
$k_{\mathrm{pyr}\to\mathrm{ala}}$ [s^{-1}]	$0.02507 \pm 1.07E-03$	$0.02518 \pm 4.97E-04$	$0.02832 \pm 1.02E-04$
$k_{\mathrm{pyr}\to\mathrm{bc}}$ [s^{-1}]	$0.00379 \pm 1.51E-03$	$0.00381 \pm 2.67E-04$	$0.00392 \pm 4.48E-04$
$T_{1\mathrm{lac}}$ [s]	16.36 ± 0.620	16.28 ± 0.488	14.13 ± 0.629
$T_{1\mathrm{ala}}$ [s]	14.48 ± 0.752	14.38 ± 0.552	12.18 ± 0.578
$T_{1\mathrm{bc}}$ [s]	14.11 ± 4.78	14.11 ± 1.19	13.46 ± 2.051
$T_{1\mathrm{pyr}}$ [s]	16.67 ± 0.676	16.82 ± 0.845	N/A*

* According to (1), 2SDM only fits for $k_{\mathrm{pyr}\to x}$ exchange rates and the corresponding T_1 values.
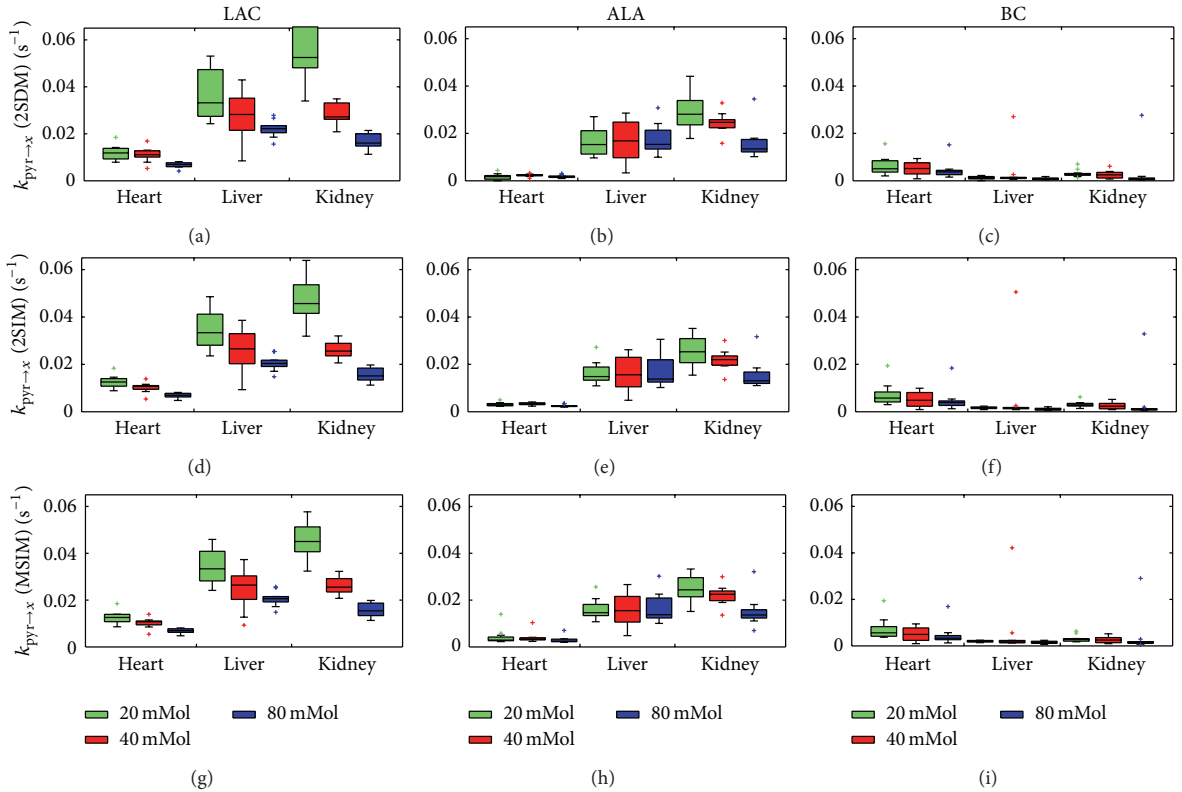

FIGURE 2: Metabolic conversion rates of LAC (left), ALA (center), and BC (right) obtained for heart, kidney, and liver predominant slices at 20, 40, and 80 mM concentrations (0.1, 0.2, and 0.4 mmol/kg doses) for 2SDM (top), 2SIM (center), and MSIM (bottom). Every box plot displays minima, 25th percentiles, medians, 75th percentiles, maxima, and outliers.

Note that for both MSIM and 2SIM the residuals have a distinct pattern. The pattern indicates that a linear injection rate does not fully model biological activity. In [9], the input function is modeled as a trapezoidal instead of a linear input, but the authors provide no residual analysis. On the other hand, assuming no input function by establishing a fixed initial PYR concentration [25] or solving the differential linear system may not fully account for the entire kinetic time course of the measured signals. In any case, this should be considered as a limitation for both models.

4.2. Model Comparison. For all of the experimental data, parameters were obtained utilizing the 2SDM, the 2SIM, and the MSIM. While a single implementation of MSIM brought forth parameter values for all downstream metabolites, an independent implementation for LAC, ALA, and BC was necessary in the two-site models. Since all three models were applied on exactly the same experimental data, the comparison between them and to the results obtained for the integrated metabolite signal ratios obtained from Janich et al. [5] directly allows assessing model accuracy separated from biological variability and experiment related inaccuracies like low SNR levels. Results from one exemplary minimization are shown in Table 1; Table 2 displays mean estimated $T_{1\mathrm{pyr}}$ values for all experiments and their respective SNR levels; and Figure 2 details the obtained metabolic conversion rates for all three models.

TABLE 2: T_{1pyr} calculated for MSIM and 2SIM and corresponding SNR levels for all concentrations and slices (mean ± standard deviation).

	T_{1PYR} (MSIM)	T_{1PYR} (2SIM)	SNR
20 mMol			
Heart	8.93 ± 2.68	9.04 ± 2.82	15.52 ± 3.87
Liver	22.14 ± 12.26	24.25 ± 14.28	8.62 ± 2.03
Kidney	27.63 ± 12.11	61.61 ± 91.27	11.63 ± 1.87
40 mMol			
Heart	10.02 ± 2.81	10.17 ± 2.88	44.57 ± 15.56
Liver	20.70 ± 3.72	22.83 ± 8.44	20.14 ± 6.36
Kidney	21.11 ± 7.04	21.73 ± 9.20	27.58 ± 5.38
80 mMol			
Heart	10.85 ± 5.98	10.94 ± 6.11	84.65 ± 32.32
Liver	25.75 ± 7.90	25.88 ± 7.89	23.06 ± 14.60
Kidney	20.69 ± 10.38	20.00 ± 10.33	29.61 ± 12.95

Conversion rates and T_{1PYR} values calculated with MSIM tended to be lower than those of 2SIM and these in turn are lower than 2SDM (see Tables 1 and 2). Although performance is very similar for all models, reduced data spread can be observed in PYR to LAC conversion in kidney predominant tissue (Figure 2). Since MSIM fits up to nine parameters simultaneously, estimated error from the parameter covariance matrix was usually higher for MSIM.

Additionally, for an exemplary dataset, a noise analysis of all three models was implemented by adding Gaussian noise to different extent. Parameters were first obtained from an exemplary minimization with MSIM and were then subsequently used for time curve simulation. Every model was then fit 1,000 times with different initial parameters to this simulated time curve to create a model specific ground truth. Finally, based once again on 1,000 iterations, the simulated dataset was corrupted with random Gaussian noise and minimized with each model. Figure 3 displays mean and standard deviation of $k_{pyr \to lac}$ values up to a 10% noise level.

Figure 3 illustrates that although all models yield the same results in noise-free data, with increasing noise both bias and standard deviation of the two-site models 2SIM and 2SDM increase. As a consequence, the resulting metabolic conversion rates obtained from these two-site models increasingly suffer from systematic under- or overestimation. In contrast, the simulation demonstrates that the MSIM model remains bias-free, even with increased noise level, while exhibiting the smallest standard deviation compared to the two-site models.

From experimental results, it is clear that SNR increases with higher concentrations of injected PYR and that 20 mMol injections in liver and kidney predominant tissue had the lowest SNR (with corresponding noise levels of nearly 10%), whereas SNR in heart was generally higher but had a larger standard deviation (Table 2). According to noise simulations, it is precisely in low SNR regions that MSIM is expected to perform with lower deviations. Standard deviations for T_{1pyr} values and reduced data spread in 20 mMol k_{pyr} quantification, especially in kidney predominant tissue, are indications that this holds.
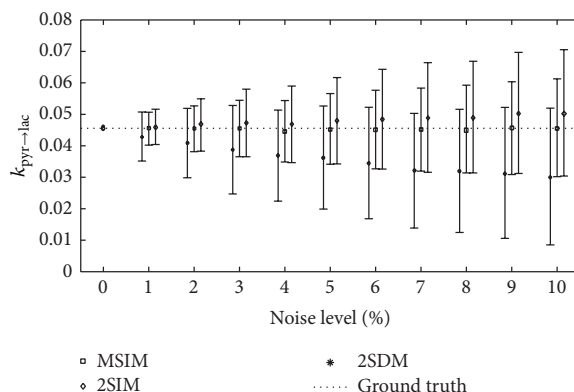

FIGURE 3: Noise level analysis for exemplary simulated data. Error bars show mean ± standard deviation.

4.3. Pyruvate Dose Assessment. The effects of PYR dose on Wistar rats were examined through the injection of solutions with concentrations of 20, 40, and 80 mM (doses of 0.1, 0.2, and 0.4 mmol/kg) hyperpolarized PYR. Kinetic data was obtained for all downstream metabolites and visualized with the same box plots used in [5]. With this approach, a direct comparison between the results previously obtained and the results obtained with kinetic modeling could be made, using median values as a distance dimension between the results obtained by the different models, rather than as confirmatory values (see Figure 2). As in [5], all median values suggest saturation effects. A more detailed assessment of the PYR dose effects on metabolism and its biological interpretation can be found in [5].

4.4. Tumor Evaluation. In tumor cells, it is well known that conversion from PYR to LAC is elevated even in the presence of oxygen [29, 30]. Additionally, some tumors show changes in alanine transaminase activity, leading to suppression of conversion of PYR to ALA [31–34]. Both effects were quantified by comparing experimental data obtained from a healthy rat and a rat with mammary carcinoma and using MSIM to obtain conversion rate parameters (see Figure 4). It can be seen that, for the same dose, the $k_{pyr \to lac}$ conversion rate was more than four times larger in tumor cells than healthy cells and the $k_{pyr \to ala}$ rate was more than 18 times larger in healthy cells than tumor cells. Therefore, obtained conversion rates provide a quantitative metric of metabolic differences between healthy and tumor cells.

5. Discussion and Conclusion

Three different kinetic modeling methods were implemented and investigated for the quantification of time-dependent metabolite levels. The two-site exchange differential model (2SDM) and two-site exchange integral model (2SIM) assume a two-site interaction between pyruvate (PYR) and one specific metabolite. The proposed multisite exchange integral model (MSIM) takes into account various downstream metabolites in one system and allows fitting in a one-step process. That is, all of the parameters are generated in a single
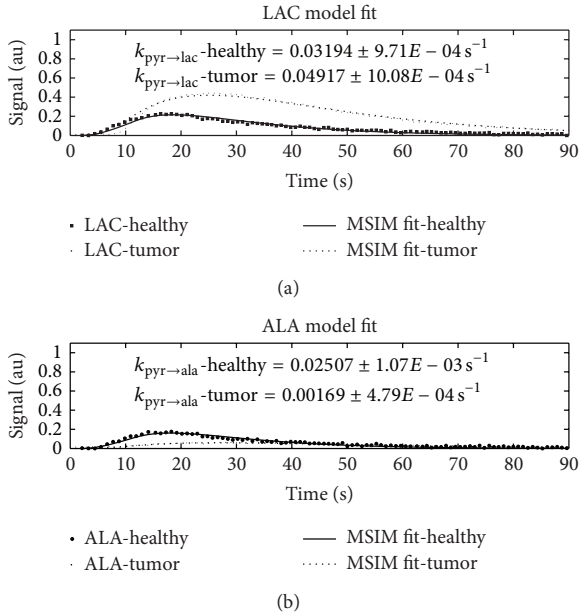
(a)

(b)

FIGURE 4: Comparison of $k_{\mathrm{pyr}\to\mathrm{lac}}$ and $k_{\mathrm{pyr}\to\mathrm{ala}}$ conversion rates between a healthy rat (from an 80 mM dose in kidney predominant tissue) and a rat with mammary carcinoma.

minimization, avoiding the need for separate implementations for every specific metabolite and resulting in a robust, optimal convergence far from the imposed constraints.

The three models were compared by taking median values as a distance dimension and, using exemplary simulated data, performing a noise analysis. In this analysis, metabolic exchange rate values obtained with 2SDM and 2SIM showed a bias with increasing noise levels. On the other hand, MSIM showed almost no bias, maintaining the average computed value close to the ground truth even at high noise levels, with smaller standard deviations than 2SDM and 2SIM.

Using the experimental data of [5], all kinetic models were compared between different PYR concentrations to assess the effect of increased PYR doses on *in vivo* metabolism. Results obtained from all three kinetic models were very similar; however, MSIM yielded smaller data spread for metabolic conversion in low SNR experiments and more accurate effective T_1 values for PYR as downstream metabolite rates are taken into account during the optimization, while effective T_1-estimation in 2SIM requires postprocessing corrections.

MSIM was then further utilized to evaluate model performance in disease. Obtained conversion rates from MSIM showed significant differences in healthy cells in comparison to tumor cells, where LAC conversion was elevated and ALA conversion, on the other hand, was suppressed.

Extending two-site models into a multisite model yields both biological and numerical insight. Biologically, it has been shown that calculated rates give proof of the saturation effects studied in [5] and can be used to quantify metabolic differences between normal and tumor cells. Numerically, a one-step fitting process with parameter interdependency

performs marginally better than other fitting methods, particularly in regions with low SNR. Further work with the MSIM model will focus on pixelwise metabolic mapping of cellular activity and its application to different metabolic systems.

Abbreviations

x:	Index of downstream metabolites: lactate, alanine, bicarbonate, and pyruvate-hydrate
$k_{\mathrm{pyr}\to x}$:	Metabolic conversion rate from pyruvate to x
LDH:	Lactate dehydrogenase
ALT:	Alanine transaminase
PDH:	Pyruvate dehydrogenase
CA:	Carbonic anhydrase
2SDM:	Two-site differential model
2SIM:	Two-site integral model
MSIM:	Multisite integral model
$M_x(t)$:	Time dependent signal for metabolite x
$M_{\mathrm{pyr}}(t)$:	Time dependent pyruvate signal
$f(\mathrm{FA})$:	Flip angle function
t_{arrival}:	Time of pyruvate arrival
t_{end}:	Time at which pyruvate is no longer injected
I_{pyr}:	Pyruvate injection rate
r_x:	Metabolite signal decay
r_{pyr}:	Pyruvate signal decay rate without metabolic conversion rates
R_{pyr}:	Pyruvate signal decay rate including metabolic conversion rates
lb:	Vector of lower bounds
ub:	Vector of upper bounds
m:	Index of all metabolites (lactate, alanine, pyruvate, and bicarbonate)
t_i:	Sampling times
β:	Vector of optimization parameters
$y_{m,i}$:	Measured data point for metabolite m and time step t_i
$M_m(t,\beta)$:	Time dependent signal of metabolite m as a function of parameters β.

Conflict of Interests

Acknowledgments

Radiology Research and Practice   9

References

[1] K. M. Brindle, "NMR methods for measuring enzyme kinetics *in vivo*," *Progress in Nuclear Magnetic Resonance Spectroscopy*, vol. 20, no. 3, pp. 257–293, 1988.

[2] J. H. Ardenkjær-Larsen, B. Fridlund, A. Gram et al., "Increase in signal-to-noise ratio of >10,000 times in liquid-state NMR," *Proceedings of the National Academy of Sciences of the United States of America*, vol. 100, no. 18, pp. 10158–10163, 2003.

[3] K. Golman, R. In 't Zandt, and M. Thaning, "Real-time metabolic imaging," *Proceedings of the National Academy of Sciences of the United States of America*, vol. 103, no. 30, pp. 11270–11275, 2006.

[4] M. E. Bizeau, C. Short, J. S. Thresher, S. R. Commerford, W. T. Willis, and M. J. Pagliassotti, "Increased pyruvate flux capacities account for diet-induced increases in gluconeogenesis in vitro," *American Journal of Physiology*, vol. 281, no. 2, pp. R427–R433, 2001.

[5] M. A. Janich, M. I. Menzel, F. Wiesinger et al., "Effects of pyruvate dose on *in vivo* metabolism and quantification of hyperpolarized ^{13}C spectra," *NMR in Biomedicine*, vol. 25, no. 1, pp. 142–151, 2012.

[6] H. J. Atherton, M. A. Schroeder, M. S. Dodd et al., "Validation of the *in vivo* assessment of pyruvate dehydrogenase activity using hyperpolarised ^{13}C MRS," *NMR in Biomedicine*, vol. 24, no. 2, pp. 201–208, 2011.

[7] S. E. Day, M. I. Kettunen, F. A. Gallagher et al., "Detecting tumor response to treatment using hyperpolarized 13C magnetic resonance imaging and spectroscopy," *Nature Medicine*, vol. 13, no. 11, pp. 1382–1387, 2007.

[8] M. L. Zierhut, Y.-F. Yen, A. P. Chen et al., "Kinetic modeling of hyperpolarized ^{13}C$_1$-pyruvate metabolism in normal rats and TRAMP mice," *Journal of Magnetic Resonance*, vol. 202, no. 1, pp. 85–92, 2010.

[9] D. M. Spielman, D. Mayer, Y.-F. Yen, J. Tropp, R. E. Hurd, and A. Pfefferbaum, "In vivo measurement of ethanol metabolism in the rat liver using magnetic resonance spectroscopy of hyperpolarized [1-^{13}C]pyruvate," *Magnetic Resonance in Medicine*, vol. 62, no. 2, pp. 307–313, 2009.

[10] O. Khegai, R. F. Schulte, M. A. Janich et al., "Apparent rate constant mapping using hyperpolarized [1–^{13}C]pyruvate," *NMR in Biomedicine*, vol. 27, no. 10, pp. 1256–1265, 2014.

[11] J. M. Park, S. Josan, T. Jang et al., "Metabolite kinetics in C6 rat glioma model using magnetic resonance spectroscopic imaging of hyperpolarized [1-^{13}C]pyruvate," *Magnetic Resonance in Medicine*, vol. 68, no. 6, pp. 1886–1893, 2012.

[12] S. Josan, D. Spielman, Y.-F. Yen, R. Hurd, A. Pfefferbaum, and D. Mayer, "Fast volumetric imaging of ethanol metabolism in rat liver with hyperpolarized [1-^{13}C]pyruvate," *NMR in Biomedicine*, vol. 25, no. 8, pp. 993–999, 2012.

[13] M. I. Kettunen, D.-E. Hu, T. H. Witney et al., "Magnetization transfer Measurements of exchange between hyperpolarized [1-^{13}C]pyruvate and [1-^{13}C]lactate in a murine lymphoma," *Magnetic Resonance in Medicine*, vol. 63, no. 4, pp. 872–880, 2010.

[14] P. E. Z. Larson, A. B. Kerr, C. Leon Swisher, J. M. Pauly, and D. B. Vigneron, "A rapid method for direct detection of metabolic conversion and magnetization exchange with application to hyperpolarized substrates," *Journal of Magnetic Resonance*, vol. 225, pp. 71–80, 2012.

[15] C. Harrison, C. Yang, A. Jindal et al., "Comparison of kinetic models for analysis of pyruvate-to-lactate exchange by hyperpolarized ^{13}C NMR," *NMR in Biomedicine*, vol. 25, no. 11, pp. 1286–1294, 2012.

[16] D. K. Hill, M. R. Orton, E. Mariotti et al., "Model free approach to kinetic analysis of real-time hyperpolarized ^{13}C magnetic resonance spectroscopy data ," *PLoS ONE*, vol. 8, no. 9, Article ID e71996, 2013.

[17] L. Z. Li, S. Kadlececk, H. N. Xu et al., "Ratiometric analysis in hyperpolarized NMR (I): test of the two-site exchange model and the quantification of reaction rate constants," *NMR in Biomedicine*, vol. 26, no. 10, pp. 1308–1320, 2013.

[18] F. A. Gallagher, M. I. Kettunen, and K. M. Brindle, "Biomedical applications of hyperpolarized ^{13}C magnetic resonance imaging," *Progress in Nuclear Magnetic Resonance Spectroscopy*, vol. 55, no. 4, pp. 285–295, 2009.

[19] M. F. Santarelli, V. Positano, G. Giovannetti et al., "How the signal-to-noise ratio influences hyperpolarized ^{13}C dynamic MRS data fitting and parameter estimation," *NMR in Biomedicine*, vol. 25, no. 7, pp. 925–934, 2012.

[20] M. E. Merritt, C. Harrison, C. Storey, F. M. Jeffrey, A. D. Sherry, and C. R. Malloy, "Hyperpolarized ^{13}C allows a direct measure of flux through a single enzyme-catalyzed step by NMR," *Proceedings of the National Academy of Sciences of the United States of America*, vol. 104, no. 50, pp. 19772–19777, 2007.

[21] S. M. Kazan, S. Reynolds, A. Kennerley et al., "Kinetic modeling of hyperpolarized 13C pyruvate metabolism in tumors using a measured arterial input function," *Magnetic Resonance in Medicine*, vol. 70, no. 4, pp. 943–953, 2013.

[22] C. Yang, C. Harrison, E. S. Jin et al., "Simultaneous steady-state and dynamic ^{13}C NMR can differentiate alternative routes of pyruvate metabolism in living cancer cells," *The Journal of Biological Chemistry*, vol. 289, no. 9, pp. 6212–6224, 2014.

[23] F. Wiesinger, I. Miederer, M. I. Menzel et al., "Metabolic rate constant mapping of hyperpolarized 13C pyruvate," ISMRM 3282, 2010.

[24] L. Vanhamme, A. van den Boogaart, and S. van Huffel, "Improved method for accurate and efficient quantification of mrs data with use of prior knowledge," *Journal of Magnetic Resonance*, vol. 129, no. 1, pp. 35–43, 1997.

[25] T. Harris, G. Eliyahu, L. Frydman, and H. Degani, "Kinetics of hyperpolarized ^{13}C$_1$-pyruvate transport and metabolism in living human breast cancer cells," *Proceedings of the National Academy of Sciences of the United States of America*, vol. 106, no. 43, pp. 18131–18136, 2009.

[26] T. Xu, D. Mayer, M. Gu et al., "Quantification of in vivo metabolic kinetics of hyperpolarized pyruvate in rat kidneys using dynamic ^{13}C MRSI," *NMR in Biomedicine*, vol. 24, no. 8, pp. 997–1005, 2011.

[27] J. D. Shearer, G. P. Buzby, J. L. Mullen, E. Miller, and M. D. Caldwell, "Alteration in pyruvate metabolism in the liver of tumor-bearing rats," *Cancer Research*, vol. 44, no. 10, pp. 4443–4446, 1984.

[28] D. M. Bates and D. G. Watts, *Nonlinear Regression Analysis and Its Applications*, John Wiley & Sons, New York, NY, USA, 2008.

[29] O. Warburg, "On the origin of cancer cells," *Science*, vol. 123, no. 3191, pp. 309–314, 1956.

[30] H. Lu, R. A. Forbes, and A. Verma, "Hypoxia-inducible factor 1 activation by aerobic glycolysis implicates the Warburg effect in carcinogenesis," *The Journal of Biological Chemistry*, vol. 277, no. 26, pp. 23111–23115, 2002.

[31] W. Droge, H.-P. Eck, H. Kriegbaum, and S. Mihm, "Release of L-alanine by tumor cells," *The Journal of Immunology*, vol. 137, no. 4, pp. 1383–1386, 1986.

[32] L. Brennan, C. Hewage, J. P. G. Malthouse, and G. J. McBean, "Gliotoxins disrupt alanine metabolism and glutathione production in C6 glioma cells: a ^{13}C NMR spectroscopic study," *Neurochemistry International*, vol. 45, no. 8, pp. 1155–1165, 2004.

[33] H. R. Harding, F. Rosen, and C. A. Nichol, "Depression of Alanine Transaminase Activity in the Liver of Rats Bearing Walker Carcinoma 256," *Cancer Research*, vol. 24, pp. 1318–1323, 1964.

[34] S. M. Ronen, A. Volk, and J. Mispelter, "Comparative NMR study of a differentiated rat hepatoma and its dedifferentiated subclone cultured as spheroids and as implanted tumors," *NMR in Biomedicine*, vol. 7, no. 6, pp. 278–286, 1994.

3.1.2 *Hyperpolarized ^{13}C Metabolic Magnetic Resonance Spectroscopy and Imaging*

Peer-reviewed Journal Paper and Scientific Video Protocol[1]

Authors: E. Kubala, KA. Muñoz-Álvarez, G. Topping, C. Hundshammer, B. Feuerecker, **PA. Gómez**, G. Pariani, F. Schilling, SJ. Glaser, MI. Menzel, M. Schwaiger

Abstract: In the past decades, new methods for tumor staging, restaging, treatment response monitoring, and recurrence detection of a variety of cancers have emerged in conjunction with the state-of-the-art positron emission tomography with ^{18}F—fluorodeoxyglucose ($[^{18}$F]—FDG PET). ^{13}C MRSI is a minimally invasive imaging method that enables the monitoring of metabolism *in vivo* and in real time. As with any other method based on ^{13}C Nuclear Magnetic Resonance (NMR), it faces the challenge of low thermal polarization and a subsequent low signal-to-noise ratio due to the relatively low gyromagnetic ratio of ^{13}C and its low natural abundance in biological samples. By overcoming these limitations, Dynamic Nuclear Polarization (DNP) with subsequent sample dissolution has recently enabled commonly used NMR and Magnetic Resonance Imaging (MRI) systems to measure, study, and image key metabolic pathways in various biological systems. A particularly interesting and promising molecule used in ^{13}CMRSI is $[1-^{13}$C]pyruvate, which, in the last ten years, has been widely used for *in vitro*, preclinical, and, more recently, clinical studies to investigate the cellular energy metabolism in cancer and other diseases. In this article, we outline the technique of dissolution DNP using a 3.35 T preclinical DNP hyperpolarizer and demonstrate its usage in *in vitro* studies. A similar protocol for hyperpolarization may be applied for the most part in *in vivo* studies as well. To do so, we used lactate dehydrogenase (LDH) and catalyzed the metabolic reaction of $[1-^{13}$C]pyruvate to $[1-^{13}$C]lactate in a prostate carcinoma cell line, PC3, *in vitro* using ^{13}CMRSI.

Contribution of thesis author: Development and implementation of kinetic modeling, manuscript revision.

---

1 Scientific video protocol is available here: https://www.jove.com/video/54751/hyperpolarized-13c-metabolic-magnetic-resonance-spectroscopy

Video Article

Hyperpolarized ^{13}C Metabolic Magnetic Resonance Spectroscopy and Imaging

Eugen Kubala*[1,2,3], Kim A. Muñoz-Álvarez*[1], Geoffrey Topping[1], Christian Hundshammer[1,2], Benedikt Feuerecker[1], Pedro A. Gómez[3,4], Giorgio Pariani[1,5,6], Franz Schilling[1], Steffen J. Glaser[2], Rolf F. Schulte[3], Marion I. Menzel[3], Markus Schwaiger[1]

[1]Department of Nuclear Medicine, Klinikum rechts der Isar, Technische Universität München

[2]Department of Chemistry, Technische Universität München

[3]GE Global Research

[4]Zentralinstitut für Medizintechnik der Technischen Universität München (IMETUM), Technische Universität München

[5]Institute for Biological and Medical Imaging (IBMI), Helmholtz Zentrum München

[6]IDG Institute of Developmental Genetics, Helmholtz Zentrum München

*These authors contributed equally

Correspondence to: Eugen Kubala at eugen.kubala@tum.de

URL: http://www.jove.com/video/54751
DOI: doi:10.3791/54751

Abstract

In the past decades, new methods for tumor staging, restaging, treatment response monitoring, and recurrence detection of a variety of cancers have emerged in conjunction with the state-of-the-art positron emission tomography with ^{18}F-fluorodeoxyglucose ([^{18}F]-FDG PET). ^{13}C magnetic resonance spectroscopic imaging (^{13}CMRSI) is a minimally invasive imaging method that enables the monitoring of metabolism *in vivo* and in real time. As with any other method based on ^{13}C nuclear magnetic resonance (NMR), it faces the challenge of low thermal polarization and a subsequent low signal-to-noise ratio due to the relatively low gyromagnetic ratio of ^{13}C and its low natural abundance in biological samples. By overcoming these limitations, dynamic nuclear polarization (DNP) with subsequent sample dissolution has recently enabled commonly used NMR and magnetic resonance imaging (MRI) systems to measure, study, and image key metabolic pathways in various biological systems. A particularly interesting and promising molecule used in ^{13}CMRSI is [1-^{13}C]pyruvate, which, in the last ten years, has been widely used for *in vitro*, preclinical, and, more recently, clinical studies to investigate the cellular energy metabolism in cancer and other diseases. In this article, we outline the technique of dissolution DNP using a 3.35 T preclinical DNP hyperpolarizer and demonstrate its usage in *in vitro* studies. A similar protocol for hyperpolarization may be applied for the most part in *in vivo* studies as well. To do so, we used lactate dehydrogenase (LDH) and catalyzed the metabolic reaction of [1-^{13}C]pyruvate to [1-^{13}C]lactate in a prostate carcinoma cell line, PC3, *in vitro* using ^{13}CMRSI.

Video Link

The video component of this article can be found at http://www.jove.com/video/54751/

Introduction

Presently, the most widely used clinical method for tumor staging, restaging, treatment response monitoring, and recurrence detection of a wide variety of cancers is [^{18}F]-FDG PET.[1] However, recently, several novel and alternative approaches have emerged. One of those methods is ^{13}CMRSI. This technique involves the introduction of the ^{13}C-molecule into a biological sample, followed by minimally invasive MRI to assess the metabolism *in vitro* or *in vivo* in real time. Nevertheless, the biggest challenge of ^{13}CMRSI, compared to the other methods such as [^{18}F]-FDG PET or computed tomography, is its low signal-to-noise ratio.

The NMR signal is directly proportional to the level of polarization, a ratio of the spin ½ nuclei population difference in two energy states to the total population (**Figure 1A**). The polarization is a product of the gyromagnetic ratio (γ) of the nuclei and the applied magnetic field strength over the temperature. A typical polarization of ^{1}H nuclei is in the order of 0.001% to 0.005% at 3 T, which gives a relatively poor signal-to-noise ratio. Today's state-of-the-art MRI has been a successful imaging method only due to the high abundance of ^{1}H in biological samples and the high gyromagnetic ratio of ^{1}H (γ_{1H} = 42.576 MHz/T). However, observing other nuclei, such as carbon, is more demanding. The only stable, magnetically active carbon isotope, ^{13}C, makes up only 1.1% of all carbon atoms. In addition, the gyromagnetic ratio of ^{13}C (γ_{13C} = 10.705 MHz/T) is four times lower than that of ^{1}H, leading to a lower detection efficiency. In summary, the low ^{13}C abundance and low γ_{13C} cause thermal ^{13}C measurements to achieve 0.0176% of the sensitivity of a ^{1}H-NMR measurement *in vivo*.

Dynamic Nuclear Polarization

A method to overcome the relatively poor sensitivity of ^{13}C measurements is DNP. It was originally described for metals in 1953 by Albert W. Overhauser. In his article, he stated: "It is shown that if the electron spin resonance of the conduction electrons is saturated, the nuclei will be polarized to the same degree they would be if their gyromagnetic ratio were that of the electron spin."[2] Later that year, Carver and Slichter experimentally confirmed Overhauser's hypothesis[3]. In 1958, Abragam and Proctor described this effect for electrons in liquids and named it the "solid effect." At temperatures below 4 K, electron-spin polarization reaches nearly 100% and is more than three orders of magnitude higher than the nuclear-spin polarization (**Figure 1B**)[4]. This occurs because the gyromagnetic ratio of the electron (γ_e = 28024.944 MHz/T) is three orders of magnitude higher than the nuclear gyromagnetic ratios. The weak interactions between electrons and nuclei, such as the Overhauser effect, the solid effect, the cross effect, and the thermal mixing effect, allow the transfer of polarization from electron spins to nuclear spins using microwave irradiation with a frequency close to the corresponding electron paramagnetic resonance (EPR) frequency[5,6]. DNP theory has been further developed to involve more electrons and thermal mixing. Nevertheless, to date, no unified quantitative theoretical description of DNP has been published[7,8].
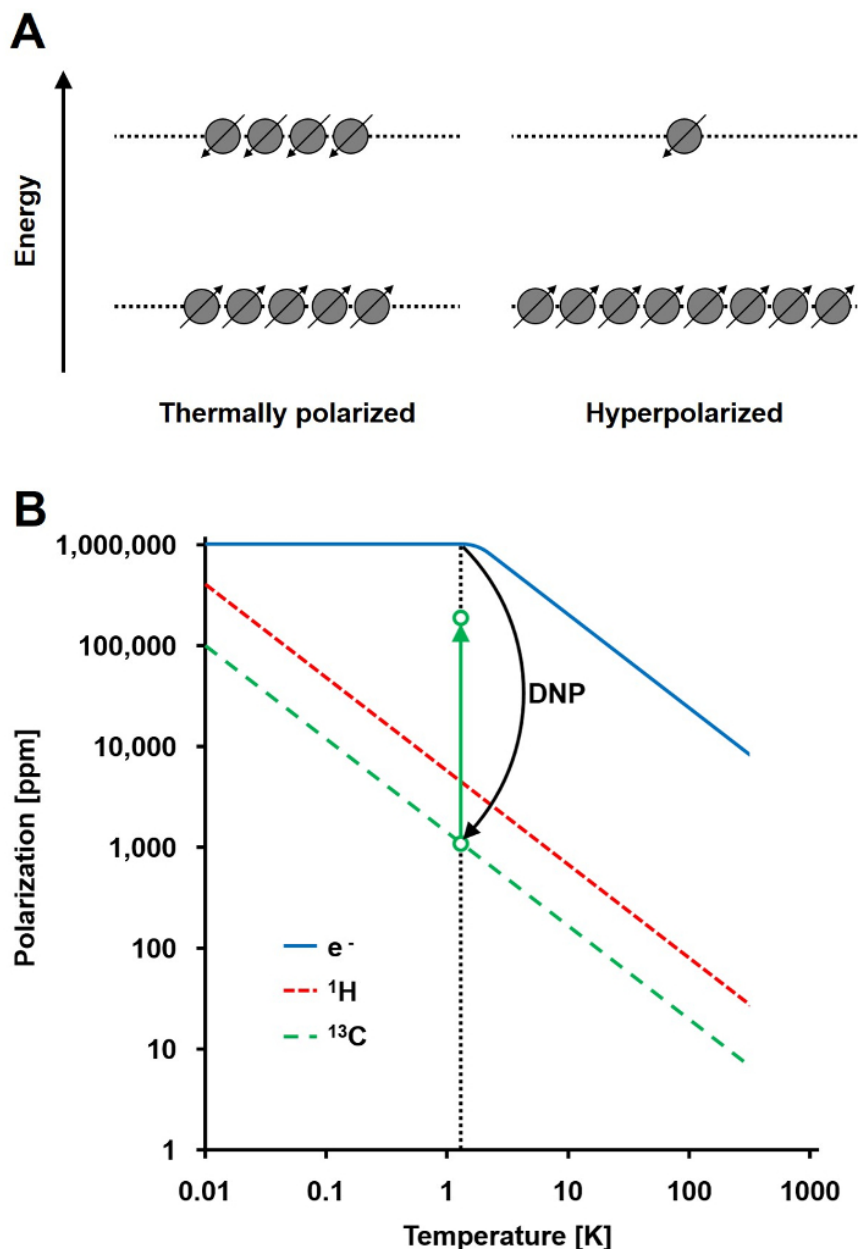
Figure 1: Understanding Dynamic Nuclear Polarization and Hyperpolarization. A) A schematic comparison of the spin population in the thermal equilibrium polarization state and the hyperpolarized state. **B)** The polarization is dependent upon temperature. The polarization of an electron (e-) reaches 100% below 1.4 K. The DNP allows the transfer of the polarization from the e- to the ^{13}C nuclei, which increases their polarization up to 10[5]-fold. Please click here to view a larger version of this figure.

To introduce DNP in studies of biological systems using ^{13}C NMR, subsequent rapid sample dissolution had to be developed. 50 years after Overhauser's hypothesis, Jan H. Ardenkjaer-Larsen *et al.* solved the technically challenging issue of bringing the hyperpolarized frozen

sample into the liquid state with minimal hyperpolarization loss[6]. Dissolution DNP opened a new field of research called ^{13}CMRSI, providing a new method to investigate and characterize various disease states[9,10]. As stable carriers of an unpaired electron, a trityl radical tris (8-carboxy-2,2,6-tetra-(hydroxyethyl)-benzo-[1,2-4,5]-bis-(1,3)-dithiole-4-yl)-methyl sodium salt (OX063) or (2,2,6,6-Tetramethylpiperidin-1-yl)oxyl (TEMPO) is usually used. These are mixed with the desired ^{13}C-labeled molecule and exposed to microwave irradiation with a frequency close to the corresponding EPR frequency. Using this technique, the polarization of ^{13}C nuclei can be increased up to 37%[11]. This results in a 10^5-fold polarization enhancement compared to the thermal equilibrium polarization[11,12]. However, as soon as the microwave irradiation is stopped and/or the ^{13}C-molecule is transferred to the liquid state, the polarization decays with the longitudinal relaxation time (T_1) of the ^{13}C nucleus that was polarized. Thus, the invention of fast dissolution techniques or any subsequent technique shortening the time before experimental measurement (*i.e.,* injection) is crucial for biological applications[13].

There are three major requirements that the candidate molecule needs to fulfill for successful ^{13}CMRSI studies. First, the ^{13}C nucleus of interest has to have a sufficiently long T_1 (> 10 s). The choice of the ^{13}C-label is crucial. The best candidate nuclei are carbons with no direct contact with ^{1}H-nuclei *via* a bond. It also needs to be rapidly metabolized within 2 - 3 T_1 times, resulting in a downstream metabolic product with a significantly different chemical shift from the original substance. The sample mixture must also form an amorphous glass when in a solid state so that the spatial distribution decreases the distance between the electron and ^{13}C, allowing the transfer of polarization. If the candidate molecule does not form amorphous glass naturally, it needs to be highly soluble in a glassing agent, such as glycerol or dimethyl sulfoxide[14]. These requirements result in a relatively small number of candidate molecules. However, even after the successful discovery of a suitable molecule, developing a working protocol for hyperpolarization can be technically challenging[9,14,15].

In recent years, several substrates have been successfully polarized, such as [1-^{13}C]pyruvate[12,16-36], [2-^{13}C]pyruvate[37], [1-^{13}C]ethyl pyruvate[38], [1-^{13}C]lactate[39], [1-^{13}C]fumarate[40-43], ^{13}C-bicarbonate[36,44,45], [1-^{13}C]sodium acetate[43,46-49], ^{13}C-urea[6,36,50,51], [5-^{13}C]glutamine[15,52,53], [1-^{13}C]glutamate[53,54], [1-^{13}C]2-oxoglutarate[55], [1-^{13}C]alanine, and others[14,56]. A particularly interesting and commonly used substrate for hyperpolarization is [1-^{13}C]pyruvate. It is widely used in preclinical studies to investigate the cellular energy-metabolism in various diseases[14,17,22]. [1-^{13}C]pyruvate meets all the requirements for successful hyperpolarization, including a relatively long T_1 and rapid transport across the cell membrane before subsequently being metabolized. Preclinical studies with [1-^{13}C]pyruvate are currently being translated into the clinic[57].

Metabolism of Pyruvate

It is well known that there is a direct link between mutations in a cancer cells' DNA and changes in their metabolic pathways. Already in the 1920s, Otto Warburg discovered that there is an increased metabolism of glucose and production of lactate in tumors compared to healthy tissue[58-60]. Subsequently, various alternations in other metabolic pathways, such as the pentose-phosphate pathway, the tricarboxylic acid cycle, oxidative phosphorylation, and the synthesis of nucleotides and lipids, have been described.

Pyruvate is the final product of glycolysis. In the tumor, it undergoes anaerobic glycolysis catalyzed by LDH[61] and reacts with the reduced form of the coenzyme nicotinamide adenine dinucleotide (NADH), resulting in lactate and the oxidized form of the coenzyme (NAD$^+$). Alternatively, pyruvate undergoes a transamination reaction with glutamate to form alanine, catalyzed by alanine transaminase (ALT). Both reactions are readily reversible. Pyruvate also undergoes decarboxylation catalyzed by pyruvate dehydrogenase (PDH) to carbon dioxide and acetyl-CoA, representing an irreversible reaction at this step. Alternations in these reaction rates can be linked to tumor metabolism[17,21,22,25,62]. The metabolic pathways are summarized in **Figure 2**.
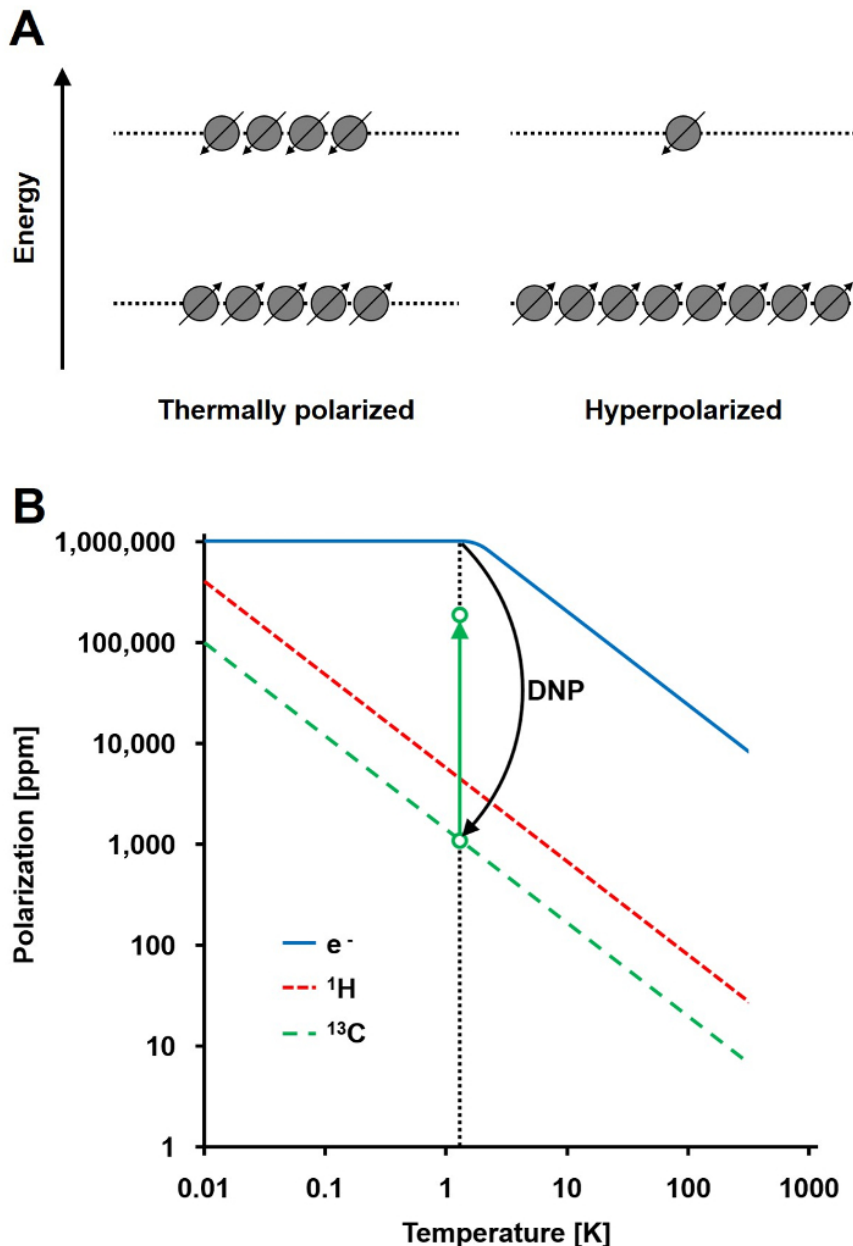
Figure 2: Diagram of the major metabolic reaction of pyruvate. Pyruvate/lactate conversion is catalyzed by LDH, and pyruvate/alanine conversion is catalyzed by ALT. Pyruvate is irreversibly converted to acetyl-CoA and CO_2 by PDH, and CO_2 is in a pH-dependent equilibrium with bicarbonate[80]. Please click here to view a larger version of this figure.

The detection of hyperpolarized [1-13C]pyruvate and its metabolites has been previously demonstrated in the rat heart[37,63-65], liver[66], muscle, and kidney[62,67]. One study demonstrated significant differences in the lactate-to-alanine ratio between the normal and fasted rat liver[66] and demonstrated a highly elevated and hyperpolarized [1-13C]lactate level in liver cancer[68,69]. There is evidence that the tumor grade can be identified in a transgenic adenocarcinoma of mouse prostate (TRAMP) using hyperpolarized [1-13C]pyruvate[22], with the hyperpolarized lactate levels showing a high correlation with the histological grade of the excised tumors. The alanine catalyzed from pyruvate by ALT has also been suggested as a useful marker in rat hepatocellular carcinoma[23].

Measuring the pyruvate-lactate metabolic flux has been used for monitoring ischemia[63,65,70] and as a response to treatment with cytotoxic chemotherapy[17,40], targeted drugs[24,25,41], or radiotherapy[26] in animal models. It has also been used for the detection of the phosphatidylinositol 3-kinase (PI3K) inhibitor LY294002 response in glioblastoma and breast cancer mouse models[25]. Changes in pyruvate metabolism in brain tumors[26] and prostate cancer[24,71] have also been observed after treatment.

Prostate Carcinoma

Prostate carcinoma is the predominant cancer in elderly men and the second leading cancer related to death in men worldwide[72]. To date, no reliable, non-invasive methods are available for an early diagnosis and characterization of prostate cancer[73,74], emphasizing the urgent need for novel metabolic imaging techniques to enable stringent detection and staging of patients. Prostate carcinoma was used as a model to demonstrate the possibilities of dissolution DNP combined with ^{13}CMRSI in patients[57]. This work was continued in a first clinical trial employing [1-^{13}C]pyruvate and ^{13}CMRSI for the imaging of prostate cancer, and it has just recently has been completed (NCT01229618).

The motivation behind this work was to illustrate in more detail and for a wider audience the application of the ^{13}CMRSI method in a preclinical setting with cells. Measuring the LDH-catalyzed metabolism of [1-^{13}C]pyruvate to [1-^{13}C]lactate *in vitro* in the PC3 prostate carcinoma cell line, we demonstrate the possible application of dissolution DNP in *in vitro* studies and address the crucial steps and challenges during experiments.

Protocol

1. Sample Stock Solution Preparation

1. Add gadoterate meglumine (GadM, 0.5 mol/L) to concentrated [1-^{13}C]pyruvic acid to give a final concentration of 1-mmol/L GadM. Add trityl radical tris (8-carboxy-2,2,6,6-tetra-(hydroxyethyl)-benzo-[1,2-4,5]-bis-(1,3)-dithiole-4-yl)-methyl sodium salt (OX063) to this mixture to give a final concentration of 15 mmol/L. Vortex until complete dissolution.
   NOTE: This stock solution preparation is designed for usage with a 3.35-T preclinical DNP hyperpolarizer. When a 7-T clinical hyperpolarizer is used, the gadoterate meglumine is not required because, at a higher magnetic field, its benefits are negligible. The addition of a gadolinium-based contrast agent increases the achievable solid-state polarization and also the polarization rate. However, in the liquid state, the contrast agent shortens the T_1 relaxation time.

2. Growing the Cell Culture

1. Grow PC3 cells in a culture flask with a 125-cm^2 growth area. Use F-12K medium containing 10% fetal calf serum (FCS) and maintain the cells at 37 °C in a humidified atmosphere at 5% CO_2. Before the dissolution step, remove the medium from the culture flask.
   NOTE: Each cell line requires a particular preparation protocol for cell propagation. Consult the requirements with the cell line provider.

3. Preparation of the Cells for the Experiment

1. Remove the cell medium and wash the cells with ~ 10 mL of phosphate-buffered saline (PBS).
2. Add 5 mL of trypsin to the flask and return the cell culture flasks to the incubator for 3 to 5 min.
3. Add ~ 5 mL of F-12K medium to deactivate the trypsin.
4. Count the cells using an automatic cell counter. Mix 10 µL of the cell solution with 10 µL of the stain solution. Mix well with the pipette and transfer 10 µL of the mixture into the chamber of a "counting glass".
5. Remove and count the cells in the flask(s). Transfer the appropriate volumes containing the desired number of cells (*e.g.,* 5 x 10^6 up to 10^8) into plastic vials.
6. Centrifuge the cells at 1,200 x g for 5 min and discard the supernatant.
7. Re-suspend the cells in the F-12K medium containing 10% FCS to a total volume of 800 µL and transfer them into a reaction cup (2 mL). Place the reaction cup into a plastic vial filled with warm water.

4. Dissolution Agent Preparation

NOTE: The dissolution agent is a liquid that is used to dissolve the hyperpolarized sample. In biological applications, dissolution is usually performed with H_2O-based or deuterium oxide (D_2O)-based buffers, such as PBS or tris(hydroxymethyl)aminomethane (Tris), containing 1 g/L ethylenediaminetetraacetic acid (EDTA).

1. Preparation of 20 mmol/L PBS buffer
   1. To prepare 100 mL of the dissolution agent, dissolve 36 mg of monosodium phosphate (NaH_2PO_4), 247 mg of disodium phosphate (Na_2HPO_4), and 10 mg of EDTA in a solution of 20 mmol/L sodium hydroxide (NaOH) in D_2O. Mix properly until complete dissolution.
      NOTE: EDTA (1 g/L) is added to the buffer to eliminate possible ferromagnetic ions, which can spoil the hyperpolarization. The NaOH is used to neutralize the pyruvic acid in a 1:1 mol ratio to reach a pH of 7.4.

5. Variable Temperature Insert (VTI) Cooldown

1. In the DNP-NMR polarizer program main window, click on "Cooldown."
   NOTE: This switches on the vacuum pump and evacuates the VTI to approximately 5.0 mbar. Subsequently, the needle valve between the VTI and the liquid helium reservoir fully opens, allowing liquid helium to flow into the VTI. The flow rate is regulated by the needle valve to maintain the optimal amount of liquid helium in the VTI until it reaches the helium boiling temperature. Then, the VTI is evacuated to almost complete vacuum, and the temperature reaches approximately 1.4 K. The VTI is filled with liquid helium up to 65%. At this point, the instrument is ready for sample insertion.

6. Sample Preparation and Insertion

1. Using a micropipette, add ~ 8 µL of ^{13}C-labeled sample stock solution into a plastic cup.

2. Attach the plastic cup to the insertion rod and initiate the sample insertion process by pressing "Insert sample" in the main program window. Select "Normal sample" and click "Continue."
   NOTE: During this process, the needle valve first closes to discontinue the flow of liquid helium into VTI, and the pressure in the VTI then increases. The sample holder inside the VTI is raised from the liquid helium, the inlet valve at the top of the VTI opens, and a gaseous helium flow is introduced from the inlet valve to prevent outside contamination by air moisture.
3. When prompted, push the insertion rod with the attached plastic cup down into the VTI. Make sure to reach the sample holder at the bottom of the VTI. Otherwise, the gaseous helium can push the sample out of the VTI.
4. Detach and remove the insertion rod.
5. Finish the procedure by clicking "Next" in the dialog window. The sample insertion procedure should not take longer than 10 s.
   NOTE: The inlet valve then closes, the gaseous helium flow is discontinued, the sample holder with the sample cup is submerged into liquid helium, and the needle valve is opened to allow the liquid helium to flow into the VTI. After 5 - 10 min, the VTI is cooled below 1.4 K, allowing all of the free electrons to be polarized.
6. Confirm that the plastic cup with the sample was introduced correctly into the VTI by checking that it is not attached to the insertion rod or pushed out from the VTI by helium gas. Then click "Finish."

7. Microwave Sweep (optional)

NOTE: A microwave sweep allows the determination of the optimal microwave frequency to maximize the hyperpolarization rate of the ^{13}C nuclei in the target compound.

1. To measure the microwave sweep, start the RINMR program, type "HYPERSENSENMR," and click "Select Config" and "Do Microsweep."
2. To initiate the process, select the "calibrate" tab on the main program window.
3. Click "Generate" and choose the beginning and ending frequency (*e.g.,* 94.100 GHz-94.200 GHz), the frequency step size (*e.g.,* 20 MHz), the power (100 mW), and the time (60 s). Click "Continue," "Enable," and "Start."
   NOTE: With these settings, the hyperpolarizer first polarizes the sample for 60 s using a microwave frequency of 94.100 GHz and a power of 100 mW. Then, it applies a 90° radio-frequency (RF) pulse and acquires the hyperpolarized ^{13}C signal using the built-in spectrometer. These steps are repeated for each step in specified frequency range. For subsequent hyperpolarization, choose the microwave frequency with the maximal signal amplitude measured.

8. Polarization

1. To measure the polarization build-up, start the RINMR program, type "HYPERSENSENMR," and click "Select Config" and "Solid Build-up."
2. In the DNP-NMR polarizer program main window, click "Polarization" to initiate the hyperpolarization process.
3. Choose the optimal microwave frequency (obtained during the microwave sweep) and the power (*e.g.,* 100 mW) for the sample and click "Next."
4. Enable "Polarization build-up monitoring" and click "Finish."
5. Polarize the sample to > 95% (~ 60 min for [1-^{13}C]pyruvate).
   NOTE: During the polarization, microwaves are guided into the VTI and to the sample, causing the ^{13}C spins to align with the hyperpolarized unpaired electron spins. To measure the hyperpolarization buildup, RF pulses with a flip angle (FA) of 5° are applied periodically (*e.g.,* every 300 s), and the resulting signal is plotted as a polarization build-up curve.

9. Dissolution

1. When the polarization reaches > 95%, initiate the dissolution process by clicking "Dissolution" in the DNP-NMR polarizer program main window.
2. Choose the dissolution process from the drop-down menu and click "Next."
   NOTE: The polarizer allows one to define the desired dissolution process by choosing the timing of the chasing gas.
3. Load ~ 5 mL of the dissolution agent through the top valve into a heated vessel in the dissolution part of the polarizer. Calculate the exact volume of the dissolution agent needed using following equation:

$$V_{DA} = \frac{m_{pa}}{cMm_{PA}m_{OX063}m_{GadM}}$$

   where V$_{DA}$ is the wanted volume of dissolution agent, m$_{PA}$, m$_{OX063}$, and m$_{Gad}$ are the masses of the pyruvate, OX063 and gadoterate meglumine, respectively, added to the sample stock solution.
4. Place the dissolution stick in the active position above the inlet valve.
   NOTE: This allows the instrument to connect its dissolution instrumentation to the sample cup in the VTI.
5. Click "Finish" to start the dissolution process.
   NOTE: The dissolution agent is pressurized to 3 bar by helium gas and is subsequently heated up to 200 °C, causing an increase in pressure. When the pressure reaches 10 bar, the needle valve closes to discontinue the flow of liquid helium into the VTI. The sample holder raises the cup from the liquid helium. The dissolution stick is lowered into the VTI and connected to the sample cup. The conditioned dissolution agent is pushed by the pressure, which results from the heating vessel containing the dissolution buffer and helium gas, through the dissolution stick to the cup, causing a rapid dissolution of the sample. The solution then flows out into the collection flask via plastic tubing. The dissolution stick with the attached cup is then raised from the VTI.
6. Move the dissolution stick with the attached cup to the "cleaning" position and finish the process by clicking "Finish."

10. Detection of the ^{13}C Hyperpolarized Signal

1. ^{13}C metabolic magnetic resonance spectroscopy *in vitro*

1. Mix 200 µL of the 20-mmol/L dissolved hyperpolarized sample from the collection flask with 800 µL of the cell solution.
   NOTE: The resulting final concentration of [1-^{13}C]pyruvate is 4 mmol/L.
2. Mix the suspension well using a micropipette and transfer ~ 600 µL into a 5-mm NMR tube.
3. Insert the 5-mm NMR tube into the 1-T NMR spectrometer. In the main window of the software, click "Run" to start the measurement, applying series of one hundred 10° RF pulses every 3 s.
   NOTE: Measure the time between the initial mixing of the hyperpolarized sample with the cells and the start of the spectroscopic acquisition. Ensure that the mixing procedure does not exceed 30 s to minimize polarization loss.

2. ^{13}C metabolic magnetic resonance imaging
   1. To build a container for the *in vitro* experiments using the MRI spectrometer, take a 5-mL syringe and connect it to a catheter (d = 1.2 mm) that is long enough to reach from the spectrometer's iso-center to the approachable area of the spectrometer.
   2. Fill the *in vitro* container with the cell solution of the desired concentration for the experiment (*e.g.,* 10^8) or with an enzymatic solution.
   3. Place an *in vitro* container at the isocenter of the MRI magnet. Place a ^{13}C-tuned radio frequency receiver coil on the container. Place a concentrated ^{13}C-labeled calibration phantom (*e.g.,* 10-mol/L ^{13}C-urea) nearby.
   4. Insert the "*in vitro* container" near the iso-center of the NMR scanner.
   5. Run the scanner's standard 3-plane localization sequence and adjust the *in vitro* container's position to the iso-center, as needed.
   6. Run a ^{1}H T2-weighted "anatomical" sequence covering the *in vitro* container localization. Use the following settings: 2D spin echo with axial orientation, repetition time (TR) = 2,000 ms, echo time (TE) = 20 ms, slice thickness = 1 mm, field of view covering the *in vitro* container, and 16 echoes per excitation. Ensure that field shimming is done on protons during this step.
   7. In the anatomical images, select 5 contiguous slices centered on the region of interest. Prescribe a ^{13}C spectroscopic calibration acquisition covering the selected anatomical slices. Use the following settings: 2D Block-Siegert calibration sequence with axial orientation 12 x 12 centric encoded, TR = 1,000 ms, slice thickness = 5 mm, field of view matching anatomical images, number of scans (NS) = 64, bandwidth = 5,000 Hz, and FA = 90°.
   8. Select the ^{13}C spectroscopic calibration sequence (for more information, see Schulte *et al.* 2011)[75] from the pulse sequence library. Download the pulse sequence to the scanner from the computer by clicking "Download." Click on "Spectra Prescan" to run the spectroscopic prescan. In the spectrum magnitude plot, adjust the peak from the ^{13}C calibration phantom to the center of the scanner frequency. Set the receiver gains to the maximum. Click "Start" to run the ^{13}C spectroscopic calibration sequence. Note the reported transmit gain and centric frequency.
   9. Set a ^{13}C chemical shift imaging (CSI) acquisition covering the selected anatomical slices. Use the following settings: 2D echo-planar spectroscopic imaging (EPSI) with axial orientation 12 x 12 centric encoded, TR = 400 ms, slice thickness = 5 mm, field of view matching anatomical images, NS = 300, and bandwidth = 5,000 Hz.
      NOTE: EPSI samples a single line in k-space repeatedly after one RF excitation to acquire both spatial and spectral information simultaneously. For more information about the acquisition techniques, see the article by Durst *et al.* 2015[76].
   10. Download the ^{13}C CSI sequence and run the spectroscopic prescan. Adjust the scanner frequency and transmit the gain as specified by the calibration sequence output.
   11. After the hyperpolarized solution is deposited in the collection flask, draw up ~ 3 mL into a syringe and then inject it into the catheter connected to the *in vitro* container. Start the acquisition. After the acquisition is complete, save the raw data file for subsequent reconstruction.

11. Data Reconstruction

1. Apply one of the two described kinetic models to analyze the acquired data.
   1. In the first method for describing the LDH kinetics, kinetic value (k), compare the sum of the lactate signal (M$_{LAC}$) to the signal of all hyperpolarized molecules (M$_x$)[21,77].

   $$k = \frac{M_{LAC}(t)}{\sum M_x(t)}$$

   2. In the other method, measure the lactate and pyruvate signals over time and fit these to a kinetic model[17,25,71]. To solve the metabolic exchange rate, $k_{PA \to LAC}$, and the effective signal decay rate of lactate, r_{LAC}, use the following linear differential equations using the two-site exchange differential model, yielding for lactate:

   $$\frac{dM_{LAC}(t)}{dt} = +k_{PA \to LAC} M_{PA} - r_{LAC} M_{LAC}$$

Note: The effective lactate signal decay rate r_{LAC} is dependent upon the lactate longitudinal relaxation time ($T_{1,LAC}$), the opposite metabolic exchange rate from lactate to pyruvate $k_{LAC \to PA}$, the applied FA and TR, and the signal intensity of pyruvate (M$_{PA}$) and lactate (M$_{LAC}$), taking into account the irreversible signal reduction after each successive excitation:

$$r_{LAC} = k_{LAC \to PA} + \frac{1}{T_{1,LAC}} + \frac{1 - \cos FA}{TR}$$

Therefore, r_{LAC} results in a single, inseparable term of signal decay. Since it is possible to correct for the flip angle and the repetition time, and even though there is a flux LAC→PA, we assume that the exchange rate from lactate to pyruvate ($k_{LAC \to PA}$) does not need to be included in the calculation, based on the results of Harrison *et al.* 2012[78]. Their results show that the $k_{LAC \to PA}$ does not play as crucial a role as one would assume. This mode allows the T_1 relaxation time of lactate to be quantified. This model is independent of pyruvate administration to the measurement, which, in the case of *in vitro* experiments, is not crucial and can be neglected. It does, however, play an important role for *in vivo* measurements[79].

Representative Results

The results of the "microwave sweep" are illustrated in **Figure 3**. It shows that the optimal microwave frequency for the [1-^{13}C]pyruvate sample is at 94.156 GHz for the local 3.35-T hyperpolarizer. All following hyperpolarization experiment (n = 14) were performed using this microwave frequency with a power of 100 mW. The microwave irradiation was applied for 60 to 80 min, leading to a solid-state hyperpolarization higher than 90%. The results are presented in **Figure 4**. The hyperpolarized [^{13}C]pyruvate was mixed with 5×10^6 (n = 2), 10^7 (n = 2), 2×10^7 (n = 1), 3×10^7 (n = 2), 4×10^7 (n = 1), 6×10^7 (n = 2), 8×10^7 (n = 2), and 10^8 (n = 1) of the prostate cancer cell line PC3.

The resulting data are summarized in **Figure 5** and **Figure 6**. Acquired data with spectral and temporal resolution are shown in **Figure 5A-D** and **Figure 6A-D**, with only a temporal resolution for each molecule observed (**Figure 5E-H** and **Figure 6E-H**), and with only a spectral resolution (**Figure 5I-L** and **Figure 5I-L**). We have observed three major hyperpolarized signals representing [1-^{13}C]pyruvate, [1-^{13}C]pyruvate hydrate, and [1-^{13}C]lactate, with chemical shifts at 173 ppm, 181 ppm, and 185 ppm, approximately relative to the trimethylsilyl propanoic acid (TMSP) at pH 7.4 and temperature 20 °C. The signal ratios between the three metabolites are summarized in **Table 1**. The data show a clear correlation between the lactate signal and the number of cells present in the sample (**Figure 7**). However, the results from the experiments with less than 2×10^7 cells exhibit significant deviation, likely due to a low signal-to-noise ratio. Therefore, we suggest using more cells than this for further experiments. When the relative lactate signal (kinetic value) is normalized by the number of cells (**Figure 8**), it clearly demonstrates similar uptake and metabolism throughout all of the cells. However, there is a trend of decreasing lactate production per cell with an increasing number of cells. We believe that one of the causes of reduced cell metabolic activity is a very high concentration of cells in a very small volume, resulting in the increased viscosity of the sample. The results of the two-site exchange differential model are summarized in **Table 2** and shown in **Figure 9**. The data follow a trend similar to the previous model: increasing $k_{PA \to LAC}$ with an increasing number of cells. However, this model results in a steeper increase of the kinetics with the number of cells. When the metabolic exchange rate $k_{PA \to LAC}$ is normalized to the number of cells, we can again see a clear trend of decreasing $k_{PA \to LAC}$ with an increasing number of cells (**Figure 10**).

Figure 11 demonstrates the possibility of the addition of spatial localization to the experiment. It shows a phantom injected with 80 mmol/L hyperpolarized [1-^{13}C]pyruvate next to a 10 mol/L ^{13}C-urea phantom. The technique allows the attainment of a spectrum with temporal and special resolution (**Figure 11A**) or of the signal decay of the chosen metabolite signals in time (**Figure 11B**). The spectra in the time domain can also be summed to receive a better signal-to-noise ratio (**Figure 11C**). The special resolution allows the choice of the desired frequency region of the ^{13}C spectrum belonging to certain metabolites, such as [1-^{13}C]pyruvate (**Figure 11D**), [1-^{13}C]pyruvate hydrate (**Figure 11E**), or reference ^{13}C-urea (**Figure 11F**). It can be co-registered with a ^{1}H image. The pulse sequence used (EPSI) allows the acquisition of an image of the whole slice every 4.9 s. In summary, this technique can provide data with a spatial, temporal, and spectral resolution for any metabolite.
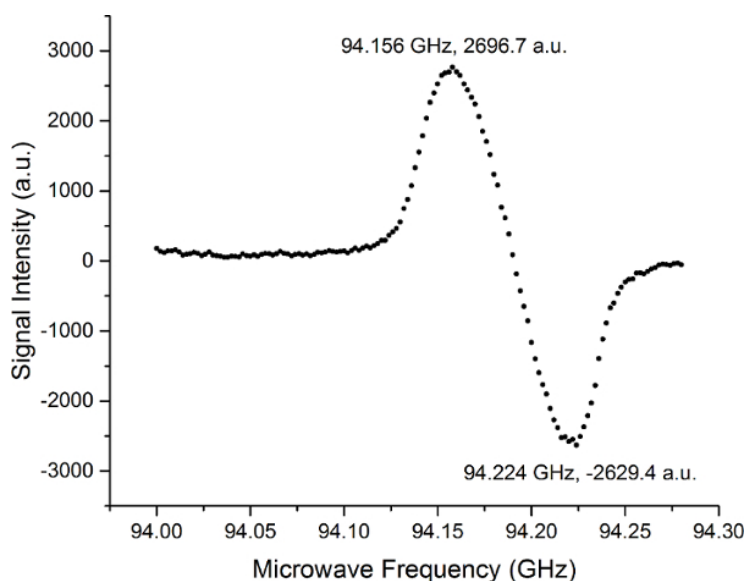
Figure 3: Results of a Microwave Sweep with [1-^{13}C]pyruvate at the Local 3.35-T Hyperpolarizer. The result of the measurements determining the optimal microwave frequency to maximize the hyperpolarization rate of ^{13}C nuclei in the target compound of [1-^{13}C]pyruvate. The microwave sweep has a shape of an EPR absorption spectrum. The shape and separation of the peaks are based on the radical used (in this case, trityl radical), and the biggest influence have a solid effect and thermal mixing. Please click here to view a larger version of this figure.
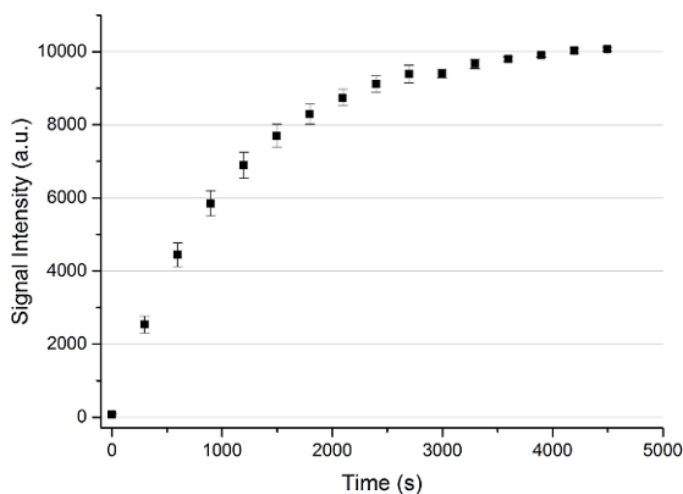
Figure 4: Solid State Polarization Buildup of a [1-^{13}C]pyruvate Sample. An average of n = 13 solid-state polarization buildups with the error represented by the standard deviation measured every 300 s for up to 4,500 s. Please click here to view a larger version of this figure.
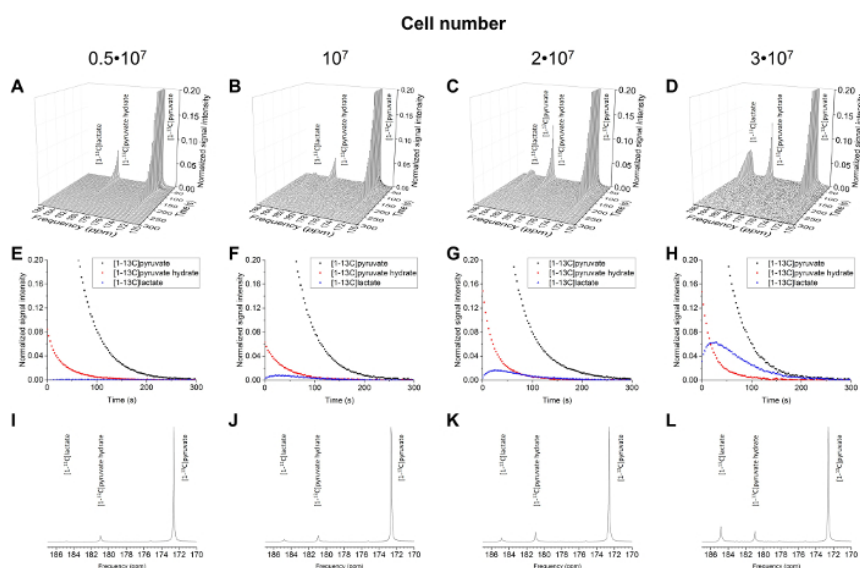
Figure 5: Results of the ^{13}C NMR Spectroscopy for the Number of Cells (5 x 10^6 to 3 x 10^7 cells). The acquired data plotted with spectral and temporal resolution (**A-D**), plotted with temporal resolution only for [1-^{13}C]pyruvate, [1-^{13}C]pyruvate hydrate, and [1-^{13}C]lactate (**E-H**), and plotted with spectral resolution only, summing all time steps (**I-L**). Please click here to view a larger version of this figure.
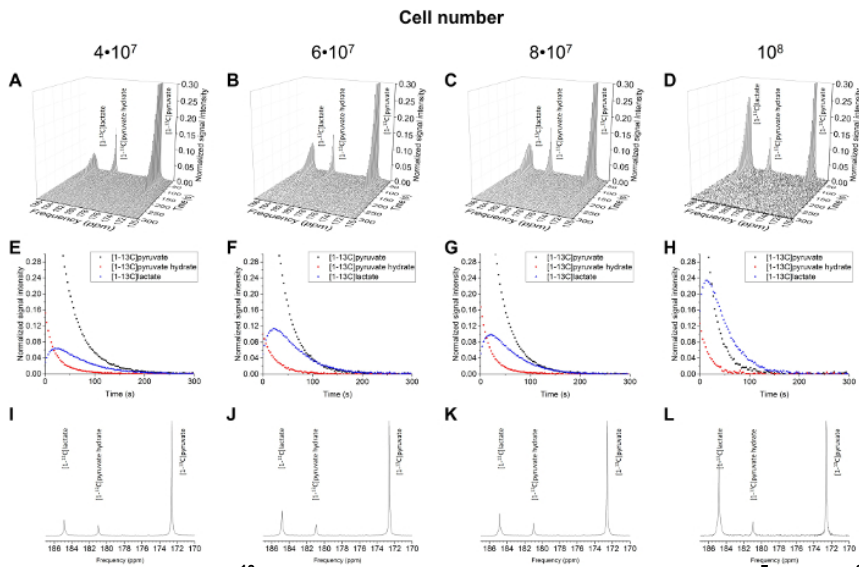
Figure 6: Results of the ^{13}C NMR Spectroscopy for the Number of Cells (4 x 10^7 to 1 x 10^8 cells). The acquired data plotted with spectral and temporal resolution (**A-D**), plotted with temporal resolution only for [1-^{13}C]pyruvate, [1-^{13}C]pyruvate hydrate, and [1-^{13}C]lactate (**E-H**), and plotted with spectral resolution only, summing all time steps (**I-L**). Please click here to view a larger version of this figure.
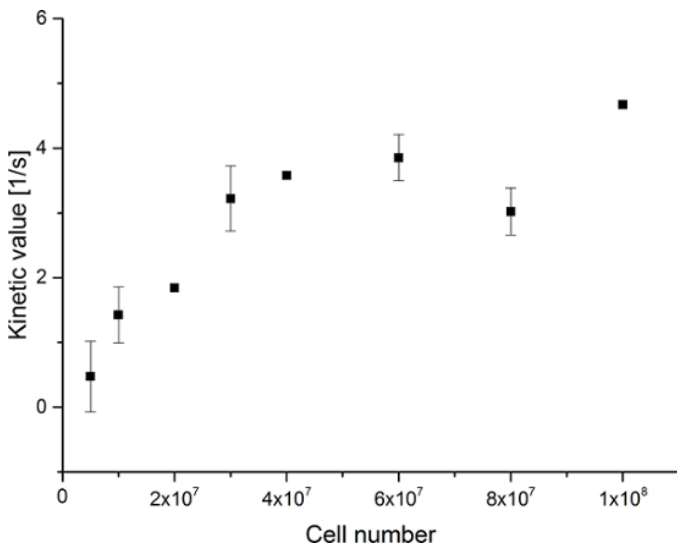
Figure 7: Results of the Simple Metabolite Ratio Kinetic Modeling. Data represents the ratio of the [1-^{13}C]lactate signal to the sum of [1-^{13}C]pyruvate, [1-^{13}C]pyruvate hydrate, and [1-^{13}C]lactate versus the number of cells in the experiments. The error represents the standard deviation. Please click here to view a larger version of this figure.
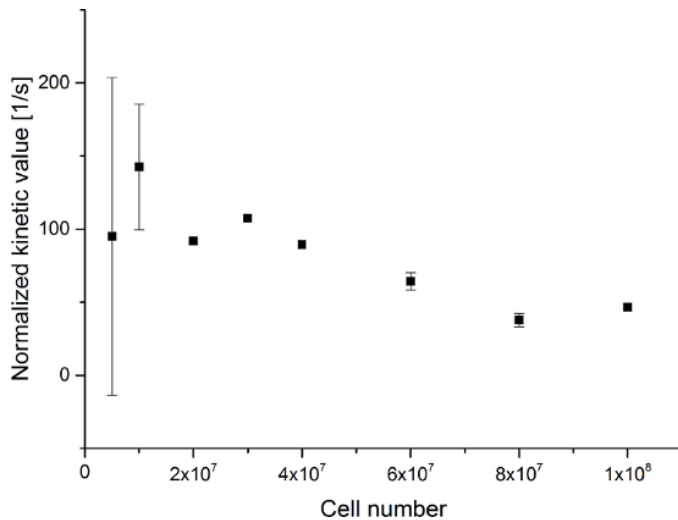
Figure 8: Results of the Simple Metabolite Ratio Kinetic Modeling Normalized to the Number of Cells. The data represent the ratio of the [1-^{13}C]lactate signal to the sum of [1-^{13}C]pyruvate, [1-^{13}C]pyruvate hydrate, and [1-^{13}C]lactate normalized to the number of cells versus the number of cells in the experiments. The error represents the standard deviation. Please click here to view a larger version of this figure.
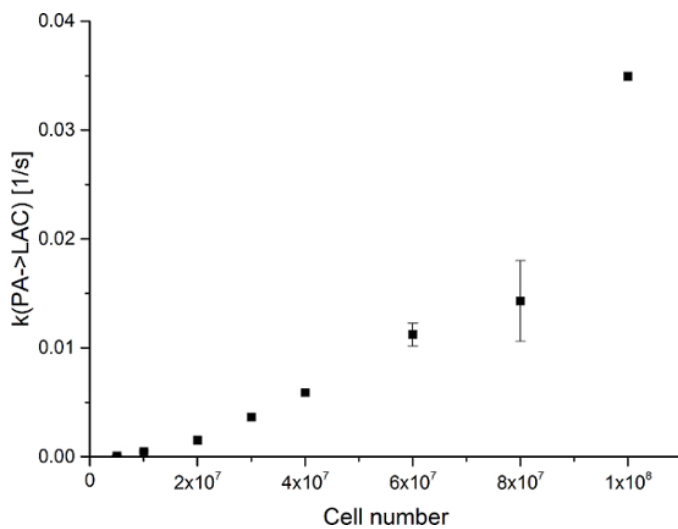
Figure 9: Results of the Two-site Exchange Differential Model. The data represent the metabolic exchange rate ($k_{PA \to LAC}$) versus the number of cells in the experiments. The error represents the standard deviation. Please click here to view a larger version of this figure.
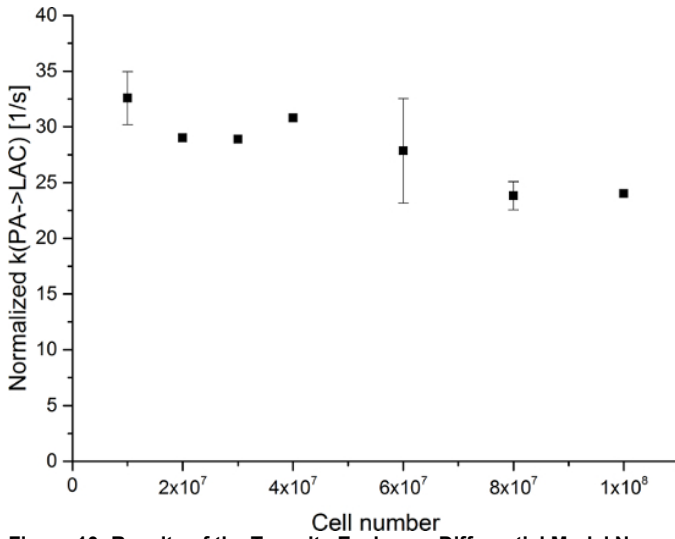
Figure 10: Results of the Two-site Exchange Differential Model Normalized to the Number of Cells. The data represent the metabolic exchange rate ($k_{PA \rightarrow LAC}$) normalized to the number of cells versus the number of cells in the experiments. The error represents the standard deviation. Please click here to view a larger version of this figure.
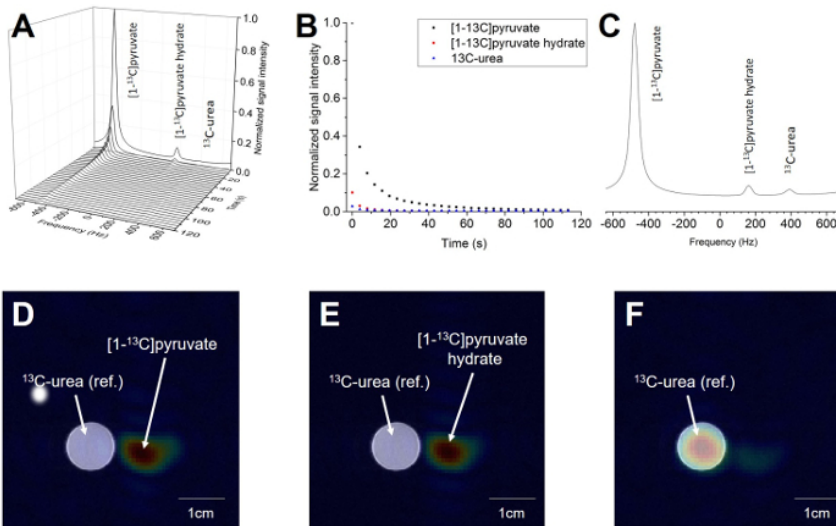
Figure 11: Result of Magnetic Resonance Imaging of the Hyperpolarized [1-^{13}C]pyruvate Probe. A) The spectrum acquired over the whole slice and all time steps. **B)** The decay of the [1-^{13}C]pyruvate and [1-^{13}C]pyruvate hydrate signal over time. The third signal is the 10 M ^{13}C-urea localization reference. **C)** The spectrum acquired from the whole spatial and temporal resolution. **D)** The ^{1}H image overlaid with the ^{13}C image of the summed [1-^{13}C]pyruvate signal over all time steps. **E)** The ^{1}H image overlaid with the ^{13}C image of the summed [1-^{13}C]pyruvate hydrate signal over all time steps. **F)** The ^{1}H image overlaid with the ^{13}C image of the summed ^{13}C-urea signal over all time steps (reference). The ^{13}C-signal in C-E is normalized to the maximum of the signal of the specific metabolite. Please click here to view a larger version of this figure.

	Cell number							
	5×10^6 (n=2)	10^7 (n=2)	2×10^7 (n=1)	3×10^7 (n=2)	4×10^7 (n=1)	6×10^7 (n=2)	8×10^7 (n=2)	10^8 (n=1)
[1-^{13}C] pyruvate	92.9 ± 1.4	91.7 ± 1.0	86.7	77.5 ± 2.7	76	69.7 ± 0.5	65.9 ± 3.7	42.9
[1-^{13}C] pyruvate hydrate	6.8 ± 1.2	6.7 ± 1.6	9.5	10.1 ± 1.8	8.9	7.7 ± 1.5	10.4 ± 0.2	13.4
[1-^{13}C] lactate	0.3 ± 0.3	1.6 ± 0.6	3.8	12.4 ± 4.5	15.1	22.5 ± 1.1	23.7 ± 3.5	43.7

Table 1: The Relative Ratio of Hyperpolarized Metabolites with Respect to the Different Number of Cells.

	Cell number							
	5×10^6 (n=2)	10^7 (n=2)	2×10^7 (n=1)	3×10^7 (n=1)	4×10^7 (n=1)	6×10^7 (n=2)	8×10^7 (n=2)	10^8 (n=1)
$k_{PA \rightarrow LAC}$ [$*10^{-4}$]	0.924±0.870	4.984±1.19	15.135	36.289	58.904	112.174±10.491	114.3±37.059	349.234

Table 2: Results of the Two-site Exchange Differential Model.

Discussion

^{13}CMRSI with hyperpolarized probes is a promising method to monitor metabolism in real time *in vitro* and *in vivo*. One very important aspect when employing this experimental process is the proper standardization, especially regarding *in vitro* experiments. First, the preparation of the sample needs to be done properly and consistently to achieve the same concentration of hyperpolarized material in each experiment. This requires a precise weighing of both the sample to be hyperpolarized and the buffer. If the concentration is not correct, the final pH of the solution is not precise, which can have an influence on T_1 and the cells' responses. It is also crucial to handle the cells as uniformly as possible. The cells should always be prepared in such a way that there is a minimal delay between cell harvest and the subsequent experiment in order to minimize the duration of time the cells are kept at a very high concentration and low volume. Variation in the cell preparation protocol, such as a different preparation times or temperatures, could result in substantial variations in the obtained data. The mixing of the sample with the cells should also be standardized. It is important to measure the time between the additions of the tracer to the cell suspension and the beginning of the measurement, because this can vary; during the data analysis, this should be considered.

The correct choice of the data analysis and kinetic modeling is crucial in the interpretation of the acquired data. The simple model is suitable for a linear one-way reaction with a constant exchange rate of two metabolites. As described in the introduction, pyruvate undergoes several enzymatic reactions and, more importantly, it also undergoes a non-enzymatic reversible-exchange reaction with pyruvate hydrate. This reaction played a crucial role in the experiments, and its effect is well demonstrated in the experiment with 8×10^7 cells. Although **Table 1** indicates that the pyruvate hydrate relative concentration is similar to other experiments, when closely investigated in **Figure 6D**, it shows a much higher pyruvate hydrate signal at the beginning of the experiment compared to the other experiments. However, when the temporal resolution is summed up, this important information is lost and causes an error in the reconstruction of the data. On the other hand, the two-site exchange differential model is a more robust and precise description of the kinetics because it includes the temporal resolution in the calculation. Thus, it includes the non-enzymatic exchange with pyruvate hydrate, even if it rapidly exchanges with pyruvate during the measurement.

There are various imaging strategies to choose between to observe the hyperpolarized signal or to track the metabolism of a hyperpolarized molecule in preclinical and clinical studies. Durst *et al.* demonstrated the advantages and disadvantages of different pulse sequnces[76]. The free induction decay chemical shift imaging (FIDCSI) sequence is relatively robust but has limited use for multi-slice and temporally resolved imaging. Echo-planar spectroscopic imaging (EPSI) is robust for gradient issues and off-resonance effects but, it is prone to reconstruction artifacts. The iterative decomposition of water and fat with echo asymmetric and least-squares estimation (IDEAL)[81], spiral chemical shift imaging (ISPCSI), pulse sequence[35], and spiral chemical shift imaging (SPCSI) have high encoding efficiencies but are sensitive to B_0 inhomogeneity. The choice of the sequence will depend on the scanner characteristics, the biological question, and the system being investigated.

There are many requirements that need to be fulfilled for successful hyperpolarization. However, there are also several limitations that the hyperpolarized ^{13}CMRSI technique is nowadays facing. The primary and unchangeable limitation is the T_1 relaxation time of the ^{13}C nucleus in the molecule, which defines the amount of detectable signal available at the specific time of measurement. The signal is lowered by each RF excitation that causes a loss of the hyperpolarization signal repeatedly during data acquisition. Another limitation is the relatively long time period that is required to hyperpolarize a molecule. This typically takes from 30 to 90 min.

In comparison to other techniques of molecule imaging, such as [^{18}F]-FDG PET, hyperpolarized ^{13}CMRSI does not require tumors with increased glycolytic metabolic pathways and therefore, increased glucose consumption. The technique shows a real metabolic flux in real time. On the other hand, [^{18}F]-FDG PET does not give direct information about metabolism but only indirect information about accumulation in the metabolically active area. This could cause a false negative result, where the tumor seems to be metabolically inactive but is actually using different metabolic pathways, such as glutaminolysis, as the carbon source for proliferation.

In conclusion, dissolution DNP can be used in a variety of applications to study an unlimited list of diseases (such as diabetes)[82], measure pH[15,36,45], or monitor metabolic changes in various types of cancer. These measurements can be accomplished on different levels, from *in vitro* cell experiments, through preclinical studies using animal models (such as mice, rats, rabbits, pigs, and dogs), to recent human clinical studies[57]. The future clinical applications will feature a very powerful and noninvasive diagnostic tool that could not only detect and localize the disease but also allow the observation of the treatment response in real time[83].

Disclosures

Rolf F. Schulte and Marion I. Menzel are employed with GE Global Research.

Acknowledgements

References

1. Rohren, E. M., Turkington, T. G., & Coleman, R. E. Clinical applications of PET in oncology. *Radiology*. **231** (2), 305-332 (2004).
2. Overhauser, A. W. Polarization of Nuclei in Metals. *Phys. Rev.* **92** (2), 411-415 (1953).
3. Carver, T. R., & Slichter, C. P. Polarization of Nuclear Spins in Metals. *Phys. Rev.* **92** (1), 212-213 (1953).
4. Abragam, A., & Proctor, W. G. Spin Temperature. *Phys. Rev.* **109** (5), 1441-1458 (1958).
5. Abragam, a & Goldman, M. Principles of dynamic nuclear polarisation. *Reports Prog. Phys.* **41** (3), 395-467 (2001).
6. Ardenkjaer-Larsen, J. H., Fridlund, B., *et al.* Increase in signal-to-noise ratio of > 10,000 times in liquid-state NMR. *Proc. Natl. Acad. Sci. U. S. A.* **100** (18), 10158-10163 (2003).
7. Shimon, D., Hovav, Y., Feintuch, A., Goldfarb, D., & Vega, S. Dynamic nuclear polarization in the solid state: a transition between the cross effect and the solid effect. *Phys. Chem. Chem. Phys.* **14** (16), 5729-5743 (2012).
8. Serra, S. C., Rosso, A., & Tedoldi, F. Electron and nuclear spin dynamics in the thermal mixing model of dynamic nuclear polarization. *Phys. Chem. Chem. Phys.* **14** (38), 13299-13308 (2012).
9. Gallagher, F. A., Kettunen, M. I., & Brindle, K. M. Biomedical applications of hyperpolarized 13C magnetic resonance imaging. *Prog. Nucl. Magn. Reson. Spectrosc.* **55** (4), 285-295 (2009).
10. Hurd, R. E., Yen, Y.-F., Chen, A., & Ardenkjaer-Larsen, J. H. Hyperpolarized 13C metabolic imaging using dissolution dynamic nuclear polarization. *J. Magn. Reson. Imaging*. **36** (6), 1314-1328 (2012).
11. Ardenkjaer-Larsen, J. H., Fridlund, B., *et al.* Increase in signal-to-noise ratio of > 10,000 times in liquid-state NMR. *Proc. Natl. Acad. Sci. U. S. A.* **100** (18), 10158-10163 (2003).
12. Golman, K., in 't Zandt, R., & Thaning, M. Real-time metabolic imaging. *Proc. Natl. Acad. Sci.* **103** (30), 11270-11275 (2006).
13. Comment, A., Rentsch, J., *et al.* Producing over 100 ml of highly concentrated hyperpolarized solution by means of dissolution DNP. *J. Magn. Reson.* **194** (1), 152-155 (2008).
14. Brindle, K. M., Bohndiek, S. E., Gallagher, F. A., & Kettunen, M. I. Tumor imaging using hyperpolarized 13C magnetic resonance spectroscopy. *Magn. Reson. Med.* **66** (2), 505-519 (2011).
15. Gallagher, F. A., Kettunen, M. I., Day, S. E., Lerche, M., & Brindle, K. M. 13C MR spectroscopy measurements of glutaminase activity in human hepatocellular carcinoma cells using hyperpolarized 13C-labeled glutamine. *Magn. Reson. Med.* **60** (2), 253-257 (2008).
16. Chen, A. P., Albers, M. J., *et al.* Hyperpolarized C-13 spectroscopic imaging of the TRAMP mouse at 3T-initial experience. *Magn. Reson. Med.* **58** (6), 1099-1106 (2007).
17. Day, S. E., Kettunen, M. I., *et al.* Detecting tumor response to treatment using hyperpolarized 13C magnetic resonance imaging and spectroscopy. *Nat. Med.* **13** (11), 1382-1387 (2007).
18. Schroeder, M. A., Swietach, P., *et al.* Measuring intracellular pH in the heart using hyperpolarized carbon dioxide and bicarbonate: a 13C and 31P magnetic resonance spectroscopy study. *Cardiovasc. Res.* **86** (1), 82-91 (2010).
19. Hurd, R. E., Yen, Y.-F., Tropp, J., Pfefferbaum, A., Spielman, D. M., & Mayer, D. Cerebral dynamics and metabolism of hyperpolarized [1-(13C)]pyruvate using time-resolved MR spectroscopic imaging. *J. Cereb. Blood Flow Metab.* **30** (10), 1734-1741 (2010).
20. Golman, K., Zandt, R. I., Lerche, M., Pehrson, R., & Ardenkjaer-Larsen, J. H. Metabolic imaging by hyperpolarized 13C magnetic resonance imaging for in vivo tumor diagnosis. *Cancer Res.* **66** (22), 10855-10860 (2006).
21. Park, I., Larson, P. E. Z., *et al.* Hyperpolarized 13C magnetic resonance metabolic imaging: application to brain tumors. *Neuro. Oncol.* **12** (2), 133-144 (2010).
22. Albers, M. J., Bok, R., *et al.* Hyperpolarized 13C lactate, pyruvate, and alanine: noninvasive biomarkers for prostate cancer detection and grading. *Cancer Res.* **68** (20), 8607-8615 (2008).
23. Yen, Y.-F., Le Roux, P., *et al.* T(2) relaxation times of (13)C metabolites in a rat hepatocellular carcinoma model measured in vivo using (13)C-MRS of hyperpolarized [1-(13)C]pyruvate. *NMR Biomed.* **23** (4), 414-423 (2010).
24. Dafni, H., Larson, P. E. Z., *et al.* Hyperpolarized 13C spectroscopic imaging informs on hypoxia-inducible factor-1 and myc activity downstream of platelet-derived growth factor receptor. *Cancer Res.* **70** (19), 7400-7410 (2010).
25. Ward, C. S., Venkatesh, H. S., *et al.* Noninvasive detection of target modulation following phosphatidylinositol 3-kinase inhibition using hyperpolarized 13C magnetic resonance spectroscopy. *Cancer Res.* **70** (4), 1296-1305 (2010).
26. Day, S. E., Kettunen, M. I., *et al.* Detecting response of rat C6 glioma tumors to radiotherapy using hyperpolarized [1- 13C]pyruvate and 13C magnetic resonance spectroscopic imaging. *Magn. Reson. Med.* **65** (2), 557-563 (2011).
27. Johannesson, H., Macholl, S., & Ardenkjaer-Larsen, J. H. Dynamic Nuclear Polarization of [1-13C]pyruvic acid at 4.6 tesla. *J. Magn. Reson.* **197** (2), 167-175 (2009).
28. Durst, M., Koellisch, U., *et al.* Bolus tracking for improved metabolic imaging of hyperpolarised compounds. *J. Magn. Reson.* **243**, 40-46 (2014).
29. Khegai, O., Schulte, R. F., *et al.* Apparent rate constant mapping using hyperpolarized [1-(13C)]pyruvate. *NMR Biomed.* **27** (10), 1256-1265 (2014).
30. Sogaard, L. V., Schilling, F., Janich, M. A., Menzel, M. I., & Ardenkjaer-Larsen, J. H. In vivo measurement of apparent diffusion coefficients of hyperpolarized (1)(3)C-labeled metabolites. *NMR Biomed.* **27** (5), 561-569 (2014).
31. Aquaro, G. D., Frijia, F., *et al.* 3D CMR mapping of metabolism by hyperpolarized 13C-pyruvate in ischemia-reperfusion. *JACC. Cardiovasc. Imaging*. **6** (6), 743-744 (2013).
32. Menzel, M. I., Farrell, E. V, *et al.* Multimodal assessment of in vivo metabolism with hyperpolarized [1-13C]MR spectroscopy and 18F-FDG PET imaging in hepatocellular carcinoma tumor-bearing rats. *J. Nucl. Med.* **54** (7), 1113-1119 (2013).
33. Schilling, F., Duwel, S., *et al.* Diffusion of hyperpolarized (13) C-metabolites in tumor cell spheroids using real-time NMR spectroscopy. *NMR Biomed.* **26** (5), 557-568 (2013).
34. Schulte, R. F., Sperl, J. I., *et al.* Saturation-recovery metabolic-exchange rate imaging with hyperpolarized [1-13C] pyruvate using spectral-spatial excitation. *Magn. Reson. Med.* **69** (5), 1209-1216 (2013).
35. Wiesinger, F., Weidl, E., *et al.* IDEAL spiral CSI for dynamic metabolic MR imaging of hyperpolarized [1-13C]pyruvate. *Magn. Reson. Med.* **68** (1), 8-16 (2012).

36. Wilson, D. M., Keshari, K. R., *et al.* Multi-compound polarization by DNP allows simultaneous assessment of multiple enzymatic activities in vivo. *J. Magn. Reson.* **205** (1), 141-147 (2010).
37. Schroeder, M. A., Atherton, H. J., *et al.* Real-time assessment of Krebs cycle metabolism using hyperpolarized 13C magnetic resonance spectroscopy. *FASEB J. Off. Publ. Fed. Am. Soc. Exp. Biol.* **23** (8), 2529-2538 (2009).
38. Hurd, R. E., Yen, Y.-F., *et al.* Metabolic imaging in the anesthetized rat brain using hyperpolarized [1-13C] pyruvate and [1-13C] ethyl pyruvate. *Magn. Reson. Med.* **63** (5), 1137-1143 (2010).
39. Chen, A. P., Kurhanewicz, J., *et al.* Feasibility of using hyperpolarized [1-13C]lactate as a substrate for in vivo metabolic 13C MRSI studies. *Magn. Reson. Imaging.* **26** (6), 721-726 (2008).
40. Witney, T. H., Kettunen, M. I., *et al.* Detecting treatment response in a model of human breast adenocarcinoma using hyperpolarised [1-(13C)pyruvate and [1,4-(13C)(2)]fumarate. *Br. J. Cancer.* **103** (9), 1400-1406 (2010).
41. Bohndiek, S. E., Kettunen, M. I., *et al.* Detecting tumor response to a vascular disrupting agent using hyperpolarized (13)C magnetic resonance spectroscopy. *Mol. Cancer Ther.* **9** (12), 3278-3288 (2010).
42. Gallagher, F. A., Kettunen, M. I., *et al.* Production of hyperpolarized [1,4-13C2]malate from [1,4-13C2]fumarate is a marker of cell necrosis and treatment response in tumors. *Proc. Natl. Acad. Sci. U. S. A.* **106** (47), 19801-19806 (2009).
43. Jensen, P. R., Peitersen, T., *et al.* Tissue-specific short chain fatty acid metabolism and slow metabolic recovery after ischemia from hyperpolarized NMR in vivo. *J. Biol. Chem.* **284** (52), 36077-36082 (2009).
44. Gallagher, F. A., Kettunen, M. I., *et al.* Magnetic resonance imaging of pH in vivo using hyperpolarized 13C-labelled bicarbonate. *Nature.* **453** (7197), 940-943 (2008).
45. Scholz, D. J., Janich, M. A., *et al.* Quantified pH imaging with hyperpolarized 13C-bicarbonate. *Magn. Reson. Med.* **73** (6), 2274-2282 (2015).
46. Koellisch, U., Gringeri, C. V., *et al.* Metabolic imaging of hyperpolarized [1-(13) C]acetate and [1-(13) C]acetylcarnitine - investigation of the influence of dobutamine induced stress. *Magn. Reson. Med.* **74** (4), 1011-1018 (2015).
47. Koellisch, U., Laustsen, C., *et al.* Investigation of metabolic changes in STZ-induced diabetic rats with hyperpolarized [1-13C]acetate. *Physiol. Rep.* **3** (8) (2015).
48. Jensen, P. R., Meier, S., Ardenkjaer-Larsen, J. H., Duus, J. O., Karlsson, M., & Lerche, M. H. Detection of low-populated reaction intermediates with hyperpolarized NMR. *Chem. Commun.* (34), 5168-5170 (2009).
49. Koelsch, B. L., Keshari, K. R., Peeters, T. H., Larson, P. E. Z., Wilson, D. M., & Kurhanewicz, J. Diffusion MR of hyperpolarized 13C molecules in solution. *Analyst.* **138** (4), 1011-1014 (2013).
50. Golman, K., Ardenkjaer-Larsen, J. H., Petersson, J. S., Mansson, S., & Leunbach, I. Molecular imaging with endogenous substances. *Proc. Natl. Acad. Sci. U. S. A.* **100** (18), 10435-10439 (2003).
51. von Morze, C., Larson, P. E. Z., *et al.* Imaging of Blood Flow Using Hyperpolarized [(13)C]Urea in Preclinical Cancer Models. *J. Magn. Reson. Imaging.* **33** (3), 692-697 (2011).
52. Chiavazza, E., Kubala, E., *et al.* Earth's magnetic field enabled scalar coupling relaxation of 13C nuclei bound to fast-relaxing quadrupolar 14N in amide groups. *J. Magn. Reson.* **227**, 35-38 (2013).
53. Jensen, P. R., Karlsson, M., Meier, S., Duus, J., & Lerche, M. H. Hyperpolarized amino acids for in vivo assays of transaminase activity. *Chem. - A Eur. J.* **15** (39), 10010-10012 (2009).
54. Gallagher, F. A., Kettunen, M. I., *et al.* Detection of tumor glutamate metabolism in vivo using 13C magnetic resonance spectroscopy and hyperpolarized [1-13C]glutamate. *Magn. Reson. Med.* **66** (1), 18-23 (2011).
55. Chaumeil, M. M., Larson, P. E. Z., *et al.* Hyperpolarized [1-13C] glutamate: a metabolic imaging biomarker of IDH1 mutational status in glioma. *Cancer Res.* **74** (16), 4247-4257 (2014).
56. Keshari, K. R., & Wilson, D. M. Chemistry and biochemistry of 13C hyperpolarized magnetic resonance using dynamic nuclear polarization. *Chem. Soc. Rev.* **43** (5), 1627-1659 (2014).
57. Nelson, S. J., Kurhanewicz, J., *et al.* Metabolic Imaging of Patients with Prostate Cancer Using Hyperpolarized [1-13C]Pyruvate. *Sci. Transl. Med.* **5** (198), 198ra108-198ra108 (2013).
58. Warburg, O. On the origin of cancer cells. *Science.* **123** (3191), 309-314 (1956).
59. Warburg, O., Wind, F., & Negelein, E. {Ü}ber den Stoffwechsel von Tumoren im K{ö}rper. *Klin. Wochenschr.* **5** (19), 829-832 (1926).
60. Barnes, A. B., Paepe, G. De, *et al.* High-Field Dynamic Nuclear Polarization for Solid and Solution Biological NMR. *Appl. Magn. Reson.* **34** (3-4), 237-263 (2008).
61. Koukourakis, M. I., Giatromanolaki, A., Sivridis, E., Gatter, K. C., & Harris, A. L. Pyruvate dehydrogenase and pyruvate dehydrogenase kinase expression in non small cell lung cancer and tumor-associated stroma. *Neoplasia.* **7** (1), 1-6 (2005).
62. Golman, K., & Petersson, J. S. Metabolic Imaging and Other Applications of Hyperpolarized ^{13}C[1]. *Acad. Radiol.* **13** (8), 932-942 (2016).
63. Golman, K., Petersson, J. S., *et al.* Cardiac metabolism measured noninvasively by hyperpolarized 13C MRI. *Magn. Reson. Med.* **59** (5), 1005-1013 (2008).
64. Merritt, M. E., Harrison, C., Storey, C., Jeffrey, F. M., Sherry, A. D., & Malloy, C. R. Hyperpolarized 13C allows a direct measure of flux through a single enzyme-catalyzed step by NMR. *Proc. Natl. Acad. Sci. U. S. A.* **104** (50), 19773-19777 (2007).
65. Merritt, M. E., Harrison, C., Storey, C., Sherry, A. D., & Malloy, C. R. Inhibition of carbohydrate oxidation during the first minute of reperfusion after brief ischemia: NMR detection of hyperpolarized 13CO2 and H13CO3-. *Magn. Reson. Med.* **60** (5), 1029-1036 (2008).
66. Hu, S., Chen, A. P., *et al.* In vivo carbon-13 dynamic MRS and MRSI of normal and fasted rat liver with hyperpolarized 13C-pyruvate. *Mol. imaging Biol. MIB Off. Publ. Acad. Mol. Imaging.* **11** (6), 399-407 (2009).
67. Kohler, S. J., Yen, Y., *et al.* In vivo 13 carbon metabolic imaging at 3T with hyperpolarized 13C-1-pyruvate. *Magn. Reson. Med.* **58** (1), 65-69 (2007).
68. Hu, S., Lustig, M., *et al.* 3D compressed sensing for highly accelerated hyperpolarized (13)C MRSI with in vivo applications to transgenic mouse models of cancer. *Magn. Reson. Med.* **63** (2), 312-321 (2010).
69. Kurhanewicz, J., Vigneron, D. B., *et al.* Analysis of cancer metabolism by imaging hyperpolarized nuclei: prospects for translation to clinical research. *Neoplasia.* **13** (2), 81-97 (2011).
70. Schroeder, M. A., Cochlin, L. E., Heather, L. C., Clarke, K., Radda, G. K., & Tyler, D. J. In vivo assessment of pyruvate dehydrogenase flux in the heart using hyperpolarized carbon-13 magnetic resonance. *Proc. Natl. Acad. Sci. U. S. A.* **105** (33), 12051-12056 (2008).
71. Zierhut, M. L., Yen, Y.-F., *et al.* Kinetic modeling of hyperpolarized 13C1-pyruvate metabolism in normal rats and TRAMP mice. *J. Magn. Reson.* **202** (1), 85-92 (2010).
72. Dennis, L. K., & Resnick, M. I. Analysis of recent trends in prostate cancer incidence and mortality. *Prostate.* **42** (4), 247-252 (2000).

73. Jambor, I., Borra, R., *et al.* Functional imaging of localized prostate cancer aggressiveness using 11C-acetate PET/CT and 1H-MR spectroscopy. *J. Nucl. Med.* **51** (11), 1676-1683 (2010).
74. Presti, J. C. J., Hricak, H., Narayan, P. A., Shinohara, K., White, S., & Carroll, P. R. Local staging of prostatic carcinoma: comparison of transrectal sonography and endorectal MR imaging. *AJR. Am. J. Roentgenol.* **166** (1), 103-108 (1996).
75. Schulte, R. F., Sacolick, L., *et al.* Transmit gain calibration for nonproton MR using the Bloch-Siegert shift. *NMR Biomed.* **24** (9), 1068-1072 (2011).
76. Durst, M., Koellisch, U., *et al.* Comparison of acquisition schemes for hyperpolarised (1)(3)C imaging. *NMR Biomed.* **28** (6), 715-725 (2015).
77. Janich, M. A., Menzel, M. I., *et al.* Effects of pyruvate dose on in vivo metabolism and quantification of hyperpolarized (1)(3)C spectra. *NMR Biomed.* **25** (1), 142-151 (2012).
78. Harrison, C., Yang, C., *et al.* Comparison of kinetic models for analysis of pyruvate-to-lactate exchange by hyperpolarized 13 C NMR. *NMR Biomed.* **25** (11), 1286-1294 (2012).
79. Gómez Damián, P. A., Sperl, J. I., *et al.* Multisite Kinetic Modeling of (13)C Metabolic MR Using [1-(13)C]Pyruvate. *Radiol. Res. Pract.* **2014**, 871619 (2014).
80. Talbot, J.-N., Gutman, F., *et al.* PET/CT in patients with hepatocellular carcinoma using [(18)F]fluorocholine: preliminary comparison with [(18)F]FDG PET/CT. *Eur. J. Nucl. Med. Mol. Imaging.* **33** (11), 1285-1289 (2006).
81. Reeder, S. B., Pineda, A. R., *et al.* Iterative decomposition of water and fat with echo asymmetry and least-squares estimation (IDEAL): application with fast spin-echo imaging. *Magn. Reson. Med.* **54** (3), 636-644 (2005).
82. Laustsen, C., Ostergaard, J. A., *et al.* Assessment of early diabetic renal changes with hyperpolarized [1-(13) C]pyruvate. *Diabetes. Metab. Res. Rev.* **29** (2), 125-129 (2013).
83. Serrao, E. M., & Brindle, K. M. Potential Clinical Roles for Metabolic Imaging with Hyperpolarized [1-(13)C]Pyruvate. *Front. Oncol.* **6**, 59 (2016).

ENCODING FOR MOTION: DIFFUSION AND PERFUSION

4.1 PEER-REVIEWED PUBLICATIONS

In this section, two publications are presented, where novel data reconstruction and processing techniques are demonstrated to accelerate data acquisition and provide multiple outputs from the same input data. Spatio-temporal MRI Reconstruction by Enforcing Local and Global Regularity via Dynamic Total Variation and Nuclear Norm Minimization and Robust Reconstruction of Accelerated Perfusion MRI Using Local and Nonlocal Constraints show principled algorithmic developments to reconstruct dynamic MRI data from highly undersampled measurements.

4.1.1 *Spatio-temporal MRI Reconstruction by Enforcing Local and Global Regularity via Dynamic Total Variation and Nuclear Norm Minimization*

Peer-reviewed Conference Paper

Authors: C. Ulas, **PA. Gómez**, JI. Sperl, C. Preibisch, BH. Menze

Abstract: In this paper, we propose a new spatio-temporal reconstruction scheme for the fast reconstruction of Dynamic Magnetic Resonance Imaging (dMRI) data from undersampled k-space measurements. To utilize both spatial and temporal redundancy in dMRI sequences, our method investigates the potential benefits of enforcing local spatial sparsity constraints on the difference to a reference image for each frame and additionally exploiting the low-rank property of global spatio-temporal signal via Nuclear Norm (NN) minimization. We present here an iterative algorithm that solves the convex optimization problem in an alternating fashion. The proposed method is tested on in-vivo 3D cardiac MRI and Dynamic Susceptibility Contrast (DSC)-MRI brain perfusion datasets. In comparison to two state-of-the-art methods, numerical experiments demonstrate the superior performance of our method in terms of reconstruction accuracy.

Contribution of thesis author: Algorithmic discussions and implementation, manuscript revision and editing.

SPATIO-TEMPORAL MRI RECONSTRUCTION BY ENFORCING LOCAL AND GLOBAL REGULARITY VIA DYNAMIC TOTAL VARIATION AND NUCLEAR NORM MINIMIZATION

Cagdas Ulas [†¶⋆]   *Pedro A. Gómez* [†¶]   *Jonathan I. Sperl* [¶]   *Christine Preibisch* [‡]   *Bjoern H. Menze* [†§]

[†] Department of Computer Science, TU München, Munich, Germany
[§] Institute for Advanced Study, TU München, Munich, Germany
[‡] Neuroradiology, Klinikum rechts der Isar der TU München, Munich, Germany
[¶] GE Global Research, Munich, Germany

ABSTRACT

In this paper, we propose a new spatio-temporal reconstruction scheme for the fast reconstruction of dynamic magnetic resonance imaging (dMRI) data from undersampled k-space measurements. To utilize both spatial and temporal redundancy in dMRI sequences, our method investigates the potential benefits of enforcing local spatial sparsity constraints on the difference to a reference image for each frame and additionally exploiting the low-rank property of global spatio-temporal signal via nuclear norm (NN) minimization. We present here an iterative algorithm that solves the convex optimization problem in an alternating fashion. The proposed method is tested on in-vivo 3D cardiac MRI and dynamic susceptibility contrast (DSC)-MRI brain perfusion datasets. In comparison to two state-of-the-art methods, numerical experiments demonstrate the superior performance of our method in terms of reconstruction accuracy.

Index Terms— compressed sensing, dynamic MR imaging, low-rank approximation, total variation, nuclear norm

1. INTRODUCTION

Dynamic magnetic resonance imaging (dMRI) is an important medical imaging technique that enables the visualization of anatomical and functional changes of internal body structures through time, resulting in a spatio-temporal signal. Although MRI is a non-invasive, non-ionizing technology and provides an unmatched quality in soft tissue contrast, physical and physiological limitations on scanning speed makes this an inherently slow process [1]. Besides, there is a trade-off between the spatial and temporal resolution. The reason is that acquiring fewer k-space samples than those dictated by the Nyquist criterion accelerates the process significantly, but exhibits aliasing artifacts in image space. Fortunately, dynamic MR sequences usually provide redundant information in both spatial and temporal domains, which allows the reduction of acquisition time by using compressed sensing (CS) approaches [2, 3]. More recently, CS theory has been applied to MRI enabling highly accurate reconstructions from fewer k-space measurements depending on the assumption of sparsity of the reconstructed data under some transform domain [4].

In recent years, researchers have proposed sophisticated CS-based reconstruction methods that exploit both spatial and temporal redundancies of the entire dataset, such as spatio-temporal total variation [5], dictionary learning [6], and low-rank approximation and sparsity [5, 7]. In general, dynamic MR images are temporally correlated due to slow changes of the same organ(s) through the whole image sequence, and such high correlation in the temporal domain has been successfully investigated based on a sparsity constraint in the temporal domain for dMRI reconstruction [6]. As an extension of the conventional spatial total variation (TV), a new sparsity inducing norm called dynamic total variation (dTV) [8] has been recently introduced to utilize both spatial and temporal correlations in online reconstruction.

In this paper, we make an attempt to integrate two fundamentally different approaches for CS-based reconstruction: we enforce local coherences at the pixel-level via dynamic total variation (dTV) and global regularity in the full spatio-temporal domain via a nuclear norm (NN) minimization constraint. We present the dTV/NN optimization in a joint formal framework which allows us to rely on an iterative minimization algorithm. The joint minimization problem is solved iteratively by utilizing an alternating minimization strategy. The proposed method is validated on two different dynamic MR sequences with comparisons to state-of-the-art methods.

Our main contributions can be summarized as follows: We propose a novel reconstruction scheme that iteratively enforces not only the local (spatial) regularity in every single frame but also the global (spatio-temporal) regularity of a full sequence. To this end, we introduce a reconstruction model that is jointly using dTV sparsity and nuclear norm penalties, exploiting both the sparsity of inter-frame differences and the low-rank structure of the dynamic MR sequences in the full

spatio-temporal space. Our approach also employs, for the first time, the dTV sparsity inducing norm in an offline reconstruction scheme.

2. METHODS

2.1. Problem formulation

Here, we denote $\mathbf{X}^{3D}$ as a dMRI sequence to be represented as a spatio-temporal 3D volume of size $P = N \times N \times T$, i.e., the images are of size $N \times N$ and T is the total number of frames in the sequence. Let X_t denote the MR image matrix at the tth frame, y_t is the k-space data for the tth frame and $\mathbb{T} = \{1, 2, ..., T\}$ is the set of frame number indices. The main objective here is to reconstruct all X_t's, $t \in \mathbb{T}$, from the collected k-space measurements y_t's. The MR imaging equation for each frame is formulated as

$$y_t = \mathcal{F}_t x_t + \eta \tag{1}$$

where $\mathcal{F}_t$ denotes the undersampling 2D Fourier operator for frame t, i.e., $\mathcal{F}_t = R_t \mathcal{F}_{2D}$, where $R_t \in \mathbb{R}^{m \times N}$, $m \ll N$, is the undersampling mask to acquire only a subset Ω of k-space, x_t denotes the MR image vector formed by row/column concatenation of X_t and $\eta \in \mathbb{C}^m$ is additive Gaussian noise in k-space. We stack the data for all the frames of the MR sequence as columns and denote them as follows: $Y = [y_1|y_2|...|y_T]$, $X = [x_1|x_2|...|x_T]$, and $\mathcal{F}_u = \mathrm{diag}\{\mathcal{F}_1, \mathcal{F}_2, .., \mathcal{F}_T\}$.

We propose solving the following optimization problem for the reconstruction of dMRI sequences:

$$\min_X \quad \nu_1 \|X\|_* + \nu_2(dTV(X, \bar{x}))$$
$$\text{s.t.} \quad \|\mathcal{F}_u X - Y\|_2^2 \leq \epsilon \tag{2}$$

where ν_1 and ν_2 are respective regularization parameters for the two terms, and $\|X\|_*$ denotes the nuclear norm of X and is calculated as

$$\|X\|_* = \sum_i \sigma_i(X)$$

where $\sigma_i(X)$ represents the ith singular value of X. For an image x_t with N^2 pixels, $dTV(X, \bar{x})$ can be defined as

$$dTV(X, \bar{x}) = \sum_{t \in \mathbb{T}} \sum_{n=1}^{N^2} \sqrt{(\nabla_x(x_t - \bar{x})_n)^2 + (\nabla_y(x_t - \bar{x})_n)^2}$$

where $\bar{x}$ is the reference image calculated by averaging all the frames in the sequence, ∇_x and ∇_y represent the finite-difference matrices along the x and y dimensions respectively.

Let us introduce new variables $z_t = x_t - \bar{x}$ and $b_t = y_t - \mathcal{F}_t \bar{x}$, then the problem (2) can be reformulated as follows:

$$\min_{X,z} \quad \nu_1 \|X\|_* + \nu_2 \sum_{t \in \mathbb{T}} \|z_t\|_{TV}$$
$$\text{s.t.} \quad \begin{cases} \|\mathcal{F}_u X - Y\|_2^2 \leq \epsilon \\ \|\mathcal{F}_t z_t - b_t\|_2^2 \leq \epsilon, \ \forall t \end{cases} \tag{3}$$

where $z = [z_1, ..., z_T]$ and $\|z_t\|_{TV} = \|[D_1 z_t, D_2 z_t]\|_{2,1}$, where D_1 and D_2 are two $N^2 \times N^2$ first order finite-difference matrices in vertical and horizontal directions, and $\ell_{2,1}$ norm is the summation of the ℓ_2 norm of each row, $[\mathbf{a_1}, \mathbf{a_2}]$ denotes concatenating two vectors $\mathbf{a_1}$ and $\mathbf{a_2}$ horizontally.

2.2. Image reconstruction algorithm

The optimization problem (3) is convex and we choose to split it into two simpler subproblems that can be efficiently solved with greedy algorithms. Alternating the solution of these two subproblems iteratively will give an approximate solution to Eq. (3). In this approach, an approximate generic solution is refined towards a better solution.

- **Subproblem 1 :** *Enforcing local (spatial) regularity*

$$\min_{z_t} \quad \frac{1}{2}\|\mathcal{F}_t z_t - b_t\|_2^2 + \nu_2\|z_t\|_{TV}, \ \forall t \tag{4}$$

For each frame x_t in the sequence, we solve the optimization problem (4) to reconstruct each frame individually given a reference image $\bar{x}$. This guarantees that the sum of TV norms in Eq. (3) is also minimized. The problem (4) can be efficiently solved by the fast iteratively reweighted least squares (FIRLS) algorithm [9] based on preconditioned conjugate gradient. This algorithm provides fast convergence and low computational cost by designing a new preconditioner which can be accurately approximated using the properties of the Fourier transform and diagonally dominant structure of the $\mathcal{F}_t^H \mathcal{F}_t$ matrix, where H denotes the conjugate transpose. We refer the reader to [9] for more details on FIRLS.

- **Subproblem 2 :** *Enforcing spatio-temporal regularity*

$$\min_X \quad \frac{1}{2}\|\mathcal{F}_u X - Y\|_2^2 + \nu_1\|X\|_* \tag{5}$$

The spatio-temporal signal representation of a dMRI sequence can be arranged as a 2D matrix of X, where each column represents a vectorized image frame. Due to the repetitive structure of the dMRI sequence between consecutive frames, and the resulting high correlation between each column of X, this matrix can be generally approximated to be low-rank, i.e., X has only a few significant singular values.

By exploiting the low-rank property of X, we can solve a low-rank matrix recovery problem using convex nuclear norm as a prior. In this way, we pose low-rank matrix recovery as a nuclear norm regularized linear least squares problem as stated in (5). This problem can be solved iteratively through an accelerated proximal gradient (APG) algorithm [10]. The algorithm provides a computationally efficient way of recovering low-rank matrices iteratively and consists of two main steps: a first order update and a proximal projection of the penalty that is solved via the singular value thresholding operator, i.e., $S_\alpha(\mathbf{G}) = \mathbf{U} \, \mathrm{diag}\{(\mathbf{\Sigma} - \alpha)_+\}\mathbf{V}^H$, where $\mathbf{U}$, $\mathbf{\Sigma}$, $\mathbf{V}$ are obtained from singular value decomposition of $\mathbf{G}$.

Our proposed scheme follows an iterative refinement of an

Algorithm 1 NNMdTV reconstruction

1: **Input:** $Y, \nu_1, \nu_2, \mathcal{F}_u, IterNo$
2: **Output:** X
3: **Initialize:** $X = X_0 = \mathcal{F}_u^H Y, \bar{x} = \bar{x}_0 = mean(\mathcal{F}_u^H Y)$
4: **for** $i = 1$ to $IterNo$ **do**
5:     **for each** $t \in \{1, 2, ..., T\}$ **do**
6:         $\hat{z}_t \leftarrow \arg\min_{z_t} \quad \frac{1}{2}\|\mathcal{F}_t z_t - b_t\|_2^2 + \nu_2\|z_t\|_{TV}$
7:         $x_t \leftarrow \hat{z}_t + \bar{x}_i$
8:     **end for**
9:     Form updated $X_i = [x_1|x_2|...|x_T]$
10:     $X_i \leftarrow \arg\min_{X} \quad \frac{1}{2}\|\mathcal{F}_u X - Y\|_2^2 + \nu_1\|X\|_*$
11:     $\bar{x}_i \leftarrow mean(X_i)$
12: **end for**

---

initial solution. First, we start with zero-filled sequence and iteratively improve the previous reconstruction by first solving the Subproblem 1 for each frame and refining this solution by solving the Subproblem 2 as a following step. Second, in each iteration we update the reference image that is used for solving Subproblem 1, providing a better reference image given as the input to the problem (4), thus yielding more accurate reconstructions. Throughout the paper we will simply term our proposed method as NNMdTV. Algorithm 1 summarizes the steps of the NNMdTV algorithm.

3. EXPERIMENTS AND RESULTS

3.1. Experimental setup

We evaluate our method on two different types of dynamic MR sequences. We use an in-vivo breath-hold cardiac perfusion sequence [8] of size $192 \times 192 \times 40$ and a dynamic susceptibility contrast (DSC)-MRI brain perfusion sequence of size $128 \times 128 \times 60$ with normalized intensities. Both sequences are artificially corrupted by multiplying its corresponding k-space representation with a binary undersampling mask and subsequently adding complex Gaussian white noise with a standard deviation σ. A radial sampling mask is used to simulate undersampling. The same undersampling mask is used for all frames in our experiments.

3.2. Evaluation

For quantitative evaluation, we adopt the Peak Signal-to-Noise Ratio (PSNR) as the metric in our experiments. We compare our method with two state-of-the-art methods: k-t SLR [5] and dynamic total variation (dTV) [8]. The codes of dTV and k-t SLR reconstruction methods are downloaded from each author's website and for k-t SLR we use the default parameter settings in the package for all experiments. For dTV reconstruction, we use the first frame as the reference frame with $1/4$ sampling rate and $1/6$ sampling rate for the remaining frames. The sampling rate for all frames is also

set to $1/6$ for NNMdTV and k-t SLR. To ensure fair comparison, the parameters settings used in dTV reconstruction are also used in our NNMdTV method for all experiments. For the NNMdTV method, we set $\nu_1 = 5 \times 10^{-8}$, $\nu_2 = 0.001$ and $IterNo = 5$ for both sequences. The noise standard deviation is set to $\sigma = 10^{-5}$ for all reconstruction methods.

3.3. Experimental results

In Figs. 1 and 2, we present qualitative results for the DSC brain and cardiac perfusion datasets respectively. Fig. 1 shows the temporal profile of the DSC brain data along a fixed row. From the error maps (see Fig. 1(d, f, h)), it is clearly visible that NNMdTV reconstructs better result compared to other two methods. The red arrows in Fig. 1(h) show the regions where the reconstruction is improved with NNMdTV. A frame of the reconstructed cardiac sequence is shown in Fig. 2. Visible artifacts can clearly be seen on the images reconstructed by k-t SLR. In contrast, compared to the dTV, the reconstruction result of NNMdTV is more similar to the fully-sampled frame, and less noisy (see Fig. 2(h)).

Quantitative results of different methods on two perfusion datasets are shown in Fig. 3. From the figure, we can clearly observe that the proposed NNMdTV achieves the highest PSNR for each iteration and for all frames of the sequences. The graphs at the top of Fig. 3 mainly validate the fact that iteratively updated mean reference image in NNMdTV enables better reconstruction accuracy.

4. CONCLUSION

In this paper, we have proposed a new CS-based reconstruction model for dynamic MRI based on the joint minimization of local differences in each frame and global differences in the full spatio-temporal space and developed an iterative reconstruction algorithm to solve this minimization problem.
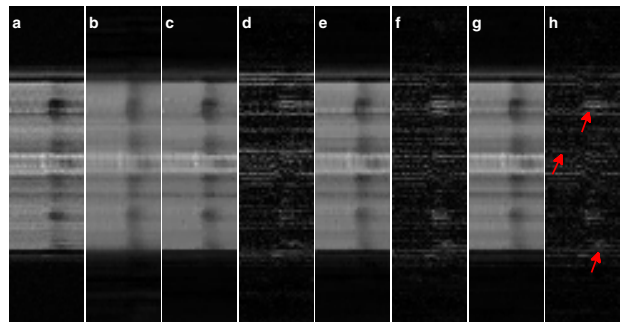
Fig. 1. Temporal profile of row 75 in the original DSC brain dataset (a), its undersampled by 6 zero-filled version (b), and reconstructions using k-t SLR (c), dTV (e), and NNMdTV (g) with their respective errors multiplied by 3 (d, f, h).
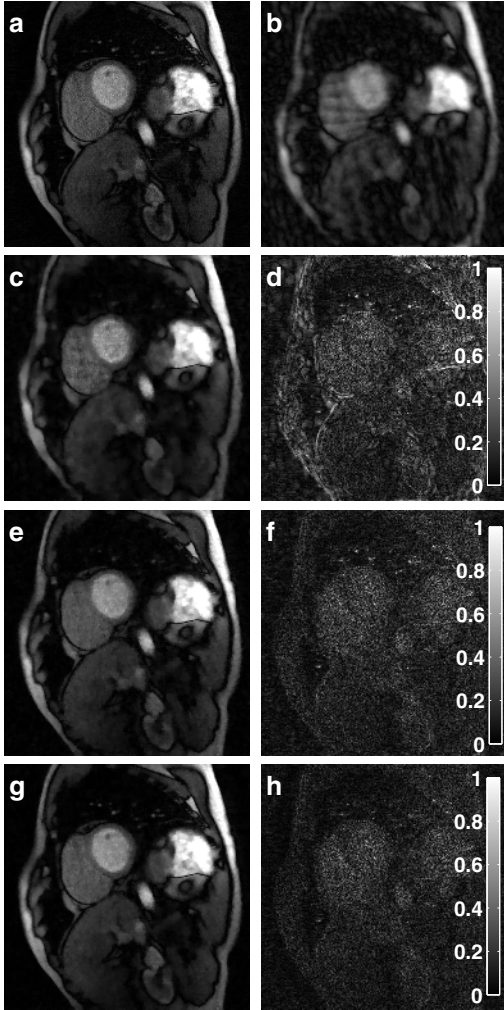
Fig. 2. Visual comparison of a fully sampled frame of cardiac dataset (a), its undersampled by 6 zero-filled version (b), and reconstructions using k-t SLR (c), dTV (e), and NNMdTV (g) with their respective errors magnified by 4 (d, f, h).

Experiments on two different perfusion datasets have demonstrated the effectiveness of our method over the state-of-the-art. Future work will aim at extending our method with the use of patch-wise redundancies of spatio-temporal neighborhoods in adjacent frames and making it more robust to noisy scenarios and large inter-frame motion.

5. REFERENCES

[1] P. A. Gomez et al., "Learning a spatiotemporal dictionary for magnetic resonance fingerprinting with compressed sensing," in *1st Int. Work. on Patch-based Techniques in Medical Imaging, MICCAI*, October 2015.
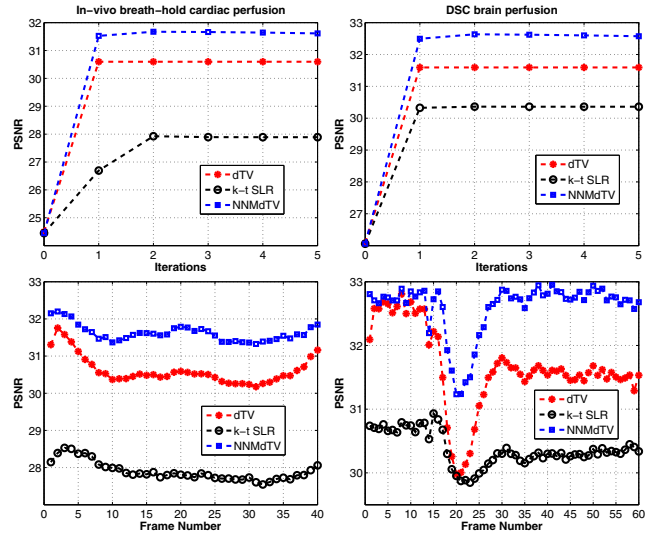
Fig. 3. PSNR comparisons of different reconstruction methods. Cardiac dataset (left), DSC brain dataset (right).

[2] M. Lustig, D. Donoho, and J. Pauly, "Sparse MRI: The application of compressed sensing for rapid MR imaging," *Magn. Reson. Med.*, vol. 58, no. 6, pp. 1182–1195, 2007.

[3] U. Gamper, P. Boesiger, and S. Kozerke, "Compressed sensing in dynamic MRI," *Magn. Reson. Med.*, vol. 59, no. 2, pp. 365–373, 2008.

[4] N. Vaswani and W. Lu, "Modified-CS: Modifying compressive sensing for problems with partially known support," *IEEE Trans. Signal Process.*, vol. 58, no. 9, pp. 4595–4607, 2011.

[5] S. G. Lingala, Y. Hu, E. DiBella, and M. Jacob, "Accelerated dynamic MRI exploiting sparsity and low-rank structure: k-t SLR," *IEEE Trans. on Med. Imag.*, vol. 30, no. 5, pp. 1042–1054, May 2011.

[6] J. Caballero, A.N. Price, D. Rueckert, and J. Hajnal, "Dictionary learning and time sparsity for dynamic MR data reconstruction," *IEEE Trans. on Med. Imag.*, vol. 33, no. 4, pp. 979–994, April 2014.

[7] B. Zhao, J. P. Haldar, A. G. Christodoulou, and Z.-P. Liang, "Image reconstruction from highly undersampled (k,t)-space data with joint partial separability and sparsity constraints," *IEEE Trans. on Med. Imag.*, vol. 31, no. 9, pp. 1809–1820, September 2012.

[8] C. Chen, Y. Li, L. Axel, and J. Huang, "Real time dynamic MRI with dynamic total variation," in *Proc. 17th Int. Conf. MICCAI*, 2014, LNCS, pp. 138–145.

[9] C. Chen, J. Huang, L. He, and H. Li, "Preconditioning for accelerated iteratively reweighted least squares in structured sparsity reconstruction," in *IEEE Conference on Computer Vision and Pattern Recognition (CVPR)*, June 2014, pp. 2713–2720.

[10] K. C. Toh and S. Yun, "An accelerated proximal gradient algorithm for nuclear norm regularized linear least squares problems," *Pacific Journal of Optimazition*, vol. 6, pp. 615–640, 2010.

4.1.2   *Robust Reconstruction of Accelerated Perfusion MRI Using Local and Nonlocal Constraints*

Peer-reviewed Conference Paper

Authors: C. Ulas, **PA. Gómez**, F. Krahmer, JI. Sperl, MI. Menzel, BH. Menze

Abstract: Dynamic perfusion MRI is a commonly used imaging technique that allows to measure the tissue perfusion in an organ of interest via assessment of various hemodynamic parameters such as blood flow, blood volume, and mean transit time. In this paper, we tackle the problem of recovering perfusion MR images from undersampled k-space data. We propose a novel reconstruction model that jointly penalizes spatial (local) incoherence on temporal differences obtained based on a reference image and the patch- wise (nonlocal) dissimilarities between spatio-temporal neighborhoods of MR sequence. Furthermore, we introduce an efficient iterative algorithm based on a proximal-splitting scheme that solves the joint minimization problem with fast convergence. We evaluate our method on Dynamic Susceptibility Contrast (DSC)-MRI brain perfusion datasets as well as on a publicly available dataset of in-vivo breath-hold cardiac perfusion. Our proposed method demonstrates superior reconstruction performance over the state-of-the-art methods and yields highly accurate estimation of perfusion time profiles, which is very essential for the precise quantification of clinically relevant perfusion parameters.

Contribution of thesis author: Algorithmic discussions and implementation, manuscript revision and editing.

Robust Reconstruction of Accelerated Perfusion MRI Using Local and Nonlocal Constraints

Cagdas Ulas[1,3]( ), Pedro A. Gómez[1,3], Felix Krahmer[2], Jonathan I. Sperl[3], Marion I. Menzel[3], and Bjoern H. Menze[1,4]

[1] Computer Science, Technische Universität München, Munich, Germany
cagdas.ulas@tum.de
[2] Applied Numerical Analysis, Technische Universität München,
Munich, Germany
[3] GE Global Research, Munich, Germany
[4] Institute for Advanced Study, Technische Universität München,
Munich, Germany

Abstract. Dynamic perfusion magnetic resonance (MR) imaging is a commonly used imaging technique that allows to measure the tissue perfusion in an organ of interest via assessment of various hemodynamic parameters such as blood flow, blood volume, and mean transit time. In this paper, we tackle the problem of recovering perfusion MR images from undersampled k-space data. We propose a novel reconstruction model that jointly penalizes spatial (local) incoherence on temporal differences obtained based on a reference image and the patchwise (nonlocal) dissimilarities between spatio-temporal neighborhoods of MR sequence. Furthermore, we introduce an efficient iterative algorithm based on a proximal-splitting scheme that solves the joint minimization problem with fast convergence. We evaluate our method on dynamic susceptibility contrast (DSC)-MRI brain perfusion datasets as well as on a publicly available dataset of in-vivo breath-hold cardiac perfusion. Our proposed method demonstrates superior reconstruction performance over the state-of-the-art methods and yields highly accurate estimation of perfusion time profiles, which is very essential for the precise quantification of clinically relevant perfusion parameters.

1   Introduction

Medical diagnosis and research heavily employ perfusion-weighted magnetic resonance imaging (MRI) techniques to estimate the blood flow and volume through examination of the spatio-temporal changes of the signal intensities following the injection of a blood bolus via exogenous paramagnetic tracers. In neuroimaging, these techniques have become widespread clinical tools in the diagnosis of stroke – for the assessment of the tissue at risk –, and the treatment of patients with cerebrovascular disease. One of the major obstacles in the clinical use of perfusion imaging is the need to track the rapid kinetics of contrast agent (tracer) uptake for accurate perfusion quantification [6]. Moreover, the short scanning

time available for each frame often results in limited spatial and temporal resolution, or poor signal-to-noise ratio (SNR) images. In order to improve the spatial or temporal resolution, one widely used approach is to accelerate the acquisition of each frame through the undersampling of k-space by acquiring only a subset of k-space lines [3,15]. However, the undersampling often results in aliasing artifacts in image space and in the context of perfusion MRI, accurate reconstruction of the complete temporal perfusion signal with its peak and high dynamics becomes an even more challenging task.

In recent years, various approaches have been proposed to solve the reconstruction problem in related dynamic imaging tasks, considering, such as piecewise smoothness in the spatial domain [17], high correlation and sparsity in the temporal domain [3,4,10], sparse representations of local image regions via learned dictionaries [3] and low-rank property of MR sequences in the full spatiotemporal space [10,14,17]. Although these methods allow highly accurate reconstructions from fewer k-space data, the main drawback is that their performance is very sensitive to motion and rapid intensity changes occurring over the duration of image acquisition as encountered in perfusion MRI. In addition, these methods often result in over smooth and blurry image regions that are lacking finer details when the acquired data are contaminated with high noise.

In this paper, we integrate two fundamentally different approaches that both increase the robustness of the reconstruction for perfusion MRI: (i) we enforce pixel-wise local sparsity constraint on the temporal differences that limits the overall dynamic of the perfusion time series, (ii) we enforce patch-wise similarity constraint on the spatio-temporal neighborhoods of whole MR sequence, which provides smooth spatial image regions with less temporal blurring especially when there is significant inter-frame motion and noise. We present the main optimization problem in a joint formal framework and introduce a new proximal splitting strategy that benefits from the weighted-average of proximals – thus, overcome a key limitation of the widely used Fast Composite Splitting Algorithm (FCSA) [9] –, and efficiently solves the joint minimization problem with fast convergence. The proposed method is validated on different types of MR perfusion datasets in comparison with the state-of-the-art methods and extensive experiments demonstrate the superior performance of our method in terms of reconstruction accuracy and accurate estimation of perfusion time profiles from undersampled k-space data even when being presented with high noise levels.

Contributions. Our main contributions are four-fold: (1) We present a new reconstruction scheme which cannot only produce high-quality spatial images for dynamic MRI but also enable to reconstruct the complete temporal signal dynamics for perfusion MRI from undersampled k-space data (Sect. 2). (2) We introduce an efficient proximal-splitting algorithm based on a generalized forward-backward splitting scheme [13]. This algorithm provides fast convergence and can be easily applied to various medical image applications that consider optimization problems where the objective function is the sum of several convex regularization terms (Sect. 3). (3) We demonstrate the efficiency and effectiveness of our method by comparing with state-of-the-art techniques on clinical

datasets (Sect. 4). (4) Our proposed reconstruction model can enable accurate quantification of clinically useful perfusion parameters while accelerating the acquisition through the use of fewer k-space samples.

2   Formulation

Throughout the paper we consider the reconstruction problem only on 2D+t data (i.e., on a single slice followed over time), however the idea presented here can also easily be extended to 3D+t data. We assume that $X^{3D} \in \mathbb{C}^{M \times N \times T}$ is a 2D perfusion image series represented as a spatio-temporal 3D volume. Let $x_t \in \mathbb{C}^{M \times N}$ denote one perfusion MR frame at time t with $M \times N$ pixels, y_t is the corresponding undersampled k-space measurements of x_t, and $\mathbb{T} = \{1, 2, ..., T\}$ is the set of frame number indices in the sequence. The main goal is to recover all x_t's from the collected k-space measurements y_t's. The observation model between x_t and y_t can be mathematically formulated as

$$y_t = R_t(\mathcal{F}_{2D} x_t + \eta) \tag{1}$$

where R_t denotes the undersampling mask to acquire only a subset of k-space, $\mathcal{F}_{2D}$ is the 2D Fourier Transform operator and η is additive Gaussian noise in k-space. We also denote the partial 2D Fourier operator for frame t as $\mathcal{F}_t = R_t \mathcal{F}_{2D}$, and stack the $\mathcal{F}_t$ for all frames of the sequence as $\mathcal{F}_u = \text{diag}\{\mathcal{F}_1, \mathcal{F}_2, .., \mathcal{F}_T\}$.

We propose solving the following optimization problem for the reconstruction of perfusion MR sequences:

$$\hat{X} = \arg\min_X \left\{ \frac{1}{2} \|\mathcal{F}_u X - Y\|_2^2 + \lambda_1 \mathcal{G}_1(X) + \lambda_2 \mathcal{G}_2(X) \right\} \tag{2}$$

where $X \in \mathbb{C}^{MN \times T}$ denotes the whole perfusion MRI sequence and $Y \in \mathbb{C}^{MN \times T}$ represents the collection of all the k-space measurements. λ_1 and λ_2 are the tuning parameters for two regularization terms.

Local ($\mathcal{G}_1$) regularizer: The first regularization term in (2) penalizes the sum of spatial finite differences on the difference images calculated based on a reference for every image frame $x_t \in \mathbb{C}^{M \times N}$, and this term is named as dynamic total variation (TV) [4] and for the whole MR sequence, it can be defined as

$$\mathcal{G}_1(X) = \sum_{t \in \mathbb{T}} \sum_{n=1}^{M \times N} \sqrt{\left(\nabla_x (x_t - \bar{x})_n\right)^2 + \left(\nabla_y (x_t - \bar{x})_n\right)^2} \tag{3}$$

where $\bar{x}$ is the reference image computed by averaging all the frames in MR sequence, ∇_x and ∇_y represent the finite-difference operators along the x and y dimensions, respectively. The intuition behind using dynamic TV over standard TV is that it is better adjusted to the variation in time, and this regularizer serves as a penalty on the overall dynamic of the temporal perfusion signal.

Nonlocal ($\mathcal{G}_2$) regularizer: The second regularization term in (2) penalizes the weighted sum of ℓ_2 norm distances between spatio-temporal neighborhoods (patches) of MR sequence, and this penalty term can be specified by [16]

$$\mathcal{G}_2(X) = \sum_{(\mathrm{p}_x,\mathrm{p}_y,\mathrm{p}_t)\in\Omega} \sum_{(\mathrm{q}_x,\mathrm{q}_y,\mathrm{q}_t)\in\mathcal{N}_{\mathrm{p}}} w(\mathrm{p},\mathrm{q})\|P_{\mathrm{p}}(\mathrm{X}^{3D}) - P_{\mathrm{q}}(\mathrm{X}^{3D})\|_2^2 \qquad (4)$$

where $\mathrm{p} = (\mathrm{p}_x, \mathrm{p}_y, \mathrm{p}_t)$ and $\mathrm{q} = (\mathrm{q}_x, \mathrm{q}_y, \mathrm{q}_t)$ are two voxels, and the voxel of interest is $\mathrm{p} \in \Omega$, where $\Omega = [0, M] \times [0, N] \times [0, T]$. The term $P_{\mathrm{p}}(\mathrm{X}^{3D})$ denotes a spatio-temporal 3D patch of the MR sequence centered at voxel p. We represent $\mathcal{N}_{\mathrm{p}}$ as a 3D search window around voxel p, and the size of the patch should be smaller than the size of the search window. We simply denote N_p and N_w as the size of a patch and search window, respectively. The weights $w(\mathrm{p},\mathrm{q})$ are determined based on ℓ_2 norm distance between the patches and calculated as

$$w(\mathrm{p},\mathrm{q}) = e^{-\frac{\|P_{\mathrm{p}}(\mathrm{X}^{3D}) - P_{\mathrm{q}}(\mathrm{X}^{3D})\|_2^2}{h^2}} \qquad (5)$$

where h is a smoothing parameter controlling the decay of the exponential function. The use of exponential weighting ensures that a voxel which is more similar to the voxel of interest in terms of Euclidean distance receives higher weight.

This regularizer is capable of exploiting the similarities between patch pairs in adjacent frames and it can enforce smooth solutions in the spatio-temporal neighbourhoods of MR sequence even when there is significant inter-frame motion and high noise introduced during acquisition.

3   Algorithm

To efficiently solve the primal problem (2), we propose to apply a proximal-splitting framework to this problem. Before describing our proximal-splitting based algorithm, we should first give the definition of a proximal map.

Proximal map: Given a continuous convex function $g(x)$ and a scalar $\rho > 0$, the proximal operator associated to convex function g can be defined as [9]

$$prox_\rho(g)(z) := \underset{x\in\mathcal{H}}{\arg\min} \left\{ \frac{1}{2\rho}\|x - z\|_2^2 + g(x) \right\} \qquad (6)$$

Now we can reformulate the problem (2) as the following denoising problem

$$\hat{X} = \underset{X}{\arg\min} \left\{ \frac{1}{2}\|X - X_g\|_2^2 + \rho\lambda_1\mathcal{G}_1(X) + \rho\lambda_2\mathcal{G}_2(X) \right\} \qquad (7)$$

Since each of the regularization term in the cost function (2) is convex, the problem (7) can be represented as the proximal map of the sum of two regularization terms as described in Fast Composite Splitting Algorithm (FCSA) [9]

$$\hat{X} = prox_\rho(\lambda_1\mathcal{G}_1 + \lambda_2\mathcal{G}_2)(X_g) \qquad (8)$$

The problem (7) admits to a unique solution as given in (8). However, the proximity operator of the sum of two functions is usually intractable. To compute it iteratively, one can adopt an efficient proximal-splitting method to this problem. Proximal-splitting methods are first-order iterative algorithms that solve relatively large-scale optimization problems with several nonsmooth penalties. They operate by splitting the convex objective function to minimize and generating individual subproblems which are evaluated easily via proximal operators.

To solve our main problem in (7), we split the objective function into two individual subproblems that we term $\mathcal{G}_1$-subproblem and $\mathcal{G}_2$-subproblem.

$\mathcal{G}_1$**-subproblem:** The proximal map for this subproblem can be defined as

$$X_{\mathcal{G}_1} = prox_\rho(\lambda_1 \mathcal{G}_1)(X_g) = \arg\min_X \left\{ \frac{1}{2\rho}\|X - X_g\|_2^2 + \lambda_1 \mathcal{G}_1(X) \right\} \qquad (9)$$

In order to solve the subproblem (9), we first reformulate it by introducing new variables $d_t = x_t - \bar{x}$ and $d_g^t = X_g^t - \bar{x}$, in this way the problem turns into

$$\hat{d} = \arg\min_d \left\{ \sum_{t \in \mathbb{T}} \left(\frac{1}{2\rho}\|d_t - d_g^t\|_2^2 + \lambda_1 \|d_t\|_{TV} \right) \right\} \qquad (10)$$

where $d = \{d_1, ..., d_T\}$ and $\|d_t\|_{TV} = \|[Q_1 d_t, Q_2 d_t]\|_{2,1}$, where Q_1 and Q_2 are two $MN \times MN$ first order finite difference matrices in vertical and horizontal directions, and $\ell_{2,1}$ norm is the sum of the ℓ_2 norm of each row of given matrix.

Given a reference image $\bar{x}$, the cost function in (10) can be minimized individually for every frame x_t of MR sequence. This guarantees that the sum of the costs in (10) is also minimized. The cost function can be efficiently minimized by using the fast iteratively reweighted least squares (FIRLS) algorithm [5] based on preconditioned conjugate gradient method. This algorithm enables fast convergence and low computational cost by adopting a new preconditioner which can be accurately approximated using the diagonally dominant structure of the matrix $\mathcal{F}_t^H \mathcal{F}_t$, where H is the conjugate transpose. Once the problem (10) is solved, the estimated solution for problem (9) can be calculated as

$$\hat{X}_{\mathcal{G}_1} = \left[\hat{d}_1 + \bar{x}, \hat{d}_2 + \bar{x}, ..., \hat{d}_T + \bar{x} \right] \qquad (11)$$

$\mathcal{G}_2$**-subproblem:** The proximal map for $\mathcal{G}_2$ subproblem can be specified by

$$X_{\mathcal{G}_2} = prox_\rho(\lambda_2 \mathcal{G}_2)(X_g) = \arg\min_X \left\{ \frac{1}{2\rho}\|X - X_g\|_2^2 + \lambda_2 \mathcal{G}_2(X) \right\} \qquad (12)$$

The problem (12) can be solved using a two-step alternating minimization scheme in an iterative projections onto convex sets (POCS) framework [11]. In each iteration, the first step involves the projection of image estimate onto the data fidelity term via a steepest descend update and the second step performs the minimization of the neighborhood penalty term on the projected data. The minimization of the penalty function in (12) is equivalent to applying non-local

42   C. Ulas et al.

means (NLM) filter [2] to the projected images. This is mathematically derived in [12] with a single assumption that only one sub-iteration of the penalty term is performed with constant and predetermined weights. The mathematical formulation of a NLM filter is given as [12]

$$\hat{X}(\mathrm{p}_x, \mathrm{p}_y, \mathrm{p}_t) = \frac{\sum_{(\mathrm{q}_x, \mathrm{q}_y, \mathrm{q}_t) \in \mathcal{N}_\mathrm{p}} w(\mathrm{p}, \mathrm{q}) X(\mathrm{q}_x, \mathrm{q}_y, \mathrm{q}_t)}{\sum_{(\mathrm{q}_x, \mathrm{q}_y, \mathrm{q}_t) \in \mathcal{N}_\mathrm{p}} w(\mathrm{p}, \mathrm{q})} \tag{13}$$

We have now iterative solvers for each subproblem $\mathcal{G}_1$ and $\mathcal{G}_2$. In this work, we have developed an efficient algorithm by adopting a generalized forward-backward splitting (GFBS) framework [13] that minimizes the sum of multiple convex functions. Basically, FCSA and GFBS are operator-splitting algorithms and they both use forward-backward schemes. The main difference between GFBS and FCSA is that GFBS enables the use of weighted-average of the outputs of individual proximal mappings for finitely many convex functions, whereas FCSA only applies simple averaging. The weighted-average of the outputs of proximals may practically yield better results depending on the effectiveness of each penalty (regularization) term employed in various applications.

We further accelerate the convergence of the algorithm with an additional acceleration step similar to the Fast Iterative Shrinkage-Thresholding Algorithm (FISTA) [1]. This step adaptively increases the value of step size parameter (α_k) through iterations and make it sufficiently close to 1. Our proposed reconstruction algorithm is outlined in Algorithm 1. The most computationally expensive step of our algorithm is solving each proximal map. Fortunately, the computation of proximal maps can be done in parallel since there is no dependency between the inputs of proximity operators. All the other steps involve adding and multiplying vectors or scalars, and are thus very cheap in terms of computational complexity. The GFBS method has been shown to converge when $\gamma < 2/L$ if the convex function $f = \frac{1}{2}\|X - X_g\|_2^2$ has a Lipschitz continuous gradient with constant L [13]. We refer the readers to original GFBS paper [13] for details concerning the proof of the convergence of the algorithm.

4   Experiments

Experimental Setup: We evaluate our method on two different types of perfusion MRI datasets. We use three DSC-MRI brain perfusion sequences ($128 \times 128 \times 60$) and one in-vivo breath-hold cardiac perfusion sequence[1] ($192 \times 192 \times 40$) from [4] with normalized intensities. All the perfusion datasets used in the experiments are acquired with full-sampling and the fully-sampled sequences are artificially corrupted by multiplying its corresponding k-space representation with a binary undersampling mask and subsequently adding Gaussian white noise. To simulate undersampling, we retrospectively apply a time-varying variable density Cartesian mask in our experiments (see Fig. 1). The sampling ratio is set to 1/4 for brain sequences and 1/6 for cardiac sequence.

---

[1] Available at: http://web.engr.illinois.edu/~cchen156/SSMRI.html.


Algorithm 1. Proposed algorithm

Input: Undersampled k-space data Y, $\mathcal{F}_u$, λ_1, λ_2
Initialize: $z_1^0 = z_2^0 = \mathcal{F}_u^H Y$, w_1, w_2, $X^0 = \sum_{i=1}^2 w_i z_i^0$, $\alpha_0 = 0.5$, $\gamma = 1$, $k = 0$
while *stopping criteria not met* **do**

$\quad X_g = X^k - \gamma \mathcal{F}_u^H(\mathcal{F}_u X^k - Y)$;

$\quad z_1^{k+1} = z_1^k + \alpha_k(prox_{\frac{\gamma}{w_1}}(2\lambda_1 \mathcal{G}_1)(X^k + X_g - z_1^k) - X^k)$;

$\quad z_2^{k+1} = z_2^k + \alpha_k(prox_{\frac{\gamma}{w_2}}(2\lambda_2 \mathcal{G}_2)(X^k + X_g - z_2^k) - X^k)$;

$\quad X^{k+1} = w_1 z_1^{k+1} + w_2 z_2^{k+1}$;

$\quad \alpha_{k+1} = 1 + 2(\alpha_k - 1)/(1 + \sqrt{1 + 4(\alpha_k)^2})$;

$\quad k \leftarrow k + 1$;

end
Output: Reconstructed image data X

We compare our method with three state-of-the-art reconstruction methods: the dynamic total variation (DTV) [4], (k,t)-space via low-rank plus sparse prior (kt-RPCA) [14], and fast total variation and nuclear norm regularization (FTVNNR) [17]. To ensure fair comparison, similar to the experiments presented in [3], we empirically fine-tune the optimal regularization parameters for all methods individually for each dataset and depending on noise level. For our proposed method, we specifically set $\lambda_2 = 0.25$ for all noise levels and set $\lambda_1 = 0.025$ for relatively high level noise and $\lambda_1 = 0.001$ for low noise levels. We test the following noise levels and report the results: $\sigma = \{10^{-1}, 5 \times 10^{-2}, 10^{-2}, 5 \times 10^{-3}, 10^{-3}\}$. For the proposed method, we set $N_w = 7 \times 7 \times 7$, $N_p = 5 \times 5 \times 5$, and $w_1 = w_2 = 0.5$ for all sequences. We consider using small cubic neighborhoods for N_w and N_p since large neighborhoods drastically increase the computation time. To reduce the computational burden, we also employ an optimized blockwise version of the non-local means filter that was proposed by Coupé et al. [7] for 3D medical data. We adopt the Peak Signal-to-Noise Ratio (PSNR) as the metric for quantitative evaluation. Instead of directly calculating PSNR on a whole image or 3D sequence, we employ a region-based analysis by calculating the PSNR on randomly selected 100 image blocks (50×50) in 2D frames. This allows us to test for statistical differences using paired t-test when comparing different methods.

Results: Figures 1 and 2 demonstrate a single reconstructed frame of the first and third brain perfusion dataset, respectively, and the estimation of perfusion time profiles averaged over voxels inside a small region of interest. The results in Fig. 1 reveal that kt-RPCA and FTVNNR show quite similar performances, and the DTV yields both better reconstruction and estimation of perfusion signal compared to these two methods. Compared with all three methods, our proposed method can achieve the best reconstruction and very accurate estimation of perfusion time profiles even when the k-space measurements are contaminated with a relatively high level noise ($\sigma = 5 \times 10^{-2}$). The reconstruction results of our method are also statistically significant (p-value $< 10^{-5}$) when compared with all other methods. Moreover, both kt-RPCA and FTVNNR result in over spatial
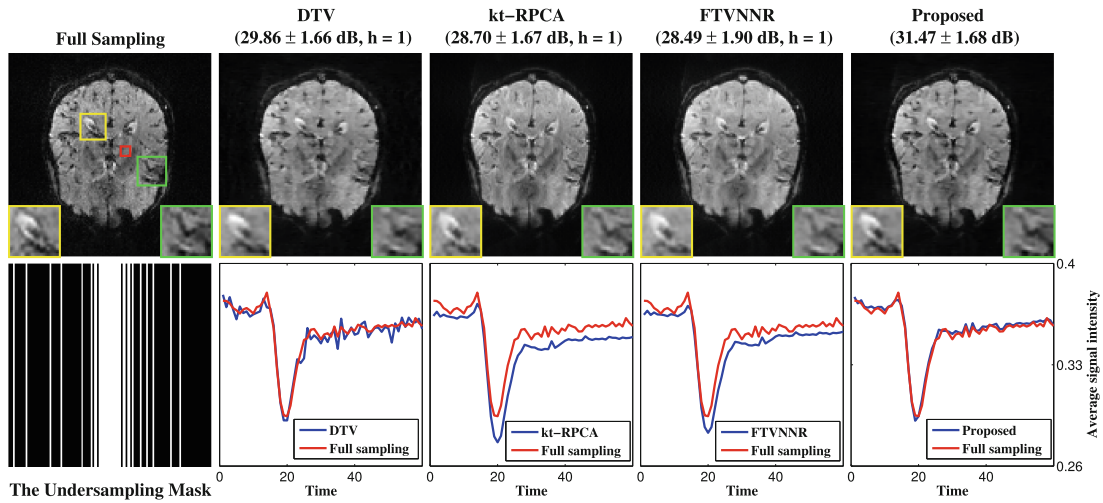
Fig. 1. (Top) Results (mean±std, h-value) of the 22nd frame of the first brain dataset and close-up views of two regions of interest (yellow and green square). h = 1 specifies the statistical significance between the results of proposed and compared method, (Bottom) An exemplary undersampling mask and for each method, estimation of perfusion time profiles averaged over the voxels inside the red square shown in top-left figure. The standard deviation of added Gaussian noise is $\sigma = 5 \times 10^{-2}$. Our method achieves both the best frame-based reconstruction and the most accurate estimation of peaks and temporal pattern of perfusion signal. (Color figure online)
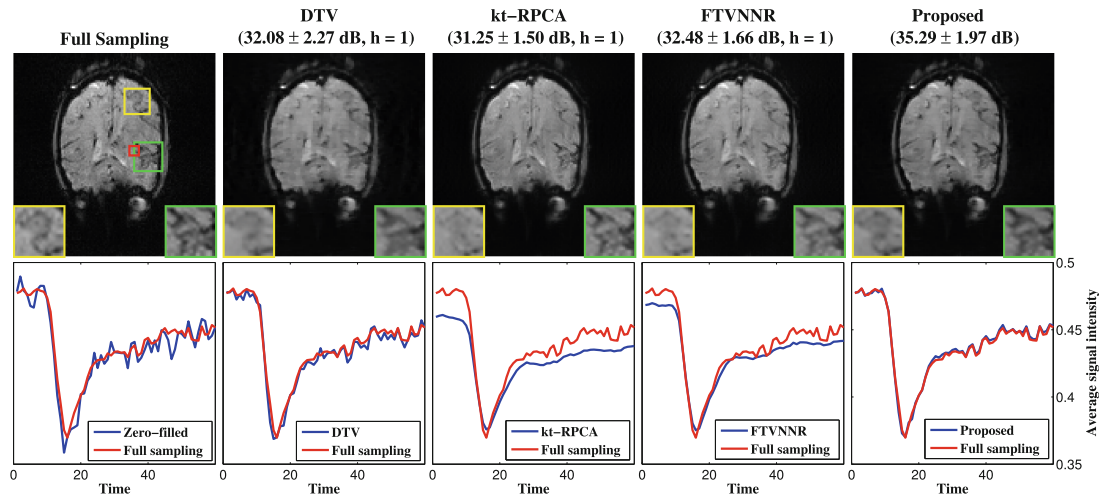
Fig. 2. (Top) Results (mean±std, h-value) of the 15th frame of the third brain dataset and close-up views of two regions of interest (yellow and green square), (Bottom) For each method, estimation of perfusion time profiles averaged over the voxels inside the red square shown in top-left figure. The standard deviation of added Gaussian noise is $\sigma = 10^{-3}$. Our method again achieves both the best frame-based reconstruction and the most accurate estimation of peaks and temporal pattern of perfusion signal. (Color figure online)

smoothing (see close-up views in Fig. 1) and along time as well, which can be clearly seen from smoothening of the perfusion peaks in the third-fourth column of Fig. 1. In contrast, the proposed method reconstructs a perfusion pattern that is in good agreement with the pattern of the fully sampled data (see Fig. 1 bottom fifth column), and produces less blurry image regions and sharper edges. The perfusion time profiles obtained from the third dataset (see Fig. 2 bottom plots) also demonstrate the success of our proposed method. Considering the spatial outputs, when looking at details in close-up views of Fig. 2, the reconstructions obtained by kt-RPCA and FTVNNR are more blurry and thus lacking some finer details in yellow region, whereas the reconstruction obtained by proposed method involves more finer information in yellow region and provides sharper edges in green region.
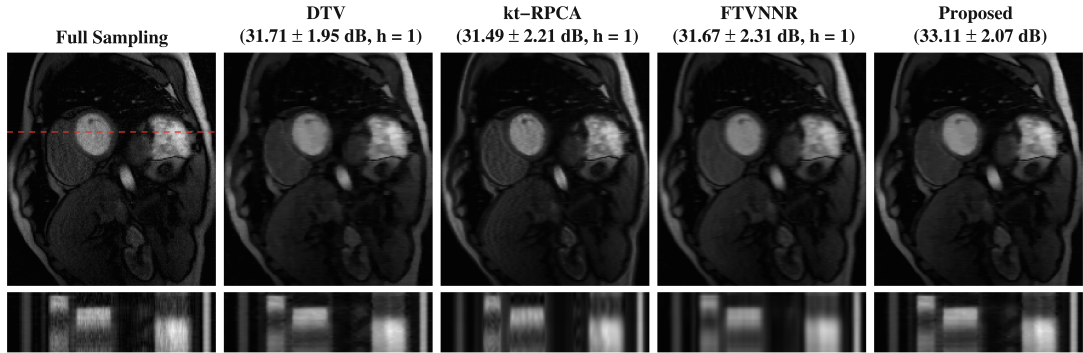
Fig. 3. (Top) Results of the 18th frame of the cardiac dataset with added noise $\sigma = 10^{-2}$, (Bottom) Temporal cross sections by the red dashed line. All methods can produce high quality spatial frames, however, our method yields less noisy and blurry temporal profiles, and the aliasing artifacts are also mostly removed. (Color figure online)

We also validate our method on a cardiac perfusion data from [4] and the results are presented in Fig. 3. All methods here can produce high quality images, however, when looking temporal cross sections at bottom, it can be observed that our method gives less noisy and with lower aliasing artifacts reconstruction on myocardium surface while FTVNNR provides more blurry result. The reason is that our method can utilize both local consistency in temporal differences and nonlocal similarities between spatio-temporal neighborhoods of MR sequence while the FTVNNR does not explicitly exploit sparsity in temporal domain.

Quantitative results of different reconstruction methods on both brain and cardiac perfusion datasets are shown in Fig. 4. Note that the NLM only solves the $\mathcal{G}_2$-subproblem of Sect. 3. From the figure, one can clearly see that our proposed method achieves the highest mean PSNR for all noise levels applied. The running time of all methods on the brain and cardiac datasets is provided in Table 1. Compared with the other three methods, our method needs the highest amount of processing time. However, due to its faster convergence, our method

46   C. Ulas et al.
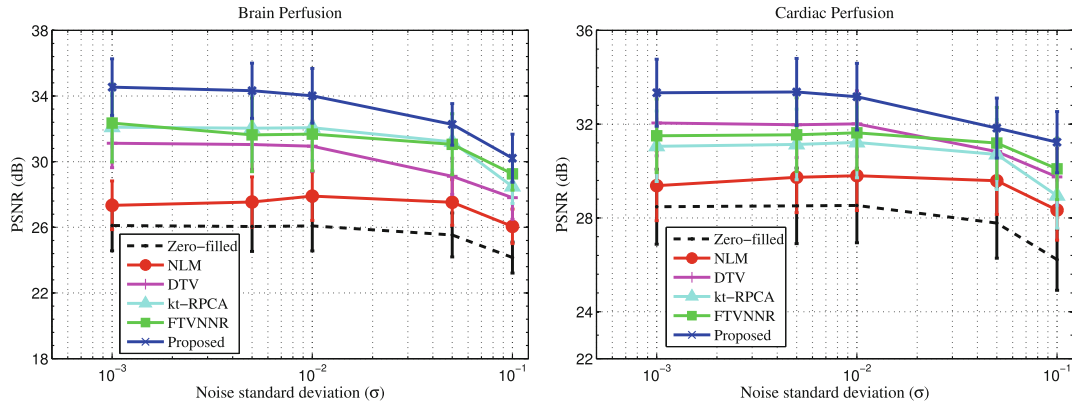
Fig. 4. PSNR results versus noise std (σ) for (left) Brain, (right) Cardiac datasets. Our joint local and nonlocal regularization based method performs the best.

can achieve the best reconstruction accuracy within the first 3–4 iterations on average, which approximately takes 4.5 min for cardiac dataset on a desktop with Intel Xeon CPU E3-1226 v3 Processor.

Table 1. The time cost of different reconstruction methods.

Time (Seconds)	DTV	kt-RPCA	FTVNNR	Proposed
Brain ($128 \times 128 \times 60$)	54.5	194.5	74.3	304.6
Cardiac ($192 \times 192 \times 40$)	46.2	263.9	81.7	278.1

5 Conclusion

We have presented a robust reconstruction model for perfusion MRI, which is based on a joint regularization of pixel-wise and patch-wise spatio-temporal constraints. Numerical experiments validate the efficiency of our method over the state-of-the-art methods in terms of reconstruction accuracy and estimation of perfusion time profiles in varying noise conditions. We also introduce an iterative algorithm that efficiently solves convex optimization problems with mixtures of regularizers. Our algorithm provides fast convergence and can be easily extended to other medical image applications, in particular denoising and super-resolution. The proposed method can be also extended to parallel MR imaging [8] and be applied to multi-coil data. Future work will aim at expanding our work with the fitting of pharmacokinetic models and quantitative analysis of perfusion parameters on 3D+t brain perfusion data using partial k-space measurements.

Robust Reconstruction of Accelerated Perfusion MRI   47

References

1. Beck, A., Teboulle, M.: A fast iterative shrinkage-thresholding algorithm for linear inverse problems. SIAM J. Imag. Sci. **2**(1), 183–202 (2009)
2. Buades, A., Coll, B., Morel, J.M.: A non-local algorithm for image denoising. In: IEEE Conference on Computer Vision and Pattern Recognition (CVPR), vol. 2, pp. 60–65 (2005)
3. Caballero, J., Price, A.N., Rueckert, D., Hajnal, J.: Dictionary learning and time sparsity for dynamic MR data reconstruction. IEEE Trans. Med. Imag. **33**(4), 979–994 (2014)
4. Chen, C., Li, Y., Axel, L., Huang, J.: Real time dynamic MRI with dynamic total variation. In: Golland, P., Hata, N., Barillot, C., Hornegger, J., Howe, R. (eds.) MICCAI 2014. LNCS, vol. 8673, pp. 138–145. Springer, Heidelberg (2014). doi:10.1007/978-3-319-10404-1_18
5. Chen, C., et al.: Preconditioning for accelerated iteratively reweighted least squares in structured sparsity reconstruction. In: IEEE Conference on Computer Vision and Pattern Recognition (CVPR), pp. 2713–2720 (2014)
6. Conturo, T.E., et al.: Arterial input functions for dynamic susceptibility contrast MRI: requirements and signal options. J. Mag. Reson. Imag. **22**, 697–703 (2005)
7. Coupé, P., Yger, P., Prima, S., Hellier, P., Kervrann, C., Barillot, C.: An optimized blockwise nonlocal means denoising filter for 3-D magnetic resonance images. IEEE Trans. Med. Imag. **27**(4), 425–441 (2008)
8. Deshmane, A., Gulani, V., Griswold, M.A., Seiberlich, N.: Parallel MR imaging. J. Mag. Reson. Imag. **36**(1), 55–72 (2012)
9. Huang, J., Zhang, S., Metaxas, D.N.: Efficient MR image reconstruction for compressed MR imaging. Med. Imag. Anal. **15**(5), 670–679 (2011)
10. Lingala, S.G., Hu, Y., DiBella, E., Jacob, M.: Accelerated dynamic MRI exploiting sparsity and low-rank structure: k-t SLR. IEEE Trans. Med. Imag. **30**(5), 1042–1054 (2011)
11. Marks, R.J.: Alternating projections onto convex sets. In: Jansson, P.A. (ed.) Deconvolution of Images and Spectra, 2nd edn. Academic Press, Orlando (1996)
12. Protter, M., Elad, M., Takeda, H., Milanfar, P.: Generalizing the nonlocal-means to super-resolution reconstruction. IEEE Trans. Imag. Proc. **18**(1), 36–51 (2009)
13. Raguet, H., Fadili, J., Peyré, G.: A generalized forward-backward splitting. SIAM J. Imag. Sci. **6**(3), 1199–1226 (2013)
14. Trémoulhéac, B., Dikaios, N., Atkinson, D., Arridge, S.R.: Dynamic MR image reconstruction-separation from undersampled (k-t)-space via low-rank plus sparse prior. IEEE Trans. Med. Imag. **33**(8), 1689–1701 (2014)
15. Ulas, C., Gómez, P., Sperl, J.I., Preibisch, C., Menze, B.H.: Spatio-temporal MRI reconstruction by enforcing local and global regularity via dynamic total variation and nuclear norm minimization. In: IEEE 13th International Symposium on Biomedical Imaging (ISBI), pp. 306–309 (2016)
16. Yang, Z., Jacob, M.: Nonlocal regularization of inverse problems: a unified variational framework. IEEE Trans. Imag. Proc. **22**(8), 3192–3203 (2013)
17. Yao, J., Xu, Z., Huang, X., Huang, J.: Accelerated dynamic MRI reconstruction with total variation and nuclear norm regularization. In: Navab, N., Hornegger, J., Wells, W.M., Frangi, A.F. (eds.) MICCAI 2015. LNCS, vol. 9350, pp. 635–642. Springer, Heidelberg (2015). doi:10.1007/978-3-319-24571-3_76

4.2 RELEVANT PEER-REVIEWED ABSTRACTS

Abstracts related to motion encoding techniques focus on alternative methods for signal reconstruction, processing, and modeling. Fitting the Diffusional Kurtosis Tensor to Rotated Diffusion MR Images shows a simplified kurtosis model that reduces the number of free parameters without compromising quantification accuracy. Theory, Validation and Aplication of Blind Source Separation to Diffusion MRI for Tissue Characterisation and Partial Volume Correction presents Blind Source Separation (BSS), a technique to separate mixed signals by taking advantage of multiple measurements. Finally, A Robust Reconstruction Method for Quantitative Perfusion MRI: Application to Brain Dynamic Susceptibility Contrast (DSC) Imaging demonstrates a robust reconstruction framework that combines spatial and temporal penalty functions.

4.2.1   *Fitting the Diffusional Kurtosis Tensor to Rotated Diffusion MR Images*

Peer-reviewed Conference Abstract

Authors: PA. Gómez, T. Sprenger, MI. Menzel, JI. Sperl

In: *Proc Intl Soc Mag Reson Med* (2015) [33]

Abstract: Estimating the diffusional kurtosis tensor requires fitting a model with 22 free parameters to noisy diffusion signals, and is subject to low accuracy. We propose a variation of the model that makes use of the main directions of diffusion, only requiring the fitting of 10 parameters. Monte Carlo simulations and experiments on volunteer datasets indicate that the reduced version of the model has less bias than the full model, particularly in white matter areas with high fractional anisotropy.

Contribution of thesis author: Model development and evaluation, experimental design, abstract preparation and editing.

Fitting the Diffusional Kurtosis Tensor to Rotated Diffusion MR Images

Pedro A Gómez[1,2], Tim Sprenger[1,2], Marion I Menzel[2], Jonathan I Sperl[2]

[1]Computer Science, Technische Universität München, Munich, Germany
[2]GE Global Research, Munich, Germany

Abstract. Estimating the diffusional kurtosis tensor requires fitting a model with 22 free parameters to noisy diffusion signals, and is subject to low accuracy. We propose a variation of the model that makes use of the main directions of diffusion, only requiring the fitting of 10 parameters. Monte Carlo simulations and experiments on volunteer datasets indicate that the reduced version of the model has less bias than the full model, particularly in white matter areas with high fractional anisotropy.

1   Introduction

Diffusion Kurtosis Imaging (DKI) allows for the characterization of the non-Gaussian diffusion of water within a biological tissue [3]. Kurtosis is quantified by deriving scalar metrics from the fourth order kurtosis tensor, obtained in turn from fitting the measured diffusion signal to a model with 22 free parameters. Fitting this model is prone to low accuracy and high bias of the derived scalar metrics due to the low SNR of diffusion weighted images and the Rician nature of the noise distribution [5]. We hypothesize that a simpler version of the model, i.e. one that only requires the fitting of 10 free parameters, should have a lower bias and higher accuracy than the standard model. We develop this model based on the assumption that the cross-terms of the diffusion and kurtosis tensors are eliminated if the diffusion encoding space (q-space) of every voxel is rotated into the main directions of diffusion before fitting.

2   Theory

The second order diffusion tensor $\mathbf{D} \in \mathbb{R}^{3 \times 3}$ and the fourth order kurtosis tensor $\mathbf{W} \in \mathbb{R}^{3 \times 3 \times 3 \times 3}$ are related to the measured diffusion signal S by:

$$S(b) = S_0 \cdot \exp\left(-b \sum_{i,j} g_i g_j D_{i,j} + \frac{b^2}{6}\left(\sum_i \frac{D_{ii}}{3}\right)^2 \sum_{i,j,k,l} g_i g_j g_k g_l W_{ijkl}\right), \quad (1)$$

where S_0 is the non-weighted signal, b corresponds to the b-value of the diffusion experiment, and g_n represents the n-th component of the directional unit vector

2   Gómez et al.
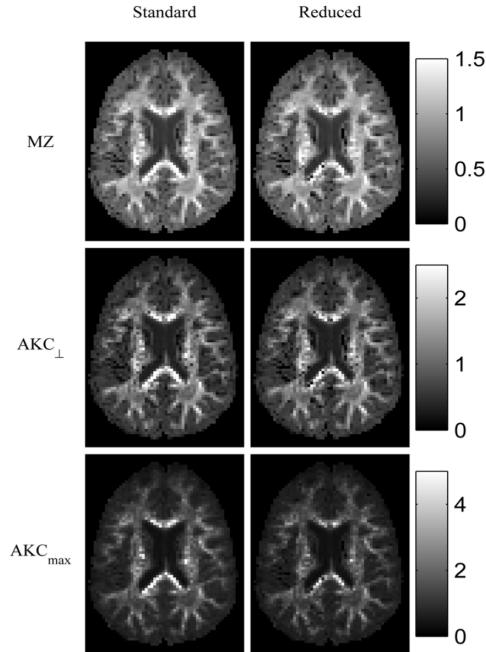
Fig. 1. Different kurtosis contrasts estimated from the standard (left column) and reduced (right column) models.

$\mathbf{g} \in \mathbb{R}^3$. We develop the reduced version of the model in three steps: first, we estimate the main directions of diffusion; second, we rotate the diffusion encoding space (q-space) of every voxel into its principal coordinates using the Eigenvectors of the diffusion tensor; and third, we fit the data in the rotated coordinate system to:

$$S(b') = S_0 \cdot \exp\left(-b' \sum_i \lambda_i + \frac{b'^2}{6}\left(\sum_i \frac{\lambda_i}{3}\right)^2 \sum_{i,j} g_i g_j \hat{W}_{ij}\right), \qquad (2)$$

In (2) the cross-terms are neglected, yielding a direct calculation of the Eigenvalues λ_i of the diffusion tensor and reducing the amount of free parameters to 10: S_0, the three Eigenvalues of the diffusion tensor, and six coefficients from the kurtosis tensor, which is now second order instead of fourth.

3   Methods

Two experiments were performed to assess the performance of the reduced model. In the first experiment we fitted both models to a volunteer dataset.

Fitting the Diffusional Kurtosis Tensor to Rotated Diffusion MR Images   3
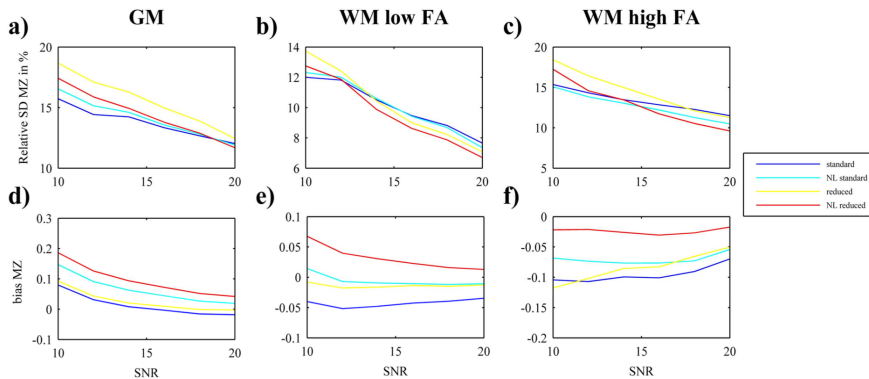
Fig. 2. Estimated standard deviation (SD) (a-c) and bias (d-f) from the Monte Carlo Simulation for characteristic a/d) gray matter (GM), b/e) white matter (WM) with low fractional anisotropy (FA), and c/f) WM with high FA voxels.

Acquisition was performed in a 3T GE MR750 clinical MR scanner (GE Healthcare, Milwaukee, WI, USA) using a 32-channel head coil (single shot EPI, single spin echo, TE =80.7 ms, TR = 1.8 s, 96x96, FOV=24 cm) and a 3-shell DKI acquisition with 25, 35 and 70 non collinear directions and corresponding b-values of 750, 1070, and 3,000 s/mm^2 [4]. Post-processing on the data included motion correction, skull extraction [2], and the estimation of rotationally invariant kurtosis metrics [1]. The second experiment consisted of a Monte Carlo simulation for three representative voxel types: one gray matter (GM) voxel and two white matter (WM) voxels, one with high and one with low fractional anisotropy (FA). The FA for each of these voxels was defined as: 0.17 for GM, 0.50 for WM with low FA, and 0.79 for WM with high FA. These three standard voxels were artificially corrupted with Rician noise to different extent and fit to both versions of the model in a linear and non-linear (NL) manner. The simulation consisted of a total of 1,000 instances for six SNR levels ranging from 10 to 20. The bias was calculated by subtracting the mean of the different instances to the ground truth voxels, while the accuracy was quantified in terms of the standard deviation (SD) of the noise instances.

4   Results

Figure 1 depicts mean kurtosis (MZ), orthogonal apparent kurtosis coefficient (AKC$_\perp$), and maximum apparent kurtosis coefficient (AKC$_{max}$) estimated from linear fitting of both the standard and reduced model. In areas of known high anisotropy, such as the areas near the corpus callosum, the estimated kurtosis maps were smaller than the maps of the standard model. Figure 2 shows the bias and standard deviation of MZ for the different methods in the three standard voxels. In areas of WM with high FA the bias of the non-linear implementation

4   Gómez et al.

of the reduced model was significantly less than the other implementations of the model.

5   Discussion

We propose to reduce the standard kurtosis model by fitting the measured diffusion data in a rotated coordinate system. This implementation reduces the amount of free parameters from 22 to 10 by making use of an initial estimation of the main directions of diffusion. Even at a reduction of over 50% of parameters, the method yields comparable parametric maps, stability, and bias. Furthermore, results indicate that the reduced model yields parametric maps with a reduced bias in areas of high anisotropy.

References

1. Hui, E.S., Cheung, M.M., Qi, L., Wu, E.X.: Towards better MR characterization of neural tissues using directional diffusion kurtosis analysis. NeuroImage 42, 122–134 (2008)
2. Jenkinson, M., Beckmann, C.F., Behrens, T.E.J., Woolrich, M.W., Smith, S.M.: FSL. NeuroImage 62, 782–790 (2012)
3. Jensen, J.H., Helpern, J.A., Ramani, A., Lu, H., Kaczynski, K.: Diffusional kurtosis imaging: the quantification of non-gaussian water diffusion by means of magnetic resonance imaging. Society of Magnetic Resonance in Medicine 53, 1432–1440 (2005)
4. Poot, D.H.J., den Dekker, A.J., Achten, E., Verhoye, M., Sijbers, J.: Optimal experimental design for diffusion kurtosis imaging. IEEE transactions on medical imaging 29, 819–829 (2010)
5. Veraart, J., Poot, D.H.J., Van Hecke, W., Blockx, I., Van der Linden, A., Verhoye, M., Sijbers, J.: More accurate estimation of diffusion tensor parameters using diffusion Kurtosis imaging. Magnetic resonance in medicine : official journal of the Society of Magnetic Resonance in Medicine / Society of Magnetic Resonance in Medicine 65, 138–145 (2011)

4.2.2 *Theory, Validation and Aplication of Blind Source Separation to Diffusion MRI for Tissue Characterisation and Partial Volume Correction*

Peer-reviewed Conference Abstract

Authors: M. Molina-Romero, **PA. Gómez**, JI. Sperl, AJ. Stewart, DK. Jones, MI. Menzel, BH. Menze

In: *Proc Intl Soc Mag Reson Med* (2017) [60]

Abstract: Here we present Blind Source Separation (BSS) as a new tool to analyze multi-echo diffusion data. This technique is designed to separate mixed signals and is widely used in audio and image processing. Interestingly, when it is applied to diffusion MRI, we obtain the diffusion signal from each water compartment, what makes BSS optimal for partial volume effects correction. Besides, tissue characteristic parameters are also estimated. Here, we first state the theoretical framework; second, we optimize the acquisition protocol; third, we validate the method with a two compartments phantom; and finally, show an in-vivo application of partial volume correction.

Contribution of thesis author: Discussion of algorithmic implementation and experimental design, abstract revision and editing.

Theory, Validation and Application of Blind Source Separation to Diffusion MRI for Tissue Characterisation and Partial Volume Correction

Miguel Molina-Romero[1,2], Pedro A Gómez[1,2], Jonathan I Sperl[2],
Andrew J Stewart[3], Derek K Jones[4], Marion I Menzel[2], Bjoern H Menze[1]

[1]Computer Science, Technische Universität München, Munich, Germany
[2]GE Global Research, Munich, Germany
[3]EMRIC, Cardiff University, Cardiff, UK
[4]CUBRIC School of Psychology, Cardiff University, Cardiff, UK

Abstract. Here we present blind source separation (BSS) as a new tool to analyse multi-echo diffusion data. This technique is designed to separate mixed signals and is widely used in audio and image processing. Interestingly, when it is applied to diffusion MRI, we obtain the diffusion signal from each water compartment, what makes BSS optimal for partial volume effects correction. Besides, tissue characteristic parameters are also estimated. Here, we first state the theoretical framework; second, we optimise the acquisition protocol; third, we validate the method with a two compartments phantom; and finally, show an in-vivo application of partial volume correction.

1   Purpose

The compartmental nature of tissue is generally accepted [1,7,11,14,17,19]. The diffusion-weighted MRI (dMRI) signal depends on the relaxation times of the compartments ($T2_i$), their diffusivities (D_i), volume fractions (f_i) and proton density (S_0). The simultaneous contribution of these parameters results in a lack of specificity to each independent effect and induces a bias [13,16] on the diffusion metrics known as partial volume contamination. Specificity and partial volume correction problems have been addressed independently [2,6,9,13,14]. Here we present blind source separation (BSS) as a new approach in dMRI that separates mixed signals and yields tissue microstructure parameters, tackling both problems at once.

2   Methods

2.1   Theory

This method is based on three assumptions: 1) tissue is made of water compartments with different diffusivities [6,14]; 2) there is no water exchange [1]; and 3) each compartment has a different $T2$ [6,11,14]. Hence, we can describe the

2   Molina-Romero et al.
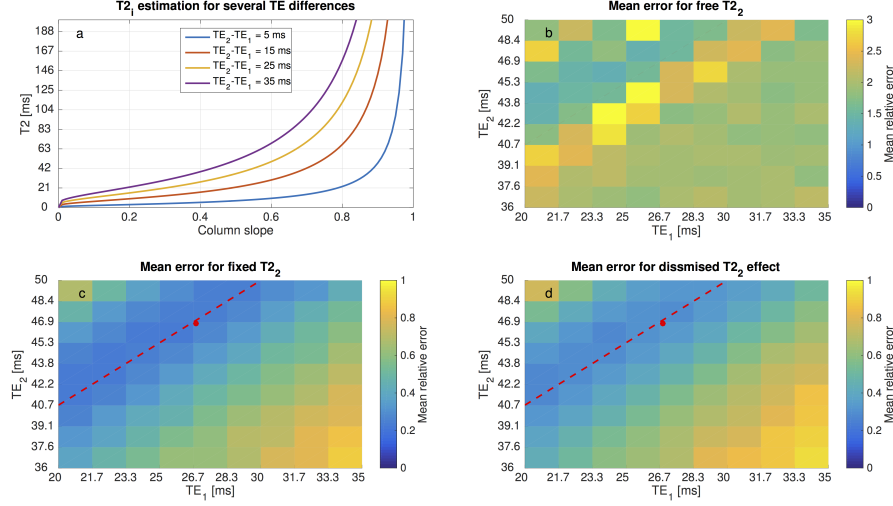
Fig. 1. (b-d) Mean error of the parameter estimations. (a) Relationship between the slope of the columns of $\mathbf{A}$ and the estimation of $T2$ for several TE differences. When the slope of the columns tends towards 1 ($T2 \gg TE$), the estimation of $T2$ is in the asymptotic region and thus uncertain. This uncertainty can be observed in (b) where the minimum error is larger than in (c,d) for fixed $T2_2$ and dismissed $T2_2$ effect. Notice that the optimal TE pairs are marked by the red dashed lines. The red dots mark the TE pair used for phantom validation experiment.

measured diffusion signal as the weighted sum of the compartmental sources. These weights depend only on the volume fraction (f) and the ratio between the compartmental $T2_i$ and the experimental TE_j. Therefore, varying TE modifies the weights and the system can be expressed as a BSS problem:

$$\begin{bmatrix} X(TE_1, \Delta, q) \\ \vdots \\ X(TE_M, \Delta, q) \end{bmatrix} = \begin{bmatrix} f_1 e^{TE_1/T2_1} & \cdots & f_N e^{TE_1/T2_N} \\ \vdots & \ddots & \vdots \\ f_1 e^{TE_M/T2_1} & \cdots & f_N e^{TE_M/T2_N} \end{bmatrix} \begin{bmatrix} S_1(\Delta, q) \\ \vdots \\ S_N(\Delta, q) \end{bmatrix} S_0 \qquad (1)$$

$$\mathbf{X} = \mathbf{AS}, \qquad (2)$$

where $\mathbf{X}$ are the measurements for several TEs, $\mathbf{A}$ the mixing matrix, $\mathbf{S}$ the compartmental diffusion source, M the number of measurements, and N the number of compartments. Here, among the possible BSS solutions [18], and unlike in [12], we use a sparsifying transform [15] followed by non-negative sparse coding [8].

Here we focus on two-compartment environments ($N = M = 2$). Besides, when $T2_i$ is larger than the TEs (i.e. CSF), the exponential term can be dismissed ($\exp(TE_j/T2_i) \approx 1$) and thus the $T2_i$. Alternatively, $T2_i$ can be fixed to
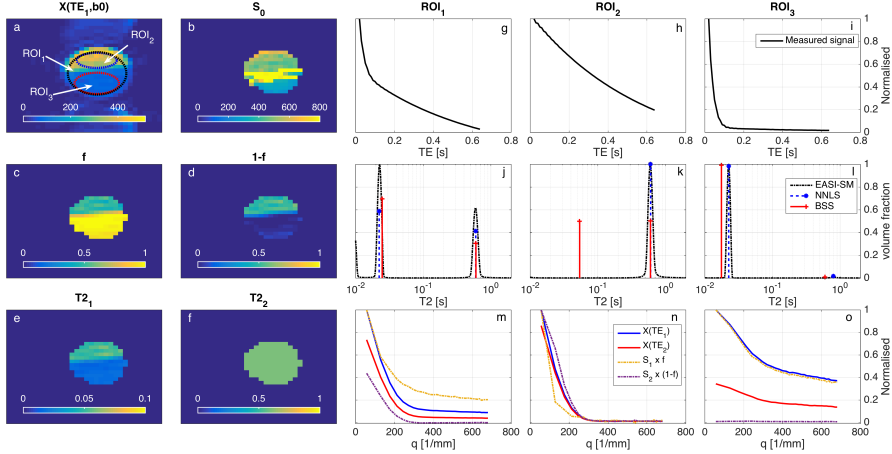
Fig. 2. (a) b0 image at $TE_1 = 26\ ms$ with ROIs overlaid. Each ROI represents a possible case: ROI$_1$ ($f \approx 0.5$), whole phantom; ROI$_2$ ($f \approx 0$), water; ROI$_3$ ($f \approx 1$), yeast. (b) Signal intensity at $TE = 0\ ms$. Volume fractions for the associated intra-cellular (c) and extra-cellular (d) compartments. $T2$ for the intra-cellular (e) and extra-celullar (f) cell compartments. Averaged multi-echo signal for each ROI (g,h,i) and the corresponding $T2$ spectral fitting with NNLS and EASI-SM (j,k,l) compared with the volume fractions and $T2$s estimated by BSS ($T2_2$ fixed at 0.6 s according to NNLS and EASI-SM). Measured and separated diffusion signals for each ROI (m,n.o).

an expected value if prior knowledge is available (i.e. T2$_{CSF} \approx 2\ s$ 6). We study the effect both approximations on the error of the parameter estimation.

We perform three experiments to: 1) find the range of optimal TEs; 2) validate our method; and 3) show an application. Figure 4 contains the experimental details.

2.2 Optimisation simulations

Tissue with two compartments was simulated with known $T2$s (22 and 597 ms) for restricted and free diffusion signals [4]. We ran a simulation experiment varying TE and f (11 points) to calculate the mean error for all the parameter combinations and find the optimal TE region for free, fixed and dismissed $T2_2$.

2.3 Phantom validation

For validation, we used a phantom made of yeast and water (1:1) as a two compartments sample [5]. A multi-echo experiment was acquired and $T2$s fitted with NNLS [10] and EASI-SM [3]. Besides, BSS was applied on the diffusion dataset fixing $T2_2 = 0.6\ s$ (NNLS). Finally, results from the three methods were compared.

4   Molina-Romero et al.
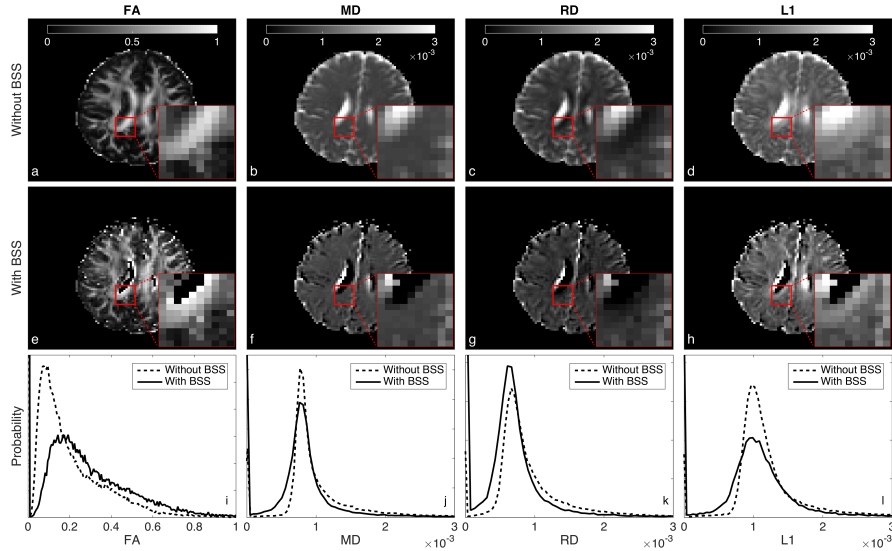
Fig. 3. Comparison of DTI metrics with and without CSF contamination correction by BSS. Histograms of values for the whole brain (i-l) show an increase of FA, and a decrease of MD, RD and L1. Both effects are consistent with the elimination of the CSF contribution. Besides, we observe a significant increase of FA in the borders of the ventricles (zoomed area), where the contamination is expected to be high. Notice that BSS mostly crops the ventricles and the external CSF and increases the contrast of the white matter.

2.4   In vivo

A young female volunteer went under a DTI acquisition. CSF signal was extracted from the data using BSS, fixing $T2_2 = 2\ s$ [11]. Finally, DTI metrics with and without correction were compared.

3   Results and discussion

3.1   Optimisation simulations

Fig 1a depicts $T2$ versus the slope of a column of $\mathbf{A}$. As the slope tends towards 1, the estimation falls into an asymptotic region increasing the uncertainty on the $T2$ estimation. Therefore, fixing its value or dismissing its contribution reduces the mean error of the parameter estimations (Fig. 1b-d). Moreover, fixing the $T2$ value performs slightly better than dismissing its effect (Fig. 1c-d).

3.2   Phantom validation

Fig.2g-o compare the results of BSS against NNLS and EASI-SM in a ROI-based analysis. Fig. 2j,l show agreement of $T2_1$ and f with NNLS and EASI-SM for

		Optimisation	Validation	In-Vivo
Diffusion acquisition	TR	Inf	3 s	4 s
	TE_1	20-35 ms (10 points)	26 ms	73 ms
	TE_2	36-50 ms (10 points)	46 ms	110 ms
	#Diffusion directions	1	1	41
	#b-values	33	33	2
	Range of b-values	0-13504 s/mm^2	70-10048 s/mm^2	0-1000 s/mm^2
	Reverse polarity	No	No	Yes
	Resolution	1 voxel	32x32	96x96
	Sequence	PGSE	STEAM	PGSE
T2 mapping	TR		2.5 s	
	#TEs		64	
	Range of TEs		10-640 ms	
	NEX		4	
	Resolution		32x32	
	Sequence		SE	
	Scanner	Simulated	9.4T Biospec 94/20 (Bruker, Ettlingen, Germany)	3T HDx MRI (GE, Milwaukee, WI)

Fig. 4. Experimental setups for the optimisation simulation, the phantom validation and the in-vivo experiment.

ROI_1 and ROI_3. Besides, in Fig. 1m, S_1 (associated with intra-cellular space) describes a restricted diffusion signal similar as in Fig 2o, and S_2 (associated with extra-cellular space) shows a free diffusion behaviour as in Fig. 2n. Both findings are in agreement with the simulations and indicate that BSS successfully separates signals from two compartments. Interestingly, BSS disentangles measurements from ROI_2 into two similar and equally scaled sources (Fig. 2n) indicating that only one source exists. For illustration, Fig. 2b-f show that the voxel-based maps generated with BSS are consistent with the ROI based analysis.

3.3   In vivo

In Fig. 3, with BSS, we observe an increase of the fractional anisotropy (FA) (a,e,i) and a reduction of the mean diffusivity (MD) (b,f,j), radial diffusivity (RD) (c,g,k), and tensor's main eigenvalue (L1) (d,h,l). This is consistent with the elimination of the CSF contribution. Also, we notice that with BSS the ventricles are extracted and white matter structures are better defined, especially the voxels at the border of the ventricles (zoomed area).

6   Molina-Romero et al.

4   Conclusions

Here we show that BSS of diffusion data is a suitable technique to separate compartmental sources. We demonstrate that this method is appropriate for partial volume correction. Besides, tissue volume fraction, relaxation and diffusivity parameters are estimated allowing for simultaneous tissue characterisation.

5   Acknowledgments

References

1. Assaf, Y., Basser, P.J.: Composite hindered and restricted model of diffusion (CHARMED) MR imaging of the human brain. NeuroImage 27, 48–58 (2005)
2. Benjamini, D., Basser, P.J.: Use of marginal distributions constrained optimization (MADCO) for accelerated 2D MRI relaxometry and diffusometry. Journal of Magnetic Resonance 271, 40–45 (2016)
3. Björk, M., Zachariah, D., Kullberg, J., Stoica, P.: A multicomponent T 2 relaxometry algorithm for myelin water imaging of the brain. Magnetic Resonance in Medicine (2015)
4. Cook, P.A., Bai, Y., Nedjati-Gilani, S., Seunarine, K.K., Hall, M.G., Parker, G.J., Alexander, D.C.: Camino: Open-Source Diffusion-MRI Reconstruction and Processing. Proc Intl Soc Mag Reson Med (2014)
5. Cory, D.G.: Measurement of translational displacement probabilities by NMR: An indicator of compartmentation. Magnetic Resonance in Medicine 14(3), 435–444 (1990)
6. Does, M.D., Gore, J.C.: Compartmental study of diffusion and relaxation measured in vivo in normal and ischemic rat brain and trigeminal nerve. Magnetic resonance in medicine 43(6), 837–44 (2000)
7. Ferizi, U., Schneider, T., Witzel, T., Wald, L.L., Zhang, H., Wheeler-Kingshott, C.A., Alexander, D.C.: White matter compartment models for in vivo diffusion MRI at 300mT/m. NeuroImage 118, 468–483 (2015)
8. Hoyer, P.: Non-negative sparse coding. In: Proceedings of the 12th IEEE Workshop on Neural Networks for Signal Processing. pp. 557–565. IEEE (2002)
9. Kim, D., Kim, J.H., Haldar, J.P.: Diffusion-Relaxation Correlation Spectroscopic Imaging (DR-CSI): An Enhanced Approach to Imaging Microstructure. Proc Intl Soc Mag Reson Med (2016)
10. Lawson, C.L., Hanson, R.J.: Solving Least Squares Problems. Society for Industrial and Applied Mathematics (1995)
11. Mackay, A., Laule, C., Vavasour, I., Bjarnason, T., Kolind, S., M7dler, B.: Insights into brain microstructure from the T 2 distribution. Magnetic Resonance Imaging 24, 515–525 (2006)
12. Molina-Romero, M., Gómez, P.A., Sperl, J.I., Jones, D.K., Menzel, M.I., Menze, B.H.: Tissue microstructure characterisation through relaxometry and diffusion MRI using sparse component analysis. ISMRM Workshop on Breaking the Barriers of Diffusion MRI (2016)

13. Pasternak, O., Sochen, N., Gur, Y., Intrator, N., Assaf, Y.: Free water elimination and mapping from diffusion MRI. Magnetic Resonance in Medicine 62(3), 717–730 (2009)
14. Peled, S., Cory, D.G., Raymond, S.A., Kirschner, D.A., Jolesz, F.A.: Water diffusion, T(2), and compartmentation in frog sciatic nerve. Magnetic resonance in medicine 42(5), 911–8 (1999)
15. Ravishankar, S., Bresler, Y.: 0 Sparsifying Transform Learning with Efficient Optimal Updates and Convergence Guarantees. arXiv preprint arXiv:11501.02859 pp. 1–16 (2015)
16. Santis, S.D., Assaf, Y., Jones, D.: The influence of T2 relaxation in measuring the restricted volume fraction in diffusion MRI. Proc Intl Soc Mag Reson Med (2016)
17. Stanisz, G.J., Wright, G.A., Henkelman, R.M., Szafer, A.: An analytical model of restricted diffusion in bovine optic nerve. Magnetic Resonance in Medicine 37(1), 103–111 (1997)
18. Yu, X., Hu, D., Xu, J.: Blind source separation: theory and applications. Wiley (2014)
19. Zhang, H., Schneider, T., Wheeler-Kingshott, C.A., Alexander, D.C.: NODDI: Practical in vivo neurite orientation dispersion and density imaging of the human brain. NeuroImage 61(4), 1000–1016 (2012)

4.2.3 *A Robust Reconstruction Method for Quantitative Perfusion MRI: Application to Brain Dynamic Susceptibility Contrast (DSC) Imaging*

Peer-reviewed Conference Abstract

Authors: C. Ulas, **PA. Gómez** JI. Sperl, C. Preibisch, MI. Menzel, A. Haase, BH. Menze

Abstract: We propose a robust reconstruction model for dynamic perfusion Magnetic Resonance Imaging (MRI) from undersampled k-space data. Our method is based on a joint penalization of the pixel-wise incoherence on temporal differences and patch-wise dissimilarities between spatio-temporal neighborhoods of perfusion image series. We evaluate our method on dynamic susceptibility contrast Dynamic Susceptibility Contrast (DSC)-MRI brain perfusion datasets and demonstrate that the proposed reconstruction model can achieve up to 8-fold acceleration by yielding improved spatial reconstructions and providing highly accurate matching of perfusion time-intensity curves, thus leading to more precise quantification of clinically relevant perfusion parameters over two existing reconstruction methods.

Contribution of thesis author: Discussion of algorithmic implementation and experimental design, abstract revision and editing.

A Robust Reconstruction Method for Quantitative Perfusion MRI: Application to Brain Dynamic Susceptibility Contrast (DSC) Imaging

Cagdas Ulas[1,2], Pedro A Gomez[1,2], Jonathan I Sperl[2], Christine Preibisch[3], Marion I Menzel[2], Axel Haase[4], and Bjoern H Menze[1]

[1]Department of Computer Science, Technische Universität München, Germany
[2]GE Global Research, Garching, Germany
[3]Department of Neuroradiology, Technische Universität München, Germany
[4]Zentralinstitut fur Medizintechnik, Technische Universität München, Germany
cagdas.ulas@tum.de

Abstract. We propose a robust reconstruction model for dynamic perfusion magnetic resonance imaging (MRI) from undersampled k-space data. Our method is based on a joint penalization of the pixel-wise incoherence on temporal differences and patch-wise dissimilarities between spatio-temporal neighborhoods of perfusion image series. We evaluate our method on dynamic susceptibility contrast (DSC)-MRI brain perfusion datasets and demonstrate that the proposed reconstruction model can achieve up to 8-fold acceleration by yielding improved spatial reconstructions and providing highly accurate matching of perfusion time-intensity curves, thus leading to more precise quantification of clinically relevant perfusion parameters over two existing reconstruction methods.

1   Purpose

Perfusion-weighted MR imaging (PWI) is a widely used imaging technique that allows to measure the hemodynamic parameters of perfusion through the examination of spatio-temporal changes of signal intensities following the injection of bolus via exogenous contrast agents. Although PWI techniques have become widespread clinical tools for the assessment of tumor malignancy, quantitative PWI requires high temporal resolution to capture the rapid kinetics of contrast agent uptake, high spatial resolution to accurately delineate spatial boundaries, and high signal-to-noise ratio (SNR) to enable precise fitting of quantitative model parameters [6]. With such severe limitations, quantitative PWI can greatly benefit from dynamic imaging reconstruction techniques [4,1,8]. This work presents a new reconstruction model that is specifically developed for PWI and is capable of producing high-quality spatial images and reconstructing the complete temporal signal dynamics, hence enabling accurate estimation of perfusion parameters from accelerated acquisitions.

2   Methods

Our reconstruction model integrates two different data-driven constraints for the reconstruction of PWI: (i) the pixel-wise sparsity constraint on the temporal differences of the image series, limiting the overall dynamic of the perfusion time series, (ii) the patch-wise similarity constraint on the spatio-temporal neighborhoods of the whole data, providing smooth image regions with less temporal blurring when there are high inter-frame intensity changes. The proposed model can be formulated as,

$$\hat{X} = \arg\min_{X} \left\{ \frac{1}{2} \|\mathcal{F}_u X - Y\|_2^2 + \lambda_1 \mathcal{G}_1(X) + \lambda_2 \mathcal{G}_2(X) \right\} \tag{1}$$

where X denotes the perfusion image series to be reconstructed, Y represents undersampled k-space data, λ_1 and λ_2 are the regularization parameters. The first regularizer here penalizes the sum of pixel-wise differences on the temporal difference images with respect to a reference image, and defined as,

$$\mathcal{G}_1(X) = \sum_{t \in \mathbb{T}} \sum_{n=1}^{M \times N} \sqrt{\left(\nabla_x (x_t - \bar{x})_n\right)^2 + \left(\nabla_y (x_t - \bar{x})_n\right)^2} \tag{2}$$

where $\bar{x}$ is the reference image calculated by averaging all temporal frames, ∇_x and ∇_y are the finite-difference operators along x and y dimensions, respectively. This regularizer is better adjusted to the variation in time. The second regularizer penalizes the weighted sum of ℓ_2 norm distances between spatio-temporal (3D) patches of the image series, and this term is specified by,

$$\mathcal{G}_2(X) = \sum_{(\mathrm{p}_x, \mathrm{p}_y, \mathrm{p}_t) \in \Omega} \sum_{(\mathrm{q}_x, \mathrm{q}_y, \mathrm{q}_t) \in \mathcal{N}_{\mathrm{p}}} w(\mathrm{p}, \mathrm{q}) \|P_{\mathrm{p}}(\mathrm{X^{3D}}) - P_{\mathrm{q}}(\mathrm{X^{3D}})\|_2^2 \tag{3}$$

where $P_{\mathrm{p}}(\mathrm{X^{3D}})$ is a 3D patch centered at voxel p, $\mathcal{N}_{\mathrm{p}}$ is a 3D search window around p. The weights $w(\mathrm{p}, \mathrm{q})$ are determined using exponentially weighted ℓ_2 norm distance. This regularizer can exploit similarities between patch pairs and enforce smooth solutions by averaging distance-wise close patches. To efficiently solve the optimization in (1), we adopt an accelerated iterative algorithm based on a generalized forward-backward splitting framework [5].

We evaluate our method using 5 DSC image series acquired within a PET/MR study on brain tumor hypoxia. Data were acquired using a 3T Siemens mMR Biograph scanner with a 2D dynamic single-shot gradient-echo EPI sequence (TR/TE = 1500/30 ms, flip angle = 70°, voxel size = $1.8 \times 1.8 \times 4$ mm^3, 60 dynamics). A bolus of 15 ml Gd-DTPA (Magnevist, 0.5 mmol/ml) was injected 3 minutes after an initial bolus of 7.5 ml with 4 ml/s injection rate. We compare our method with two reconstruction methods: SparseSENSE with multiple constraints [3] and k-t RPCA [7]. For fair comparison, we empirically fine-tuned the optimal regularization parameters for each method. Undersampling was retrospectively done via variable density Poisson-disc sampling [9]. A tracer kinetic model [2] based on intravascular indicator-dilution theory was used for estimating perfusion parameters. Concordance correlation coefficients (CCCs) were used to quantitatively compare the perfusion maps.

A Robust Reconstruction Method for Quantitative Perfusion MRI   3
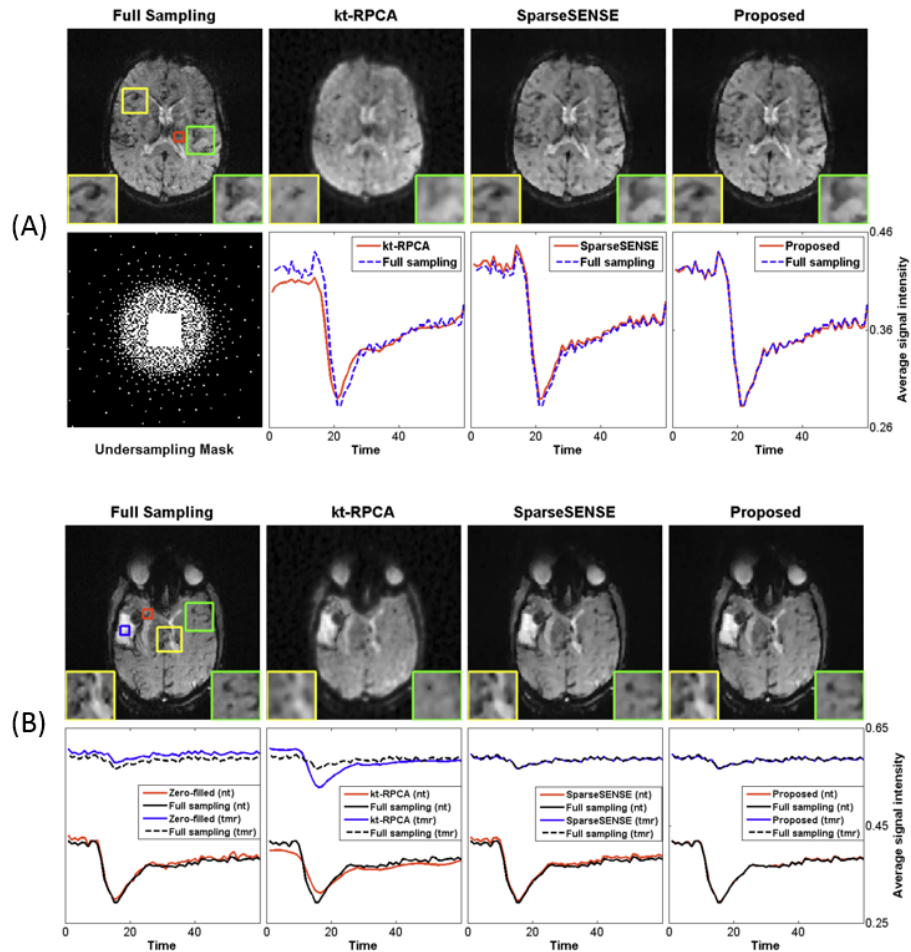
Fig. 1. Spatial reconstructions of a single frame and time-intensity curves (TIC) averaged over the region of interests (ROIs) of Subject 1 (A) and Subject 2 (B) obtained with an 8-fold acceleration factor. Subfigure (A) also displays an exemplary undersampling mask in the bottom-left figure. For each frame, close-up views of two regions (yellow and green square) are also displayed. Subfigure (B) shows the TICs obtained from both non-tumor (nt) and tumor (tmr) region. Our method achieves the most accurate estimation of peaks and temporal patterns of perfusion signal, whereas spatial reconstructions are quite close to those obtained by SparseSENSE.

4   Ulas et al.
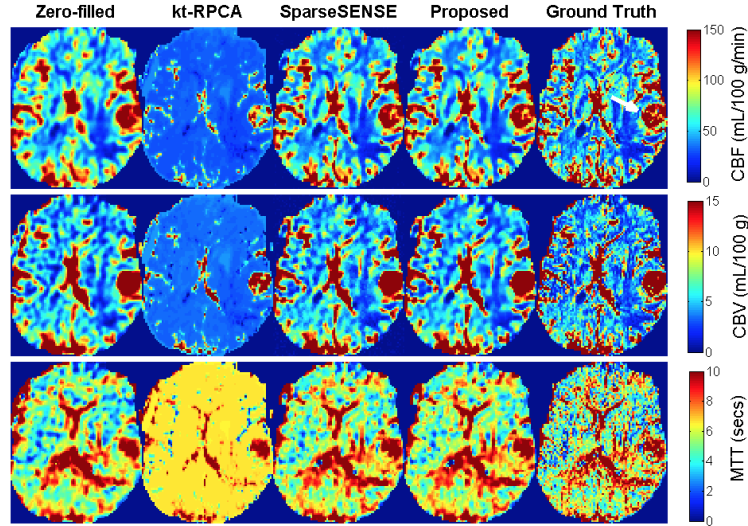
Fig. 2. Perfusion parameter maps (CBF, CBV, MTT) of Subject 3 obtained by different methods with an 8-fold acceleration. The tumor region is marked by a white arrow in the Ground Truth CBF image. The proposed method results in perfusion maps where most of the structures are preserved and appear sharper compared to SparseSENSE, but some finer details are missing due to undersampling. The kt-RPCA reconstruction method produces highly inaccurate perfusion maps as expected by the mismatch of TICs shown in Figure 1. This method does not explicitly exploit variation in temporal domain, which makes it inadequate for quantitative PWI.

3   Results

Figure 1 displays the results of both spatial reconstructions and estimated perfusion time-intensity curves (TICs) of all methods obtained from two different subjects with an 8-fold acceleration. The proposed method yields the most accurate matching of peaks and temporal pattern of perfusion signal and produces acceptable spatial reconstructions together with SparseSENSE. Figure 2 demonstrates resulting perfusion maps of different reconstruction methods with an 8-fold acceleration. Our method produces maps that are closer to the GT maps obtained by fully sampled data and provide sharper edges compared to SparseSENSE. The inefficiency of kt-RPCA for quantitative PWI is also demonstrated in Figure 2. Figure 3 shows how the quality of perfusion maps of a subject decreases depending on increasing acceleration rates, and this evidence is quantitatively assessed and illustrated for another subject in Figure 4. Figure 5 reports the average CCCs of CBF and CBV parameters obtained from all methods with increasing acceleration rates. Our method yields the best CCCs up to 8-fold acceleration and shows similar performance like SparseSENSE at further accelerations.

A Robust Reconstruction Method for Quantitative Perfusion MRI   5
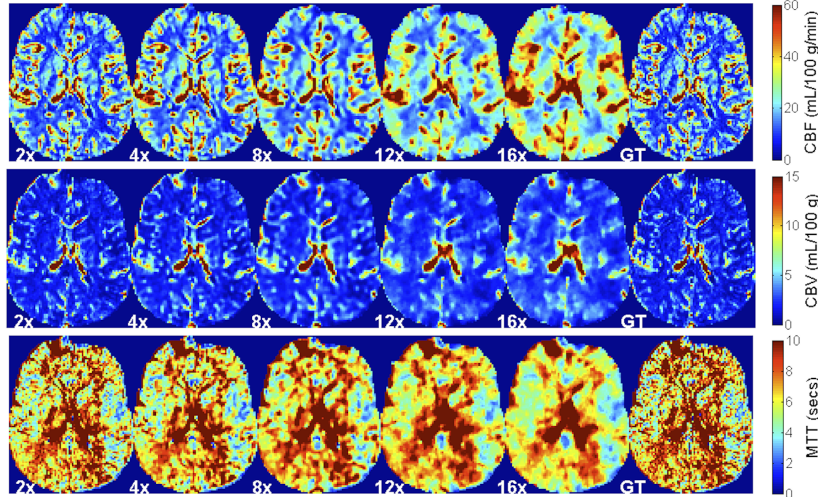
Fig. 3. Perfusion parameter maps (CBF, CBV, MTT) of Subject 1 resulting from our proposed reconstruction method with respect to different acceleration factors and Ground Truth (GT) perfusion maps for comparison. The estimated perfusion maps appear highly accurate up to 8-fold acceleration but the maps start to deteriorate and show over-smooth regions at higher acceleration rates..

4   Discussion

This study presents an efficient reconstruction method for quantitative PWI, which jointly exploits the temporal variations in pixel-wise and patch-wise level. The processing time of our method on a single-slice DSC-MRI dataset is around 4-5 minutes (on a Intel desktop). The maximum acceleration achieved with our method could be further increased with the use of a high-spatial resolution data. However, high-spatial resolution is not clinically realistic for PWI because a high temporal resolution is necessary to accurately track the kinetics of the tracer.

References

1. Chen, C., Li, Y., Axel, L., Huang, J.: Real time dynamic MRI by exploiting spatial and temporal sparsity. Magnetic Resonance Imaging 34(4), 473 – 482 (2016), http://www.sciencedirect.com/science/article/pii/S0730725X15002702

6   Ulas et al.
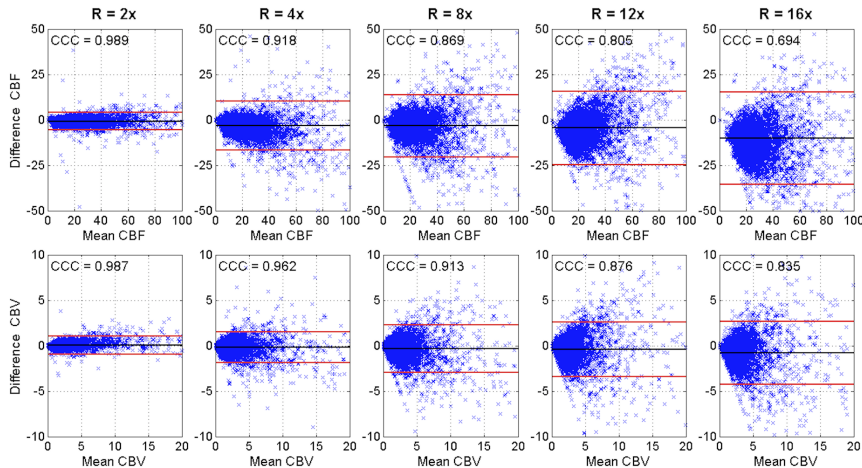
Fig. 4. Bland-Altman plots and 95% confidence intervals within two red lines for CBF (top) and CBV (bottom) parameters of Subject 4 depending on different acceleration factors, resulting from our proposed reconstruction. The bias and variance of the difference between estimated and ground truth parameter values generally become larger when the acceleration rate increases. The estimated concordance correlation coefficients (CCCs) are displayed at the top-left corner of each plot. CCCs decrease with increasing acceleration, which coincides with the changes of bias and variance.

| Method | Acceleration Rate | | | | |
	R=2x	R=4x	R=8x	R=12x	R=16x
Zero-filled	(0.75, 0.73)	(0.78, 0.80)	(0.74, 0.73)	(0.59, 0.52)	(0.62, 0.59)
kt-RPCA	(0.58, 0.65)	(0.53, 0.59)	(0.47, 0.53)	(0.37, 0.43)	(0.31, 0.39)
SparseSENSE	(0.89, 0.91)	(0.90, **0.93**)	(0.84, 0.86)	(0.75, **0.74**)	(0.76, 0.75)
Proposed	(**0.91**, **0.96**)	(**0.91**, **0.93**)	(**0.86**, **0.87**)	(**0.76**, 0.72)	(**0.77**, **0.76**)

Fig. 5. Average concordance correlation coefficients (CCCs) of two perfusion parameters (CBF, CBV) obtained from 5 subjects data with respect to increased acceleration rates. The values in brackets refer to CBF and CBV, respectively. The best values for each acceleration rate are highlighted in bold. Our method yields the best CCCs up to 8-fold acceleration and result in very similar quantitative values like SparseSENSE at 12-fold and 16-fold accelerations. The kt-RPCA method performs even worse than Zero-filled reconstruction since it leads to over-smoothing of the temporal perfusion signal, which can be easily observed in Figure 1.

2. Fang, R., Zhang, S., Chen, T., Sanelli, P.: Robust low-dose CT perfusion deconvolution via tensor total-variation regularization. IEEE Transactions on Medical Imaging 34(7), 1533–1548 (July 2015)

A Robust Reconstruction Method for Quantitative Perfusion MRI   7

3. Lebel, R.M., Jones, J., Ferre, J.C., Law, M., Nayak, K.S.: Highly accelerated dynamic contrast enhanced imaging. Magnetic Resonance in Medicine 71(2), 635–644 (2014), `http://dx.doi.org/10.1002/mrm.24710`

4. Lingala, S.G., Hu, Y., DiBella, E., Jacob, M.: Accelerated dynamic MRI exploiting sparsity and low-rank structure: k-t SLR. IEEE Transactions on Medical Imaging 30(5), 1042–1054 (May 2011)

5. Raguet, H., Fadili, J., Peyr, G.: A generalized forward-backward splitting. SIAM Journal on Imaging Sciences 6(3), 1199–1226 (2013), `http://dx.doi.org/10.1137/120872802`

6. Smith, D.S., Li, X., Gambrell, J.V., Arlinghaus, L.R., Quarles, C.C., Yankeelov, T.E., Welch, E.B.: Robustness of quantitative compressive sensing mri: The effect of random undersampling patterns on derived parameters for DCE- and DSC-MRI. IEEE Transactions on Medical Imaging 31(2), 504–511 (Feb 2012)

7. Trmoulhac, B., Dikaios, N., Atkinson, D., Arridge, S.R.: Dynamic MR image reconstruction-separation from undersampled (k,t)-space via low-rank plus sparse prior. IEEE Transactions on Medical Imaging 33(8), 1689–1701 (Aug 2014)

8. Ulas, C., Gomez, P.A., Sperl, J.I., Preibisch, C., Menze, B.H.: Spatio-temporal MRI reconstruction by enforcing local and global regularity via dynamic total variation and nuclear norm minimization. In: 2016 IEEE 13th International Symposium on Biomedical Imaging (ISBI). pp. 306–309 (April 2016)

9. Vasanawala, S., Murphy, M., Alley, M., Lai, P., Keutzer, K., Pauly, J., Lustig, M.: Practical parallel imaging compressed sensing MRI: Summary of two years of experience in accelerating body MRI of pediatric patients. In: 2011 IEEE International Symposium on Biomedical Imaging: From Nano to Macro. pp. 1039–1043 (March 2011)

MULTIPARAMETRIC MAPPING: MR FINGERPRINTING AND BEYOND

5.1 PEER-REVIEWED PUBLICATIONS

The three publications presented here on multiparametric mapping techniques focus on using multi-contrast datasets for parameter quantification, including anatomical labeling. In Joint Reconstruction of Multi-Contrast MRI for Multiple Sclerosis Lesion Segmentation, a joint reconstruction framework that exploits mutual information from different contrast weighted images is evaluated with respect to its ability to subsequently segment lesions in the brain. Learning a Spatiotemporal Dictionary for Magnetic Resonance Fingerprinting with Compressed Sensing demonstrates how machine learning techniques can be incorporated into a an MRF reconstruction coupled with CS. Moreover, Simultaneous Parameter Mapping, Modality Synthesis, and Anatomical Labeling of the Brain with MR Fingerprinting pushes this idea even further, by showing how additional quantitative information — including tissue labels — can be estimated from an MRF acquisition by matching small spatiotemporal patches of the acquired data to an existing database.

5.1.1 *Joint Reconstruction of Multi-Contrast MRI for Multiple Sclerosis Lesion Segmentation*

Peer-reviewed Conference Paper

Authors: PA. Gómez, JI. Sperl, T. Sprenger, C. Metzler-Baddeley, DK. Jones, P. Saemann, M. Czisch, MI. Menzel, BH. Menze

In: *Bildverarbeitung für die Medizin 2015* (2015) [34]

Abstract: A joint reconstruction framework for multi-contrast MRI images is presented and evaluated. The evaluation takes place in function of quality criteria based on reconstruction results and performance in the automatic segmentation of Multiple Sclerosis (MS) lesions. We show that joint reconstruction can effectively recover artificially corrupted images and is robust to noise.

Contribution of thesis author: Algorithmic development and implementation, experimental design, data analysis, manuscript preparation and editing.

Joint Reconstruction of Multi-Contrast MRI for Multiple Sclerosis Lesion Segmentation

Pedro A Gómez[1,2,3], Jonathan I Sperl[3], Tim Sprenger[2,3],
Claudia Metzler-Baddeley[4], Derek K Jones[4], Philipp Saemann[5],
Michael Czisch[5], Marion I Menzel[3], Bjoern H Menze[1]

[1]Computer Science, Technische Universität München, Munich, Germany
[2]Medical Engineering, Technische Universität München, Munich, Germany
[3]GE Global Research, Munich, Germany
[4]CUBRIC, School of Psychology, Cardiff University, Cardiff, Wales, UK
[5]Max Plank Institute of Psychiatry, Munich, Germany
`pedro.gomez@tum.de`

Abstract. A joint reconstruction framework for multi-contrast MR images is presented and evaluated. The evaluation takes place in function of quality criteria based on reconstruction results and performance in the automatic segmentation of Multiple Sclerosis (MS) lesions. We show that joint reconstruction can effectively recover artificially corrupted images and is robust to noise.

1 Introduction

Multi-contrast MR imaging enables the quantification of metrics that provide information on tissue micro-structure. In the domain of neuroimaging, these metrics deepen our understanding of the brain in both health and disease, and could potentially assess the early onset of neurological disorders, such as Multiple Sclerosis (MS). Quantitative metrics are obtained from different MRI techniques, generating multiple contrasts and a wide-range of information regarding tissue micro-structure. Obtaining this information, however, comes at the expense of long acquisition times and low signal to noise ratios (SNR).

One possibility for overcoming the limitation of long scan times is through accelerated data acquisitions by compressed sensing (CS). In Diffusion Spectrum Imaging (DSI), acceleration by CS has been successfully demonstrated [1] and is currently being validated in clinical settings. A different approach is to use spatial context to increase data quality without further incrementing acquisition times. One of these methods, presented by Haldar et al. [2], takes advantage of structural correlations between datasets to perform a statistical roint reconstruction. This is achieved by incorporating gradient information from all contrasts into the regularization term of a maximum likelihood estimation.

In this study we evaluate the performance of joint reconstruction under different noise levels. Furthermore, we investigate the performance of this approach using a metric that evaluates the segmentation accuracy of MS lesions – i.e.,

156   Gómez et al.

the tasks the images were acquired for – rather than focusing on the common reconstruction error calculated from image intensities.

2   Materials and methods

2.1   Data acquisition

Five volunteers were scanned with a 3T GE HDx MRI system (GE Medical Systems, Milwuakee, WI) using an eight channel receive only head RF coil. MRI datasets were acquired for a HARDI protocol, a mcDESPOT [3] protocol, and a high resolution T1 weighted anatomical scan (FSPGR). The HARDI protocol consisted of 60 gradient orientations around a concentric sphere with $b = 1200$ s/mm^2 and 6 baseline images at $b=0$. HARDI datasets were corrected for motion using FSL's FLIRT and FNIRT [4] and both HARDI and mcDESPOT were rigidly registered to the T1 anatomical scan with FLIRT [3].

Seven MS patients were scanned with a CS-DSI acquisition protocol using a GE MR750 scanner (GE Medical Systems, Milwaukee, WI). The CS-DSI protocol comprised of 514 volumes acquired on a Cartesian grid with maximal b-value $= 3000$ s/mm^2. Additionally, high resolution T1, T2, and FLAIR contrasts were acquired. DSI volumes were co-registered to the first $b=0$ image, corrected for motion using FLIRT and FNIRT, and a brain mask was obtained using BET [4]. T1, T2 and FLAIR images were down-sampled to the same resolution as the DWIs and all of the volumes were once again co-registered with each other. Finally, for every patient, 11 slices were selected and lesions were manually labelled using a basic region growing algorithm on thresholding FLAIR intensity values.

2.2   Multi-constrast joint reconstruction

In a first experiment we want to evaluate whether joint reconstruction can effectively remove noise and maintain data quality in datasets of our multi-contrast sequence. To this end, we studied the reconstruction error under different noise level and optimized the necessary regularization parameters.

After data acquisition and pre-processing, volunteer datasets were artificially corrupted with homogeneous Rician noise and reconstructed using joint reconstruction. Then, or a given set of M images, the reconstructed data $\hat{\mathbf{x}}$ was obtained from the corrupted data $\mathbf{y}$ using

$$\left\{\hat{\mathbf{x}}^1, \hat{\mathbf{x}}^2, \ldots, \hat{\mathbf{x}}^M\right\} = \underset{\{\mathbf{x}^1,\mathbf{x}^2,\ldots,\mathbf{x}^M\}}{\arg\min} \sum_{m=1}^{M} \mu_m^2 \left\|\mathbf{F}_m \mathbf{x}^m - \mathbf{y}^m\right\|_2^2 + \Phi\left(\mathbf{x}^1, \mathbf{x}^2, \ldots, \mathbf{x}^M\right)$$

(1)

where $\mathbf{F}$ is the Fourier encoding operator, μ is a parameter that adjusts data consistency, and $\Phi\left(\cdot\right)$ is a regularization term. As in [2], we define the regularization term as the finite differences over all images. We have to optimize μ and Φ as a function of data quality.

2.3 Lesion segmentation

In a second experiment we evaluate the performance of a joint reconstruction for our sequence using *not* the reconstruction performance of the images, but the DICE scores of an automatic lesion segmentation algorithm. Here, we compare the DICE scores of the ground truth patient datasets with corrupted and jointly reconstructed versions of the datasets.

Random forests have already been implemented to segment MS lesions in multi-contrast MR images, achieving performance comparable to other state of the art segmentation methods [5]. We also propose the use of discriminative classifiers within a random framework to classify voxels, but, given the nature of our patient data, replace context rich features with scalar diffusion features calculated from the CS-DSI protocol.

The feature vector consists of a total of 27 features: three structural MRI intensity channels (T1, T2, and FLAIR), eight diffusion features and 16 kurtosis features. Diffusion features were estimated from the Eigenvalue decomposition of the diffusion tensor $\mathbf{D} \in \mathbb{R}^{3 \times 3}$, while kurtosis features were estimated from projections of the fourth order kurtosis tensor $\mathbf{W} \in \mathbb{R}^{3 \times 3 \times 3 \times 3}$ into spherical and elliptical coordinates. Both tensors were calculated by fitting the data to the diffusional kurtosis model defined in [6] and to a version of the model with a coordinate system rotated into the main directions of diffusion.

The classification task with random forests was accomplished using Matlab's (The Mathworks, Inc) Statistics Toolbox. For this work, a total of 30 trees were grown from four randomly selected datasets and the trained forest was fit to the other three patients. Every tree received a randomly subsampled dataset of voxels and lesion voxels where weighted to proportional to non-lesion voxels.
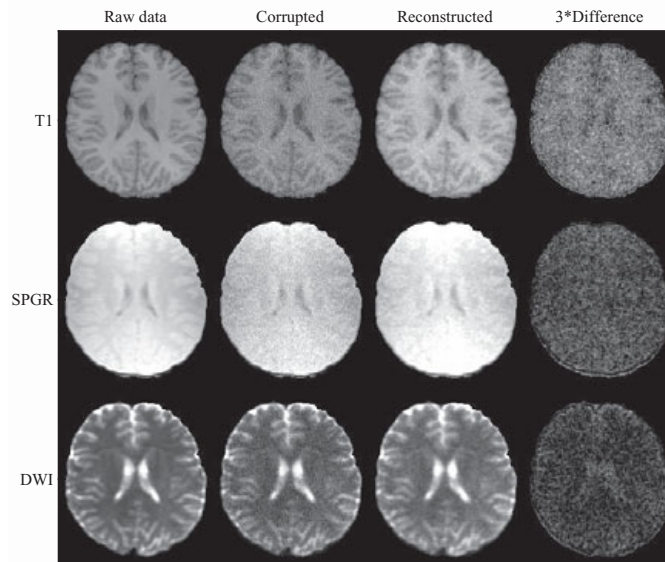
Fig. 1. Reconstructed datasets from a noisy input. Rows show, from top to bottom, three different acquisition protocols: T1, SGPR, and DWI. Columns, from left to right, display: raw data, data corrupted with $\sigma = 4\%$ homogeneous Rician noise, reconstructed data, and absolute difference between the raw data in the first column and the reconstructed data in the third column multiplied times three for better visualization.

158   Gómez et al.

3   Results

3.1   Optimization of joint reconstruction parameters

In the first experiment we determine regularization parameters of the joint reconstruction algorithm that are optimal for our imaging sequence. We use the high resolution volunteer data set.

Volunteer datasets were artificially corrupted with homogeneous Rician noise and reconstructed with different parameter settings. The three regularization parameters, which control for data consistency, regularization, and sensitivity of edge detection, were optimized in function of the remaining noise fraction (RNF) of the reconstructed images, and the root mean square error (RMSE) and structural similarity index (SSIM) [7] of these images to the original raw data.

Tab. 1 shows exemplary results for a given parameter set with optimized regularization parameters, and Fig. 1 provides a visual comparison of each of the reconstructed contrasts. In this example, joint reconstruction was able to remove more than 75% of the artificially added Rician noise, leading to RNF computations between 17.7 and 24.7%.
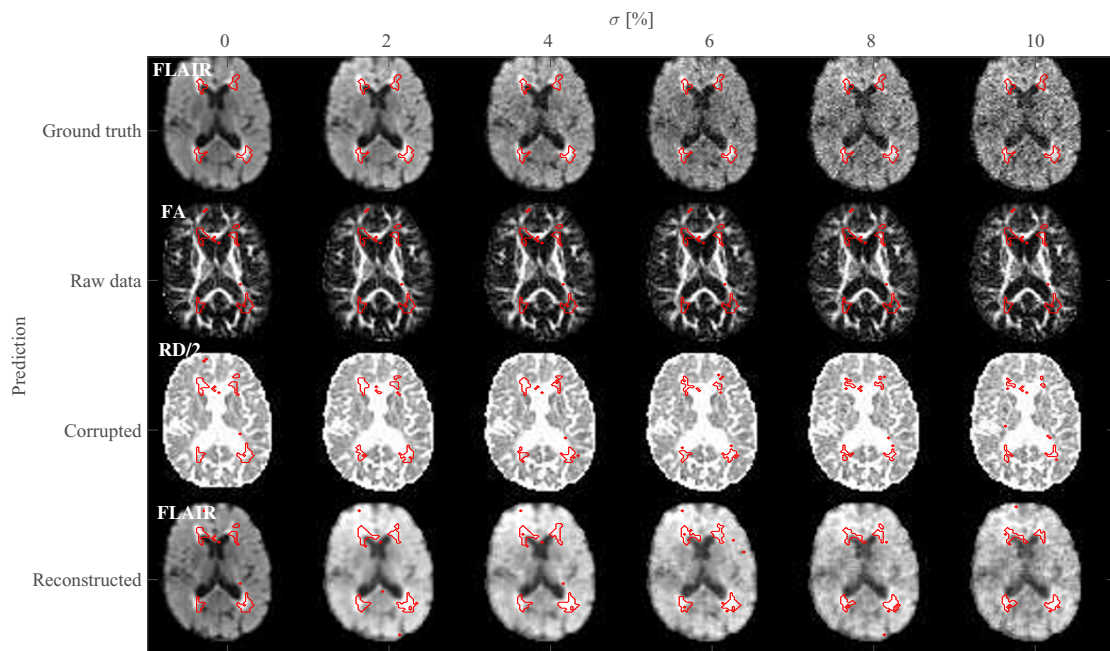
Fig. 2. Segmentation performance with respect to noise. Each row shows a different contrast, indicated in white letters, and the labeled lesions for ground truth (top row) plus predictions on raw data, corrupted data and reconstructed data (bottom three rows). Note that fractional anisotropy (FA) and radial diffusivity (RD) maps weren't directly corrupted, but estimated from corrupted data. RD is shown divided by two for better visualization.

Quality criteria	Protocol		
	T1	MCDESPOT	DWI
$\sigma_{\hat{\mathbf{x}}}$ [%]	0.992	0.981	0.981
RNF	0.177	0.238	0.247
RMSE	0.090	0.050	0.042
SSIM	0.711	0.683	0.772

Table 1. Quality metrics estimated for different jointly reconstructed datasets. Every dataset was individually corrupted with $\sigma = 4\%$ homogeneous Rician noise and jointly reconstructed using (1).

3.2 Evaluation of MS lesion segmentation accuracy

The second experiment evaluated whether joint reconstruction can effectively remove noise without losing critical information, such as the borders between lesions and non-lesions. We evaluate the scores on the patient data set.

For five different noise levels, the following was done: homogeneous Rician noise was added to all of the images to corrupt them, images were subsequently reconstructed using joint reconstruction, two different kurtosis and diffusion models were fit to the corrupted and reconstructed datasets, and lesion segmentation was performed. The experiment was repeated over 10 iterations and a mean DICE score for every noise level was obtained. Fig. 2 shows the segmentation results of an exemplary dataset and Fig. 3 displays the general performance and robustness to noise.

As seen in Figs. 2 and 3, joint reconstruction has a significant impact on segmentation results. At low noise levels, jointly reconstructed datasets yield lower DICE scores than raw data and even noisy datasets. This is most likely do
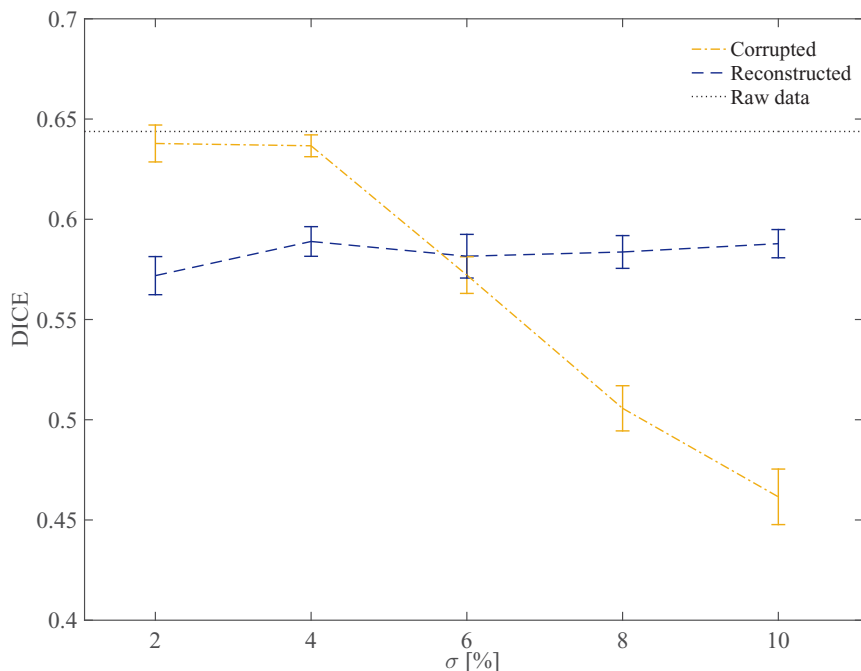
Fig. 3. DICE scores for corrupted and reconstructed datasets as a function of noise levels. Plots show mean ± standard deviation of 10 iterations and the black line indicates the average DICE score obtained from raw data.

160   Gómez et al.

to the fact that joint reconstruction has a smoothing effect and that, for certain parameter settings, small edge structures are ignored and blurred out. These small edge structures include the boundary between lesions and non-lesions, especially since this boundary is not completely clear or the same in the multiple contrasts. As noise levels increase, DICE scores of corrupted datasets decrease while reconstructed datasets maintain similar values.

4   Discussion

In this work, joint reconstruction was evaluated for multi-contrast MR images according to multiple criteria and the role of the method on lesion segmentation was further studied. From this analysis, it was established that joint reconstruction has a significant impact on lesion segmentation, especially at low noise levels, where over-smoothing can lead to decreased performance of the segmentation algorithm. On the other hand, joint reconstruction proved to be robust to noise, and at higher noise levels, was able to remove noise while still capturing the differences between lesions and non-lesions.

Parameter settings play a crucial role on the joint reconstruction framework. Optimizing parameters with respect to the reconstruction errors may not lead to the parameter set that is optimal for lesion segmentation. Furthermore, data quality of each particular dataset also affects the optimal parameter set. Consequently, future work will focus on developing novel, disease-specific and data-adaptive metrics that effectively discriminate between normal state and disease and that can be used to optimize the entire imaging pipeline from data acquisition to analysis.

References

1. Menzel MI, Tan ET, Khare K, et al. Accelerated diffusion spectrum imaging in the human brain using compressed sensing. Magn Reson Med. 2011;66:1226–33.
2. Haldar JP, Wedeen VJ, Nezamzadeh M, et al. Improved diffusion imaging through SNR-enhancing joint reconstruction. Magn Reson Med. 2013;69(1):277–89.
3. Deoni SCL, Rutt BK, Arun T, et al. Gleaning multicomponent T1 and T2 information from steady-state imaging data. Magn Reson Med. 2008;60:1372–87.
4. Jenkinson M, Beckmann CF, Behrens TEJ, et al. FSL. NeuroImage. 2012;62:782–90.
5. Geremia E, Clatz O, Menze BH, et al. Spatial decision forests for MS lesion segmentation in multi-channel magnetic resonance images. NeuroImage. 2011;57:378–90.
6. Jensen JH, Helpern JA, Ramani A, et al. Diffusional kurtosis imaging: the quantification of non-gaussian water diffusion by means of magnetic resonance imaging. Magn Reson Med. 2005;53:1432–40.
7. Wang Z, Bovik AC, Sheikh HR, et al. Image quality assessment: from error visibility to structural similarity. IEEE Trans Image Process. 2004;13:600–12.

5.1.2 *Learning a Spatiotemporal Dictionary for Magnetic Resonance Fingerprinting with Compressed Sensing*

Peer-reviewed Conference Paper

Authors: PA. Gómez, C. Ulas, JI. Sperl, T. Sprenger, M. Molina-Romero, MI. Menzel, BH. Menze

In: *MICCAI Patch-MI Workshop* LNCS 9467 (2015), pp. 112 – 119 [35]

Abstract: Magnetic Resonance Fingerprinting (MRF) is a novel technique that allows for the fast and simultaneous quantification of multiple tissue properties, progressing from qualitative images, such as T1- or T2-weighted images commonly used in clinical routines, to quantitative parametric maps. MRF consists of two main elements: accelerated pseudorandom acquisitions that create unique signal evolutions over time and the voxel-wise matching of these signals to a dictionary simulated using the Bloch equations. In this study, we propose to increase the performance of MRF by not only considering the simulated temporal signal, but a full spatiotemporal neighborhood for parameter reconstruction. We achieve this goal by first training a dictionary from a set of spatiotemporal image patches and subsequently coupling the trained dictionary with an iterative projection algorithm consistent with the theory of Compressed Sensing (CS). Using data from BrainWeb, we show that the proposed patch-based reconstruction can accurately recover T1 and T2 maps from highly undersampled k-space measurements, demonstrating the added benefit of using spatiotemporal dictionaries in MRF.

Contribution of thesis author: Algorithmic development and implementation, experimental design, data analysis, manuscript preparation and editing.

Learning a Spatiotemporal Dictionary
for Magnetic Resonance Fingerprinting
with Compressed Sensing

Pedro A. Gómez[1,2,3]( ), Cagdas Ulas[1], Jonathan I. Sperl[3], Tim Sprenger[1,2,3],
Miguel Molina-Romero[1,2,3], Marion I. Menzel[3], and Bjoern H. Menze[1]

[1] Computer Science, Technische Universität München, Munich, Germany
`pedro.gomez@tum.de`
[2] Biomedical Engineering, Technische Universität München, Munich, Germany
[3] GE Global Research, Munich, Germany

Abstract. Magnetic resonance fingerprinting (MRF) is a novel technique that allows for the fast and simultaneous quantification of multiple tissue properties, progressing from qualitative images, such as T1- or T2-weighted images commonly used in clinical routines, to quantitative parametric maps. MRF consists of two main elements: accelerated pseudorandom acquisitions that create unique signal evolutions over time and the voxel-wise matching of these signals to a dictionary simulated using the Bloch equations. In this study, we propose to increase the performance of MRF by not only considering the simulated temporal signal, but a full spatiotemporal neighborhood for parameter reconstruction. We achieve this goal by first training a dictionary from a set of spatiotemporal image patches and subsequently coupling the trained dictionary with an iterative projection algorithm consistent with the theory of compressed sensing (CS). Using data from BrainWeb, we show that the proposed patch-based reconstruction can accurately recover T1 and T2 maps from highly undersampled k-space measurements, demonstrating the added benefit of using spatiotemporal dictionaries in MRF.

1 Introduction

Quantitative magnetic resonance imaging (qMRI) techniques measure relevant biological parameters, providing a profound characterization of the underlying tissue. In contrast to conventional weighted MRI, where the image signal is represented by intensity values and different tissues are described relative to each other, qMRI generates parametric maps of absolute measures that have a physical interpretation, leading to reduced bias and reproducible diagnostic information. On the other hand, obtaining quantitative maps is a time consuming task. It requires the repeated variation of typical MR acquisition parameters, such as flip angle (FA) or repetition time (TR), and the fitting of the measured signal to a model in order to estimate the parameters of interest, including the MR specific longitudinal (T1) and transversal (T2) relaxation times. Long acquisition times, together with high sensitivity to the imaging device

and system setup, are the main restrictions to clinical applications of qMRI techniques.

A recently proposed qMRI method, magnetic resonance fingerprinting (MRF), aims to overcome these limitations through accelerated pseudorandom acquisitions [6]. It is based on the idea that pseudorandom variations on acquisition parameters cause the signal response for different tissue types to be unique. This unique signal evolution can be matched to a precomputed dictionary created from known combinations of the parameters of interest (e.g. T1 and T2). Therefore, by matching the measured signal to one atom in the dictionary, all of the parameters used to simulate the corresponding atom can be simultaneously extracted. Furthermore, since the form of the signal evolution used for pattern matching is known *a priori*, MRF is less sensitive to measurement errors, facilitating accelerated acquisitions through the undersampling of the measurement space (k-space). It should be noted that, so far, all matching is done for one-dimensional temporal signals only.

The notion of reconstructing signals from undersampled measurements comes from the theory of compressed sensing (CS) [5]. CS has been successfully applied to accelerate parameter mapping [4] and recently Davies et al. [3] demonstrated a CS strategy for MRF that does not rely on pattern matching for error suppression and has exact recovery guarantees, resulting in increased performance for shorter pulse sequences. The authors further extend their CS model to exploit global spatial structure by enforcing sparsity in the wavelet domain of the estimated density maps, slightly improving the performance of their approach.

Spatial information can also be incorporated locally by using image patches. Patch-based dictionaries have the advantage of being able to efficiently represent complex local structure in a variety of image processing tasks. Furthermore, the use of overlapping patches allows for averaging, resulting in the removal of both noise and incoherent artefacts caused by undersampling. Patch-based dictionaries have been previously used for the task of MR image reconstruction [7], where the sparsifying dictionary was learnt directly from the measured data, resulting in accurate reconstructions for up to six fold undersampling.

In this work, we propose to use a dictionary with both temporal and local spatial information for parametric map estimation. We create a training set by using the Bloch equations to simulate the temporal signal response over a predefined spatial distribution obtained from anatomical images and train a spatiotemporal dictionary by clustering similar patches. The trained dictionary is incorporated into a patch-based iterative projection algorithm to estimate T1 and T2 parametric maps. We see two main benefits of our approach:

1. Incorporating spatial data increases the atom length, i.e. the amount of descriptive information available per voxel, requiring less temporal points for an accurate reconstruction.
2. Training improves the conditioning of the dictionary by creating atoms distinct to each other, leading to a better signal matching.

The rest of this paper is structured as follows. In Sect. 2 we describe the method, in particular the proposed patch-based algorithm for MRF. Section 3

depicts the experiments and demonstrates the application of recovering parametric maps from undersampled data, and in Sect. 4 we offer conclusions.

2 Methods

The goal of MRF is to obtain parametric maps $\boldsymbol{\theta} \in \mathbb{R}^{N \times Q}$ from a sequence of undersampled measurements $\mathbf{Y} \in \mathbb{C}^{M \times T}$, where Q is the number of tissue relaxation parameters (T1 and T2), T is the sequence length, every map $\boldsymbol{\theta}_q \in \mathbb{R}^N$ has a total of N voxels, every measurement $\mathbf{y}_t \in \mathbb{C}^M$ is sampled M times, and $M \ll N$. This is achieved in three steps: image reconstruction, template matching, and parameter extraction.

Image reconstruction is the task of obtaining the image sequence $\mathbf{X} \in \mathbb{C}^{N \times T}$ from the measurements $\mathbf{Y}$. This is generally formulated as a inverse problem: $\mathbf{Y} = \mathbf{EX}$, where $\mathbf{E} \in \mathbb{C}^{M \times N}$ is the encoding operator. The reconstructed image is then matched to a precomputed dictionary $\mathbf{D} \in \mathbb{C}^{T \times L}$ of L atoms, to find the dictionary atom $\mathbf{d}_l \in \mathbb{C}^T$ that best describes it. This is done at every voxel location $\mathbf{x}_n \in \mathbb{C}^T$ by selecting the entry l_n that maximizes the modulus of the atom and the conjugate transpose of the signal:

$$\hat{l}_n = \arg \max_{\substack{l \\ l=1,\ldots,L}} |\mathbf{x}_n^* \mathbf{d}_l| \tag{1}$$

where both, $\mathbf{d}_l$ and $\mathbf{x}_n$, were previously normalized to have unitary length. Finally, the T1 and T2 parameters used to construct the matching entry are assigned to the voxel n, creating $\boldsymbol{\theta}_n = \{T1_n, T2_n\}$. Thus, by repeating the matching over all voxels of the image, the parametric T1 and T2 maps are found.

Davies et al. [3] interpret the template matching as a projection of $\mathbf{x}_n$ onto the cone of the Bloch response manifold, and propose an iterative projection algorithm to accurately extract parametric maps. The algorithm, termed Bloch response recovery via iterated projection (BLIP), iteratively alternates between a gradient step, a projection step, and a shrinkage step to reconstruct the image sequence $\mathbf{X}$ and estimate the corresponding parameter maps $\boldsymbol{\theta}$.

2.1 Spatiotemporal Dictionary Design

Given a set of fully sampled 2D spatial parametric maps $\boldsymbol{\theta} \in \mathbb{R}^{N \times Q}$, where $N = N_i \times N_j$ and $Q = 2$, an image sequence $\mathbf{X} \in \mathbb{C}^{N \times T}$ of T temporal points can be created at each voxel using the Bloch equations to simulate the magnetization response of an inversion-recovery balanced steady state free-precession (IR-bSSFP) sequence with pseudorandomized acquisition parameters (see Fig. 1) [6]. $\mathbf{X}$ can be processed to create a spatiotemporal dictionary as follows.

Let $\mathbf{R}_n \in \mathbb{C}^{P \times N}$ be the operator that extracts 2D image patches of size $P = P_i \times P_j$, so that the spatiotemporal image patch $\tilde{\mathbf{x}}_n \in \mathbb{C}^{P \times T}$ at a given spatial location n is given by

$$\tilde{\mathbf{x}}_n = \mathbf{R}_n \mathbf{X}. \tag{2}$$
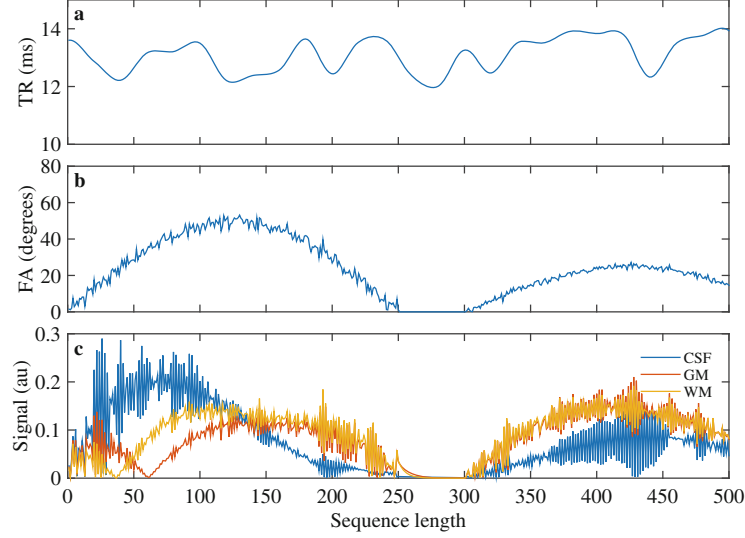
Fig. 1. Pseudorandom acquisition sequence and the corresponding signal response. **a**, TR values following a Perlin noise pattern. **b**, Flip angle series of repeating sinusoidal curves and added random values. **c**, Signal evolution for different tissue classes: white matter (WM), grey matter (GM), and cerebrospinal fluid (CSF).

It is then possible to create the patch-based image matrix $\tilde{\mathbf{X}} \in \mathbb{C}^{PT \times N}$ by concatenating the vector representation of every spatiotemporal patch of dimension $P_i \times P_j \times T$ for each spatial location in $\mathbf{X}$. Repeating the operation on $\boldsymbol{\theta}$ creates the patch-based multiparametric matrix $\tilde{\boldsymbol{\theta}} \in \mathbb{R}^{PQ \times N}$. The spatiotemporal dictionary $\tilde{\mathbf{D}} \in \mathbb{C}^{PT \times K}$ is then constructed by using k-means to cluster atoms in $\tilde{\mathbf{X}}$ with similar signal values into K clusters, averaging the corresponding T1 and T2 values in $\tilde{\boldsymbol{\theta}}$ to create the clustered patch-based matrix $\boldsymbol{\Theta} \in \mathbb{C}^{PQ \times K}$, and simulating the signal evolution for each cluster. A new simulation of the signal evolution ensures that the atoms in $\tilde{\mathbf{D}}$ correspond exactly to the entries in $\boldsymbol{\Theta}$.

2.2   Patch-Based BLIP Reconstruction (P-BLIP)

The BLIP algorithm [3] reconstructs the image sequence $\mathbf{X}$ in an iterative fashion. Given an image sequence $\mathbf{X}^{(i)}$ at iteration i, the reconstructed sequence $\mathbf{X}^{(i+1)}$ in the next iteration is determined by

$$\mathbf{X}^{(i+1)} = \mathcal{P}_{\mathcal{A}}(\mathbf{X}^{(i)} + \mu\mathbf{E}^H(\mathbf{Y} - \mathbf{E}\mathbf{X}^{(i)})), \tag{3}$$

where $\mathcal{P}_{\mathcal{A}}$ represents the projection onto the signal model $\mathcal{A}$, $\mathbf{E}^H$ is the Hermitian adjoint of the encoding operator, and μ equals the step size. P-BLIP builds on this algorithm, incorporating the patch extraction operator in (2) and an update step to make (3) applicable to a spatiotemporal signal model.

At every iteration the updated sequence $\mathbf{X}$ is transformed into the patch-based matrix $\tilde{\mathbf{X}}$ by (2). $\tilde{\mathbf{X}}$ is related to the trained dictionary $\tilde{\mathbf{D}}$ by

$$\tilde{\mathbf{X}} = \tilde{\mathbf{D}}\mathbf{W}, \tag{4}$$

116   P.A. Gómez et al.

where $\mathbf{W} \in \mathbb{R}^{K \times N}$ represents the weights. Equation 4 can be readily solved using greedy algorithms that find sparse solutions to linear systems of equations by adding a sparsity constraint to the ℓ_0-norm of each column vector $\mathbf{w}_n$:

$$\hat{\mathbf{W}} = \arg \min_{\mathbf{W}} \|\tilde{\mathbf{X}} - \tilde{\mathbf{D}}\mathbf{W}\|_2^2, \ \text{s.t.} \ \|\mathbf{w}_n\|_0 \leq \gamma, \ n = 1, ..., N. \tag{5}$$

We set the sparsity constraint to $\gamma = 1$, equivalent to finding one dictionary atom, as done in the template matching used in [3,6].

After estimating the weights, the patch-based image matrix is projected onto the dictionary by $\hat{\tilde{\mathbf{X}}} = \tilde{\mathbf{D}}\hat{\mathbf{W}}$. At this point, each voxel is overrepresented a total of P times, requiring an update step to return to the original image sequence $\mathbf{X}$. This update is achieved by averaging the P temporal signals that contribute to a given voxel location. Finally, the parametric maps $\boldsymbol{\theta}$ are estimated by applying the weights and patch-wise updates on $\boldsymbol{\Theta}$.

3   Experiments and Results

Image Data. Experiments were performed using twenty digital brain phantoms from BrainWeb [2]. Of these, ten were used to train the spatiotemporal dictionary and ten to test the performance of three different reconstruction algorithms: the original MRF reconstruction [6], BLIP [3], and the proposed P-BLIP. Experiments were designed to evaluate the performance of each algorithm as a function of sequence length and acceleration factors, and, for the case of P-BLIP, also as a function of spatial patch size. Ground truth datasets were generated by selecting a slice of crisp datasets labeled with different tissue classes, and resampling them to a matrix size of 256×256 to accelerate computations. Quantitative maps were then obtained by replacing the tissue labels with their corresponding T1 and T2 values. The values for the three main tissue types grey matter (GM), white matter (WM), and cerebrospinal fluid (CSF) were equaled to those reported in [6], while the values for the rest of the classes (fat, bone, muscle, vessels, dura matter, and connective tissue) were obtained directly from [1].

Modeling the Signal Evolution. At every voxel, the ground truth quantitative maps served as a basis to simulate the temporal evolution of the signal based on the IR-bSSFP pulse sequence with acquisition parameters displayed in Fig. 1, where the TRs follow a Perlin noise pattern, FAs are a series of repeating sinusoidal curves with added random values, and the radio frequency phase alternates between 0° and 180° on consecutive pulses. Off-resonance frequencies were not taken into account. This pulse sequence was combined with all possible combinations of a given range of T1 and T2 values to create a temporal dictionary used in both MRF and BLIP. The selected range was reported in [3], where T1 spans from 100 ms to 6000 ms and T2 from 20 ms to 1000 ms, both sampled at varying step sizes. Additionally, the dictionary included the exact T1 and T2 combinations corresponding to the different tissue classes.

Spatiotemporal Dictionary. To train the spatiotemporal dictionary used in P-BLIP, a region of interest that accounted for the entire head area was defined.
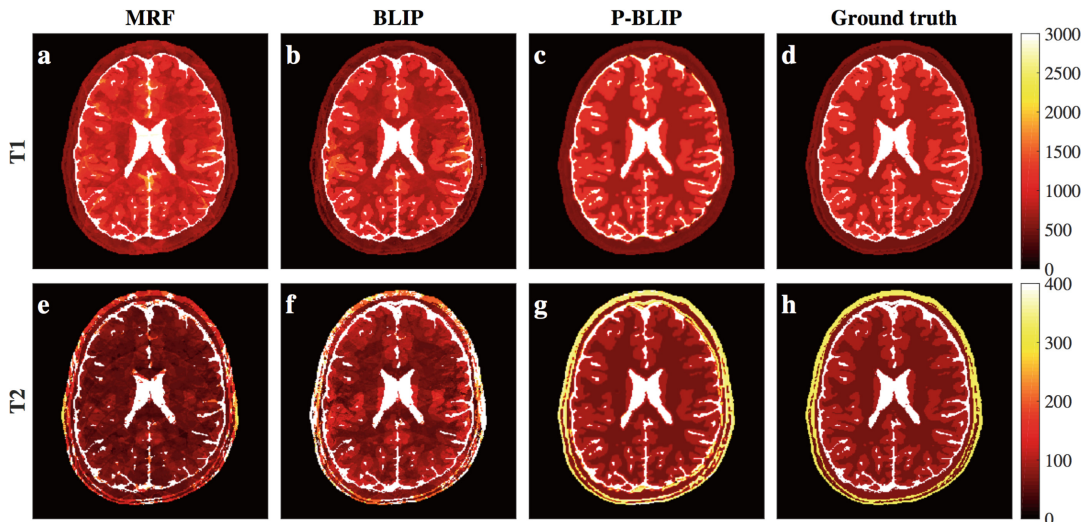
Fig. 2. Exemplary reconstruction results of one dataset with $T = 200$, $R = 10$, and $P = 3 \times 3$. The upper row shows T1 maps for all algorithms and the ground truth; and the bottom row the corresponding T2 maps. Most visible in T2 maps, subsampling artefacts can be effectively removed with P-BLIP.

The space covered by this region of interest was randomly and equally subsampled and each of the subsampled sets was assigned to a training subject. The selected parametric maps of each subject were then used as an input to train the dictionary as described in Sect. 2.1 with a total of $K = 200$ clusters.

Subsampling Strategy. We use a random EPI subsampling strategy for all experiments: the k-space is fully sampled in the read direction (k_x) and uniformly undersampled in the phase encoding direction (k_y) by an acceleration factor R. The sampling pattern is shifted by a random a number of k_y lines at every shot of the sequence.

Experimental Setup. An initial experiment was performed with spatiotemporal patches of size $3 \times 3 \times 200$ and an acceleration factor $R = 10$ to visually evaluate the reconstructed maps (see Fig. 2). Subsequently, three experiments assessed the reconstruction performance with respect to sequence length, acceleration factor and spatial patch size. The first experiment varied sequence lengths from 100 to 500 in step sizes of 100, the second experiment used acceleration factors of $R = \{2, 5, 10, 15, 20\}$, and the final experiment used spatial patches of sizes $P = \{1 \times 1, 3 \times 3, 5 \times 5, 7 \times 7\}$. The reconstruction error of the first two experiments was calculated using the signal-to-error ratio (SER) in decibels (dB), defined as $20 \log_{10} \frac{\|\mathbf{x}\|_2}{\|\mathbf{x} - \hat{\mathbf{x}}\|_2}$; and the third experiment with the SSIM values [8].

Results. Figure 2 displays the reconstructed parametric maps of an exemplary dataset. The MRF estimates show the characteristic ghosting artefacts caused by sub-Nyquist sampling. BLIP removes most of these artefacts from the T1 estimation, though they are still visible in the T2 maps. P-BLIP effectively removes these artefacts from both maps, resulting in reconstructions very close to the ground truth. These visual observations can be confirmed with quantitative
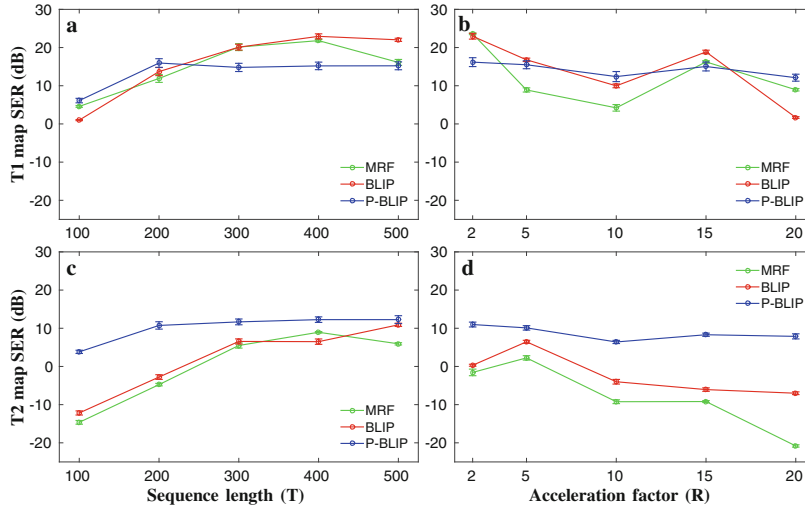
Fig. 3. a,c, Performance as a function of sequence length with $R = 10$, $P = 3 \times 3$; and **b,d**, as a function of acceleration factor with $T = 200$, $P = 3 \times 3$. P-BLIP is best in estimating T2 maps and shows better results for shorter sequences and higher acceleration for T1 maps.

Table 1. Average SSIM values for T1 and T2 map estimation with respect to different spatial patch sizes, $T = 200$ and $R = 10$.

Method	Baseline		Proposed: P-BLIP			
	MRF	BLIP	1×1	3×3	5×5	7×7
T1	0.761	0.814	0.848	**0.852**	0.691	0.625
T2	0.616	0.591	0.769	**0.857**	0.667	0.601

results. Figure 3c and d show how P-BLIP achieves better T2 estimates independently of the sequence length or acceleration factor. On the other hand, T1 maps for P-BLIP remain relatively constant for sequence lengths larger than 100 (Fig. 3a) and all acceleration factors (Fig. 3b), whilst the performance of MRF and BLIP increases with the sequence length and lower acceleration factors. The reason for these results is twofold. First, the IR-bSSFP sequence is mostly T1-weighted, favoring a better T1 matching over T2 matching for all methods. Second, a trained dictionary containing a longer sequence, but fixed K, is less flexible, and if the trained dictionary does not exactly contain the ground truth values, the quantitative error will be higher.

Table 1 indicates the performance of P-BLIP for different patch sizes in comparison to the performance of MRF and BLIP. A spatial patch size of $P = 1 \times 1$ implies that the training dataset was created from voxel-wise temporal evolutions and that the trained dictionary is a clustered version of the temporal dictionary. It can be seen that clustering a temporal dictionary alone improves the reconstruction with respect to MRF and BLIP, and that the spatiotemporal dictionary further improves these results for $P = 3 \times 3$. At larger spatial patch sizes the results begin to decline, indicating that the cluster size of $K = 200$ is not enough to capture the entire spatial variability of the parametric maps.

4   Conclusions

This work presents a novel patch-based reconstruction scheme for MRF consistent with the theory of CS. It is based on a spatiotemporal signal model and relies on the training of the corresponding dictionary from a set of examples. This patch-based scheme shows improved performance for shorter pulse sequences and at higher acceleration factors, leading to an increased efficiency of parameter mapping with MRF.

An important discussion point of our approach is the size of the dictionary in terms of space, time, and atoms. Larger spatial patches allow, in theory, for the acquisition of less temporal points, but the amount of atoms in the dictionary should in turn be large enough to account for large spatial variability. We have seen from our results that a dictionary size of $K = 200$ is not enough for spatial patch sizes larger than 3×3 for structures in the brain. A potencial solution to this shortcoming might be to make K dependant on the atom length or arbitrarily large at the cost of computational complexity. This point is currently under investigation and future work will focus on extending the method to incorporate 3D spatial patches and applying it to real datasets.

References

1. Aubert-Broche, B., Evans, A.C., Collins, L.: A new improved version of the realistic digital brain phantom. NeuroImage **32**, 138–145 (2006)
2. Aubert-Broche, B., Griffin, M., Pike, G.B., Evans, A.C., Collins, D.L.: Twenty new digital brain phantoms for creation of validation image data bases. IEEE Trans. Med. Imaging **25**(11), 1410–1416 (2006)
3. Davies, M., Puy, G., Vandergheynst, P., Wiaux, Y.: A compressed sensing framework for magnetic resonance fingerprinting. SIAM J. Imaging Sci. **7**(4), 2623–2656 (2014)
4. Doneva, M., Börnert, P., Eggers, H., Stehning, C., Sénégas, J., Mertins, A.: Compressed sensing reconstruction for magnetic resonance parameter mapping. Magn. Reson. Med. **64**, 1114–1120 (2010)
5. Donoho, D.L.: Compressed sensing. IEEE Trans. Inf. Theor. **52**, 1289–1306 (2006)
6. Ma, D., Gulani, V., Seiberlich, N., Liu, K., Sunshine, J.L., Duerk, J.L., Griswold, M.A.: Magnetic resonance fingerprinting. Nature **495**, 187–192 (2013)
7. Ravishankar, S., Bresler, Y.: MR image reconstruction from highly undersampled k-space data by dictionary learning. IEEE Trans. Med. Imaging **30**(5), 1028–1041 (2011)
8. Wang, Z., Bovik, A.C., Sheikh, H.R., Simoncelli, E.P.: Image quality assessment: from error visibility to structural similarity. IEEE Trans. Image Proc. **13**, 600–612 (2004)

5.1.3   *Simultaneous Parameter Mapping, Modality Synthesis, and Anatomical Labeling of the Brain with MR Fingerprinting*

Peer-reviewed Conference Paper

Authors: PA. Gómez, M. Molina-Romero, C. Ulas, G. Buonincontri, JI. Sperl, DK. Jones, MI. Menzel, BH. Menze

Abstract: Magnetic Resonance Fingerprinting (MRF) quantifies various properties simultaneously by matching measurements to a dictionary of precomputed signals. We propose to extend the MRF framework by using a database to introduce additional parameters and spatial characteristics to the dictionary. We show that, with an adequate matching technique which includes an update of selected fingerprints in parameter space, it is possible to reconstruct parametric maps, synthesize modalities, and label tissue types at the same time directly from an MRF acquisition. We compare (1) relaxation maps from a spatiotemporal dictionary against a temporal MRF dictionary, (2) synthetic diffusion metrics versus those obtained with a standard diffusion acquisition, and (3) anatomical labels generated from MRF signals to an established segmentation method, demonstrating the potential of using MRF for multiparametric brain mapping.

Contribution of thesis author: Algorithmic development and implementation, experimental design, data analysis, manuscript preparation and editing.

Simultaneous Parameter Mapping, Modality Synthesis, and Anatomical Labeling of the Brain with MR Fingerprinting

Pedro A. Gómez[1,2,4( )], Miguel Molina-Romero[1,2,4], Cagdas Ulas[1,2], Guido Bouincontri[3], Jonathan I. Sperl[2], Derek K. Jones[4], Marion I. Menzel[2], and Bjoern H. Menze[1]

[1] Computer Science, Technische Universität München, Munich, Germany
`pedro.gomez@tum.de`
[2] GE Global Research, Munich, Germany
[3] INFN Pisa, Pisa, Italy
[4] CUBRIC School of Psychology, Cardiff University, Cardiff, UK

Abstract. Magnetic resonance fingerprinting (MRF) quantifies various properties simultaneously by matching measurements to a dictionary of precomputed signals. We propose to extend the MRF framework by using a database to introduce additional parameters and spatial characteristics to the dictionary. We show that, with an adequate matching technique which includes an update of selected fingerprints in parameter space, it is possible to reconstruct parametric maps, synthesize modalities, and label tissue types at the same time directly from an MRF acquisition. We compare (1) relaxation maps from a spatiotemporal dictionary against a temporal MRF dictionary, (2) synthetic diffusion metrics versus those obtained with a standard diffusion acquisition, and (3) anatomical labels generated from MRF signals to an established segmentation method, demonstrating the potential of using MRF for multiparametric brain mapping.

1 Introduction

Magnetic resonance fingerprinting (MRF) is an emerging technique for the simultaneous quantification of multiple tissue properties [7]. It offers absolute measurements of the T1 and T2 relaxation parameters (opposed to traditional weighted imaging) with an accelerated acquisition, leading to efficient parameter mapping. MRF is based on matching measurements to a dictionary of precomputed signals that have been generated for different parameters. Generally, the number of atoms in the dictionary is dictated by the amount of parameters, and the range and density of their sampling. As an alternative to continuous sampling of the parameter space, one could use measured training examples to learn the dictionary, reducing the number of atoms to only feasible parameter combinations [2]. In this work, we propose to use a database of multi-parametric datasets to create the dictionary, presenting two new features of MRF that can be achieved simultaneously with relaxation mapping: modality synthesis and automatic labeling of the corresponding tissue.

In this extended application of MRF towards image synthesis and segmentation, we follow a direction that has recently gained attention in the medical image processing literature [1,3,5,6,9,10]. The working principle behind these methods is similar: given a source image and a multi-contrast database of training subjects, it is possible to generate the missing contrast (or label) of the source by finding similarities within the database and transferring them to create a new image. The search and synthesis strategy can take several forms: it could be iterative to incorporate more information [10]; can be optimized for multiple scales and features [1]; may include a linear combination of multiple image patches [9]; or be configured to learn a nonlinear transform from the target to the source [5]. There have been several applications of synthetic contrasts, including inter-modality image registration, super-resolution, and abnormality detection [3,5,6,9,10]. Furthermore, in addition to the creation of scalar maps in image synthesis, similar techniques can be used for mapping discrete annotations; for example, in the segmentation of brain structures [1].

Inspired by these ideas, we present a method for synthesizing modalities and generating labels from magnetic resonance fingerprints. It relies on the creation of a spatiotemporal dictionary [2] and its mapping to different parameters. Specifically, in addition to the physics-based mapping of MRF signals to the T1 and T2 relaxation parameters, we train empirical functions for a mapping of the signals to diffusion metrics and tissue probabilities. We show that we can achieve higher efficiency relaxation mapping, and demonstrate how the use of a spatiotemporal context improves the accuracy of synthetic mapping and labeling.

We see three main contributions to our work. (1) We present a framework for creating a spatiotemporal MRF dictionary from a multi-parametric database (Sect. 2.1). (2) We generalize fingerprint matching and incorporate a data-driven update to account for correlations in parameter space, allowing for the simultaneous estimation of M different parameters from any fingerprinting sequence (Sect. 2.2). (3) Depending on the nature of the m-th parameter, we call it a mapping, synthesis, or labeling, and show results for all three applications (Sect. 3.1). This is the first attempt - to the best of our knowledge - to simultaneously map parameters, synthesize diffusion metrics, and estimate anatomical labels from MR fingerprints.

2   Methods

Let $\mathcal{Q} = \{Q_s\}_{s=1}^{S}$ represent a database of spatially aligned parametric maps for S subjects, where each subject $Q_s \in \mathbb{R}^{N \times M}$ contains a total of $N = N_i \times N_j \times N_k$ voxels and M maps. Every map represents an individual property, and can originate from a different acquisition or modality, or even be categorical. Our database includes the quantitative relaxation parameters T1 and T2; a non-diffusion weighted image (S0); the diffusion metrics mean diffusivity (MD), radial diffusivity (RD), and fractional anisotropy (FA); and probability maps for three tissue classes: gray matter (GM), white matter (WM), and cerebrospinal fluid (CSF). Thus, for every subject $Q_s = \{\text{T1}, \text{T2}, \text{S0}, \text{MD}, \text{RD}, \text{FA}, \text{GM}, \text{WM}, \text{CSF}\}$. We use this database to create a spatiotemporal MRF dictionary as follows.

2.1   Building a Spatiotemporal MRF Dictionary

With the relaxation parameters T1 and T2 and knowledge of the sequence variables, it is possible to follow the extended phase graph (EPG) formalism to simulate the signal evolution of a *fast imaging with steady state precession MRF* (FISP-MRF) pulse sequence [4]. In EPG the effects of a sequence on a spin system are represented by operators related to radio-frequency pulses, relaxation, and dephasing due to gradient moments. Therefore, for every voxel in all subjects, application of the EPG operators leads to a dictionary $D \in \mathbb{C}^{NS \times T}$ with a total of T temporal points (see Fig. 1).
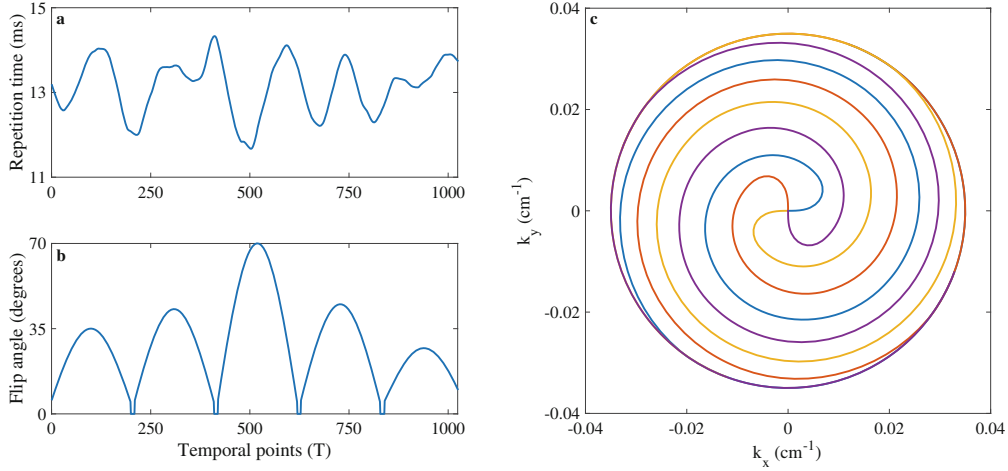
Fig. 1. FISP-MRF acquisition sequence. **a**, Repetition times following a Perlin noise pattern. **b**, Flip angles of repeating sinusoidal curves. **c**, k-space trajectory of four different spiral interleaves, 32 interleaves are required for full k-space coverage.

We further process the dictionary to incorporate spatial information by expanding each voxel with its 3D spatial neighborhood of dimension $P = P_i \times P_j \times P_k$ and compressing the temporal dimension into its first V singular vectors [8]. This results in a compressed spatiotemporal dictionary $\tilde{D} \in \mathbb{C}^{NS \times PV}$. Finally, we define a search window $W_n = W_i \times W_j \times W_k$ around every voxel n, limiting the dictionary per voxel to $\tilde{D}_n \in \mathbb{C}^{W_n S \times PV}$. The choice for a local search window has a two-fold motivation: it reduces the number of computations by decreasing the search space and it increases spatial coherence for dictionary matching [10].

Applying subject concatenation, patch extraction, and search window reduction on the database $\mathcal{Q}$ leads to a voxel-wise spatio-parametric matrix $\tilde{R}_n \in \mathbb{R}^{W_n S \times PM}$. For simplicity, we will use D and R instead of $\tilde{D}_n$ and $\tilde{R}_n$, where every dictionary entry $d_c \in \mathbb{C}^{PV}$ has its corresponding matrix entry $r_c \in \mathbb{R}^{PM}$.

2.2   Dictionary Matching and Parameter Estimation

MRF aims to simultaneously estimate several parametric maps from undersampled data. This is achieved by reconstructing an image series and matching it

to the dictionary. We reconstruct V singular images [8] and extract 3D patches from them to create the patch-based matrix $X \in \mathbb{C}^{N \times PV}$. At every voxel x_n, we find the set $\mathcal{M}_n$ of the C highest correlated dictionary entries d_c, $c = 1, .., C$, by:

$$\mathcal{M}_n = \{d_c \in D : \rho(x_n, d_c) > \tau_C\} \tag{1}$$

with the threshold value τ_C such that $|\mathcal{M}| = C$ and

$$\rho(x, d) = \frac{\langle x, d \rangle}{\|x\|_2 \|d\|_2}. \tag{2}$$

Making use of the selected entries d_c and the corresponding parametric vectors r_c, an estimated value $\tilde{q}_{n,m}$ at voxel location n in map m is determined by the weighted average of the correlation between every entry d_c and the signals x_p within Ω_n, the spatial neighborhood of n:

$$\tilde{q}_{n,m} = \frac{\sum_{p \in \Omega_n} \sum_c \rho(x_p, d_c) r_{c,pm}}{P \sum_c \rho(x_p, d_c)}, \tag{3}$$

where $r_{c,pm}$ indexes the quantitative value of voxel p centered around atom c in map m. Repeating this procedure for every voxel creates an estimate $\tilde{Q}$ of all of the parametric maps, including synthetic modalities and anatomical labels.

Data-Driven Updates. Ye et al. [10] proposed the use of intermediate results to increase spatial consistency of the synthetic maps. We take a similar approach, and define a similarity function relating image space and parameter space:

$$f(x, d, r, q, \alpha) = (1 - \alpha)\rho(x, d) + \alpha\rho(q, r) \tag{4}$$

where α controls the contributions of the correlations in image and parameter space. The selected atoms are now determined by

$$\mathcal{M}_n = \{d_c \in D, r_c \in R : f(x_n, d_c, \tilde{q}_n, r_c, \alpha) > \tau_C\}. \tag{5}$$

In the first iteration $\alpha = 0$ as we have no information on the map $\hat{Q}$ for our subject. In a second iteration we increase α, adding weight to the similarities in parameter space and compute Eq. 5 again to find a new set of dictionary atoms. The final version of the maps is given by a modified version of Eq. 3:

$$\hat{q}_{n,m} = \frac{\sum_{p \in \Omega_n} \sum_c f(x_p, d_c, \tilde{q}_n, r_c, \alpha) r_{c,pm}}{P \sum_c f(x_p, d_c, \tilde{q}_n, r_c, \alpha)}. \tag{6}$$

This procedure is essentially a 3D patch-match over a V-dimensional image space and M-dimensional parameter space, where the matching patches are combined by their weighted correlation to create a final result.
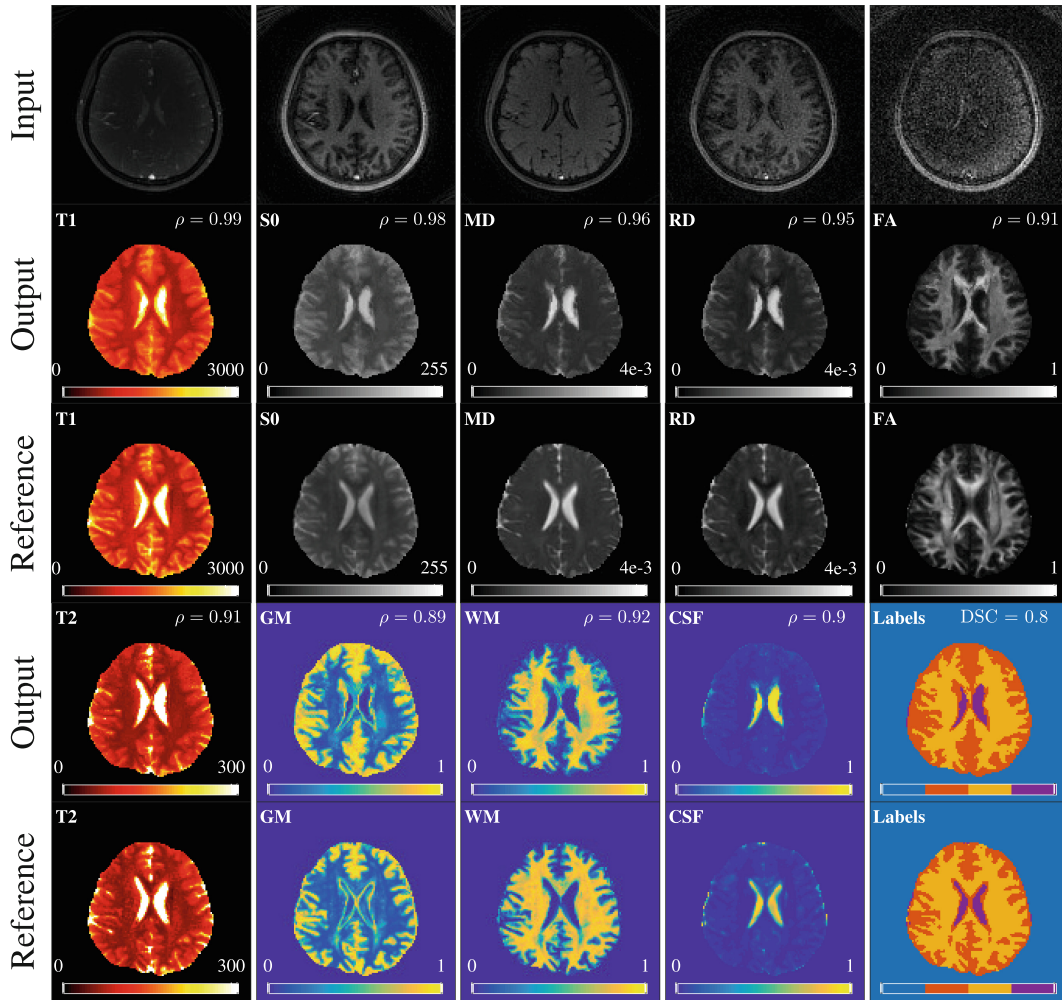
Fig. 2. Exemplary results of one test subject with $P = 3 \times 3 \times 3$. The upper row displays the first five singular images; while the second and fourth row show the output for different parametric maps and the correlation to the reference image, displayed in the third and fifth row, respectively. Additionally, the last column in rows four and five shows labels obtained from selecting the tissue class with highest probability and the dice similarity coefficient (DSC) from the output labels to the reference. The bar underneath represents, from left to right, background, GM, WM, and CSF; and the DSC was computed from the GM, WM, and CSF labels. T1 and T2 scale is displayed in ms; S0 is qualitatively scaled to 255 arbitrary units; MD and RD are in mm^2/s; FA, GM, WM, and CSF are fractional values between zero and one.

2.3 Data Acquisition and Pre-processing

We acquired data from six volunteers with a FISP-MRF pulse sequence [4] on a 3T GE HDx MRI system (GE Medical Systems, Milwaukee, WI) using an eight channel receive only head RF coil. After an initial inversion, a train of $T = 1024$ radio-frequency pulses with varying flip angles and repetition times following a Perlin noise pattern [4] was applied (see Fig. 1). We use one interleave of a zero-moment compensated variable density spiral trajectory per repetition, requiring

32 interleaves to sample a 22×22 cm field of view (FOV) with 1.7 mm isotropic resolution. We acquired 10 slices per subject with a scan time of 13.47 seconds per slice, performed a gridding reconstruction onto a 128×128 Cartesian grid, projected the data into SVD space, and truncated it to generate $V = 10$ singular images. The choice of $V = 10$ was motivated by the energy ratio, as this was the lowest rank approximation which still yielded an energy ratio of 1.0 [8]. The singular images were matched to a MRF dictionary comprising of T1 values ranging from 100 to 6,000 ms; and T2 values ranging from 20 ms to 3,000 ms.

In addition, we scanned each volunteer with a diffusion weighted imaging (DWI) protocol comprising of 30 directions in one shell with $b = 1000$ s/mm^2. The FOV, resolution, and acquired slices were the same as with MRF-FISP, resulting in a 15 min scan. We applied FSL processing to correct for spatial distortions derived from EPI readouts, skull strip, estimate the diffusion tensor and its derived metrics MD, RD, and FA; and used the non-diffusion weighted image S0 to compute probability maps of three tissue types (GM, WM, CSF) using [11]. Finally, we applied registration across all subjects to create the database.

3   Experiments and Results

For every subject, we performed a leave-one-out cross validation, wherein the dictionary was constructed from five subjects and the remaining subject was used as a test case. Following the procedure described in Sect. 2.2, we created a database of nine parametric maps (T1,T2,S0,MD,RD,FA,GM,WM,CSF) and compared the estimated metrics to the reference by their correlation.

We explored the influence of the window size W_n, the number of entries C, and the α on the estimated maps. We found correlations increased with diminishing returns as W_n increased, while adding more entries yielded smoother maps. Correlations were higher after a second iteration of data-driven updates with $\alpha > 0$, irrespective of the value of α. Nonetheless, variations of these parameters didn't have a significant effect on the overall results. To investigate the impact of using spatial information, we repeated the experiment for spatial patch sizes of $P = 1 \times 1 \times 1$, $3 \times 3 \times 3$, and $5 \times 5 \times 5$. For these experiments we used $W_n = 11 \times 11 \times 11$, $C = 5$, $\alpha = 0.5$, and two iterations.

3.1   Results

The reference T1 and T2 maps were estimated from a FISP-MRF sequence with a temporal dictionary, while we used a spatiotemporal dictionary with varying spatial patches. Estimated T1 and T2 maps were consistent with the reference, with increasing spatial smoothness for larger spatial patches. This also lead to a decrease in correlation to the reference, most notably in T2 estimation (see Fig. 3a–b), which could also be attributed noisier T2 estimates. In future experiments we will rely on standard relaxation mapping for reference comparison.

The synthetic S0 and diffusion metrics MD, RD, and FA show spatial coherence, achieving correlation values over 0.90 with respect to a standard DWI
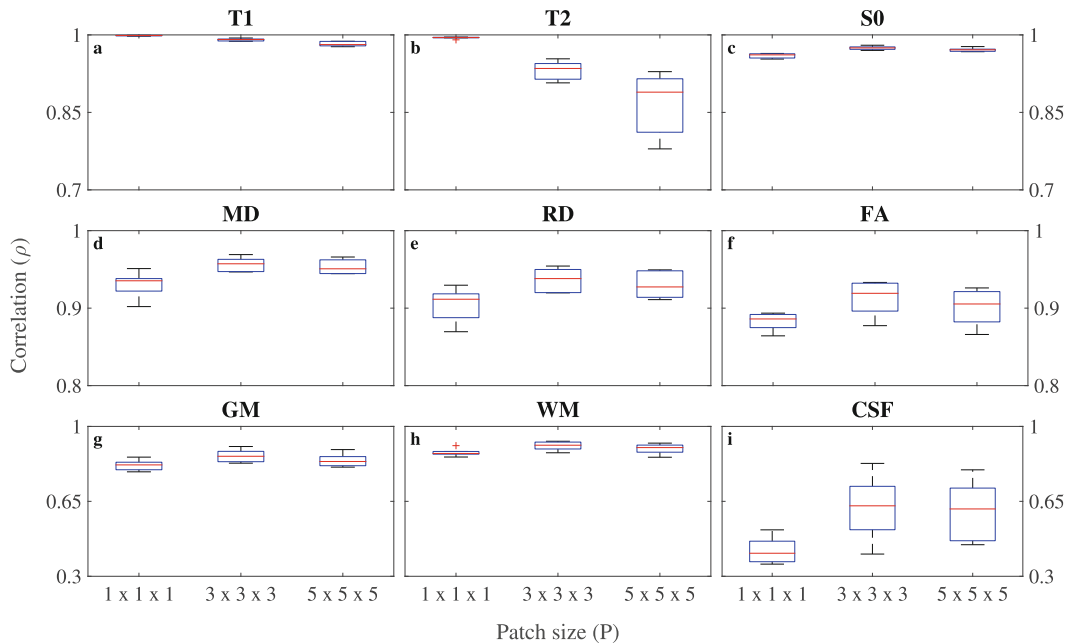
Fig. 3. Correlation as a function of spatial patches for all subjects. **a–b**, T1 and T2 parameter mapping. **c–f**, Synthesis of S0 and diffusion metrics. **g–i**, Tissue labeling.

acquisition (Fig. 2). Similar to [10], we found that FA maps were generally the least correlated to the reference. This is due to the fact that diffusion encoding in DWI acts as a proxy for underlying tissue anisotropy, whereas the measured fingerprints are not diffusion sensitive, failing to exactly recover directionality present in FA. In fact, the higher the directionality encoded in a given modality, the lower the correlation to the reference ($\overline{\rho_{S0}} > \overline{\rho_{MD}} > \overline{\rho_{RD}} > \overline{\rho_{FA}}$). Furthermore, for all cases in modality synthesis, incorporating spatial information generated increased consistency and higher correlated results (Fig. 3c–f).

Figure 2 shows the visual similarity between tissue probability maps obtained directly as an output from matching and those computed with [11] and the labels obtained by selecting the class with the highest probability. As with modality synthesis, anatomical labels improved when spatial information was taken into account (Fig. 3g–i). Particularly in CSF, incorporation of spatial information eliminated false positives, yielding better quality maps. On the other hand, thresholding of probability maps lead to an overestimation of GM labels, notably at tissue boundaries. Labeling at tissue boundaries could benefit from higher resolution scans and a multi-channel reference segmentation.

4   Discussion

This work proposes to replace a simulated temporal MRF dictionary with a spatiotemporal dictionary that can be learnt from data, increasing the efficiency of relaxation parameter mapping, and enabling the novel applications of modality synthesis and anatomical labeling. In terms of methodology, we borrow concepts

586   P.A. Gómez et al.

such as the search window and parameter space regularization from the image segmentation and synthesis literature [1,3,10], but change the input to a V-dimensional image space and the output to an M-dimensional parameter space, making it applicable to MRF. Moreover, our framework is valid for any MR sequence, provided signal evolutions can be computed from the training data.

Results indicate that it is possible to use MRF to simultaneously map T1 and T2 parameters, synthesize modalities, and classify tissues with high consistency with respect to established methods. While our method allows us to circumvent post-processing for diffusion metric estimation and tissue segmentation, it is important to note that changes in synthetic diffusion maps can only be propagated from the information available in the database. Therefore, creating the dictionary from pathology and exploring advanced learning techniques capable of capturing these changes is the subject of future work.

References

1. Giraud, R., Ta, V.T., Papadakis, N., et al.: An optimized PatchMatch for multi-scale and multi-feature label fusion. NeuroImage **124**, 770–782 (2016)
2. Gómez, P.A., Ulas, C., Sperl, J.I., et al.: Learning a spatiotemporal dictionary for magnetic resonance fingerprinting with compressed sensing. In: MICCAI Patch-MI Workshop, vol. 9467, pp. 112–119 (2015)
3. Iglesias, J.E., Konukoglu, E., Zikic, D., et al.: Is synthesizing MRI contrast useful for inter-modality analysis? MICCAI **18**(9), 1199–1216 (2013)
4. Jiang, Y., Ma, D., Seiberlich, N., et al.: MR fingerprinting using fast imaging with steady state precession (FISP) with spiral readout. MRM **74**(6), 1621–1631 (2014)
5. Jog, A., Carass, A., Roy, S., et al.: MR image synthesis by contrast learning on neighborhood ensembles. Med. Image Anal. **24**(1), 63–76 (2015)
6. Konukoglu, E., van der Kouwe, A., Sabuncu, M.R., Fischl, B.: Example-based restoration of high-resolution magnetic resonance image acquisitions. In: Mori, K., Sakuma, I., Sato, Y., Barillot, C., Navab, N. (eds.) MICCAI 2013, Part I. LNCS, vol. 8149, pp. 131–138. Springer, Heidelberg (2013)
7. Ma, D., Gulani, V., Seiberlich, N., et al.: Magnetic resonance fingerprinting. Nature **495**, 187–192 (2013)
8. McGivney, D., Pierre, E., Ma, D., et al.: SVD compression for magnetic resonance fingerprinting in the time domain. IEEE TMI **0062**, 1–13 (2014)
9. Roy, S., Carass, A., Prince, J.L.: Magnetic resonance image example based contrast synthesis. IEEE TMI **32**(12), 2348–2363 (2013)
10. Ye, D.H., Zikic, D., Glocker, B., et al.: Modality propagation: coherent synthesis of subject-specifc scans with data-driven regularization. MICCAI **8149**, 606–613 (2013)
11. Zhang, Y., Brady, M., Smith, S.: Segmentation of brain MR images through a hidden Markov random field model and the expectation-maximization algorithm. IEEE TMI **20**, 45–57 (2001)

5.2 RELEVANT PEER-REVIEWED ABSTRACTS

The abstracts in this section show novel methods in tissue segmentation and parameter quantification. In 3D Magnetic Resonance Fingerprinting with a Clustered Spatiotemporal Dictionary, an unsupervised learning approach to create an MRF dictionary is presented. Spiral Keyhole Imaging for MR Fingerprinting demonstrates an effective unaliasing technique based on k-space viewsharing. Fast, Volumetric and Silent Multi-contrast Zero Echo Time Imaging shows a method for silent, distortion free, and 3D multiparametric mapping. Finally, Accelerated Parameter Mapping with Compressed Sensing: an Alternative to MR Fingerprinting removes many unnecessary components in MRF to present an optimized alternative — QTI.

5.2.1   *3D Magnetic Resonance Fingerprinting with a Clustered Spatiotemporal Dictionary*

Peer-reviewed Conference Abstract

Authors: PA. Gómez, G. Buonincontri, M. Molina-Romero, C. Ulas, JI. Sperl, MI. Menzel, BH. Menze

Abstract: We present a method for creating a spatiotemporal dictionary for Magnetic Resonance Fingerprinting (MRF). Our technique is based on the clustering of multi-parametric spatial kernels from training data and the posterior simulation of a temporal fingerprint for each voxel in every cluster. We show that the parametric maps estimated with a clustered dictionary agree with maps estimated with a full dictionary, and are also robust to undersampling and shorter sequences, leading to increased efficiency in parameter mapping with MRF.

Contribution of thesis author: Algorithmic development and implementation, experimental design, data analysis, abstract preparation and editing.

3D Magnetic Resonance Fingerprinting with a Clustered Spatiotemporal Dictionary

Pedro A Gómez[1,2], Guido Bounincontri[3], Miguel Molina-Romero[1,2], Cagdas Ulas[1,2], Jonathan I Sperl[2], Marion I Menzel[2], Bjoern H Menze[1]

[1]Computer Science, Technische Universität München, Munich, Germany
[2]GE Global Research, Munich, Germany
[3]INFN Pisa, Pisa, Italy

Abstract. We present a method for creating a spatiotemporal dictionary for magnetic resonance fingerprinting (MRF). Our technique is based on the clustering of multi-parametric spatial kernels from training data and the posterior simulation of a temporal fingerprint for each voxel in every cluster. We show that the parametric maps estimated with a clustered dictionary agree with maps estimated with a full dictionary, and are also robust to undersampling and shorter sequences, leading to increased efficiency in parameter mapping with MRF.

1 Purpose

Magnetic resonance fingerprinting (MRF) allows for the simultaneous quantification of multiple tissue properties via the matching of acquired signals to a precomputed dictionary, created by sampling a wide range of the parameter space [4]. As the parameters of interest increase, so does the dictionary size, leading to long reconstruction times. One possibility for overcoming this limitation is to use a clustered dictionary with both spatial and temporal information [2]. This work aims at increasing MRF efficiency by using a clustered spatiotemporal dictionary and incorporating it into a MRF pipeline that includes B1 mapping and a view-sharing (VS) anti-aliasing strategy [1].

2 Methods

We tested our approach using 3D MRF data of a Lister-hooded adult rat brain adult acquired with a Bruker BioSpec 47/40 system (Bruker Inc., Ettlingen, Germany) [1]. The sequence was based on SSFP-MRF [3] with Cartesian sampling, $T = 1000$ shots, and 0.5 mm isotropic resolution. A dictionary $\mathbf{D} \in \mathbb{C}^{L \times T}$ was simulated using extended phase graphs with the following ranges: T1 from 100ms to 3,000ms in 20ms steps; T2 from 20ms to 100ms in 5ms steps and from 100 to 500ms in 10ms steps; and B1 as a flip angle factor from 50% to 150% in 1% steps, resulting in a dictionary of size 840522×1000. The acquired data was matched to the dictionary to create a reference dataset.

2   Gómez et al.
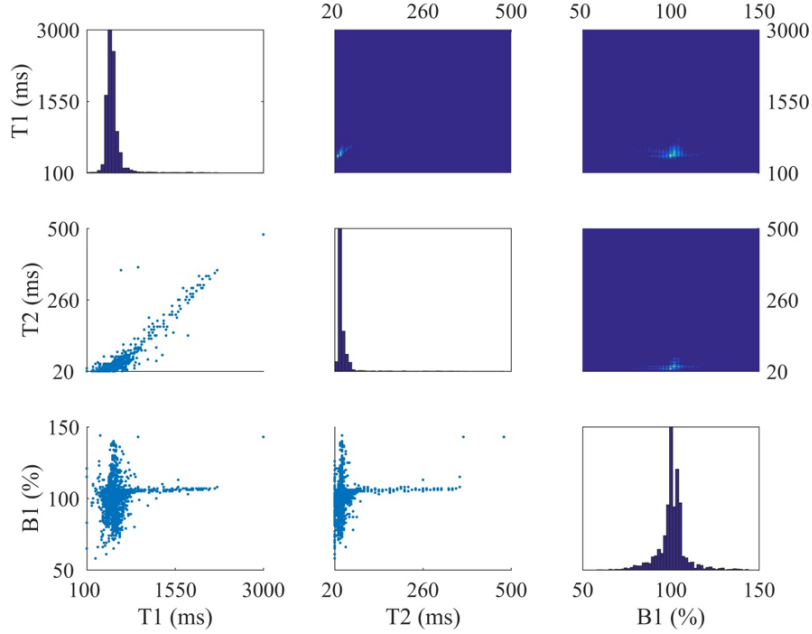
Fig. 1. Parameter distribution obtained from selected slices in the left hemisphere used as a training dataset. The upper triangle displays density plots, the diagonal histograms, and the lower triangle scatter plots. Note that parameters approach a Gaussian distribution and are densely scattered within a specific range.

Exploiting symmetry of the brain, the reference dataset was divided along the medial longitudinal fissure, separating the left and right hemisphere. The estimated parametric T1, T2 and B1 maps of the left hemisphere (see Fig. 1) were used to create spatiotemporal dictionaries of different sizes by first clustering multi-parametric (T1,T2,B1) spatial kernels using k-means and subsequently simulating the temporal signal of every voxel in each cluster. The right hemisphere of the reference dataset was then matched to dictionaries with spatial kernel sizes of $P = 1 \times 1 \times 1$ (clustered only), $P = 3 \times 3 \times 3$ and $P = 5 \times 5 \times 5$ (see Fig. 2).

We hypothesize that a dictionary that contains only feasible parameter combinations and spatial information should enable acceleration in both space and time. We test this by samplingless k-space points using a Gaussian mask in the phase encode directions with different acceleration factors (Figs. 3-4), and by reducing the sequence length (Fig. 4). Undersampled datasets were reconstructed with the original dictionary template matching (TM) [4]and with our VS approach, and compared to the reference dataset by their similarity index (SSIM) [5]. Furthermore, we study the amount of clusters required to accurately capture the entire spatio-parametric variability in our dataset by evaluating the mean

3D MRF with a Clustered Spatiotemporal Dictionary   3
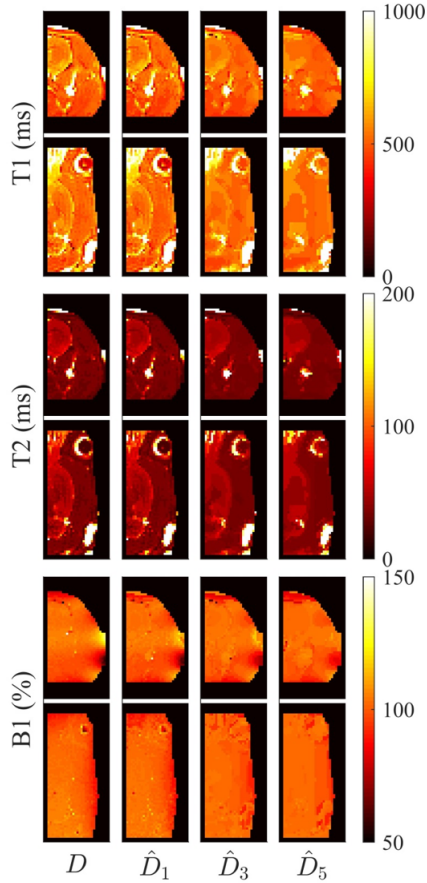
Fig. 2. Comparison of the estimated T1, T2 and B1 parametric maps from the fully sampled dataset with a temporal dictionary $\mathbf{D} \in \mathbb{C}^{L \times T}$ and three clustered dictionaries $\hat{\mathbf{D}}_{\sqrt[3]{P}} \in \mathbb{C}^{K \times TP}$ with $K = 300$, $T = 1000$, and $P = 1 \times 1 \times 1$, $3 \times 3 \times 3$, and $5 \times 5 \times 5$. Spatial smoothing obtained with and is achieved by averaging all contributing patches to a given voxel.

square error (MSE) of the training and testing data for different spatial kernels (Fig. 5).

3   Results

Figure 1 shows how the estimated parameters approximate a Gaussian distribution, and are scattered in a restricted range within the parameter space. Hence, using dictionaries trained from this distribution yields parametric maps that agree with maps estimated using the full dictionary (see Fig. 2). Figure 3 com-

4   Gómez et al.
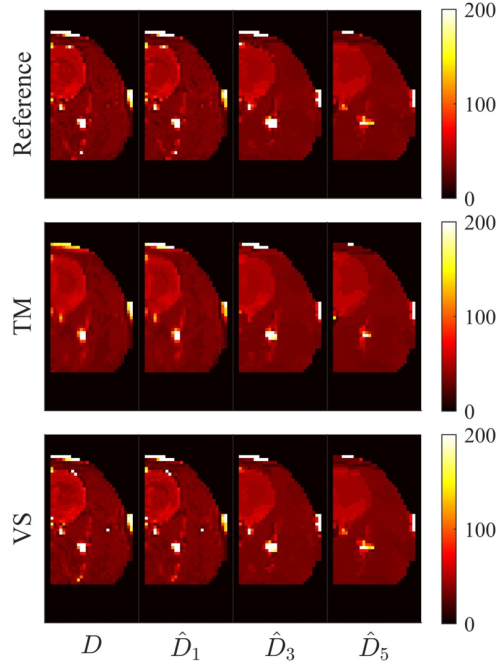
Fig. 3. Estimated T2 parametric maps from fully sampled reference data and data undersampled with an acceleration factor R=5 (20% of k-space) for two different reconstruction methods: template matching (TM) and view-sharing (VS). The clustered dictionaries $\hat{\mathbf{D}}_{\sqrt[3]{P}} \in \mathbb{C}^{K \times TP}$ consisted of $K = 300$, $T = 1000$, and $P = 1 \times 1 \times 1$, $3 \times 3 \times 3$, and $5 \times 5 \times 5$.

pares the reconstructed maps with 20% sampling of k-space, where $\mathbf{D}$ and $\hat{\mathbf{D}}_1$ combined with VS are the most similar to the reference dataset. Figure 4 shows smaller variation of the clustered dictionaries with undersampling, though having less similarity to the reference dataset in fully sampled cases. Fig. 5 evidences how the training error decreases for more clusters in all cases, while the testing error only decreases continuously for $\hat{\mathbf{D}}_1$.

4   Discussion

We use spatiotemporal dictionaries of different spatial kernel sizes with $K = 300$ clusters (0.036% of the original dictionary size) and obtain comparable parametric maps (see Fig. 2). Furthermore, Figs. 3-4 show that clustered dictionaries, especially if they contain spatial information, are more robust to undersampling and shorter sequences. Conversely, the spatial smoothing achieved with larger spatial kernels along with the constant testing errors for increasing clusters in Fig. 5 indicate that the training data does not accurately represent the testing
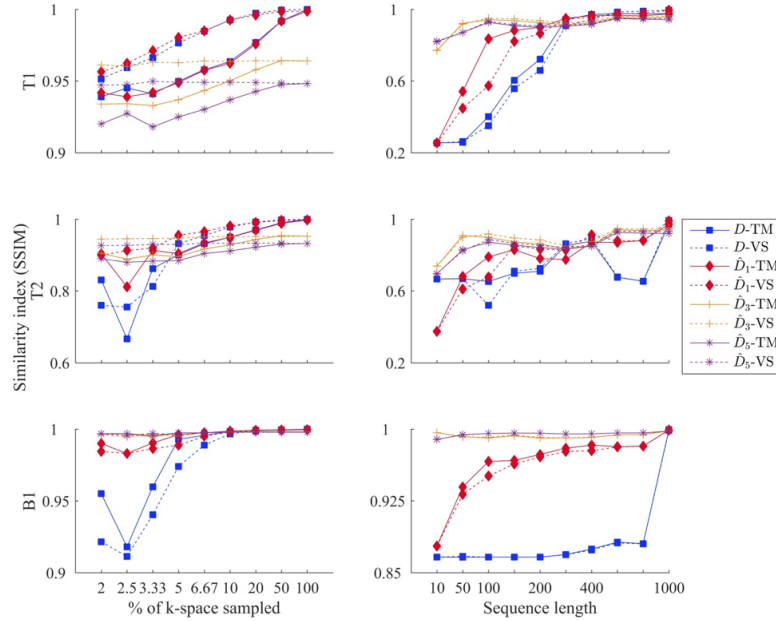
Fig. 4. Acceleration in space and time. The left column displays the SSIM for each of the dictionaries and two reconstruction methods: template matching (TM) and view-sharing (VS) for different levels of k-space sampling. The right column shows the estimated SSIM for increasing sequence length and an acceleration factor R=5 (20% of k-space).

data for kernel sizes larger than $P = 3 \times 3 \times 3$. In fact, the amount of training observations required and the corresponding size of the dictionary in terms of space, time, and clusters, leads to two important discussion points: 1) using clustering enables higher acceleration, at the expense of disregarding parameter combinations that are not present in the training set (e.g. pathology); and 2) adding spatial information increases the dimensionality of the dictionary, requiring approaches that can effectively deal with matching in high dimensional spaces.

5   Conclusions

We propose a method to create clustered MRF dictionaries and show the added benefit of combining it with a view-sharing strategy to enable both accelerated acquisitions by undersampling, and accelerated reconstructions through dictionary compression. Further investigation of data-driven approaches could pave the way towards tissue and disease specific dictionaries in clinical settings.

6   Gómez et al.
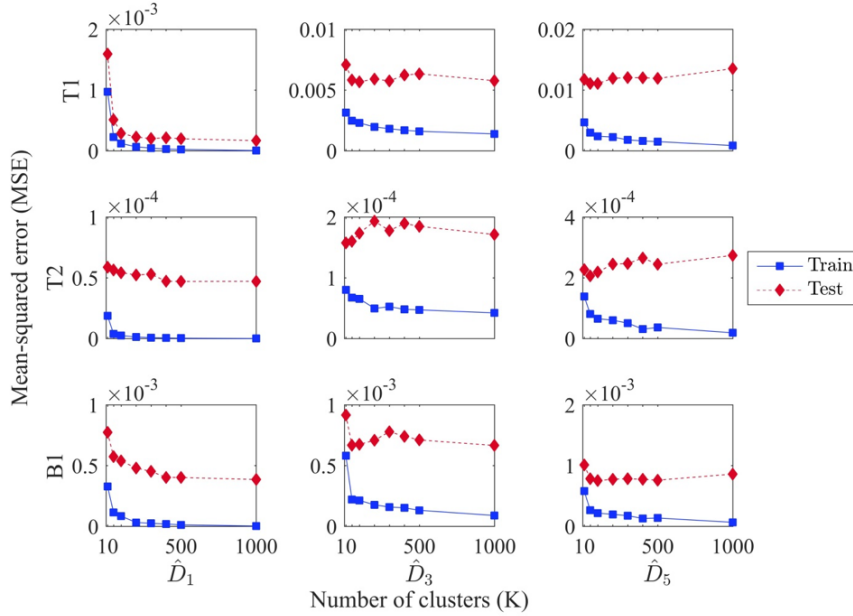
Fig. 5. Training and testing error for different cluster sizes K from the fully sampled reference dataset. For $\hat{\mathbf{D}}_1$ both the training and testing error reduce with an increasing number of clusters, while testing errors for $\hat{\mathbf{D}}_3$ and $\hat{\mathbf{D}}_5$ do not change significantly with increasing clusters.

References

1. Buonincontri, G., Sawiak, S.: Three-dimensional MR fingerprinting with simultaneous B1 estimation. Magnetic Resonance in Medicine 00, 1–9 (2015)
2. Gómez, P.A., Ulas, C., Sperl, J.I., Sprenger, T., Molina-Romero, M., Menzel, M.I., Menze, B.H.: Learning a spatiotemporal dictionary for magnetic resonance fingerprinting with compressed sensing. MICCAI Patch-MI Workshop 9467, 112–119 (2015)
3. Jiang, Y., Ma, D., Seiberlich, N., Gulani, V., Griswold, M.A.: MR Fingerprinting Using Fast Imaging with Steady State Precession (FISP) with Spiral Readout. MRM (2014)
4. Ma, D., Gulani, V., Seiberlich, N., Liu, K., Sunshine, J.L., Duerk, J.L., Griswold, M.A.: Magnetic resonance fingerprinting. Nature 495, 187–192 (2013)
5. Wang, Z., Bovik, A.C., Sheikh, H.R., Simoncelli, E.P.: Image quality assessment: From error visibility to structural similarity. IEEE Transactions on Image Processing 13, 600–612 (2004)

5.2.2 *Spiral Keyhole Imaging for MR Fingerprinting*

Peer-reviewed Conference Abstract

Authors: G. Buonincontri, L. Biagi, **PA. Gómez**, R. Schulte, M. Tosetti

In: *Proc Intl Soc Mag Reson Med* (2017) [14]

Abstract: Magnetic Resonance Fingerprinting (MRF) can be used for a fast and quantitative estimation of physical parameters in MRI. For the fast acquisition of MRF, common approaches have used non-Cartesian sampling of k-space. Here, we introduce a method for non-iterative anti-aliasing of the spiral MRF time series, based on the concept of keyhole imaging. Our approach does not change acquisition or dictionary creation and matching procedures. As frames require only minimal density compensation in k-space, noise amplification during reconstruction is reduced. After applying our algorithm, individual images from the MRF time series are artifact-free and clearer parameter maps are obtained in a shorter time while preserving the accurate quantification of MRF.

Contribution of thesis author: Algorithmic development and implementation, abstract revision.

Spiral Keyhole Imaging for MR Fingerprinting

Guido Buonincontri[1], Laura Biagi[1,2], Pedro A Gómez[3,4],
Rolf F Schulte[4], Michela Tosetti[1,2]

[1]IMAGO7 Research Center, Pisa, Italy
[2]IRCCS Stella Maris, Pisa, Italy
[3]Technische Universität München, Munich, Germany
[4]GE Global Research, Munich, Germany

Abstract. MR Fingerprinting can be used for a fast and quantitative estimation of physical parameters in MRI. For the fast acquisition of MRF, common approaches have used non-Cartesian sampling of k-space. Here, we introduce a method for non-iterative anti-aliasing of the spiral MRF time series, based on the concept of keyhole imaging. Our approach does not change acquisition or dictionary creation and matching procedures. As frames require only minimal density compensation in k-space, noise amplification during reconstruction is reduced. After applying our algorithm, individual images from the MRF time series are artifact-free and clearer parameter maps are obtained in a shorter time while preserving the accurate quantification of MRF.

1 Introduction

Magnetic resonance fingerprinting (MRF) is an efficient method to acquire quantitative parameters using MRI [6]. Fast acquisition of MRF data usually features non-Cartesian k-space sampling schemes, using variable density spirals [4,6] or radial waveforms [2]. With these strategies, sampling density is higher in areas rich of contrast information at the centre of k-space, while areas containing less image contrast, such as the edges of k-space, are sampled less frequently. One of the main advantages of MRF is that imaging frames do not require full sampling, as pattern matching can "see through" aliasing [6]. Although anti-aliasing is not required, it has been demonstrated that using anti-aliasing strategies on the imaging frames can permit higher acceleration [3,10]. Most approaches have used iterative algorithms, which come at the expense of long image reconstruction times. Recently, a non-iterative anti-aliasing scheme was demonstrated for MRF using Cartesian imaging for small animals at 4.7T, based on the concept of k-space view sharing [1]. Here, we extend this approach to spiral MRF of the human brain.

2 Methods

Our method is based on the concept of k-space view sharing. The original MRF approach applies density correction to the acquired k-space points and zero-filling to non-acquired datapoints. In our approach, k-space coordinates are first

2   Buonincontri et al.
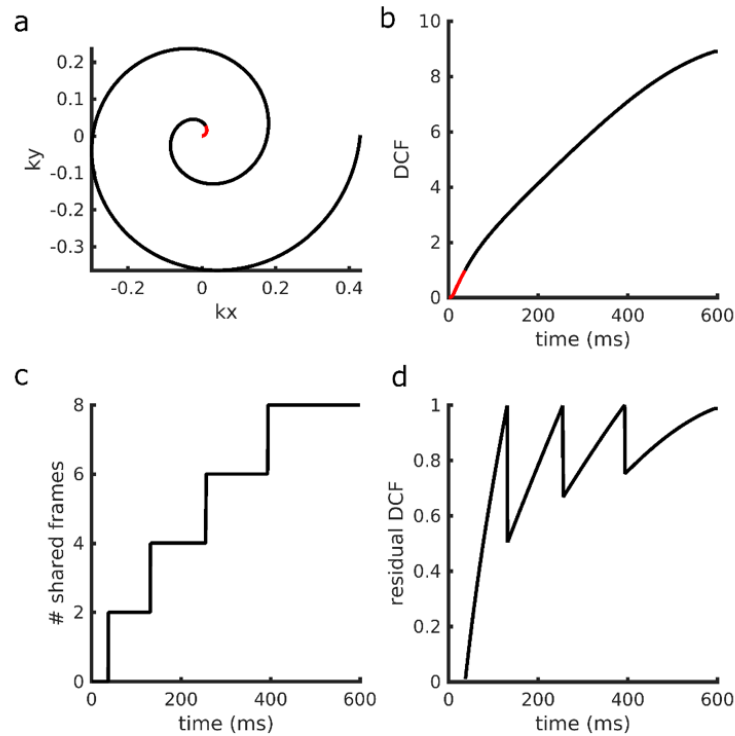
Fig. 1. Sketch of the algorithm using a spiral trajectory: oversampled part of k-space is in red, in panel a) sampling trajectory and in panel b) its corresponding DCF. In the oversampled (red) area, the algorithm applies density compensation like in regular gridding. In the undersampled area (black), data is shared with n neighbouring frames proportionally to the DCF (panel c). The residual DCF is then applied to the borrowed frames (panel d).

divided into two groups: oversampled part, where the k-space density compensation function (DCF) is less than 1, and the undersampled part, where the DCF is greater than 1 (Figure 1a). In the oversampled area, standard density compensation is applied (Figure 1b). In the undersampled area, each k-space point is shared with 2n neighbouring views. The number 2n approximates, for each k-space coordinate, the sampling density associated with the given distance to the k-space centre (Figure 1c). As this view-sharing step only accounts for odd integer DCF values, a small density correction factor is still applied to the borrowed data-points to achieve uniform sampling across all k-space points (Figure 1d).

Spiral Keyhole Imaging for MR Fingerprinting   3
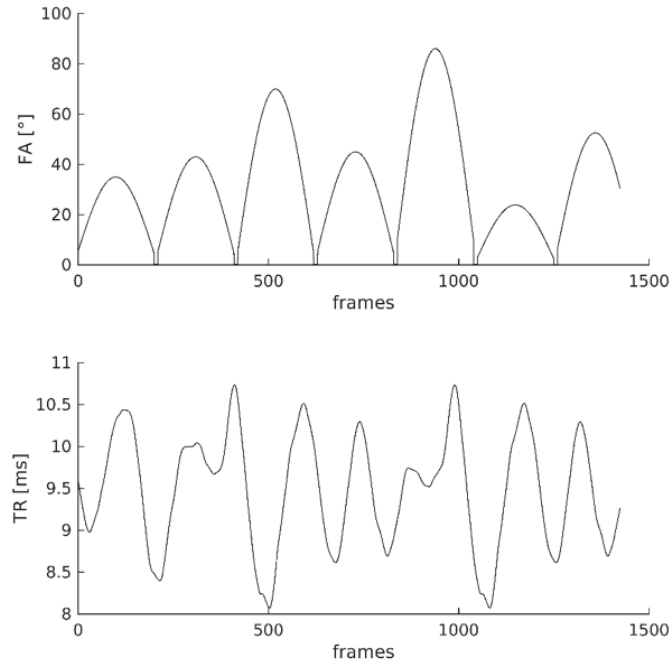
Fig. 2. Flip angle (FA) and repetition time (TR) list used for both phantom and volunteer scans.

2.1   MRF acquisition

Data was acquired using a gradient-spoiled SSFP spiral MRF sequence at 1.5T (GE HDx, 8ch receiver coil, Milwaukee USA) [4]. Dictionary creation and pattern matching were as in [6], acquisition parameter list is shown in Figure 2. To maximize spatial and temporal incoherence, we incremented the angle of the spirals each time by the golden angle [9].

2.2   Conservation of quantification and acceleration

We scanned the Eurospin TO5 phantom [5], and retrospectively performed the MRF experiment using the first 356, 712, 1078, and 1424 frames. We compared quantification values across undersampling factors and between the keyhole approach and the standard reconstruction. To evaluate the method in a more realistic case, we acquired data in one asymptomatic volunteer.

4   Buonincontri et al.
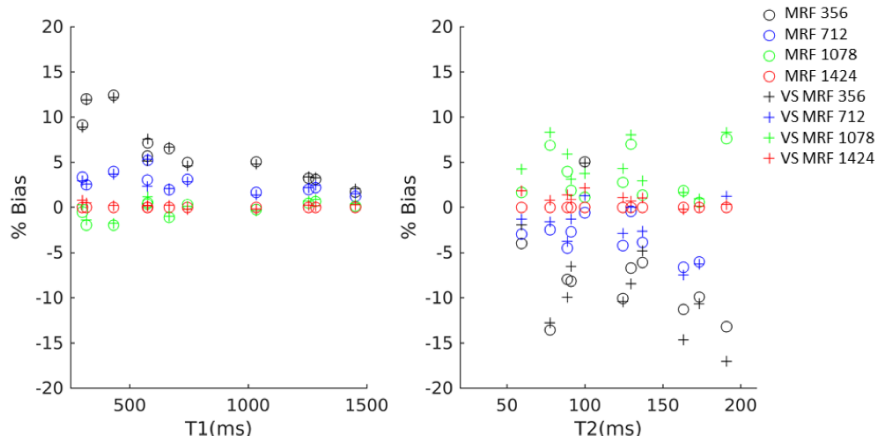
Fig. 3. . Comparison between MRF and keyhole MRF (here labelled VS MRF) across different T1 and T2 values, when acquiring 356, 712, 1078 and 1424 frames. Data are referred to MRF with 1424 frames. Bias is mainly due to the undersampling factor and is similar when applying or not applying anti-aliasing. Our anti-aliasing strategy does not affect quantification.

2.3   Conservation of image geometry

To assess whether the described anti-aliasing technique would corrupt image geometry, we scanned a resolution phantom and compared the image when applying the algorithm and when not applying it. We used visual inspection for qualitative assessment and the autofocus objective function [7] averaged across the image as a quantitative metric of conservation of the PSF.

3   Results

Figure 3 shows the effects on quantification of shortening the MRF acquisition, with and without our anti-aliasing strategy. Shortening acquisition achieved similar bias ($<5\%$ for T1 in 712 frames, $<10\%$ for T2 when acquiring 712 frames) in both cases, indicating that quantification is affected by acquisition length but not by anti-aliasing. Figure 4 displays brain images obtained with the first 754 frames only. Our anti-aliasing technique can achieve clearer T1, T2 and PD maps without increasing scan time, as well as giving diagnostically useful un-aliased frames. Figure 5 shows the effects of view sharing on a geometrical phantom, showing that image geometry is conserved when using our algorithm.

4   Discussion

Our results demonstrate anti-aliasing of MRF frames without using iterative algorithms. The concept used is similar to keyhole imaging [8], and is based

Spiral Keyhole Imaging for MR Fingerprinting 5
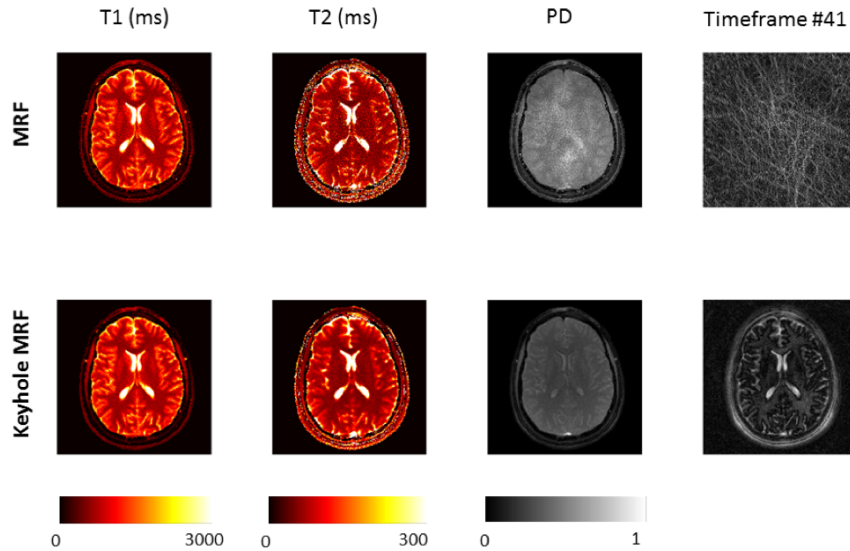
Fig. 4. Comparison of MRF without anti-aliasing and MRF with our technique. Data are obtained sampling the first 754 timeframes only, with an acquisition time of eight seconds. The last column compares imaging frame 41, tissue border enhancement can be observed in the anti-aliased frames. Keyhole MRF produces clearer images.

on the assumption that the image contrast is mainly stored in the centre of k-space, while the image details, which are mostly unchanged between frames, are in the edges of k-space. Therefore, the signal evolution for dynamic imaging can be in principle estimated well when only the central part of k-space is updated between subsequent frames. Notably, our approach requires only minimal density compensation in k-space, leading to less noise amplification. As the anti-aliased frames are free from artefacts, these can be used for radiological purposes in addition to the parameter maps.

5 Conclusions

We demonstrated keyhole spiral MRF. Our algorithm achieves significant acceleration with a preservation of the accurate quantification of MRF and does not require iterative algorithms or changes to the dictionary.

References

1. Buonincontri, G., Sawiak, S.: Three-dimensional MR fingerprinting with simultaneous B1 estimation. Magnetic Resonance in Medicine 00, 1–9 (2015)

6   Buonincontri et al.
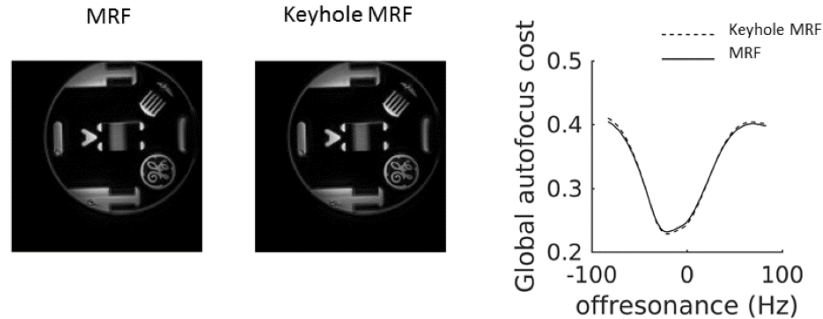
Fig. 5. Average of MRF and Keyhole MRF frames on a resolution phantom. The images have a similar level of detail. The autofocus metric averaged over the whole image is similar, indicating that the point spread function of these images is unaffected by the anti-aliasing algorithm.

2. Cloos, M.A., Knoll, F., Zhao, T., Block, K., Bruno, M., Wiggins, C., Sodickson, D.: Multiparamatric imaging with heterogenous radiofrequency fields. Nature Communication pp. 1–10 (2016)
3. Davies, M., Puy, G., Vandergheynst, P., Wiaux, Y.: A Compressed Sensing Framework for Magnetic Resonance Fingerprinting. SIAM Journal on Imaging Sciences 7(4), 2623–2656 (2014)
4. Jiang, Y., Ma, D., Seiberlich, N., Gulani, V., Griswold, M.A.: MR Fingerprinting Using Fast Imaging with Steady State Precession (FISP) with Spiral Readout. MRM (2014)
5. Lerski, R.A., de Certaines, J.D.: Performance assessment and quality control in MRI by Eurospin test objects and protocols. Magnetic resonance imaging 11(6), 817–33 (1993)
6. Ma, D., Gulani, V., Seiberlich, N., Liu, K., Sunshine, J.L., Duerk, J.L., Griswold, M.A.: Magnetic resonance fingerprinting. Nature 495, 187–192 (2013)
7. Man, L.C., Pauly, J.M., Macovski, A.: Improved automatic off-resonance correction without a field map in spiral imaging. Magnetic Resonance in Medicine 37(6), 906–913 (1997)
8. van Vaals, J.J., Brummer, M.E., Dixon, W.T., Tuithof, H.H., Engels, H., Nelson, R.C., Gerety, B.M., Chezmar, J.L., den Boer, J.A.: "Keyhole" method for accelerating imaging of contrast agent uptake. Journal of magnetic resonance imaging : JMRI 3(4), 671–5 (1993)
9. Winkelmann, S., Schaeffter, T., Koehler, T., Eggers, H., Doessel, O.: An Optimal Radial Profile Order Based on the Golden Ratio for Time-Resolved MRI. IEEE Transactions on Medical Imaging 26(1), 68–76 (2007)
10. Zhao, B., Setsompop, K., Gagoski, B., Ye, H., Adalsteinsson, E., Grant, P.E., Wald, L.L.: A Model-Based Approach to Accelerated Magnetic Resonance Fingerprinting Time Series Reconstruction. Proc Intl Soc Mag Reson Med (2016)

5.2.3 *Fast, Volumetric and Silent Multi-contrast Zero Echo Time Imaging*

Peer-reviewed Conference Abstract

Authors: X. Liu, **PA. Gómez**, T. Sprenger, AB. Solana, F. Wiesinger, MI. Menzel, JI. Sperl, BH. Menze

In: *Proc Intl Soc Mag Reson Med* (2017) [54]

Abstract: The current work aims to provide a volumetric, fast and silent method for quantitative T1 mapping with Zero Echo Time (ZTE) imaging, and generate multiple T1-weighted images at virtual inversion times. By designing an interleaved radial trajectory for ZTE, and constraining the temporal behavior of the signal with low-dimensional sub-space and spatiotemporal low rank regularization, we conducted a volumetric T1 mapping in 2 minutes with acoustic noise only 1.1dB higher than scanner background.

Contribution of thesis author: Algorithmic development and implementation, abstract revision.

Fast, Volumetric and Silent Multi-contrast Zero Echo Time Imaging

Xin Liu[1,2], Pedro A Gómez[1,2], Tim Sprenger[1,2], Ana Beatriz Solana[2],
Florian Wiesinger[2], Marion I Menzel[2], Jonathan I Sperl[2], Bjoern H Menze[1]

[1]Computer Science, Technische Universität München, Munich, Germany
[2]GE Global Research, Munich, Germany

Abstract. The current work aims to provide a volumetric, fast and silent method for quantitative T1 mapping with Zero Echo Time (ZTE) imaging, and generate multiple T1-weighted images at virtual inversion times. By designing an interleaved radial trajectory for ZTE, and constraining the temporal behavior of the signal with low-dimensional subspace and spatiotemporal low rank regularization, we conducted a volumetric T1 mapping in 2 minutes with acoustic noise only 1.1dB higher than scanner background.

1   Purpose

Zero echo time (ZTE) imaging has many favorable features, as it is distortion free, silent and can provide isotropic resolutions, however with poor image contrast [1]. The aim of this work is to generate multiple T1 contrast images at virtual inversion times (TIs) and quantitative T1 maps with magnetization prepared ZTE, in clinical feasible time and low acoustic noise to enhance patient comfort. We designed an interleaved radial trajectory to best elevate scan efficiency, and implemented a low dimensional temporal subspace and low rank (LR) regularization method [3] for reconstruction.

2   Methods

2.1   Sequence design

The radial trajectory is designed according to an interleaved Archimedean spiral trajectory [4]. The acquired data is segmented along the readout, and data segments with the same position in the readout (similar TI) from different interleaves are grouped together to generate undersampled images. The effective TI is defined as the center of the acquisition window for each segment. The trajectory of each interleave is shifted to guarantee that the undersampled volumes can uniformly cover the K space. The trajectory design is shown in Fig. 1.

2   Liu et al.
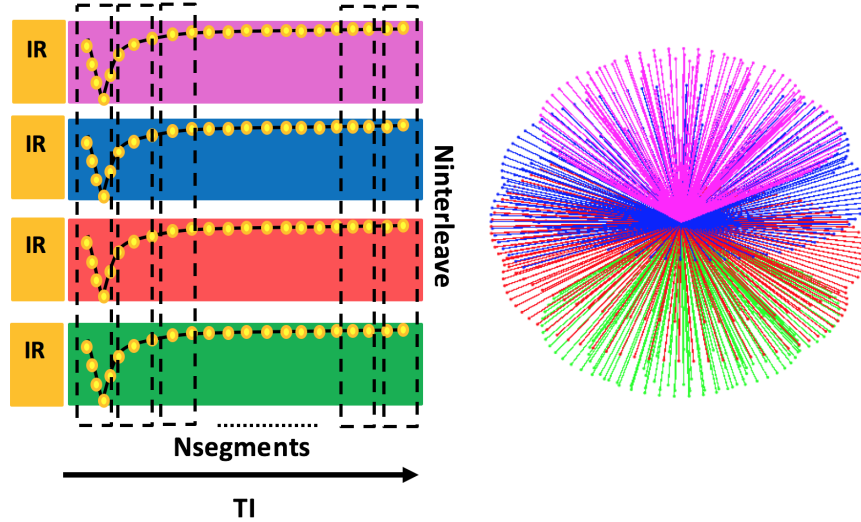
Fig. 1. Demonstration of acquisition protocol and trajectory design. Data is segmented along the readout (as illustrated in the dashed box), and segments acquired at the same inversion time (TI) are grouped together to generate under sampled images. On the left is a representation of the K space trajectory at one effective TI. Segments from different interleaves (illustrated in different colors) can uniformly cover the K space.

2.2   Data acquisition

The experiment was conducted on a GE 3T MR750w scanner with a GEM head array coil (GE Healthcare, Waukesha, WI). A phantom (DiagnosticSonar, Livingston, UK) consisting of tubes with different T1 values were used in the experiment. An adiabatic inversion recovery (IR) prepared ZTE was conducted with FOV=21.6cm, flip angle=2°, readout BW = ± 15.6 kHz, isotropic resolution of 3mm, and a waiting time of 1000ms to allow signal recovery between consecutive interleaves. The data acquisition began 40ms after the IR pulse and lasted 3000ms. Acoustic noise measurements were performed using a Bruel & Kjaer sound level meter equipped with MR compatible microphone, which was placed in-bore at scanner isocenter inside the head coil. An initial volunteer scan was also conducted with the same imaging protocol.

2.3   Data reconstruction

The compressed sensing reconstruction with low dimensional temporal subspace constraint and LR regularization was implemented [3]. The observed signal $y(t)$ can be modeled as $y = EX_t$, in which E is the encoding operator and X_t represents the temporal dynamic image series. The signal evolution is a function of tissue parameter (T1, proton density) and IR pulse flip angle (due to imperfect
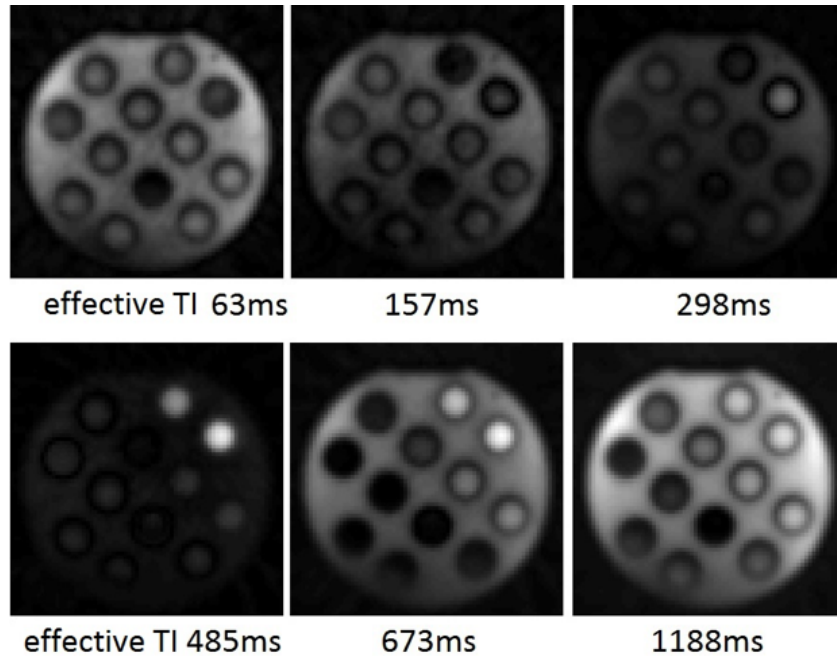
Fig. 2. The signal evolution can be observed by looking at the reconstructed temporal dynamic T1 contrast: different T1 samples come to their zero crossing at different TIs.

IR pulse), and can be approximated by temporal basis determined by the signal model. The LR regularization exploits spatiotemporal correlations and reduces the degree of freedoms in the subspace. In the current work we chose K=3 temporal coefficients, and segmented the data into 64 time points with different TIs.

3 Results

As shown in Fig. 2, the temporal behavior of different T1 samples can be observed in reconstructed image series at different virtual TIs. Fig. reffig3 shows the signal evolution before and after applying temporal subspace and LR regularization, and the fitted signal curve. Mean and standard deviation of the fitting results for each tube are shown in Table 1. Compared to vendor provided ground truth T1 values, the fitting results are similar but with an underestimation of long T1 (tube7). T1 values consistent with literature were generated in gray and white matter area from the volunteer scan, and are shown in Figure 4. However, the acquisition and reconstruction parameters need further improvement to generate decent T1 mapping in vivo. The current experiment took less than 2 minutes,

4   Liu et al.
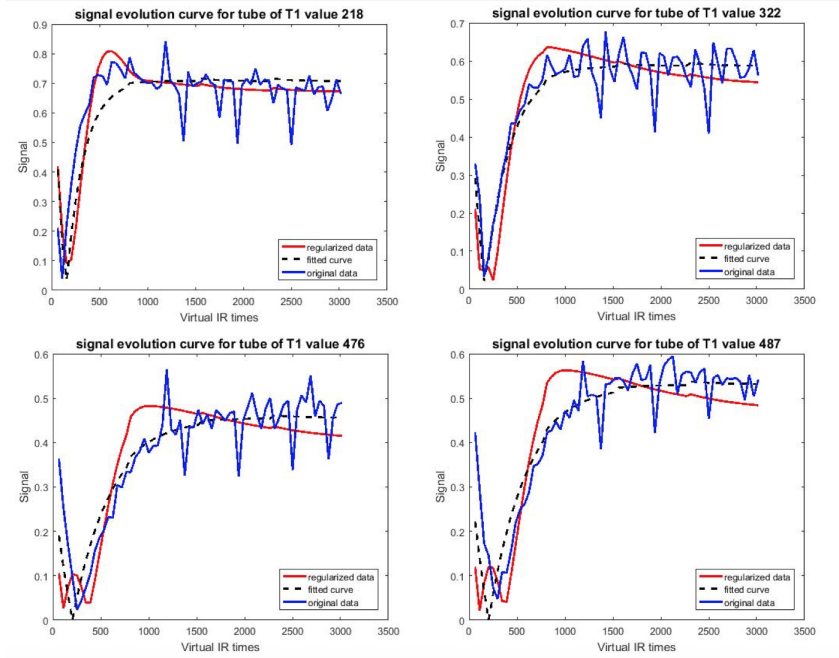
Fig. 3. The signal evolution curve of different T1 values before (blue) and after (red) applying temporal subspace and LR regularization. The fitted data curve is plotted in dashed black line.

and the acoustic noise was 71.1dB, only 1.1dB higher than the background noise (70.0dB).

Table 1. The T1 mapping results compared to the ground truth T1 value provided by vendor.

Tube number	True values (ms)	Fitted values (ms)
1	218	203.1 ± 9.8
2	322	302 ± 10.6
3	487	483.1 ± 0.3
4	476	489.8 ± 16.0
5	647	665.6 ± 3.8
6	833	812.5 ± 4.7
7	1092	980.1 ± 0.35

Fast, Volumetric and Silent Multi-contrast Zero Echo Time Imaging   5
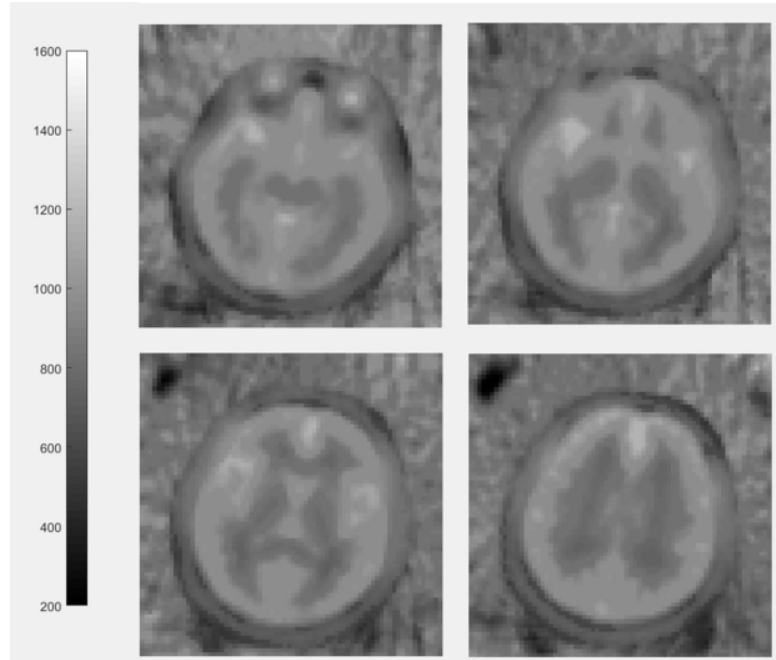
Fig. 4. The T1mapping result from preliminary volunteer scanning experiment. White matter, CSF and gray matter can be distinguished easily. The measured T1 values are around 730-800ms in white matter area, and around 950-1000ms in gray matter area, which is reasonable. However, the acquisition and reconstruction parameters need to be improved to generate decent T1 maps.

4   Discussion

In this study we conducted volumetric, fast and silent T1 mapping and reconstructed multiple T1 contrast images at virtual TIs with IR prepared ZTE. The current method was validated in T1 phantom and initially validated in volunteer scanning, yet further improvement is necessary. Unlike Cartesian or spiral trajectory, radial trajectory has no defined contrast point as it constantly updating the center of K space. Previous studies [2] used view-sharing for IR prepared radial sequence to solve the contradiction between image quality and contrast. In this work, we utilized an alternative method by having undersampled images acquired at similar TI times, and reduce undersampling artifacts by low-dimensional subspace and LR regularization. Additionally, there are several limitations that need to be improved in next steps. First, there was an underestimation bias of long T1 values, which could be improved by a longer acquisition window to better capture the dynamic relaxation curve of long T1 samples. Second, the signal model does not consider inaccurate flip angle during ZTE readout which could

6   Liu et al.

also affect the signal evolution. Including the possible flip angle variations in the signal model could increase the accuracy in calculating the temporal basis.

5   Acknowledgments

References

1. Börnert, P., Groen, J., Smink, J., Nehrke, K.: Magnetization Prepared ZTE to address Multiple Diagnostic Contrasts. Proc Intl Soc Mag Reson Med (2015)
2. Kecskemeti, S., Samsonov, A., Hurley, S.A., Dean, D.C., Field, A., Alexander, A.L.: MPnRAGE: A technique to simultaneously acquire hundreds of differently contrasted MPRAGE images with applications to quantitative T 1 mapping. Magnetic Resonance in Medicine 75(3), 1040–1053 (2016)
3. Tamir, J.I., Uecker, M., Chen, W., Lai, P., Alley, M.T., Vasanawala, S.S., Lustig, M.: T 2 shuffling: Sharp, multicontrast, volumetric fast spin-echo imaging. Magnetic Resonance in Medicine (2016)
4. Wong, S.T.S., Roos, M.S.: A strategy for sampling on a sphere applied to 3D selective RF pulse design. Magnetic Resonance in Medicine 32(6), 778–784 (1994)

5.2.4   *Accelerated Parameter Mapping with Compressed Sensing: an Alternative to MR Fingerprinting*

Peer-reviewed Conference Abstract

Authors: PA. Gómez, G. Buonincontri, M. Molina-Romero, JI. Sperl, MI. Menzel, BH. Menze

In: *Proc Intl Soc Mag Reson Med* (2017) [39]

Abstract: We introduce a method for MRI parameter mapping based on three concepts: 1) an inversion recovery, variable flip angle acquisition strategy designed for speed, signal, and contrast; 2) a compressed sensing reconstruction which exploits spatiotemporal correlations through low rank regularization; and 3) a model-based optimization to simultaneously estimate proton density, T_1, and T_2 values from the acquired measurements. Compared to Magnetic Resonance Fingerprinting (MRF), the proposed method achieves a five-fold acceleration in acquisition time, reconstructs an unaliased series of images, and does not rely on dictionary matching for parameter estimation.

Contribution of thesis author: Algorithmic development and implementation, experimental design, data analysis, abstract preparation and editing.

Accelerated Parameter Mapping with Compressed Sensing: an Alternative to MR Fingerprinting

Pedro A Gómez[1,2], Guido Bouincontri[3], Miguel Molina-Romero[1,2], Jonathan I Sperl[2], Marion I Menzel[2], Bjoern H Menze[1]

[1]Computer Science, Technische Universität München, Munich, Germany
[2]GE Global Research, Munich, Germany
[3]INFN Pisa, Pisa, Italy

Abstract. We introduce a method for MR parameter mapping based on three concepts: 1) an inversion recovery, variable flip angle acquisition strategy designed for speed, signal, and contrast; 2) a compressed sensing reconstruction which exploits spatiotemporal correlations through low rank regularization; and 3) a model-based optimization to simultaneously estimate proton density, T1, and T2 values from the acquired measurements. Compared to MR Fingerprinting, the proposed method achieves a five-fold acceleration in acquisition time, reconstructs an unaliased series of images, and does not rely on dictionary matching for parameter estimation.

1   Purpose

MR fingerprinting (MRF) [12] has recently gained attention due to its ability to simultaneously estimate multiple parametric maps within clinically feasible scan times. MRF is based on three main ingredients: a pseudorandom acquisition, the reconstruction of aliased measurements, and the matching of these measurements to a precomputed dictionary. While conceptually appealing, MRF suffers from multiple methodological shortcomings. The purpose of this work is to present an alternative method to parameter mapping that addresses these limitations by optimizing the acquisition, reconstructing unaliased measurements, and fitting the measurements in a model-based optimization not subject to the discretization of the dictionary.
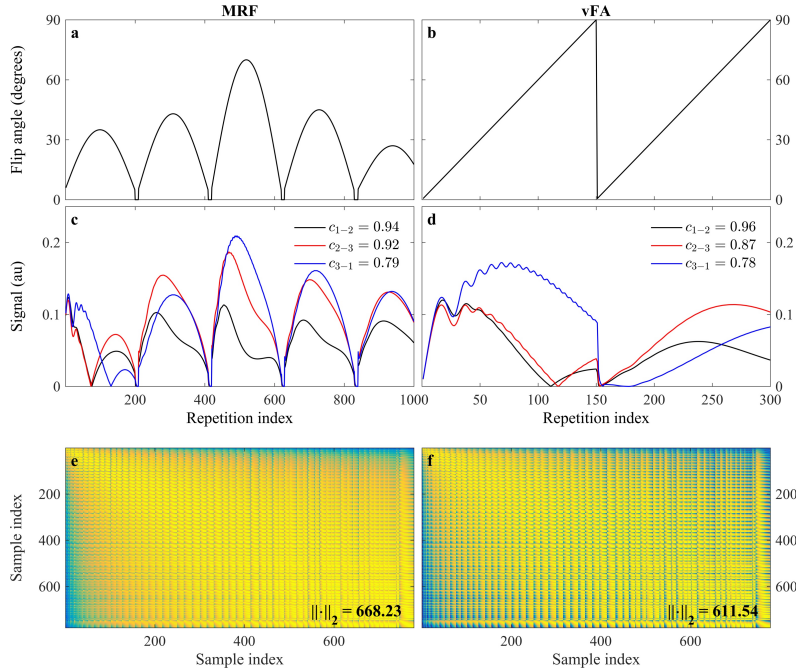
2   Methods

In an MRI experiment the observed signal $y(t)$ can be described by the combination of a spatial function with a temporal signal evolution:

$$y(t) = \int_{\mathbf{r}} \rho(\mathbf{r}) f_t(\mathbf{r}) e^{-2\pi \mathbf{k}(t) \cdot \mathbf{r}} d\mathbf{r}; \tag{1}$$

2   Gómez et al.

Fig. 1. Flip angle trajectories and correlation between observations. **a-b**, Flip angle trajectory for MRF and variable flip angles (vFA). **c-d**, Temporal signal evolution of three exemplary observations. The legend displays the correlation c between each of them. **e-f**, Correlation matrix for all observations and the norm of the matrix; where the observations are less correlated in vFA.

where $\rho(\mathbf{r})$ is the spatial distribution of the spin density at position $\mathbf{r}$, $\mathbf{k}(t)$ is the k-space trajectory, and $f_t(\mathbf{r})$ is the temporal signal, given by the recursion:

$$f_t(\mathbf{r}) = f_{t-1}(\mathbf{r})g\left(\boldsymbol{\theta}_a(t); \boldsymbol{\theta}_b(\mathbf{r})\right). \tag{2}$$

The temporal signal $f_t(\mathbf{r})$ at time t is determined by the signal value at the previous time point $f_{t-1}(\mathbf{r})$ modulated by $g(\cdot)$, a function of two different parameter sets: the temporally varying acquisition parameters $\boldsymbol{\theta}_a(t)$, e.g. flip angle $\alpha(t)$ and repetition time $T_R(t)$; and the spatially dependent biological parameters of interest $\boldsymbol{\theta}_b(\mathbf{r})$, such as $T_1(\mathbf{r})$ and $T_2(\mathbf{r})$. In MRF, the temporal signals are denoted fingerprints, where the method aims at creating unique signals for different spatial locations through pseudorandom variations of the acquisition parameters $\boldsymbol{\theta}_a(t)$. Alternatively, we chose $\boldsymbol{\theta}_a(t)$ to satisfy three criteria: speed, signal, and contrast. We increased the speed by minimizing $T_R(t)$, and optimized $\alpha(t)$ for signal and contrast using a training dataset $\mathbf{x} \in \mathbb{C}^{L \times T}$ with L observations and T time points; wherein we experimentally attempted to increase both the orthogonality between observations, and the norm within observations [3,4,8].

Accelerated Parameter Mapping with Compressed Sensing   3
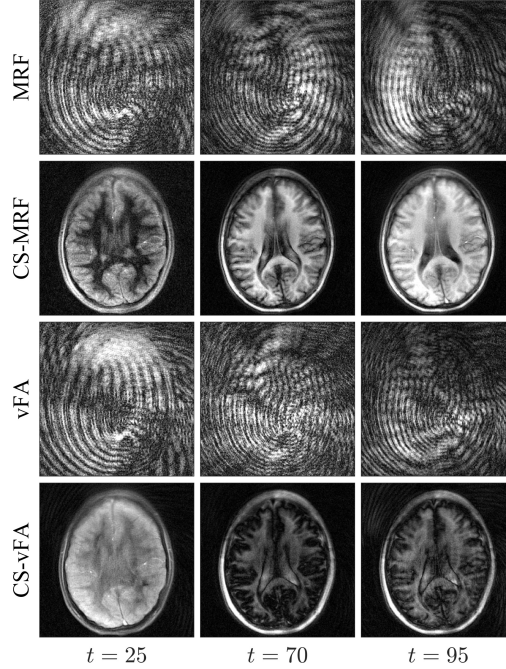
Fig. 2. Reconstructed images at different repetition indexes t. While the nuFFT operation reconstructs a series of aliased images, the proposed CS reconstruction removes the aliasing, allowing for an easier visualization of the temporal dynamics of the signal.

Whereas the original MRF reconstructs aliased images from the measurements, recent work has shown that the acquired data can also be reconstructed in an iterative framework [1,2,5,7,13,17,18]. Based on these ideas, we implemented a compressed sensing (CS) [11] reconstruction that constrains the temporal signal evolution to a low dimensional subspace [14,17], and regularizes the image series by promoting local low rank of spatiotemporal image patches [14,15]. Finally, once we reconstruct an unaliased image series, we propose to replace the matching to a simulated dictionary with an optimization based on least-squares curve fitting for the simultaneous estimationof $\rho(\mathbf{r})$, $T_1(\mathbf{r})$, and $T_2(\mathbf{r})$.

We acquired a single slice from a healthy volunteer based on the FISP implementation of MRF [10] on a GE HDx MRI system (GE Medical Systems, Milwaukee, WI), with an eight channel receive only head RF coil. After an initial inversion, a train of $T = 1000$ pulses with varying flip angles and repetition times was applied ($T_{acq} = 13.15\ s$ per slice). In addition, we acquired a train of $T = 300$ variable flip angles (vFA) with $T_R = 8\ ms$ ($T_{acq} = 2.42\ s$ per slice). For both acquisitions, we used a zero-moment compensated variable density spiral designed with $22.5 \times 22.5\ cm$ FOV, 256×256 matrix size, $1\ mm$ in-plane resolution, $5\ mm$ slice thickness, and golden angle rotations between every in-
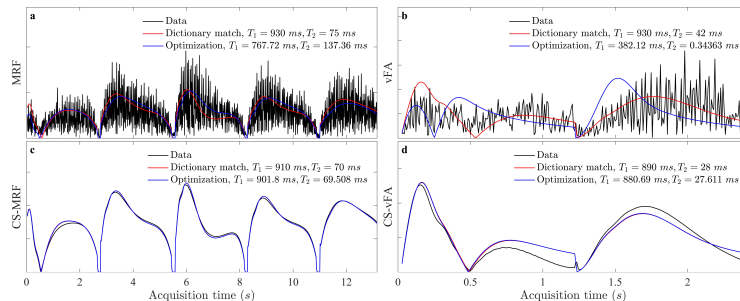
Fig. 3. Signal evolution of a single observation with dictionary matching and model-based optimization. **a-b**, The high levels of aliasing in the acquisitions lead to different parameter estimates between matching and optimization. **c-d**, Matching and optimization results are similar when the evolution is unaliased, where the optimization is not constrained to the discretization of the dictionary. The T_2 values obtained from CS-vFA present an underestimation with respect to the T_2 in MRF and CS-MRF.

terleave. Each acquisition was reconstructed using the nuFFT operator [6] and with the proposed CS method, and parameter maps were subsequently estimated with both dictionary matching and model-based optimization. We simulated the dictionary for a varying range of T_1 and T_2 values using the EPG formalism [9,16].

3 Results

We found that two linear ramps yielded T_1 and T_2 sensitivity while reducing the cost (see Fig. 1). Compared to MRF, the proposed strategy reduces the number of repetitions (Fig. 1a-b), while increasing the orthogonality of the signal evolutions between training observations (Fig. 1c-d). This acquisition, coupled with the proposed CS reconstruction, allows for the recovery of a series of unaliased images (Fig. 2), which in turn facilitate a model-based optimization for parameter mapping (Figs. 3,4).

4 Discussion

When the measurements are aliased, the optimization is subject to local minima due to high noise levels of the temporal signals, resulting in biased parameter estimates. On the other hand, as soon as the image series is unaliased, the optimization converges, yielding parametric maps that are not subject to the discretization of the dictionary. vFA maps display an underestimation of T_2 values, indicating that the vFA strategy could still benefit from better T_2 encoding using variable repetition or echo times.

Accelerated Parameter Mapping with Compressed Sensing   5
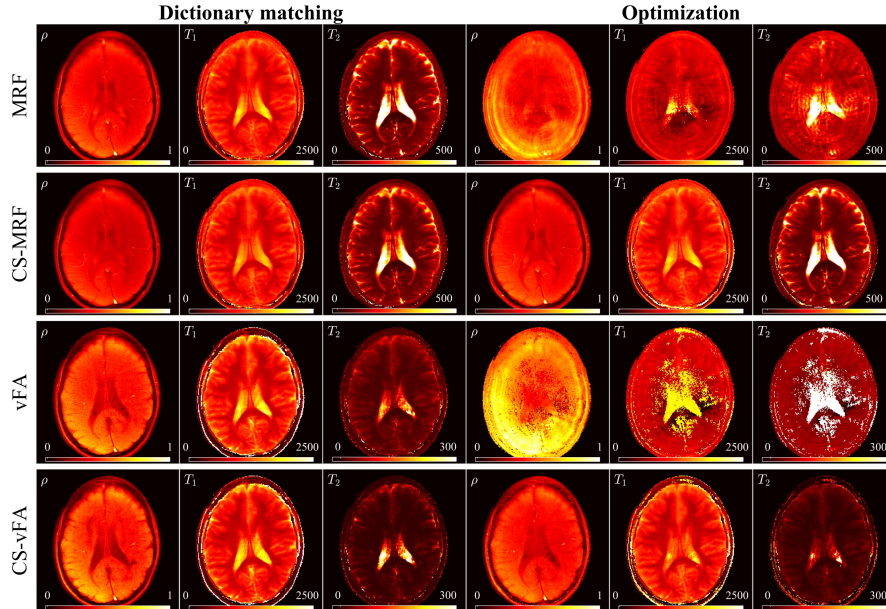
Fig. 4. Estimated parametric maps with dictionary matching and model-based optimization. Dictionary matching yields consistent results with noisy and unaliased signals, while the optimization only converges when fitting unaliased signals (rows 2 and 4, right). When fitting noisy signals, the optimization converges to local minima, leading to an incorrect estimation of parametric maps (rows 1 and 3, right). On the other hand, the optimization is not subject to dictionary discretization, allowing for a wider range of parameters in the solution space. T_2 maps in vFA are underestimated in comparison to MRF.

5   Conclusions

We demonstrated an alternative to MRF based on variable flip angles, a compressed sensing reconstruction, and a model-based optimization. Our proposal reduces the acquisition time by a factor of five, reconstructs unaliased temporal signals, and, notably, does not rely on dictionary matching for parameter estimation.

6   Acknowledgments

6   Gómez et al.

References

1. Assländer, J., Cloos, M.A., Knoll, F., Sodickson, D.K., Hennig, J., Lattanzi, R.: Low Rank Alternating Direction Method of Multipliers Reconstruction for MR Fingerprinting. arXiv eprint p. arXiv:1608.06974 (2016)
2. Cline, C.C., Chen, X., Mailhe, B., Wang, Q., Nadar, M.: AIR-MRF: Accelerated iterative reconstruction for magnetic resonance fingerprinting. Proc Intl Soc Mag Reson Med (2016)
3. Cohen, O.: Magnetic Resonance Fingerprinting Trajectory Optimization. Proc Intl Soc Mag Reson Med 1, 1 (2014)
4. Cohen, O., Sarracanie, M., Rosen, M.S., Ackerman, J.L.: In Vivo Optimized Fast MR Fingerprinting in the Human Brain. Proc Intl Soc Mag Reson Med (2016)
5. Davies, M., Puy, G., Vandergheynst, P., Wiaux, Y.: A Compressed Sensing Framework for Magnetic Resonance Fingerprinting. SIAM Journal on Imaging Sciences 7(4), 2623–2656 (dec 2014)
6. Fessler, J.A., Sutton, B.P.: Nonuniform Fast Fourier Transforms Using Min-Max Interpolation. IEEE Trans Signal Processing 51(2), 560–574 (2003)
7. Gómez, P.A., Ulas, C., Sperl, J.I., Sprenger, T., Molina-Romero, M., Menzel, M.I., Menze, B.H.: Learning a spatiotemporal dictionary for magnetic resonance fingerprinting with compressed sensing. MICCAI Patch-MI Workshop 9467, 112–119 (2015)
8. Hamilton, J.I., Wright, K.L., Jiang, Y., Hernandez-Garcia, L., Ma, D., Griswold, M., Seiberlich, N.: Pulse Sequence Optimization for Improved MRF Scan Efficiency. Proc Intl Soc Mag Reson Med 23, 3386 (2015)
9. Hennig, J.: Echoes—how to generate, recognize, use or avoid them in MR-imaging sequences. Part I: Fundamental and not so fundamental properties of spin echoes. Concepts in Magnetic Resonance 3(3), 125–143 (jul 1991)
10. Jiang, Y., Ma, D., Seiberlich, N., Gulani, V., Griswold, M.A.: MR Fingerprinting Using Fast Imaging with Steady State Precession (FISP) with Spiral Readout. MRM (2014)
11. Lustig, M., Donoho, D., Pauly, J.M.: Sparse MRI: The application of compressed sensing for rapid MR imaging. Society of Magnetic Resonance in Medicine 58, 1182–1195 (2007)
12. Ma, D., Gulani, V., Seiberlich, N., Liu, K., Sunshine, J.L., Duerk, J.L., Griswold, M.A.: Magnetic resonance fingerprinting. Nature 495, 187–192 (2013)
13. Pierre, E.Y., Ma, D., Chen, Y., Badve, C., Griswold, M.A.: Multiscale reconstruction for MR fingerprinting. Magnetic Resonance in Medicine 2492, 2481–2492 (2015)
14. Tamir, J.I., Uecker, M., Chen, W., Lai, P., Alley, M.T., Vasanawala, S.S., Lustig, M.: T 2 shuffling: Sharp, multicontrast, volumetric fast spin-echo imaging. Magnetic Resonance in Medicine (2016)
15. Trzasko, J., Manduca, A.: Local versus Global Low-Rank Promotion in Dynamic MRI Series Reconstruction. Proc Intl Soc Mag Reson Med 24(7), 4371 (2011)
16. Weigel, M.: Extended phase graphs: Dephasing, RF pulses, and echoes - pure and simple. Journal of Magnetic Resonance Imaging (2014)
17. Zhao, B., Setsompop, K., Gagoski, B., Ye, H., Adalsteinsson, E., Grant, P.E., Wald, L.L.: A Model-Based Approach to Accelerated Magnetic Resonance Fingerprinting Time Series Reconstruction. Proc Intl Soc Mag Reson Med (2016)
18. Zhao, B., Setsompop, K., Ye, H., Cauley, S., Wald, L.L.: Maximum Likelihood Reconstruction for Magnetic Resonance Fingerprinting. IEEE Trans Med Imaging 0(0), 0 (2016)

Part III

DISCUSSION AND CONCLUSION

6

DISCUSSION OF THE PRESENTED METHODS

This publication-based dissertation presents methodological advances to quantitative MRI in three different categories: hyperpolarized ^{13}C metabolic NMR, motion encoding techniques, and multiparametric mapping. In total, this thesis contains seven publications, seven abstracts, and two manuscripts currently being considered under review for publication.

In hyperpolarized ^{13}C metabolic NMR, the main focus of this thesis has been on the kinetic modeling of different metabolic pathways. By formulating a joint system of differential equations, it has been possible to infer multiple parameters with a single routine, increasing fitting robustness. The robustness of the fitting is relevant, since the quantified parameters, the metabolic exchange rates, can be subsequently used to monitor metabolism and differentiate between healthy and diseased tissue.

The contributions of this thesis with respect to motion encoding methods are related to image reconstruction, signal processing, and modeling. Work in dynamic MRI reconstruction has demonstrated that by exploiting all of the available dimensions of the data, it is possible to recover full signals from drastically undersampled measurements. Also, by using advanced algorithms from the field of machine learning, the undersampling level can be further increased without compromising the quality of the computed scalar metrics. Signal processing techniques, such as BSS, have enabled the separation of entangled signals stemming from different tissue compartments inside a single voxel. Finally, alternative modeling methods, including simplified kurtosis models, have been presented for the computation of scalar metrics.

The multiparametric mapping techniques presented in this work have been mainly inspired by MRF. This dissertation contains several methodological improvements to MRF, including the *learning* of a dictionary from data, creating new maps and contrasts, and automatically labeling different tissues as an output of the processing pipeline. Moreover, advances in MRF have led to the creation of an alternative acquisition and reconstruction method, namely QTI, which is scalable into higher dimensions, more efficient, and more robust than MRF.

Finally, this work contains several limitations: to have impact in healthcare, the technical advances shown here require further methodological development, reproducibility studies, and clinical validation. This is the subject of future work.

OUTLOOK AND FUTURE WORK

7

The advances presented in this thesis have been possible by building on state-of-the-art research at the intersection of Computer Science and MRI physics. Notably, the work in this thesis relies on PI, CS, MRF, and machine learning to improve quantitative MRI. Certainly, progress in the field needs to be constant, leaving ample space for future work; especially with regard to QTI. On the methodological side, QTI can be further improved in many aspects such as encoding for 3D images; revisiting aspects of the sequence design to further increase efficiency; incorporating additional parameters into the model, including diffusion and magnetization transfer; or exploring the limits of QTI in terms of speed, resolution, SNR, and field strength. Clinically, QTI needs to be proven for a large cohort of patients and multiple diseases, where the estimated metrics should be specific and sensitive to pathology. Finally, commercially, only when the developed methods and algorithms behind QTI are tested, validated, and released, will their impact and reach in the healthcare sector be significant.

Additionally, the past few years have demonstrated that machine learning, especially algorithms related to deep learning [95], is becoming increasingly relevant for medical imaging. While this thesis has an important focus on machine learning, it does not cover the specific field of deep learning (author contributions in that field are collected elsewhere [30]). On the other hand, novel applications in medical image segmentation [49, 70] and reconstruction [72, 96] indicate that deep learning has just begun and will continue to transform the field. Hence, future work will also focus in this direction, combining the previously developed techniques with deep learning algorithms to further improve MRI in general, and quantitative MRI in specific. By moving in this direction, MRI can become more automatic, with the potential of eliminating cumbersome and error-prone manual tasks.

Also, the combination of deep learning with quantitative MRI techniques could significantly increase the capabilities and diagnostic value of MRI scanners, especially in situations where physical and theoretical models do not hold. For example, deep learning could play a key role when the acquired data violate the Nyquist limit, the SNR is too low, or the underlying biophysical models are too complex or inaccurate. These techniques could also relax hardware constraints, potentiating the commercialization of robust and portable devices. This in turn, would transform MRI into a commodity instead of a luxury, increasing patient access and benefiting the population and healthcare systems on a global scale.

Part IV

APPENDIX

MANUSCRIPTS IN PREPARATION OR UNDER REVIEW

A.1 MANUSCRIPTS UNDER REVIEW

A.1.1 *Ultrafast Magnetic Resonance Imaging and Parametric Mapping with Optimal Transient-state Encoding*

Peer-reviewed Journal Paper

Authors: PA. Gómez, M. Molina-Romero, P. Orihuela, G. Buonincontri, T. Rincón-Domíngez, MI. Menzel, BH. Menze

Abstract: Magnetic Resonance Imaging (MRI) is a remarkably powerful diagnostic technique. It allows for the imaging of a rich set of contrasts and the mapping of a host of parameters that enable the non-invasive study of tissue anatomy and physiology. Its extraordinary power, however, is limited by its speed: obtaining complementary information requires lengthy acquisitions, which are often infeasible or impractical within clinical settings. Here, we demonstrate that, by remaining in the transient-state and relying on physical modeling of spin dynamics to optimally encode and reconstruct signals, it is possible to generate hundreds of clinically relevant images with unique contrast alongside multiple quantitative maps and tissue labels with a single, accelerated acquisition. Our method - Quantitative Transient-state Imaging (QTI) - offers novel directions in sequence design; producing fast, accurate, and high-resolution results, drastically simplifying image processing, and paving the way to new diagnostic opportunities.

Contribution of thesis author: Algorithmic development and implementation, experimental design, data analysis, abstract preparation and editing.

Ultrafast Magnetic Resonance Imaging and Parametric Mapping with Optimal Transient-state Encoding

Pedro A Gómez[1,2], Miguel Molina-Romero[1,2], Paula Orihuela[1,2],
Guido Bouincontri[3], Teresa Rincón-Domínguez[1,2], Marion I Menzel[2],
Bjoern H Menze[1]

[1]Computer Science, Technische Universität München, Munich, Germany
[2]GE Global Research, Munich, Germany
[3]Imago7 Foundation, Pisa, Italy

Abstract. Magnetic resonance imaging (MRI) is a remarkably powerful diagnostic technique. It allows for the imaging of a rich set of contrasts and the mapping of a host of parameters that enable the non-invasive study of tissue anatomy and physiology. Its extraordinary power, however, is limited by its speed: obtaining complementary information requires lengthy acquisitions, which are often infeasible or impractical within clinical settings. Here, we demonstrate that, by remaining in the transient-state and relying on physical modelling of spin dynamics to optimally encode and reconstruct signals, it is possible to generate hundreds of clinically relevant images with unique contrast alongside multiple quantitative maps and tissue labels with a single, accelerated acquisition. Our method - quantitative transient-state imaging (QTI) - offers novel directions in sequence design; producing fast, accurate, and high-resolution results, drastically simplifying image processing, and paving the way to new diagnostic opportunities.

1   Introduction

Since Lauterbur's breakthrough idea[25], magnetic resonance imaging (MRI) has enjoyed decades of incremental improvements, evolving into an unparalleled imaging modality with the ability of providing detailed information on a tissue's structure and function. Modern MR scanners use sophisticated combinations of radiofrequency pulses and magnetic gradients to probe the complex dynamics of spins inside the human body. Through careful calibration, one can manipulate spins to produce MR signals that are 'weighted' by one or more of the multiple parameters that MR is sensitive to. Thus, different experiments with distinct acquisition parameters allow one to image a wide range of contrasts, which provide critical information in clinical settings. In its simplest form, scanners produce images weighted by the longitudinal relaxation time (T1), the transverse relaxation time (T2), and the proton density (PD). Moreover, parameter mapping

2   Gómez et al.

techniques enable the quantification of these parameters - progressing from qualitative images to quantitative maps, increasing accuracy and reproducibility of diagnostic information[47].

However, MRI's versatility comes at the expense of long acquisition times. MRI is an inherently slow technique, as it requires acquiring multiple samples along different encoding dimensions to reconstruct uncorrupted images. For instance, conventional techniques need 128 or 256 repetitions along one of the encoding dimensions to reconstruct a single weighted image with a matrix size of 128×128 or 256×256, respectively. In these acquisitions, scan times are directly proportional to the number of repetitions, and, depending on the protocol at hand, can become exceedingly long. Lengthy acquisitions mean higher risk of motion-related image distortions, decreased value in time-critical diagnostic scenarios, less patients benefitting within a certain time window, and, importantly, the acquisition of only a limited set of qualitative images, as acquiring quantitative maps further increases scan times and is often impractical in clinical MRI. Therefore, accelerating scans has long been one of the primary objectives of MR research[15,45].

The early development of fast techniques, such as fast low-angle shot imaging[15], or echo-planar imaging (EPI)[32], resulted in the widespread adoption of clinical scanners. Thereafter, despite continued efforts to accelerate acquisitions, only towards the turn of the millennium we witnessed disruptive innovations with significant impact on scanning speed. First, the introduction of parallel imaging, built on the observation that receiver coils have a spatial encoding effect, yielded speed-up factors proportional to the number of additional coils incorporated into the scanner[37]. Then, compressed sensing[29] further accelerated scans by exploiting structure and redundancy present in MR images. Both these techniques allowed us to overcome the Nyquist limit, increasing the value of MRI by enabling the reconstruction of uncorrupted images with less acquired data; that is, less repetitions. Still, while these methods result in substantial acceleration for each individual weighted image, these images ultimately represent a mere snapshot of the underlying spin dynamics - they provide information at a single point in time and a specific location in space.

Recently, MR fingerprinting (MRF)[30], emerged as a promising technique with a radical new approach to data acquisition. Instead of relying on serial repetitions for individual weighted images, MRF proposes to create unique signal evolutions in the transient-state - so-called 'fingerprints' - for the simultaneous quantification of multiple parameters with a single scan. With this technique, MRF produces quantitative maps in a scan time comparable to traditional weighted imaging, improving the scan efficiency of previous mapping methods by almost 2-fold. Unfortunately, this improvement in scan efficiency comes at a high cost. First, the pseudorandom nature of MRF acquisitions provides no indication as to how and where parameters are encoded into MRF signals, thus lacking a theoretical basis for optimising sequences beyond trial and error. Furthermore, the pattern recognition technique employed by MRF requires constructing a dictionary by simulating a signal for every parameter combination possible, a

method inherently limited in memory and precision by the dimensionality of the parameter space. Finally, neither the evolving signals, i.e. the fingerprints, nor the resulting images can be inspected or visually interpreted.

Here, we propose QTI, a novel method for data acquisition, image reconstruction, and parameter estimation. The key idea behind QTI is to combine physical modelling of spin dynamics with optimal transient-state encoding to reconstruct one image per repetition with short repetition times (TR). With our framework for designing the acquisition strategy and reconstructing signal dynamics, we open the door to a wide range of possibilities. First, we design the sequence considering specific objectives, enabling us, for example, to reconstruct the entire temporal dynamics for every voxel in the image. Second, our design guarantees that the parameters we are interested in quantifying are optimally encoded, resulting in high-resolution and accurate measurements with more than a 3-fold improvement in scan time over MRF.

Together, these two properties of QTI can fundamentally shift the way we perform MR examinations: whereas a typical scan requires hundreds of repetitions to construct a single image, we produce as many images as we have repetitions - even while using 100-fold shorter TR than EPI based techniques[28,42]. Each image provides insights into the anatomical context, it has distinctive contrasts, offering rich and complementary information with high clinical and scientific value. Also, as these images also represent voxel-wise signal dynamics, we can rely on inference techniques to find the quantitative parameters that best describe the signal evolutions.

Moreover, and most importantly, we can design sequences such that signals evolve during acquisition towards maximally discriminative tissue contrasts, significantly simplifying subsequent image processing routines, and replacing, for example, complex brain tissue segmentation algorithms[34] by simple thresholding operations.

2   Signal modelling of spin dynamics in the transient-state

In the transient-state, as opposed to the steady-state, signals evolve dynamically throughout data acquisition, causing imaging artefacts when combining measurements from multiple repetitions to form a single image. Consequently, limited efforts have been made to image[44,55] or map parameters[22] in the transient-state, whereas most steady-state methods discard transient-state signals, only characterising the signals in an effort to minimize them[7,20]. On the other hand, the transient-state signal dependence on T1 and T2 is well known[39,41], and it is possible to cope with signal alterations from one repetition to the next by formulating a model of the signal over time $f_t(\eta; \theta)$ in a recursive manner:

$$f_t(\eta; \theta) = f_{t-1} \cdot g(\eta; \theta). \tag{1}$$

In Eq. 1, the value of the function f_t at time t is determined by the value of the function at time $t-1$ modulated by the operator $g(\eta; \theta)$, which in turn depends on two variable sets: η, the design variables of a potential acquisition scheme (e.g.

4   Gómez et al.

flip angle, TR, number of repetitions); and $\theta = \{T1,T2\}$, the parameters we wish to estimate. The operator $g(\eta;\theta)$ captures alterations to the spin dynamics given by physical phenomena such as radiofrequency excitation, relaxation, or gradient dephasing and can be simulated with a framework that describes the evolution of magnetisation over time named extended phase graphs[52]. We use this signal model in three serial steps: to determine the optimal design variables η; to reconstruct the entire spatiotemporal image space, that is, the temporal function f_t for every spatial voxel in the image; and to provide a voxel-wise estimate of θ for parametric mapping.

3   Sequence design with optimal encoding

Recently, MRF proposed the use of arbitrary and random patterns of η to estimate θ. However, this pseudorandom acquisition results in suboptimal encoding of the parameters of interest and casts uncertainty into how the resulting MRF signals provide additional relevant information. QTI, contrary to MRF, designs the acquisition to achieve specific objectives, allowing for the direct use and interpretation of transient-state signals. The design also maximises parameter encoding with an accelerated acquisition, and therefore, experimental efficiency.

To achieve this, we rely on Bayesian decision theory to guide our experimental design[36,50]; where we aim at finding an acquisition scheme that maximises the expected information gain while fulfilling all design constraints. Using the signal model in Eq. 1, we can define a utility functional for the information gain provided a particular θ:

$$u(\eta;\theta) = \det \sum_t \begin{pmatrix} \frac{\partial^2 f_t}{\partial \theta_1^2} & \cdots & \frac{\partial^2 f_t}{\partial \theta_1 \theta_N} \\ \vdots & \ddots & \vdots \\ \frac{\partial^2 f_t}{\partial \theta_N \theta_1} & \cdots & \frac{\partial^2 f_t}{\partial \theta_2^2} \end{pmatrix}. \tag{2}$$

Hence, for every possible experiment we use Eq. 2 to compute the utility functional for a specific parameter combination; and, in a Bayesian manner, marginalize the utility over a prior distribution to find the overall utility:

$$U(\eta) = \int_\theta \log u(\eta;\theta)\pi(\theta)d\theta. \tag{3}$$

The prior distribution $\pi(\theta)$ was informed by literature[9,12,28,31,43,53] and represents mean T1/T2 values and standard deviations of different tissue classes of interest. In brain scans, for example, these are: grey matter (GM), white matter (WM), cerebrospinal fluid (CSF), and blood vessels (BV) (Fig. 2a). Finally, the optimal design is determined as the one that maximises the utility whilst satisfying three objectives: speed, smoothness, and contrast. Speed is determined by considering only experiments with an acquisition readout less or equal to 4 seconds per slice; smoothness is computed via the average gradient of the signals
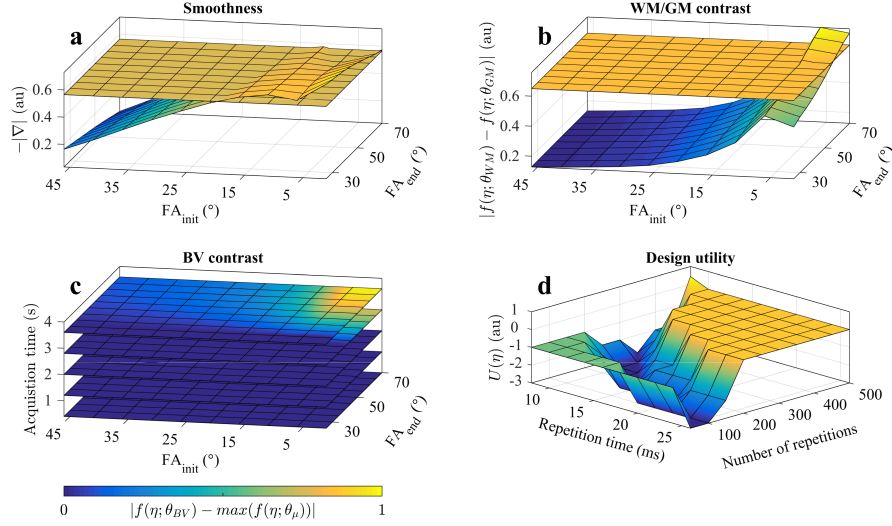
Fig. 1. Constrained Bayesian experimental design. a, Smoothness of the signals, computed by the negative of the absolute value of the gradient over time $(-|\nabla|)$ and the corresponding design threshold. Large initial flip angles produce oscillatory signals, increasing the gradient and consequently decreasing overall smoothness. The horizontal plane represents the smoothness threshold, where we consider a design as valid only if it is above the threshold **b,** WM/GM contrast, calculated by the absolute difference between mean WM and GM transient-state signals. Contrast is maximized when the initial flip angle is small and the final flip angle large. The horizontal plane refers to the contrast threshold. **c,** BV contrast over multiple acquisition times. The T1/T2 composition in BV results in contrast in lengthier acquisitions, where small initial flip angles and large final angles maximize the contrast. **d,** Design utility with constraints. Areas with zero or negative utility indicate that one or more of the design criteria were not met. -3 indicates that smoothness was below the established threshold, while -2 and -1 refer to BV and WM/GM contrast, respectively. The area with zero utility shows where the acquisition readout time exceeds 4 s (readout time = number of repetitions × repetition time).

over time, where we desire to obtain smooth transient responses by avoiding signal oscillations[7]; and WM/GM as well as BV contrast is defined as the maximal signal difference of the tissue's mean value over time (Fig. 1 and Fig. 2e).

The resulting design consists of an inversion pulse followed by a variable flip angle ramp (Fig. 2b), constant repetition and echo times (TE) with TE/TR = 2/8 ms, and an unbalanced gradient moment in each repetition. This encoding strategy, while seemingly simple, is highly efficient: the first 200 repetitions encode mostly for T1 as the magnetisation recovers from the inversion with T1 relaxation, and the last 300 repetitions encode mostly for T2, as T2 relaxation affects the amount of magnetisation available to be excited in the next repetition. Hence, tissues with longer T1 will have an inversion later in time (Fig. 2c)

6   Gómez et al.
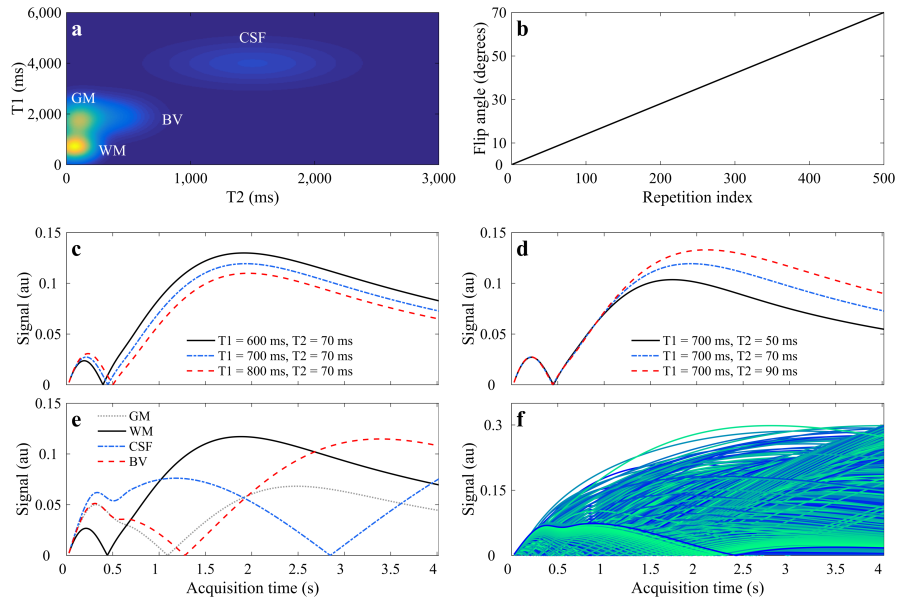
Fig. 2. Optimal encoding scheme for tissue priors and transient-state signals.
a, T1 and T2 space with Gaussian priors of four tissue classes: GM, WM, CSF, and
BV. **b**, Flip angle ramp corresponding to the optimal encoding scheme. **c-d**, Signal
evolutions for varying T1/T2 values, where **(c)** longer T1s (dashed, red line) experience
their inversion later in time and **(d)** shorter T2s (continuous, black line) produce higher
signal decay throughout the course of the experiment. **e**, Signal evolution from the mean
value of the four classes. In this example, WM/GM contrast is maximal close to the
inversion of GM, while BV contrast becomes apparent towards the end of the sequence.
d, Ensemble of signals simulated from a broad range of T1 and T2 values. As signals are
smooth and exhibit correlation, it is possible to use them to create a lower dimensional
subspace for image reconstruction.

and tissues with shorter T2 will cause a faster signal decay by allowing less mag-
netisation to recover for the next excitation (Fig. 2d). Furthermore, our design
leads to maximal WM/GM contrast at an acquisition time of approximately 1.1
seconds and BV contrast towards the end of the acquisition (Fig. 2e). Finally,
small flip angle variations generate smooth signal evolutions, wherein similar
tissue types will have similar evolutions, while different tissue types will distin-
guish from each other throughout the course of the acquisition. Therefore, one
can observe that a simulated ensemble of signals exhibits a certain level of corre-
lation, spreading a continuum over the signal space (Fig. 2f). It is precisely these
two factors, signal smoothness and correlation, that allow us to reconstruct the
spatiotemporal image space.

4 Spatiotemporal image space reconstruction and parameter estimation

If we would attempt to measure the spatiotemporal image space, the scan time would increase significantly. Even for the time-efficient MRF, rodent experiments which fully sampled the temporal signal in a 3D volume required over 17 hours of scan time[2]. Fortunately, compressed sensing provides mathematical theory for recovering full images from undersampled data by incorporating prior knowledge into the reconstruction formulation[29]. Here, prior knowledge takes the form of spatiotemporal data correlations given by the signal model and the design of the acquisition scheme.

Temporal correlations are present in the transient-state signals by design. That is, we rely on the exponential nature of the Bloch equations and use small flip angle variations such that small changes in T1/T2 will result in smooth differences over the transient-state signals (Fig. 2c-d). Spatial correlations are a given in biological tissue because similar tissue types have similar relaxation values[9,12,28,31,43,53]. For example, the GM in the cortex has longer T1 and T2 times than WM, determined by myelinated areas of the brain; and CSF, concentrated around the brain and inside the ventricles, has the longest T1 and T2 times (see Table 2 for reference values). Thus, local spatial neighbourhoods exhibit a high level of correlation in their relaxation times, and, consequently, also a high level of temporal correlation. Therefore, one can exploit these correlations with image reconstruction algorithms[1,46,56] to obtain a series of unaliased images for every point in time (Fig. 5b).

Once the images are reconstructed, we make use of high-performance computing for Bayesian inference[16] to obtain a voxel-wise estimation of T1 and T2 with their associated uncertainties. This can be done by calculating the posterior probability density function $p(\theta|x_t, f_t)$ of the parameters given the reconstructed data x_t and our signal model f_t:

$$p(\theta|x_t, f_t) = \frac{p(x_t|\theta, f_t)\pi(\theta)}{p(x_t|f_t)}. \tag{4}$$

In Eq. 4, $p(x_t|\theta, f_t)$ is the likelihood of observing the data from the model, $\pi(\theta)$ is the prior, and $p(x_t|f_t)$ is the evidence of the model. From the probability density function, we can obtain the maximum likelihood of each of the parameters in the model (T1 and T2), while PD is estimated as the scaling factor between the data and the model[30], leading to the final quantification of three parameters: T1, T2, and PD. In conclusion, QTI results in one image per repetition, 500 in this work, interpretable voxel-wise dynamics, and the corresponding parameters that best describe the signal evolution.

8   Gómez et al.

## 5   Benchmarking QTI: measurement accuracy, precision, and efficiency

In parameter mapping, developed methods can be compared against each other in terms of accuracy, precision, and efficiency of measurements. In its original form, MRF showed tremendous potential by increasing the efficiency of the previously most efficient mapping method[6] by almost a factor of 2, while maintaining measurement accuracy and precision[30]. However, the original implementation of MRF is sensitive to banding artefacts caused by inhomogeneous static fields, leading to the development of a robust version of MRF that makes use of unbalanced gradients in each repetition[24]. This version of MRF has now become state-of-the-art, has been extensively validated for reproduciblity[23], and has been used in multiple subsequent works[2,3,8,13,17,18,56]. Our proposed technique also relies on transient-state encoding and an unbalanced gradient, making both methods directly comparable.

   In Fig. 3 we provide a comparison of QTI versus MRF using agar phantoms, displaying accuracy and efficiency of measurements. Figure 4 compares dictionary matching with maximum likelihood estimations and parameter uncertainty. In Supplementary Fig. A.2 we also analyse the precision of measurements as a function of scan time. Table 1 provides a benchmark of QTI against different MRF variants in terms of resolution, time efficiency, mapping, uncertainty quantification, and imaging.

   In Fig. 3a and b we observe that QTI has a comparable accuracy to MRF, with a concordance correlation coefficient[27] to the reference of 0.9940 and 0.9945 for T1 and T2, respectively. On the other hand, Fig. 3c and d evidence that QTI is, on average, 3.90 more efficient than MRF. This increase in scan efficiency is due QTI's optimal T1 and T2 encoding with an accelerated acquisition. For T2 quantification, QTI is also more precise than MRF for shorter scans (Supplementary Fig. A.2). Figure 4 shows that matching noisy MRF data to a simulated dictionary yields the closest match within the discretization bounds of the dictionary, while the maximum likelihood estimation diverges from the reference and has high parameter uncertainty. QTI estimates with dictionary matching are also subject to the dictionary discretization, but maximum likelihood esti-

Table 1. Resolution, time efficiency, mapping, and imaging capabilities of QTI versus MRF.

	MRF			QTI	
	Ma[30]	Jiang[24]	Cloos[4]	QTI	QTI+B1
Resolution (mm^2)	2.3×2.3	1.17×1.17	1.4×1.4	1.3×1.3	1.3×1.3
Scan time per slice (s)	12	13	7-21	4	4.8
Clinical parameters	T1,T2,PD	T1,T2,PD	T1,T2,PD	T1,T2,PD	T1,T2,PD
Parameter uncertainty	No	No	No	Yes	Yes
Imaging	No	No	No	Yes	Yes
B1 mapping	No	No	Yes	No	Yes
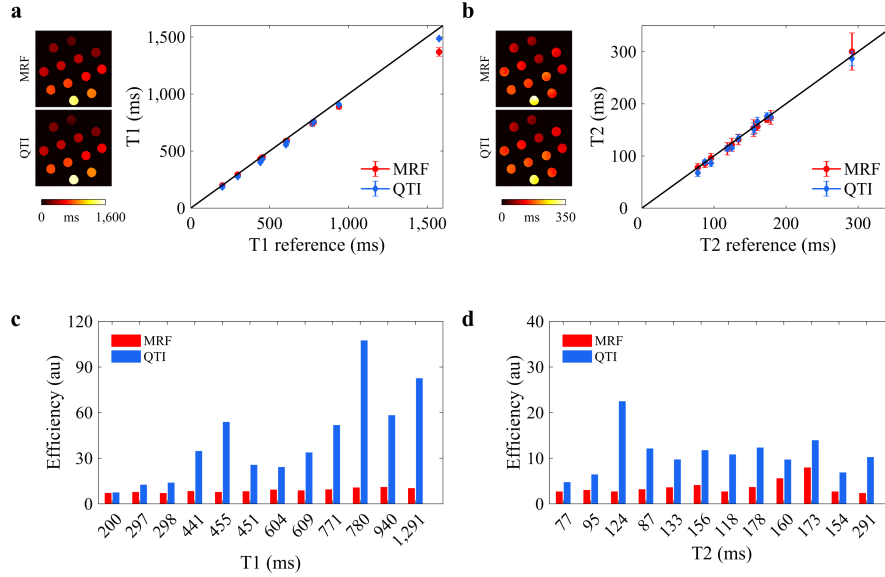
Fig. 3. Measurement accuracy and efficiency. a-b, Measurement accuracy for MRF and QTI with respect to the reference. Measurements show mean ± standard deviation over a 150 voxel region of each tube. The inset on the left of each image shows the estimated parametric maps in the phantom for each method. **c-d,** MRF and QTI efficiency. Efficiency is determined as precision per the square root of the acquisition time[30]. QTI has an average 4.8 and 3.0 higher T1 and T2 efficiency than MRF, respectively.

mates are not, and converge to a more accurate quantification with decreased uncertainty with respect to the reference. We also observed this phenomenon in volunteer data, where a maximum likelihood estimation with undersampled MRF data (Supplementary Fig. A.3) resulted in convergence to inaccurate local minima (Supplementary Fig. A.4). Our quantification of T1 and T2 of volunteer data is also consistent with literature findings for different tissue types in the brain (Table 2).

Table 2. *In vivo* data compared to literature[9,12,28,31,43,53].

|	T1 (ms)		T2 (ms)	
	QTI	Literature	QTI	Literature
Grey matter	1,248 ± 213	945−1,934	94 ± 20	61−106
White matter	799 ± 97	661−1,155	68 ± 12	52−72
Cerebrospinal fluid	4,078 ± 143	3,393−4,241	1,970 ± 408	1,000−2,500
Blood vessels	1,593 ± 316	1,465−2,017	256 ± 85	225−325

10   Gómez et al.
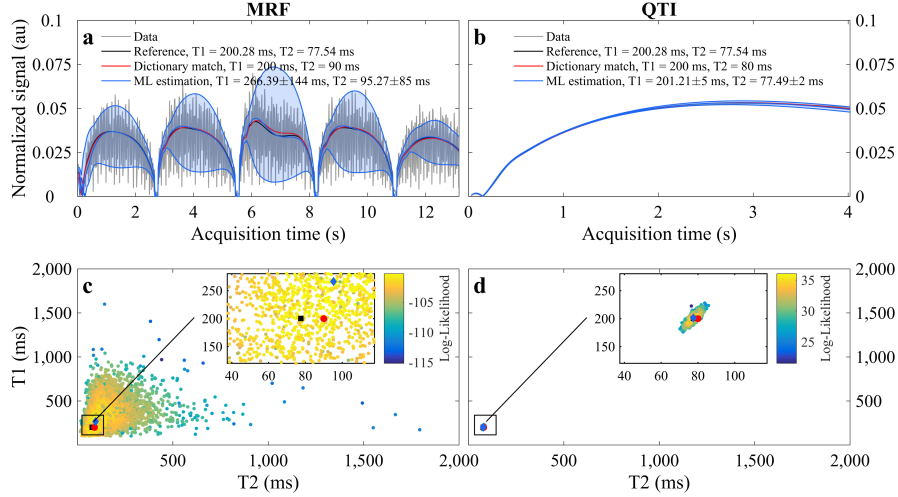
Fig. 4. Transient-state signals and parameter estimation. a-b, Transient-state signal evolutions for MRF and QTI. The parameters that best describe the signal evolutions can be estimated with dictionary matching (red), or with maximum likelihood (ML) estimations (blue). ML estimations also allow for uncertainty quantification, plotted as the light blue area. MRF signals are characteristically noisy, where dictionary matching gives the highest correlated dictionary entry to the signal to estimate T1 and T2. When the acquired data is not reconstructed with our proposed reconstruction, the estimated parameter uncertainty increases significantly **(a)**. The signal modelling for image reconstruction employed in QTI allows for the recovery of denoised signals, facilitating both dictionary matching and parameter inference with a ML estimation **(b)**. Here, the uncertainty decreases to 2.5% of the reference estimate. **c-d,** Parameter estimation in T1/T2 space. The scatter plot represents the log-likelihood of observing the parameters given the reconstructed data and the model, the black square shows the reference value, the red circle is the value estimated with dictionary matching, and the blue diamond represents the ML estimate obtained from the posterior probability density function in Eq. 4. Compared to MRF, QTI displays less uncertainty, produces estimates with higher likelihood, and closer to the reference.

6   Beyond parametric mapping: transforming image processing

QTI achieves an unconstrained, high resolution, and more efficient quantification of multiple parametric maps over previous MRF variants (Table 1), while also yielding 500 images, and an interpretable signal evolution of different tissue types (Fig. 5). For comparison, a traditional, high-resolution scan with a matrix size of 256×256 with equivalent TR would not even produce two images (it would need 512 repetitions), and MRF requires between 7 and 13.2 seconds per slice to generate parametric maps. Even when coupled with an appropriate reconstruction[5,14,56], the resulting images provide no immediate clinical
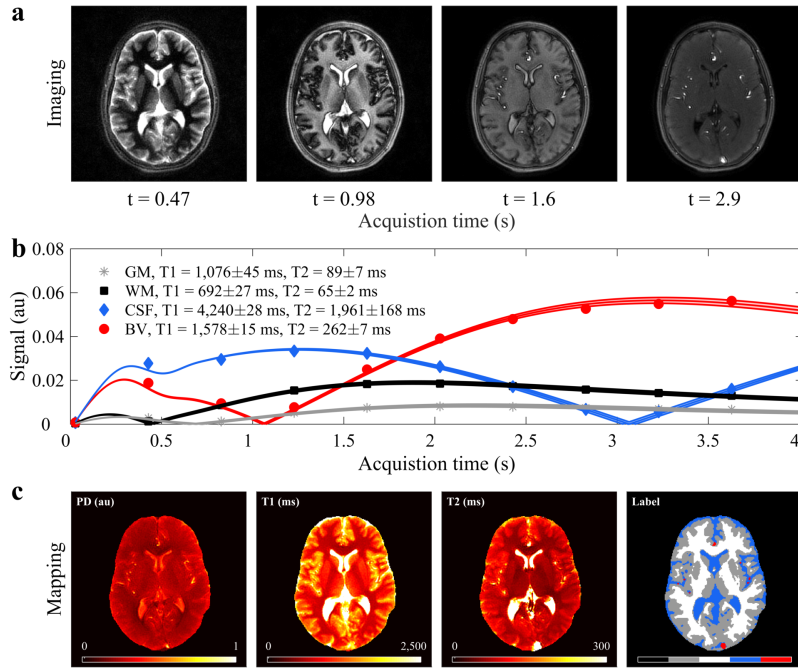
Fig. 5. Imaging, signal dynamics and parametric mapping. a, Reconstructed QTI images produce unique contrast throughout the acquisition. The contrast is also informative: at t = 0.47 s, WM is close to its inversion time, thus has low signal, followed by GM with longer T1 and then CSF with the longest T1; at t = 0.98 s, GM is approximating its inversion and WM has not yet been affected by T2 relaxation, inverting the WM/GM contrast of the previous image; at t = 1.6 s CSF signal intensity has started to decrease; and, finally, at t = 2.9 s most CSF has been nulled due to the inversion, but blood vessels, which have a shorter T1 and T2 compared to CSF, now have high signal intensity. **b**, Signal dynamics for the each of the tissue classes and the corresponding maximum likelihood and parameter uncertainty. The discrete points represent measured data points, while the continuous lines are the signals which best fit the data ± the corresponding uncertainty. **c**, Parametric maps obtained through maximum likelihood estimation. The last pane also shows corresponding tissue labels, obtained with nothing but a set of simple thresholding operations on the images in **(a)**.

information due to the pseudorandom acquisition process in MRF. Also, while QTI does not explicitly encode for transmit field inhomogeneities through B1 mapping[2,4], our formulation allows to incorporate a separate B1 map prior to parameter estimation for correction of inhomogeneous fields (Supplementary Fig. A.5). Thus, by using fast B1 mapping methods[35], QTI can be used at any field strength with increased efficiency. QTI is also scalable to high-dimensional spaces, for contrary to dictionary matching, the number of required computa-

12   Gómez et al.

tions for parameter estimation does not scale exponentially with the number of parameters in the model. These parameter estimates, alongside our signal model, can also be used to simulate any given acquisition scheme to synthesise new contrasts[51] for different image processing tasks. In fact, the amount and quality of data produced by QTI has the potential of transforming image processing through simplification. An example of this is displayed in Fig. 5, where thresholding of the images displayed in Fig. 5a leads to the tissue segmentation shown in Fig. 5c.

7   Discussion

QTI is a novel method for simultaneous imaging and multiparametric mapping that goes beyond the limit of what was previously possible in MRI. We build on cutting-edge acceleration techniques, namely parallel imaging and compressed sensing, and surpass their capabilities by incorporating optimal parameter encoding in the transient-state and physical modelling into the reconstruction formalism, enabling accurate, high-resolution results in 4.02 seconds per slice, over three times faster than MRF. Besides parametric mapping, the images generated by QTI provide unique diagnostic value. Over the dynamic evolution of different tissue types, unique contrasts will appear, allowing for a comprehensive assessment of a tissue's condition. For example, blood vessels are not clearly visible in the parametric maps, but their unique T1/T2 composition will lead to a signal hyper-intensity towards the end of the scan, enabling immediate visualization and valuation. This could significantly impact diagnosis and monitoring, for example, in stroke and other vascular diseases[11,40].

   QTI also creates new opportunities in MRI. First, it radically simplifies image processing. For instance, by selecting images with optimized contrast, simple thresholding operations lead to brain and tissue segmentation without the need of applying nonlinear image registration or classification methods. Second, the combination of temporal images with parametric maps creates new dimensions for biomarker exploration, which could potentiate the early identification of multiple diseases[47]. Also, our proposed design framework can be used to systematically encode additional MR-sensitive parameters, such as diffusion via gradient manipulation or magnetisation transfer using off-resonance pulses. Hence, QTI converts the long-time aspiration of having a single scan for multiparametric imaging and quantification into a reachable objective. Moreover, while we have provided a demonstration for 2D slices, the extension of QTI into three-dimensional spatial encoding will further increase its efficiency. Finally, QTI boosts the performance of existing imaging hardware. While we have shown fast, high-resolution results obtainable with standard clinical scanners, QTI could also push the limits of speed and resolution of scanners with more powerful image encoding gradients[42]. On the other hand, as QTI recovers spatiotemporal signal dynamics from corrupted and noisy data, it could also be used to relax hardware constraints. Thus, integrating QTI into ultralow field-strength scanners[38] would significantly increase their capabilities and diagnostic value,

potentiating the commercialization of robust, affordable, and portable MRI devices. This in turn, would transform MRI into a commodity instead of a luxury, increasing patient access and benefiting the population and healthcare systems on a global scale.

8 Methods

Signal modelling. Extended phase graphs[21,52] provide a framework to predict transient-state signal evolutions from any given acquisition sequence. They work by describing the magnetisation in terms of Fourier configuration states, where physical phenomena are characterized via matrix operations on these states. We simulate the QTI sequence by first inverting the magnetisation to the negative longitudinal plane, and subsequently simulating serial radiofrequency pulses with the flip angles from Fig. 2b. In every repetition, we collect the data at TE = 2 ms, assuming the same TE for all the collected samples, and then wait TR = 8 ms before applying the next radiofrequency pulse. Before each new radiofrequency pulse, we simulate an unbalanced gradient moment by dephasing the configuration states[24].

Bayesian experimental design. We created a grid in T1/T2 space ranging from 0 to 3/6 seconds with 20/10 ms step sizes, respectively. We simulated the prior distribution over the grid using the following mean T1/T2 values: 1,700/95 ms for GM; 685/65 ms for WM; 4,000/1,500 ms for CSF; and 1,900/275 ms for BV. For each tissue class, we generated a broad Gaussian prior (Fig. 2a) to ensure the resulting design is optimised for a wide range of values. We considered four design variables: initial flip angle from 1 to 50 degrees in 5 degree steps, final flip angle from 25 to 70 degrees in 5 degree steps, repetition times from 8 to 26 ms in 2 ms steps, and number of repetitions from 50 to 1,250 in 50 repetition steps. Only designs with an acquisition readout less or equal than 4 s were considered. For each potential design, we simulated the transient-state signal at every discrete point on the grid using the physical model of Eq. 1. We then computed the utility with Eq. 2 for each discrete point and marginalized it via Eq. 3 to find the overall utility. We also used the mean tissue values to calculate a normalized WM/GM and BV contrast and computed the gradient of the signal over time to assess smoothness. The selected design was the one with maximum utility that fulfilled all the design criteria (Fig. 1).

Temporal subspace creation and evaluation. By sampling the parameter space and simulating a signal with Eq. 1 for every sample, it is possible to create a dictionary of transient-state signal evolutions. One can then create a temporal subspace by applying principal component analysis over the signals in the dictionary[1,33,56]. We evaluated our temporal subspace based on two criteria: the sampling of the parameter space and the number of temporal coefficients used to represent it. One alternative to select the samples in parameter space is to use

14   Gómez et al.

the scheme proposed by MRF: sample a certain range with a specified density and simulate the signals for every sample. This continuous sampling approach, however, incorporates no prior knowledge into the parameter distribution and is not scalable to higher dimensional spaces. A second alternative is to use a training dataset and known tissue priors to inform the sampling. This has the advantage of significantly reducing the total number of parameter combinations, maintaining a low subspace error in areas with high sampling density (Supplementary Fig. A.1), and being scalable. The number of temporal coefficients, the second criterion for evaluating the subspace, presents a trade-off between bias and noise amplification. Supplementary Fig. A.1a and c display the normalized model error (NME)[46] for four different voxel types for both the continuously sampled dictionary and the data-driven alternative. For all cases, we can observe a sharp decrease in NME with the first four temporal coefficients and a stable decrease below 1% after six coefficients. Supplementary Fig. A.1b and d display the NME over the entire parameter space using eight subspace coefficients. The temporal subspace with the data-driven sampling and eight subspace coefficients is subsequently used to reconstruct images using spatiotemporal low rank constraints.

Image reconstruction with spatiotemporal low rank constraints. We formulate the image reconstruction problem to account for both the temporal spin dynamics and the Fourier relationship of the spatial signal. The acquired image x_t at every point in time is related to the acquired data y_t by an encoding operator $y_t = E_t x_t$; which in turn consists of three terms: $E_t = U_t FS$. U_t represents the spatial acquisition trajectory - a spiral waveform obtained with time-optimal gradient design[19], F is the non-uniform fast Fourier transform[10], and S are the coil sensitivities[48]. By additionally incorporating a temporal subspace projection[1,46,56] operation into the encoding operator, we can use iterative algorithms to reconstruct regularized subspace images. Here, we use the alternating direction method of multipliers[1,46,56,57] to reconstruct eight subspace images, regularized via a low rank thresholding on spatiotemporal images patches[14,46,49] of dimension $8 \times 8 \times 500$. We then project the subspace images back to the full temporal space to obtain the full spatiotemporal image space.

Parameter estimation and uncertainty quantification. We used $\Pi 4U$[16] for Bayesian uncertainty quantification and propagation. This high-performance computing tool relies on Transitional Markov Chain Monte Carlo Monte (TM-CMC) sampling to compute the posterior probability density function of the parameters given the data (the reconstructed voxel-wise signal) and the model (signal simulations) - see Eq. 4. From the probability density function, one can compute the maximum likelihood and corresponding parameter uncertainty (Fig. 4a-b and Fig. 5b). The maximum likelihood estimate can also be computed in a least-squares sense, by finding the parameter set that minimizes the error between the data and the model (Fig. 5c and Supplementary Figs. A.4 and A.5).

Data acquisition. We scanned the Eurospin T05 phantom[26], comprising of different vials with characteristic T1 and T2 values to perform the accuracy and efficiency analysis of QTI and MRF. For each method, we scanned the phantom with increasing acquisition times, from to 0.8 to 4.8 seconds per slice. For MRF, we also acquired 8 series of the full flip angle train (13.13 seconds per slice)[24] and processed all MRF data as in the original publications[30,24] to create a reference. For QTI, we adjusted the slopes such that they always increased to 70 degrees and we reconstructed maps using our image reconstruction and parameter estimation framework. Additionally, we scanned a single slice of a healthy volunteer (24 years, female) with MRF and QTI. For all methods, data was read out with a single arm of a variable density spiral waveform within each TR[19]. Each waveform required 18 interleaves to sample the centre of k-space and 89 to sample a full 22.5×22.5 field of view, resulting in 1.3 mm^2 in-plane resolution with 5 mm slice thickness. To increase sampling incoherence, the waveforms were rotated with the golden angle from one repetition to the next[54]. All experiments were performed on a 3T 750w scanner (GE Healthcare, Milwaukee, WI), with a 12-channel head receiver-only coil.

Statistical analysis. For each tube, we selected a central region of 150 voxels to perform statistical analysis. Both the concordance correlation coefficient and efficiency were estimated per the original MRF publications[24,30]. The concordance correlation coefficient estimates the average similarity of the quantification for all tubes with respect to the reference[27]. The efficiency is defined as the precision (mean / standard deviation) divided by the square root of the acquisition time. The time of each sequence considered for the efficiency analysis was 4.02 s for QTI (4.00 s readout plus 0.02 s inversion pulse) and 13.13 s for MRF (13.11 s readout plus 0.02 s inversion pulse).

9 Acknowledgments

References

1. Assländer, J., Cloos, M.A., Knoll, F., Sodickson, D.K., Hennig, J., Lattanzi, R.: Low rank alternating direction method of multipliers reconstruction for MR fingerprinting. Magnetic Resonance in Medicine (2017)
2. Buonincontri, G., Sawiak, S.: Three-dimensional MR fingerprinting with simultaneous B1 estimation. Magnetic Resonance in Medicine 00, 1–9 (2015)
3. Buonincontri, G., Schulte, R., Cosottini, M., Sawiak, S., Tosetti, M.: Spiral MRF at 7T with simultaneous B1 estimation. Proc Intl Soc Mag Reson Med (2016)

16   Gómez et al.

4. Cloos, M.A., Knoll, F., Zhao, T., Block, K., Bruno, M., Wiggins, C., Sodickson, D.: Multiparamatric imaging with heterogenous radiofrequency fields. Nature Communication pp. 1–10 (2016)

5. Davies, M., Puy, G., Vandergheynst, P., Wiaux, Y.: A Compressed Sensing Framework for Magnetic Resonance Fingerprinting. SIAM Journal on Imaging Sciences 7(4), 2623–2656 (2014)

6. Deoni, S.C.L., Rutt, B.K., Peters, T.M.: Rapid combined T1 and T2 mapping using gradient recalled acquisition in the steady state. Magnetic Resonance in Medicine 49, 515–526 (2003)

7. Deshpande, V.S., Chung, Y.C., Zhang, Q., Shea, S.M., Li, D.: Reduction of Transient Signal Oscillations in True-FISP Using a Linear Flip Angle Series Magnetization Preparation. Magnetic Resonance in Medicine 49(1), 151–157 (2003)

8. Doneva, M., Amthor, T., Koken, P., Sommer, K., Börnert, P.: Low Rank Matrix Completion-based Reconstruction for Undersampled Magnetic Resonance Fingerprinting Data. Proc Intl Soc Mag Reson Med (2016)

9. Ethofer, T., Mader, I., Seeger, U., Helms, G., Erb, M., Grodd, W., Ludolph, A., Klose, U.: Comparison of Longitudinal Metabolite Relaxation Times in Different Regions of the Human Brain at 1.5 and 3 Tesla. Magnetic Resonance in Medicine 50(6), 1296–1301 (2003)

10. Fessler, J.A., Sutton, B.P.: Nonuniform Fast Fourier Transforms Using Min-Max Interpolation. IEEE Trans Signal Processing 51(2), 560–574 (2003)

11. Fisher, M.: New Magnetic Resonance Techniques for Acute Ischemic Stroke. JAMA: The Journal of the American Medical Association 274(11), 908 (1995)

12. Gelman, N., Gorell, J.M., Barker, P.B., Savage, R.M., Spickler, E.M., Windham, J.P., Knight, R.A.: MR Imaging of Human Brain at 3.0 T: Preliminary Report on Transverse Relaxation Rates and Relation to Estimated Iron Content. Radiology 210(3), 759–767 (1999)

13. Gómez, P.A., Bounincontri, G., Molina-Romero, M., Ulas, C., Sperl, J.I., Menzel, M.I., Menze, B.H.: 3D Magnetic Resonance Fingerprinting with a Clustered Spatiotemporal Dictionary. Proc Intl Soc Mag Reson Med (2016)

14. Gómez, P.A., Ulas, C., Sperl, J.I., Sprenger, T., Molina-Romero, M., Menzel, M.I., Menze, B.H.: Learning a spatiotemporal dictionary for magnetic resonance fingerprinting with compressed sensing. MICCAI Patch-MI Workshop 9467, 112–119 (2015)

15. Haase, A., Frahm, J., Matthaei, D., Hanicke, W., Merboldt, K.D.: FLASH imaging. Rapid NMR imaging using low flip-angle pulses. Journal of Magnetic Resonance 67(2), 258–266 (1986)

16. Hadjidoukas, P., Angelikopoulos, P., Papadimitriou, C., Koumoutsakos, P.: Π4U: A high performance computing framework for Bayesian uncertainty quantification of complex models. Journal of Computational Physics 284, 1–21 (mar 2015)

17. Hamilton, J.I., Deshmane, A., Hougen, S., Griswold, M.A., Seiberlich, N.: Magnetic Resonance Fingerprinting with Chemical Exchange (MRF-X) for Quantification of Subvoxel T1, T2, Volume Fraction, and Exchange Rate. Proc Intl Soc Mag Reson Med 23, 16728 (2015)

18. Hamilton, J.I., Jiang, Y., Chen, Y., Ma, D., Lo, W.C., Griswold, M., Seiberlich, N.: MR fingerprinting for rapid quantification of myocardial T1, T2, and proton spin density. Magnetic Resonance in Medicine (2016)

19. Hargreaves, B.A., Nishimura, D.G., Conolly, S.M.: Time-optimal multidimensional gradient waveform design for rapid imaging. Magnetic Resonance in Medicine 51(1), 81–92 (2004)

20. Hargreaves, B.A., Vasanawala, S.S., Pauly, J.M., Nishimura, D.G.: Characterization and reduction of the transient response in steady-state MR imaging. Magnetic Resonance in Medicine 46(1), 149–158 (2001)
21. Hennig, J.: Echoes—how to generate, recognize, use or avoid them in MR-imaging sequences. Part I: Fundamental and not so fundamental properties of spin echoes. Concepts in Magnetic Resonance 3(3), 125–143 (1991)
22. Huang, T.y., Liu, Y.j., Stemmer, A., Poncelet, B.P.: T 2 Measurement of the Human Myocardium Using a T2 - Prepared Transient-State TrueFISP Sequence. Magnetic Resonance in Medicine 966, 960–966 (2007)
23. Jiang, Y., Ma, D., Keenan, K.E., Stupic, K.F., Gulani, V., Griswold, M.A.: Repeatability of magnetic resonance fingerprinting T1 and T2 estimates assessed using the ISMRM/NIST MRI system phantom. Magnetic Resonance in Medicine (2016)
24. Jiang, Y., Ma, D., Seiberlich, N., Gulani, V., Griswold, M.A.: MR Fingerprinting Using Fast Imaging with Steady State Precession (FISP) with Spiral Readout. MRM (2014)
25. Lauterbur, P.C.: Image formation by induced local interactions. Examples employing nuclear magnetic resonance. Nature 242, 190–191 (1973)
26. Lerski, R.A., de Certaines, J.D.: Performance assessment and quality control in MRI by Eurospin test objects and protocols. Magnetic resonance imaging 11(6), 817–33 (1993)
27. Lin, L.I.K.: A Concordance Correlation Coefficient to Evaluate Reproducibility. Biometrics 45(1), 255 (1989)
28. Lu, H., Nagae-Poetscher, L.M., Golay, X., Lin, D., Pomper, M., Van Zijl, P.C.M.: Routine clinical brain MRI sequences for use at 3.0 tesla. Journal of Magnetic Resonance Imaging 22(1), 13–22 (2005)
29. Lustig, M., Donoho, D., Pauly, J.M.: Sparse MRI: The application of compressed sensing for rapid MR imaging. Magnetic Resonance in Medicine 58, 1182–1195 (2007)
30. Ma, D., Gulani, V., Seiberlich, N., Liu, K., Sunshine, J.L., Duerk, J.L., Griswold, M.A.: Magnetic resonance fingerprinting. Nature 495, 187–192 (2013)
31. Mackay, A., Laule, C., Vavasour, I., Bjarnason, T., Kolind, S., M7dler, B.: Insights into brain microstructure from the T 2 distribution. Magnetic Resonance Imaging 24, 515–525 (2006)
32. Mansfield, P.: Multi-planar image formation using NMR spin echoes. Journal of Physics C: Solid State Physics 10(3), L55–L58 (1977)
33. McGivney, D., Pierre, E., Ma, D., Jiang, Y., Saybasili, H., Gulani, V., Griswold, M.: SVD compression for magnetic resonance fingerprinting in the time domain. IEEE TMI 0062, 1–13 (2014)
34. Menze, B.H., Jakab, A., Bauer, S., et al.: The Multimodal Brain Tumor Image Segmentation Benchmark (BRATS). IEEE Transactions on Medical Imaging 34(10), 1993–2024 (2015)
35. Nehrke, K., Börnert, P.: DREAM-a novel approach for robust, ultrafast, multislice B1 mapping. Magnetic Resonance in Medicine 68(5), 1517–1526 (2012)
36. Owen, D., Melbourne, A., Thomas, D., De Vita, E., Rohrer, J., Ourselin, S.: Optimisation of Arterial Spin Labelling Using Bayesian Experimental Design. MICCAI: International Conference on Medical Image Computing and Computer-Assisted Intervention 9902, 511–518 (2016)
37. Pruessmann, K.P., Weiger, M., Scheidegger, M.B., Boesiger, P.: SENSE: sensitivity encoding for fast MRI. Magnetic Resonance in Medicine 42, 952–962 (1999)

18   Gómez et al.

38. Sarracanie, M., Lapierre, C.D., Salameh, N., Waddington, D.E.J., Witzel, T., Rosen, M.S.: Low-Cost High-Performance MRI. Nature Scientific Reports pp. 1–9 (2015)
39. Scheffler, K.: On the transient phase of balanced SSFP sequences. Magnetic Resonance in Medicine 49(4), 781–783 (2003)
40. Schellinger, P.D., Jansen, O., Fiebach, J.B., Hacke, W., Sartor, K.: A Standardized MRI Stroke Protocol. Stroke 30, 765–769 (1999)
41. Schmitt, P., Griswold, M.A., Gulani, V., Haase, A., Flentje, M., Jakob, P.M.: A simple geometrical description of the TrueFISP ideal transient and steady-state signal. Magnetic Resonance in Medicine 55(1), 177–186 (2006)
42. Setsompop, K., Kimmlingen, R., Eberlein, E., et al.: Pushing the limits of in vivo diffusion MRI for the Human Connectome Project. NeuroImage 80, 220–233 (2013)
43. Smith, S.A., Edden, R.A.E., Farrell, J.A.D., Barker, P.B., Van Zijl, P.C.M.: Measurement of T1 and T2 in the cervical spinal cord at 3 Tesla. Magnetic Resonance in Medicine 60(1), 213–219 (2008)
44. Smith, T., Zun, G., Wong, E.C., Nayak, K.S.: Design and use of variable flip angle schedules in transient balanced SSFP subtractive imaging. Magnetic Resonance in Medicine 63(2), 537–542 (2010)
45. Stehling, M.K., Turner, R., Mansfield, P.: Echo-planar imaging: magnetic resonance imaging in a fraction of a second. Science 254(5028), 43–50 (1991)
46. Tamir, J.I., Uecker, M., Chen, W., Lai, P., Alley, M.T., Vasanawala, S.S., Lustig, M.: T2 shuffling: Sharp, multicontrast, volumetric fast spin-echo imaging. Magnetic Resonance in Medicine (2016)
47. Tofts, P.: Quantitative MRI of the Brain: Measuring Changes Caused by Disease. Wiley (2003)
48. Uecker, M., Lai, P., Murphy, M.J., Virtue, P., Elad, M., Pauly, J.M., Vasanawala, S.S., Lustig, M.: ESPIRiT - An eigenvalue approach to autocalibrating parallel MRI: Where SENSE meets GRAPPA. Magnetic Resonance in Medicine 71, 990–1001 (2014)
49. Ulas, C., Gomez, P.A., Sperl, J.I., Preibisch, C., Menze, B.H.: Spatio-temporal MRI Reconstruction by Enforcing Local and Global Regularity via Dynamic Total Variation and Nuclear Norm Minimization. Proceedings of International Symposium on Biomedical Imaging (ISBI) (2016)
50. Verdinelli, I., Chaloner, K.: Bayesian Experimental Design : A Review. Statistical Science 10(3), 273–304 (1995)
51. Warntjes, J.B.M., Dahlqvist Leinhard, O., West, J., Lundberg, P.: Rapid magnetic resonance quantification on the brain: Optimization for clinical usage. Magnetic Resonance in Medicine 60, 320–329 (2008)
52. Weigel, M.: Extended phase graphs: Dephasing, RF pulses, and echoes - pure and simple. Journal of Magnetic Resonance Imaging (2014)
53. Whittall, K.P., Mackay, A.L., Graeb, D.A., Nugent, R.A., Li, D.K.B., Paty, D.W.: In vivo measurement of T2 distributions and water contents in normal human brain. Magnetic Resonance in Medicine 37(1), 34–43 (1997)
54. Winkelmann, S., Schaeffter, T., Koehler, T., Eggers, H., Doessel, O.: An Optimal Radial Profile Order Based on the Golden Ratio for Time-Resolved MRI. IEEE Transactions on Medical Imaging 26(1), 68–76 (2007)
55. Worters, P.W., Hargreaves, B.A.: Balanced SSFP Transient Imaging using Variable Flip Angles for a Predefined Signal Profile. Magnetic Resonance in Medicine 64(5), 1404–1412 (2011)

56. Zhao, B., Setsompop, K., Gagoski, B., Ye, H., Adalsteinsson, E., Grant, P.E., Wald, L.L.: A Model-Based Approach to Accelerated Magnetic Resonance Fingerprinting Time Series Reconstruction. Proc Intl Soc Mag Reson Med (2016)
57. Zhao, B., Setsompop, K., Ye, H., Cauley, S., Wald, L.L.: Maximum Likelihood Reconstruction for Magnetic Resonance Fingerprinting. IEEE Trans Med Imaging (2016)

A   Supplementary Information
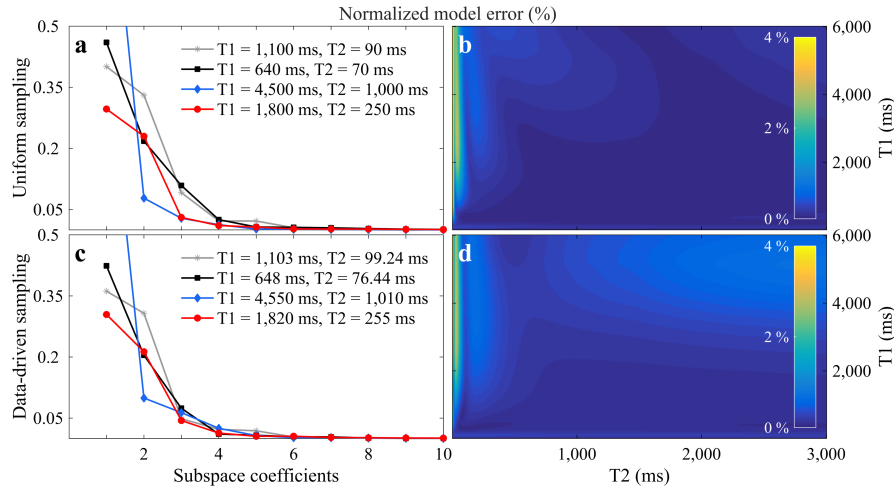
Fig. A.1. Normalized model error for subspace projection. a, c, Normalized model error (NME) as a function of temporal coefficients for each tissue type for a uniformly sampled **(a)** and data-driven **(c)** dictionary. In both cases, the NME decreases rapidly with the first four temporal coefficients and reaches levels under 1% after six coefficients. **b, d**, NME of the entire parameter space using eight subspace coefficients. Here, the NME remains below 4% for both alternatives, even when the data-driven dictionary has significantly less samples than its uniformly sampled counterpart ($\sim 1 \times 10^3$ vs $\sim 1 \times 10^6$).
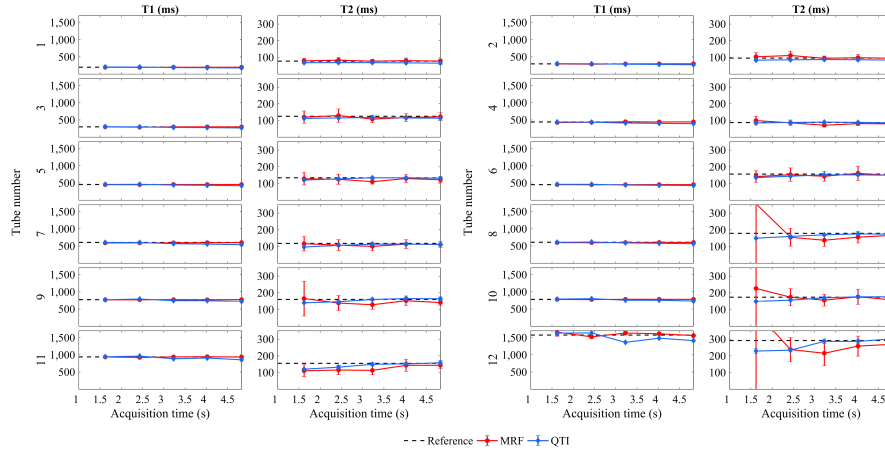
Fig. A.2. Accuracy and precision of measurements versus scan time. Every point shows mean ± standard deviation over the 150 masked voxels in each tube. Both MRF and QTI show a high degree of robustness in T1 estimates. This is due to the inversion pulse at the beginning of the sequences, yielding increased T1 sensitivity in the first two seconds of the acquisition. In QTI, T2 sensitivity becomes relevant after 200 repetitions (1.6 s) and is sufficiently encoded after 4 s, time at which QTI measurements become unbiased. T2 measurements with MRF are less precise (as evidenced by a larger standard deviation) for shorter acquisitions.
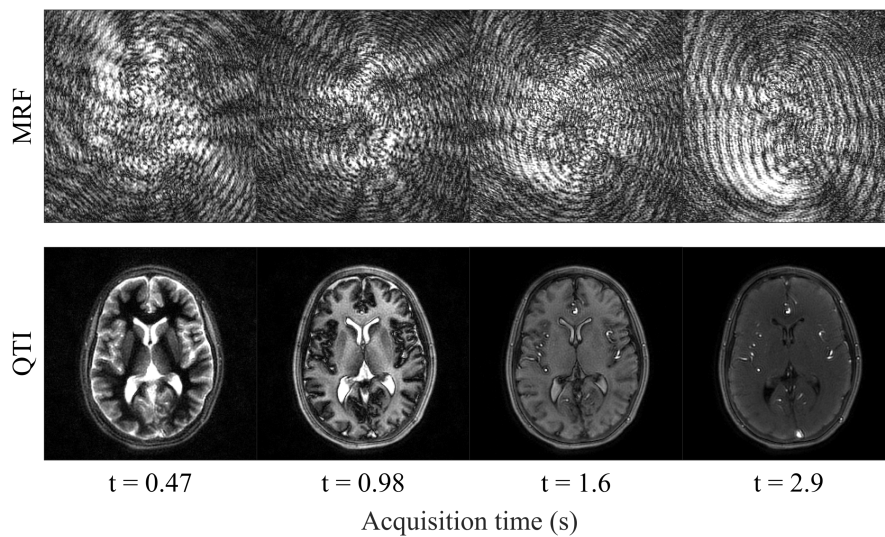
Fig. A.3. Temporal image series at different acquisition times. Whereas MRF results in aliased measurements, QTI reconstructs images by exploiting spatiotemporal data correlations. The first two images reflect maximal WM/GM contrast, while the last show the process of CSF nulling and maximisation of BV contrast (see also Fig. 2e). QTI images also shown in Fig. 5a.
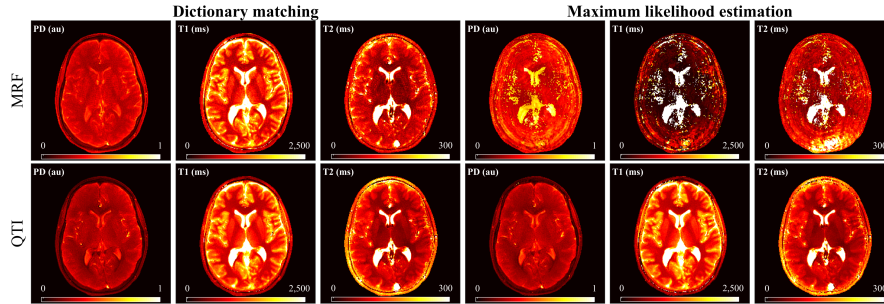
Fig. A.4. Quantitative maps versus MRF. As demonstrated previously for MRF, matching noisy data to the simulated dictionary results in consistent parametric maps[24,30]. Conversely, the high level of noise in the data restricts maximum likelihood estimations and results converge to inaccurate local minima. In QTI, the proposed reconstruction eliminates aliasing and reduces noise levels, facilitating convergence of maximum likelihood estimations. Maximum likelihood estimates of QTI are also shown in Fig. 5c.
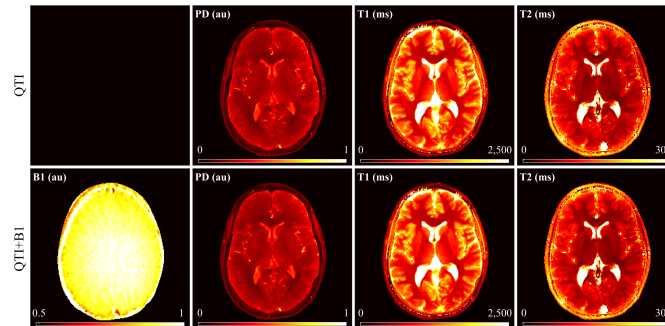
Fig. A.5. B1 mapping. B1 maps obtained with a fast B1 mapping method[35] require 0.8 s per imaging slice. Maximum likelihood estimates of QTI without B1 mapping are also shown in Fig. 5c.

A.1.2   *A Diffusion Model-free Framework with Echo Time Dependence for Brain Tissue Microstructure Characterization*

Peer-reviewed Journal Paper

Authors: M. Molina-Romero, **PA. Gómez**, JI. Sperl, DK. Jones, MI. Menzel, BH. Menze

Abstract: Purpose: The compartmental nature of brain tissue microstructure is typically studied by diffusion MRI, MR relaxometry or their correlation. Diffusion MRI rely on signal representations or biophysical models. MR Relaxometry and correlation studies are based on regularized Inverse Laplace Transform (ILT). Here we introduce a general framework to characterize microstructure that does not depend on diffusion modeling and substitutes the ill-posed ILT by BSS. This framework yields proton density, relaxation times, volume fractions and signal separation of the tissue components. **Theory and methods**: Diffusion experiments repeated for several echo times contain entangled diffusion and relaxation compartmental information on the microstructure. They can be disentangled by BSS using a physically constrained non-negative matrix factorization. **Results**: Computer simulations, phantom and in vivo results proved the disentangling capability of BSS, and its potential to estimate proton density, compartmental volume fractions and spin-spin relaxation times. **Conclusion**: Formulation of the diffusion-relaxation dependence as a BSS problem avoids diffusion modeling and ILT, circumventing geometrical simplifications of the tissue complexity and ill-posed ILT. Thus, BSS introduces a framework that paves the way to a deeper analysis of microstructure compartmentalization.

Contribution of thesis author: Discussion of algorithmic implementation and experimental design, manuscript revision and editing.

A diffusion model-free framework with echo time dependence for brain tissue microstructure characterization

Miguel Molina-Romero[1,2,*] Pedro A. Gómez[1,2] Jonathan I. Sperl[2] Derek K. Jones[3,4] Marion I. Menzel[2] Bjoern H. Menze[1]

1 Computer Science, Technical University Munich, Munich, Germany

2 GE Global Research Europe, Garching, Germany

3 CUBRIC, Cardiff University, Cardiff, UK

4 School of Psychology, Faculty of Health Sciences, Australian Catholic University, Victoria, Australia

* Corresponding author:

Name	Miguel Molina Romero
Department	Computer Science
Institute	Technical University Munich
Address	Boltzmannstr 11
	85748 Garching
	Germany
E-mail	miguel.molina@tum.de

Manuscript word count:	4996
Abstract word count:	199

Abstract

Purpose: The compartmental nature of brain tissue microstructure is typically studied by diffusion MRI, MR relaxometry or their correlation. Diffusion MRI rely on signal representations or biophysical models. MR Relaxometry and correlation studies are based on regularized inverse Laplace transform (ILT). Here we introduce a general framework to characterize microstructure that does not depend on diffusion modeling and substitutes the ill-posed ILT by blind source separation (BSS). This framework yields proton density, relaxation times, volume fractions and signal separation of the tissue components.

Theory and methods: Diffusion experiments repeated for several echo times contain entangled diffusion and relaxation compartmental information on the microstructure. They can be disentangled by BSS using a physically constrained non-negative matrix factorization.

Results: Computer simulations, phantom and in vivo results proved the disentangling capability of BSS, and its potential to estimate proton density, compartmental volume fractions and spin-spin relaxation times.

Conclusion: Formulation of the diffusion-relaxation dependence as a BSS problem avoids diffusion modeling and ILT, circumventing geometrical simplifications of the tissue complexity and ill-posed ILT. Thus, BSS introduces a framework that paves the way to a deeper analysis of microstructure compartmentalization.

Introduction

More than fifty years have passed since Stejskal and Tanner published their early work on pulsed gradient spin echo (PGSE) (39). Thereafter, diffusion weighted imaging (DWI) became an essential tool for non-destructive tissue microstructure characterization. The pioneering studies on ex vivo tissue and simulations of Krägger (25), Latour et al. (28), Szafer et al. (41) and Stanisz et al.(38) established the theoretical basis of the compartmental model of neural tissue.

These early contributions were later translated to target specific biomarkers for in vivo human studies. White matter (WM) anisotropy turned into fiber orientation with the introduction of DTI (4). The composite hindered and restricted model of diffusion MR (CHARMED) (2) extended DTI to two compartments with restricted and hindered diffusion behavior. On the same principles, the neurite orientation dispersion and density imaging (NODDI) model (47) introduced fiber orientation dispersion metrics and added an isotropic compartment. Additionally, axon diameter was addressed by AxCaliber (3) or ActiveAx (1). These and other approaches rely on diffusion signal representations, or a variety of geometrical biophysical assumptions of the underlying tissue compartments, producing a wide range of possible configuration (see (18)).

Parallel to the development of multicomponent diffusion tissue models, relaxometry addressed the compartmental nature of tissue microstructure from a different perspective (27). Multi-echo spin echo (SE) experiments combined with regularized inverse Laplace transform (ILT) for multiexponential fitting show the presence of multiple water components in the tissue. Up to date, non-negative least squares (NNLS) (30) is the gold standard to compute a regularized discrete ILT for several compartments (45, 31). Alternatively, the exponential analysis via system identification using Steiglitz–McBride (EASI-SM) for multicomponent estimation was introduced by Stoika et al. (40, 9). Moreover, mcDESPOT (16), used a spoiled gradient-recalled echo and a balanced steady-state free precession to yield relaxation, volume fractions and water exchange parameters for three compartments.

Nevertheless, the paths of diffusion MRI and MR relaxometry have been entangled over the years. Studies on ex vivo nerves with a diffusion-weighted CPMG sequence (36, 17) showed the existing relationship between compartmental T_2 decay and diffusivity. However, diffusion-weighted CPMG experiments need long acquisition times and high specific absorption rate that makes them unsuitable for human in vivo studies. Typically, two dimensional ILT was used to fit the data. This approach is highly ill-posed and requires a big amount of data for stabilization. Recently, Benjamini

et al. (6) introduced the marginal distributions constrained optimization (MADCO). A non-CPMG compressed sensing based solution that reduced the amount of necessary data for NMR diffusion-relaxation correlation experiments. Moreover, Kim et al. translated DR-COSY (11, 21) into imaging (DR-CSI) (26), using spatial regularization to reduce the necessary data and stabilize the ILT. Yet, they require specific diffusion protocols with increasing b-values along a unique diffusion direction, and repeated echoes or inversion times. Other alternatives combine diffusion models together with multicompartmental relaxation. For instance, inversion recovery DWI was used to identify fiber populations (15, 13); and WM integrity has been characterized using the axonal stick model and multiple echo times (TE) (43).

The compartmental analysis of the diffusion signal is intimately related to a recurrent issue: cerebrospinal fluid (CSF) contamination (37, 32). This problem has been tackled in several works. All the existing contributions agree on using a bi-tensor signal model: parenchyma and CSF. However, this is an ill-posed problem for a single shell and ill-conditioned for multiple shells acquisition (7). Spatial regularization was proposed by Pasternak et al. (35) relying on the local smoothness of the diffusion tensor. Later, a protocol optimization for multiple shells was presented by Hoy et al. (20), eliminating such a constraint. Other solutions regularize the problem by adding priors (42), or finding the best fitting to the model (19). Nevertheless, the CSF contribution to the diffusion signal depends on the TE. Thus, disentangling the tissue CSF volume fraction requires an approach that includes T_2 compartmental dependencies (42, 12, 34).

In the current work, we propose a general framework to study diffusion and relaxation characteristics in tissue microstructure. We entitle it as general because it does not model the compartmental diffusion behavior. Moreover, it replaces the ILT by a blind source separation (BSS) technique, reducing the minimum number of distinct echo times (to the number of compartments in the tissue) compared to ILT based methods. Other than the requirement to measure at more than one echo time, this framework is diffusion protocol agnostic. Thus, it can be used in combination with any protocol of interest. Our approach quantifies proton density (PD), compartmental volume fractions and transverse relaxation times. Importantly, it separates diffusion signals from each compartment independently, allowing for individual analyses and thus, performs CSF partial volume correction as direct application.

Theory

Following the Bloch-Torrey equation, we described the diffusion signal as a weighted sum of the signals from the compartments that compose the tissue:

$$X(TE, b) = S_0 \sum_{i=1}^{M} f_i e^{-\frac{TE}{T_{2_i}}} S_i(b). \tag{1}$$

Where, the compartmental diffusion sources S_i are weighted by their volume fraction, f_i, TE and T_{2_i}. The exponent of the ration between TE and T_{2_i} scales the contribution of each compartment to the acquired signal. Therefore, measuring at different TEs, produces distinct diffusion signals (14) with different weights from the compartmental signal sources.

As a result, the signal of a single voxel measured with a protocol accounting for multiple echoes can be formulated as:

$$\begin{bmatrix} X_1(TE_1, b) \\ \vdots \\ X_N(TE_N, b) \end{bmatrix} = S_0 \begin{bmatrix} f_1 e^{\frac{-TE_1}{T_{2_1}}} & \cdots & f_M e^{\frac{-TE_1}{T_{2_M}}} \\ \vdots & \ddots & \vdots \\ f_1 e^{\frac{-TE_N}{T_{2_1}}} & \cdots & f_M e^{\frac{-TE_N}{T_{2_M}}} \end{bmatrix} \begin{bmatrix} S_1(b) \\ \vdots \\ S_M(b) \end{bmatrix}, \tag{2}$$

where X_j, $j \in [1, N]$ are the diffusion acquisitions for N echo times. f_i and T_{2_i}, $i \in [1, M]$, are the volume fraction and T_2 decay for the ith compartment, and M is the number of compartments.

Eq. 2 can be expressed in its matrix form, $\mathbf{X}=\mathbf{AS}$. This is a matrix factorization of the measurements, $\mathbf{X} \in \mathbb{R}_{\geq 0}^{N \times n}$, into two new matrices: the mixing matrix, $\mathbf{A} \in \mathbb{R}_{\geq 0}^{N \times M}$, which is defined by the experimental TEs, the compartmental volume fractions, f, and T_2 decays; and the sources matrix, $\mathbf{S} \in \mathbb{R}_{\geq 0}^{M \times n}$, containing the diffusion sources of each sub-voxel compartment. Interestingly, we noticed from the definition of $\mathbf{A}$ that the ratio between the experimental TEs and T_{2_i}, determines the direction (or slope for $N = 2$) of the ith column vector of the mixing matrix. Therefore:

$$T_{2_i} = \frac{TE_k - TE_l}{log(\frac{a_{li}}{a_{ki}})}, \tag{3}$$

where $TE_k < TE_l$, and a_{ki} and a_{li} are the kth and lth elements of the ith column of the mixing matrix.

Additionally, diffusion is an attenuation contrast and as such, $S(b = 0) = 1$, which allows

rewriting Eq. 2 in the following form:

$$
\begin{bmatrix} X_1(TE_1, b=0) \\ \vdots \\ X_N(TE_N, b=0) \end{bmatrix} = S_0 \begin{bmatrix} e^{\frac{-TE_1}{T2_1}} & \cdots & e^{\frac{-TE_1}{T2_M}} \\ \vdots & \ddots & \vdots \\ e^{\frac{-TE_N}{T2_1}} & \cdots & e^{\frac{-TE_N}{T2_M}} \end{bmatrix} \begin{bmatrix} f_1 \\ \vdots \\ f_M \end{bmatrix}, \qquad [4]
$$

that together with $\sum_{i=1}^{M} f_i = 1$ solve for volume fractions and proton density (f_i and S_0) when the number of measurements matches the number of compartments ($M = N$). Contrary, when there exist more compartments than measurements ($M > N$), Eq. 4 is undetermined and f_i and S_0 cannot be estimated.

Factorizing **A** and **S** from **X** is known as blind source separation (BSS) (46) of mixed measurements into their generating sources (Figure 1). For BSS to identify these sources, they have to be distinct: $S_i \neq S_j \ \forall \ i \neq j$. Therefore, supported by literature (36, 17), we assumed them to be different.

There are four main approaches for BSS: principal component analysis (PCA) (24), independent component analysis (ICA) (22), non-negative matrix factorization (NMF)(8) and sparse component analysis (SCA) (10). PCA is not an applicable solution to the problem at hand because the diffusion sources are not orthogonal. ICA assumes, as prior knowledge, that the signal sources are statistically independent and have non-Gaussian distributions. However, diffusion MRI signals are correlated by the tissue structure and temperature, and they present a non-Gaussian distribution only in restricted compartments. Thus, ICA is not a suitable approach. In previous work we explored SCA (33). We found that, even though the results on simulations and real data for specific diffusion protocols were encouraging, finding a sparse and disjoint domain to meet the requirements of the method is not always possible for arbitrary diffusion protocols. We observed the same issue for a version of NMF that enforces sparsity in a similar way (34).

In the present work, we followed a BSS approach based on NMF (**X**, **A** and **S** are non-negative). Instead of sparsity, we used a popular NMF solver: alternating least squares algorithm (ALS) (8). We extended ALS to account for physically plausible limitations resulting in Algorithm 1. We referred to it as constrained alternating least squares (cALS). Literature values of compartmental T_2 (31) allowed us to limit the solution space of the columns of **A** (Eq. 3). Moreover, for in vivo data, CSF is known to be isotropic with high diffusivity ($3 \cdot 10^{-3}$ mm^2/s) (37), adding extra prior information. Constraints and priors enforce cALS to converge towards physically realistic solutions (Figure 1).

Algorithm 1 Constrained Alternating Least Squares (cALS)

1: **procedure** CALS($\mathbf{X}$)

2:     Use priors on T_2 and experimental TEs to initialize the direction of the columns of $\mathbf{A}$.

3:     **while** iter < maximum iterations **do**

4:         Solve for $\mathbf{S}$ in $\mathbf{A}^T\mathbf{A}\mathbf{S}=\mathbf{A}^T\mathbf{X}$.   ▷ Least Squares.

5:         Set all negative elements of $\mathbf{S}$ to 0.   ▷ Non-negativity.

6:         [Fix the one element of $\mathbf{S}$ to a known signal.]   ▷ If analytical expression is known.

7:         Solve for $\mathbf{A}$ in $\mathbf{S}\mathbf{S}^T\mathbf{A}^T=\mathbf{S}\mathbf{X}^T$.   ▷ Least Squares.

8:         Set all negative elements of $\mathbf{A}$ to 0.   ▷ Non-negativity.

9:         Constrain the directions of the columns of $\mathbf{A}$.   ▷ T_2 consistency.

10:     **end while**

11:     return $\mathbf{A}$

12: **end procedure**

Following the factorization of $\mathbf{A}$, we estimated T_2 and f for each compartment, as described in Eqs. 3 and 4, and recalculated the actual $\mathbf{A}$. This is an important step since the norm of the columns of the factorized $\mathbf{A}$ do not inform about the volume fractions. Then, $\mathbf{S}=\mathbf{A}^{-1}\mathbf{X}$ is calculated.

An iterative algorithm as cALS inverts $\mathbf{A}$ repeatedly. This enforced $\mathbf{A}$ to be non-singular, and thus, introduces a new requirement in our framework. Following Eq. 2, $\mathbf{A}$ is non-singular when the $T_{2_i} \neq T_{2_j} \; \forall \; i \neq j$. Hence, agreeing with literature (36, 17), we assumed transverse relaxation times from each compartment to be distinct.

Methods

1   Phantom experiment

We built a phantom based on pure water and eleven different concentrations of agar and sucrose. Hence, eleven unique combinations of T_2 and diffusivity were produced (Table 1)(29). We scanned the phantom (see below) and defined ROIs over the tubes containing the eleven concentrations. Each ROI was independently processed with BSS to study the one compartment case (see section 1.1). Moreover, we mixed the signals from two ROIs to generate a pair of two compartments dataset and feed these mixtures to our BSS solver (see section 1.2). Finally, we combined three ROIs to consider the three compartments case, and separated them with BSS (see section 1.3). We aimed

to demonstrate that our framework is able to yield T_2 estimation for one compartment; and volume fraction, T_2 estimations and diffusion signal separation for two and three compartments.

For reference, we measured a multi-echo SE acquisition (Signa HDx 3T, GE Healthcare, Milwaukee, WI), with TE values from 10 to 640 ms in 10 ms increments; TR=3460 ms; NEX=2; matrix size of 128x128; FOV of 240 mm and slice thickness of 7 mm. In addition, eleven diffusion experiments were acquired for TE ranging from 77.5 to 127.5 ms with 5 ms step. We kept constant the following parameters: FOV=240 mm; slice thickness of 7 mm; matrix size of 64x64; TR=4 s; ASSET factor of 2; A/P diffusion direction; and 41 equally spaced b-values from 0 to 2000 s/mm^2.

The multi-echo SE signals were averaged within each ROI. Each signal was fitted with NNLS (30) using a log-scaled grid with 500 points of T_2 values between 10 ms and 2 s. We used the maximum value of the NNLS T_2 spectra as the reference value of each ROI (Figure 2). Besides, we also fit the signal from each ROI with EASI-SM (9) for assurance.

1.1   One compartment

For one compartment ($M = 1$), we processed diffusion data with BSS for ten pairs of TE measurements. We used pairs of TEs ($N = 2$) to include the relaxation effects in the dataset. The short TE was fixed to 77.5 ms. For each pair, the long TE was increased from 82.5 to 127.5 ms along the measured echo times. We constrained the solution space for the estimated T_2 between 10 and 2000 ms to account for all the ROIs. No other prior information was considered. We report the evolution of the BSS estimated T_2, for each ROI and the difference between short and long TE (ΔTE), against their reference values (Figure 2).

1.2   Two compartments

For two compartments ($M = N = 2$), we created two different datasets. First, we used the diffusion data measured at the shortest TE for ROI_6 and ROI_{11} as the sources, **S**. These signals did not contain relaxation information (Figure 3a). Thus, in order to mix them together we had to compute the mixing matrix (**A**) as in in Eq. 2. To this end, we used their reference T_2 values, the experimental TEs, and a volume fraction of $f_{ROI_6} = 0.7$ (Figure 3c). We named this as *simulated* dataset, given that the signals are mixed under ideal conditions. Second, we normalized the measured data for each ROI and TE to its maximum value at the shortest TE. This allows for posterior comparison of the volume fractions. In this case, the signals already contained the relaxation information (Figure 3b). Therefore, we did not need to compute **A**. We scaled the normalized measured signals by

the given volume fraction, and added them together to create the mixed measurements, $\mathbf{X}$. We referred to this dataset as *measured* (Figure 3c). It accounts for system imperfections like signal drift, imperfect non-diffusion weighting or eddy currents. To constrain the solution of the cALS algorithm we used $T_{2_{ROI_{11}}}$ and $S_{ROI_{11}}$ as prior knowledge and searched for $T_{2_{ROI_6}}$ between 0 and 200 ms.

1.3   Three compartments

We extended the two compartments experiment to three ($M = N = 3$) by adding ROI_5. *Simulated* and *measured* datasets were created as explained for two compartments (Figures 4a, b, c, d and e). In this case, we used volume fractions: $f_{ROI_5} = 0.2$ and $f_{ROI_6} = 0.6$. To limit the solution space of the cALS algorithm, we assumed $T_{2_{ROI_{11}}}$ and $S_{ROI_{11}}$ to be prior knowledge. Besides, we constrained $T_{2_{ROI_5}}$ and $T_{2_{ROI_6}}$ values between 0 and 50 ms, and 50 and 200 ms correspondingly. For the two and three compartment experiments we report the stability of the framework, the relative error of the parameters and the disentangling capability.

2   Simulation: searching for myelin

Clinical systems require long TEs to achieve the prescribed diffusion weighting. Contrary, myelin T_2 is considerably shorter than these echo time (31). Hence, the contribution of myelin to the observed signal is very low, impeding its detection. This makes simulations at short TEs a way to study the potential of BSS to detect myelin presence in the diffusion signal.

We generated a simulated dataset for tissue with three compartments ($M = 3$) using MATLAB (The MathWorks, Natick, MA). The first compartment (S_1) had $D_1 = 0.1 \cdot 10^{-3}$ mm^2/s, $T_{2_1} = 15$ ms and $f_1 = 0.25$; the second compartment (S_2) had $D_2 = 0.7 \cdot 10^{-3}$ mm^2/s, $T_{2_2} = 70$ ms and $f_2 = 0.6$; and the third compartment (S_3) had $D_3 = 3 \cdot 10^{-3}$ mm^2/s, $T_{2_3} = 2000$ ms and $f_3 = 1 - f_1 - f_2$. T_2 values were chosen from literature to represent myelin (S_1), IE water (S_2) and CSF (S_3) (31). We ran 200 simulations adding Rician noise for an SNR=300 at b=0 s/mm^2 and the shortest echo time. Three TE values ($N = 3$) were optimized to minimize the condition number of $\mathbf{A}$. We accounted for TE values between 10 to 150 ms (Figure 5).

To constrain the matrix factorization problem, we considered T_{2_3} and S_3 as prior information. The parameter space of T_{2_1} and T_{2_2} was limited from 1 to 40 ms and 40 to 200ms respectively. We report the stability of the framework, statistics on the relative error of the estimated parameters, and the disentangling capability.

3   In vivo clinical data

We aimed to prove that BSS has potential applications in clinical settings. To this end, we ran an experiment to analyze its performance for estimating tissue parameters and correcting for CSF contamination.

3.1   Data acquisition

Two young adult volunteers, male and female with an average age of 26 years, were scanned in a 3T GE MR750w (GE Healthcare, Milwaukee, WI). The in vivo study protocol was approved by our institutional review board and prior informed consent was obtained. First, we acquired seven diffusion PGSE EPI for TE values from 75.1 to 135.1ms with 10 ms steps. These series were measured with constant parameters: FOV=240 mm; slice thickness of 4 mm; TR=6 s; matrix size 96x96; ASSET factor 2; and 30 directions. Additionally, we measured a FLAIR multi-echo SE echo planar imaging (EPI) readout for 17 equally spaced TEs ranging from 20 to 260 ms. The same imaging parameters as for the diffusion experiments were prescribed with no acceleration (ASSET=0).

3.2   Data processing

Diffusion data for all TEs were first registered with FSL's FLIRT (23) to the shortest TE volume. Then, we processed them with BSS in pairs ($M = N = 2$) with fixed short TE equal to 75.1 ms. The long TE was increased from 85.1 to 135.1 ms for a total span of ΔTE of 60 ms (Figures 7 and 6). We used literature values of CSF ($T_{2_{CSF}} = 2$ s and $D_{CSF} = 3 \cdot 10^{-3}$ mm^2/s) as prior knowledge, and constrained the possible values of $T_{2_{IE}}$ between 0 and 200 ms (31, 37). We report maps for BSS relative factorization error (Figure 6a, b , g and l), CSF volume fraction (Figure 6c, h and m), proton density (Figure 6d, i and n), $T_{2_{IE}}$ (Figure 6e, j and o) and number of compartments (Figure 6f, k and p).

For reference, FLAIR multi-echo EPI data were also registered with FLIRT to the shortest TE non-diffusion weighted volume. Then, the signal decay for each voxel was matched to a dictionary of monoexponential decays from 0 to 300 ms with a grid of 1 ms. We compared this map against the BSS $T_{2_{IE}}$ map (Figure 7).

We defined the relative error of the matrix factorization for in vivo data as follows:

$$\epsilon = \frac{|\mathbf{X} - S_0 \mathbf{A}\mathbf{S}|_2}{|\mathbf{X}|_2}. \tag{5}$$

This is an index of the performance of BSS for each voxel. Given that we calculated $\mathbf{S}=\mathbf{A}^{-1}\mathbf{X}$, this error formulation is sensitive to: 1) deviations in the proton density estimation, S_0; 2) numerical instability derived from the condition of $\mathbf{A}$; and 3) infractions of the BSS conditions due to artifacts.

Finally, BSS does not model the compartmental diffusion signal. However, to show a simple way to perform compartment independent analysis, we fitted the measured and disentangled signals to the DTI model (4). This allowed us to observe the CSF correction effect of BSS on the diffusion signal. For that, mean diffusivity (MD) and fractional anisotropy (FA) maps were derived using the FSL's FDT Toolbox (http://www.fmrib.ox.ac.uk/fsl). We fitted the measured diffusion volumes at the shortest TE, and the BSS separated signal for the IE and the CSF compartments, with standard linear regression (Figures 8 and 9).

Results

1 Phantom experiment

1.1 One compartment

There was a correlation between the estimated T_2 values for one compartment with multi-echo SE for 17 TEs and BSS for 2 TEs (Figure 2a and Table 1). The estimation of T_2 from ROI_2 to ROI_{10} showed a relative error below 10% for ΔTE equal to 50 ms (Figure 2b). The decreasing pattern of the error is due to the relationship between the slope of a column of $\mathbf{A}$ and its T_2 (Figure 2c). When ΔTE increased, the dynamic range of the slope of the columns of $\mathbf{A}$ expanded, yielding a better estimation of T_2. On the other hand, in Figure 2b, ROI_1 and ROI_{11} showed an increasing error with ΔTE. In the case of ROI_1, this is due to the low SNR of the measurements at the experimental TEs. The noise floor induced a change in the signal for longer TEs that biased the estimation of T_2. Finally, the effect observed in ROI_{11} cannot be explained by SNR nor slope-T_2 dependence. We attributed this result to an underestimation of the reference T_2, due to the incomplete recovery of the longitudinal magnetization, produced by the short experimental TR compared to the T_1 value of ROI_{11} ($T_1 = 2.2$s).

1.2   Two compartments

The disentangled signals for the *simulated* dataset replicated the profile of the reference sources (Figure 3d). Moreover, the maximum relative error on f_{S,ROI_6} and $T_{2_{S,ROI_6}}$ was below 1% for all the possible values of ΔTE. Interestingly, BSS was able to separate the signal sources of the *measured* dataset (Figure 3d). This data accounted for non-ideal conditions due to the system imperfections: signal drift, eddy currents or imperfect non-diffusion weighting, (Figure 3b, c, d and f). In that case, the relative error of the $T_{2_{S,ROI_6}}$ estimation remained under 10% for ΔTE > 10 ms. We explained the 15% error on f_{S,ROI_6} due to the differences between the *simulated* and *measured* signals at b=0, its influence on Eq. 4, and the error propagation from the estimation of T_2. Finally, we also observed a small stabilization effect in the volume fraction estimation as ΔTE increases (Figure 3f). This behavior is due to the reduction of the condition number of $\mathbf{A}$ that improves the numerical stability of the cALS algorithm (Figure 3e).

1.3   Three compartments

The condition number of $\mathbf{A}$ significantly increased in comparison to the two compartments model (Figures 3e and 4g). Results for the *simulated* data (Figure 4a, e and f), showed that signals for the compartments ROI_6 and ROI_{11} were separated in agreement with their reference. Likewise, the relative error of the $T_{2_{S,ROI_6}}$ and f_{S,ROI_6} estimations were below 1%, which agrees with a good separation. It is worth noting that the signal for the fast decaying compartment (ROI_5) was detected although heavily contaminated by the ROI_6. We explained this result by the comparable large values of the experimental TEs, that reduced its contribution to the observed signal. Equivalently, we found a 15% error in the estimation of f_{S,ROI_5} and 45% for $T_{2_{S,ROI_5}}$.

Results for the *measured* data at the lowest condition number of $\mathbf{A}$ showed that signals from ROI_6 and ROI_{11} were still separated in agreement with the reference (Figure 4f). However, the signal from ROI_5 was lost due to acquisition imperfections, bad conditioning of $\mathbf{A}$, and the small contribution of this compartment at the measured TEs. On the other hand, the estimation of $T_{2_{S,ROI_6}}$ showed stability with a relative error of 11%. Contrary, f_{S,ROI_6} was more instable due to the bad conditioning of the system and error propagation from the $T_{2_{S,ROI_6}}$ estimation.

2   Simulation: searching for myelin

Simulations for three compartments accounting for shorter minimal TE showed better stability than clinically reachable TEs for phantom data. The condition number of **A** was drastically reduced by lowering TE_1 to 10 ms and TE_2 to 38.57 ms (Figure 5a). These values hardly achievable in clinical systems. However, they speak of the potential of BSS to separate signals from three compartments, including a fast decaying species. We observed a good separation of the signal sources for all the noisy simulations (Figure 5d). The relative error of the volume fraction estimations, and T_{2_2}, are statistically below 10% (Figure 5c). Interestingly enough, the uncertainty of T_{2_1} was close to zero, with 35% a bias, denoting that cALS remains at the center of the parameter space for fast decaying components (Figure 5c). This result might be due to the small amount of information that this compartment added to the mixed measurements and low SNR.

3   In vivo clinical data

We observed that the mean relative error for the whole brain ($\langle \epsilon \rangle$) decreased as ΔTE increased (Figure 6a, b and c), in agreement with the findings in the phantom. Interestingly enough, for the maximum ΔTE, we can see how the number of compartments equals two in regions next to the ventricles and the cortex, while it is one inside the ventricles and in some deep WM areas (Figure 6k). It is also noteworthy that the pure CSF areas (e.g. the ventricles) are removed from the $T_{2_{IE}}$ map (Figure 6h and i) and the opposite effect is observed in the CSF volume fraction (Figure 5d and e), indicating a successful disentangling effect.

We compared the BSS estimated $T_{2_{IE}}$ maps as ΔTE increased with the reference map obtained from the FLAIR multi-echo SE data. We noticed how the structural similarity index (44) increased, and the mean relative error decreased with the enlargement of ΔTE (Figure 7a and b). Additionally, the histograms for both subjects tended towards the reference as the difference between the short and long echo times grew. This reflects an underestimation of $T_{2_{IE}}$ for small ΔTE that is explained by Eq. 3 and Figure 2c. Moreover, the FLAIR T_2 map showed high values in the ventricles. This might indicate imperfect CSF suppression and thus, slightly increased reference values (Figure 7a, c and d).

FA and MD maps and histograms were calculated from the BSS IE and CSF disentangled signals for both subjects (Figures 8 and 9). They displayed an overestimation of the CSF volume fraction for low ΔTE values (the low FA peak in Figure 8a and e was removed). This resulted as

a compensation effect from the previously shown underestimation of $T_{2_{IE}}$. Besides, the histograms of FA (Figure 8a and e) showed a tendency towards higher FA values, and a reduction of the low FA peak associated with free water. In general, the true IE FA histogram must lay between the standard DTI fitting (black line in Figure 8a and e) and the over-corrected ones for short ΔTE (light colored lines in Figure 8a and e). Long ΔTE seems to tend towards an homogeneous distribution of FA. Moreover, we observed an enlargement of the corpus callosum, a general recovery of peripheral WM tracts and the fornix in the colored FA maps (Figure 8b and f).

Additionally, on the MD histograms for IE water (Figure 8c and g) we reported a diminution of the number of voxels with diffusivity larger than 1 mm^2/s. Contrary, the main peak at $0.7 \cdot 10^{-3}$ mm^2/s, associated with the parenchyma, remained at its original place denoting that IE water represents non-CSF tissue. This decrement of MD was also visible in the maps (Figure 8d and h). Finally, the histograms of MD for CSF water (Figure 9) denoted a tendency towards $3 \cdot 10^{-3}$ mm^2/s as ΔTE increased, in agreement with literature (37). All these findings agreed with a disentangling of IE and CSF signals and thus, a correction of the free water partial volume effect on the diffusion signal.

Discussion

1   Disentangling the diffusion sources and free water elimination

Unlike other diffusion multicompartment models (39, 25, 47, 18, 2), and more recent contributions (43, 12) our approach does not model compartmental diffusion. Our framework relies on three assumptions: 1) microstructural water compartments have distinct T_2 relaxation times (31, 45); 2) each have different diffusion characteristics (36, 17); and 3) the effects of the water exchange at the time scale of our experiments are negligible (3, 5). Furthermore, our solution is diffusion protocol agnostic (two TEs and one non-diffusion weighted volume are necessary), allowing for a flexible design of the acquisition protocol that might include any number of diffusion directions and b-values. This is an advantage over diffusion-relaxation correlation techniques based on regularized inverse Laplace transformation (26, 6).

One direct application of the protocol agnostics nature of our framework is correcting for free water contamination. Recently Collier et al. (12) included TE dependence on the bi-exponential diffusion tensor model to regularize the fitting problem. However, they fitted the bi-exponential DTI model directly. Contrary, our solution does not assume any diffusion model, it separates the

signal from each compartment allowing for a more flexible and independent study. In this regard, the analysis of the signal associated with the CSF compartment can be seen as a disentangling quality assurance metric (Figures 8 and 9).

The range of feasible experimental echo times is limited at the lower bound by gradient performance, and SNR at the upper bound. However, in the in vivo experiments we did not reach the SNR limit. Even though, for $\Delta TE = 60$ ms the long TE was 135 ms. Thus, further exploration of the TE space or higher in plane resolutions are possible.

We want to point out the general benefit on the parameter estimation and signal separation for long ΔTE. This is not surprising and agrees the findings of with Collier et al. (12). Not only due to the relationship between $\mathbf{A}$ and T_2 expressed in Eq. 3 and plotted in Figure 2c. Also because longer differences between TEs produce a more distinct level of mixtures and thus a better codification of the information from each source. Namely, the short TE contains more information about the fast relaxing species, while the long TE is dominated by CSF.

2   Relaxation times and volume fractions estimation

BSS provides the means to estimate T_2 relaxation values and volume fractions. Interestingly, only a number of TE repetitions equal to the number of compartments that are assumed to be in the tissue is necessary. This results of the substitution of the ILT by BSS, in comparison to other techniques (31, 9, 6, 26). We reported a good agreement between $T_{2_{IE}}$ estimation of the FLAIR multi-echo SE for 17 TEs and BSS for 2 TEs, due to the factorization algorithm of $\mathbf{A}$ (cALS). In this sense, all the measurements along the diffusion space for both TEs are considered, incorporating redundancy and enforcing the estimation of T_2.

3   Stability

Four main approaches exist to the BSS problem (ICA, PCA, NMF or SCA). The choice depends on the prior knowledge on the signal sources. In our experiments we relied on NMF using a constrained version of the ALS algorithm (cALS). In this regard, cALS stability is linked to the condition of $\mathbf{A}$. An ill-conditioned mixing matrix will lead to propagation of errors due to numerical instability. Fortunately, we can optimize the experimental TEs to reduce the condition number of $\mathbf{A}$ for literature T_2 reference values. Nevertheless, the theoretical framework stated here is independent on the solver of choice. In that sense, more stable solutions to the BSS problem might be develop in the future. Benefiting the multicompartment analysis of diffusion signals.

Phantom experiments validated that BSS is able to accurately estimate T_2 for one compartment; and separate diffusion signals sources and estimate T_2 and f for two compartments. Furthermore, we also showed that scaling the cALS algorithm to three compartments is unstable at the range of the clinically available TE values.

Finally, we showed results for two volunteers that exhibit consistent disentangling and estimation patterns. This indicate that the cALS is a reproducible algorithm for CSF correction, proton density, CSF volume fraction, number of compartments and $T_{2_{IE}}$ estimation.

4   Meylin detection

Simulations proved that our method has the potential to disentangle three compartments by reducing the minimum TE of the diffusion experiments. In that sense, myelin water could be incorporated into the model (Figure 5).

Gradient performance on clinical scanners is a hardware limitation that prevent us from conducting such experiments. Typical TE values on these systems are between 60 and 75 ms for b=1000 s/mm^2, image resolution of 96x96 and ASSET factor of two. Literature values of T_2 for myelin water are around 15 ms (31), this result in a minimum loss of 55% of the signal for TE=60 ms due to transverse relaxation. Besides, the maximum content of myelin water in a voxel is 30%. Thus, for non-diffusion weighted volumes, the maximum contribution from myelin water to the measured signal is 0.5%. Undetectable even if we do not consider diffusion and noise.

Conclusions

We introduced for the first time a blind source separation formulation to express the relationship of diffusion acquisitions at different echo times. This new approach does not rely on diffusion modeling nor on inverse Laplace transform. Our results show that blind source separation allows for disentangling the diffusion signal sources generated by each sub-voxel compartment independently. Paving the way for individual analyses for each of them. Moreover, it estimates at the same time proton density, volume fractions, relaxation times and number of compartments of the underlying microstructure.

Acknowledgments

References

[1] Alexander DC, Hubbard PL, Hall MG, Moore EA, Ptito M, Parker GJM, Dyrby TB. 2010. Orientationally invariant indices of axon diameter and density from diffusion MRI. NeuroImage 52:1374–1389. doi:10.1016/j.neuroimage.2010.05.043.

[2] Assaf Y, Basser P. 2005. Composite hindered and restricted model of diffusion (CHARMED) MR imaging of the human brain. Neuroimage 27:48–58.

[3] Assaf Y, BlumenfeldKatzir T. 2008. AxCaliber: a method for measuring axon diameter distribution from diffusion MRI. Magnetic Resonance in Medicine :1347–1354doi:10.1002/mrm. 21577.

[4] Basser PJ, Mattiello J, LeBihan D. 1994. MR diffusion tensor spectroscopy and imaging. Biophysical journal 66:259–267. doi:10.1016/S0006-3495(94)80775-1.

[5] Bechter K. 2011. The peripheral cerebrospinal fluid outflow pathway – physiology and pathophysiology of CSF recirculation: A review and hypothesis. Neurology, Psychiatry and Brain Research 17:51–66. doi:10.1016/j.npbr.2011.06.003.

[6] Benjamini D, Basser PJ. 2016. Use of marginal distributions constrained optimization (MADCO) for accelerated 2D MRI relaxometry and diffusometry. Journal of Magnetic Resonance 271:40–45. doi:10.1016/j.jmr.2016.08.004.

[7] Bergmann O, Westin Cf, Pasternak O. 2016. Challenges in solving the two-compartment freewater di usion MRI model. ISMRM 24th Annual Meeting & Exhibition .

[8] Berry MW, Browne M, Langville AN, Pauca VP, Plemmons RJ. 2007. Algorithms and applications for approximate nonnegative matrix factorization. Computational Statistics & Data Analysis 52:155–173. doi:10.1016/j.csda.2006.11.006.

[9] Björk M, Zachariah D, Kullberg J, Stoica P. 2016. A multicomponent T2 relaxometry algorithm for myelin water imaging of the brain. Magnetic Resonance in Medicine 75:390–402. doi: 10.1002/mrm.25583.

[10] Bofill P, Zibulevsky M. 2001. Underdetermined blind source separation using sparse representations. Signal Processing 81:2353–2362. doi:10.1016/S0165-1684(01)00120-7.

[11] Callaghan PT, Arns CH, Galvosas P, Hunter MW, Qiao Y, Washburn KE. 2007. Recent Fourier and Laplace perspectives for multidimensional NMR in porous media. Magnetic Resonance Imaging 25:441–444. doi:10.1016/j.mri.2007.01.114.

[12] Collier Q, Veraart J, Dekker AJD, Vanhevel F, Parizel PM, Sijbers J. 2017. Solving the free water elimination estimation problem by incorporating T2 relaxation properties. ISMRM 25th Annual Meeting & Exhibition .

[13] De Santis S, Assaf Y, Jeurissen B, Jones DK, Roebroeck A. 2016. T1 relaxometry of crossing fibres in the human brain. NeuroImage 141:133–142. doi:10.1016/j.neuroimage.2016.07.037.

[14] De Santis S, Assaf Y, Jones DK. 2016. The influence of T2 relaxation in measuring the restricted volume fraction in diffusion MRI. In: ISMRM.

[15] De Santis S, Barazany D, Jones DK, Assaf Y. 2016. Resolving relaxometry and diffusion properties within the same voxel in the presence of crossing fibres by combining inversion recovery and diffusion-weighted acquisitions. Magnetic Resonance in Medicine 75:372–380. doi:10.1002/mrm.25644.

[16] Deoni S, Rutt B. 2008. Gleaning multicomponent T1 and T2 information from steadystate imaging data. Magnetic Resonance . . . .

[17] Does MD, Gore JC. 2000. Compartmental study of diffusion and relaxation measured in vivo in normal and ischemic rat brain and trigeminal nerve. Magnetic resonance in medicine : official journal of the Society of Magnetic Resonance in Medicine / Society of Magnetic Resonance in Medicine 43:837–44. doi:10.1002/1522-2594(200006)43:6<837::AID-MRM9>3.0.CO;2-O[pii].

[18] Ferizi, et al. 2014. A ranking of diffusion MRI compartment models with in vivo human brain data. Magnetic Resonance in Medicine 72:1785–92. doi:10.1002/mrm.25080.

[19] Henriques RN, Bergmann Ø, Rokem A, Pasternak O, Correia MM. 2017. Exploring the potentials and limitations of improved free-water elimination DTI techniques Results and Discussion : References References. ISMRM 25th Annual Meeting & Exhibition doi:10.1002/mrm.22055.

[20] Hoy AR, Koay CG, Kecskemeti SR, Alexander AL. 2014. Optimization of a Free Water Elimination Two-Compartment Model for Diffusion Tensor Imaging. NeuroImage :323–333doi: 10.1016/j.neuroimage.2014.09.053.

[21] Hürlimann MD, Venkataramanan L, Flaum C. 2002. The diffusion–spin relaxation time distribution function as an experimental probe to characterize fluid mixtures in porous media. The Journal of Chemical Physics 117:10223–10232. doi:10.1063/1.1518959.

[22] Hyvarinen A, Oja E. 1999. Independent Component Analysis : A Tutorial. Neural Networks 1:1–30.

[23] Jenkinson M, Smith S. 2001. A global optimisation method for robust affine registration of brain images 5:143–156.

[24] Jolliffe IT. 2002. Principal Component Analysis. Journal of the American Statistical Association 98:487. doi:10.1007/b98835. arXiv:1011.1669v3.

[25] Kärger J. 1971. Der Einfluss der Zweibereichdiffusion auf die Spinechodaempfung unter Beruecksichtigung der Relaxation bei Messungen mit der Methode der gepulsten Feldgradienten. Annalen der Physik 7:107–109.

[26] Kim D, Doyle EK, Wisnowski JL, Kim JH, Haldar JP. 2017. Diffusion-Relaxation Correlation Spectroscopic Imaging: A Multidimensional Approach for Probing Microstructure doi:10.1002/ mrm.26629.

[27] Kimmich R. 1997. NMR : Tomography, Diffusometry, Relaxometry. Springer Berlin Heidelberg.

[28] Latour LL, Svoboda K, Mitra PP, Sotak CH. 1994. Time-dependent diffusion of water in a biological model system. Proceedings of the National Academy of Sciences of the United States of America 91:1229–1233. doi:10.1073/pnas.91.4.1229.

[29] Laubach HJ, Jakob PM, Loevblad KO, Baird aE, Bovo MP, Edelman RR, Warach S. 1998. A phantom for diffusion-weighted imaging of acute stroke. Journal of magnetic resonance imaging : JMRI 8:1349–54. doi:10.1002/jmri.1880080627.

[30] Lawson CL, Hanson RJ. 1974. Solving Least Squares Problems. volume 53. doi:10.1017/CBO9781107415324.004. `arXiv:1011.1669v3`.

[31] MacKay, et al. 2006. Insights into brain microstructure from the T2 distribution. Magnetic Resonance in Medicine 24:515–25. doi:10.1016/j.mri.2005.12.037.

[32] Metzler-Baddeley C, O'Sullivan MJ, Bells S, Pasternak O, Jones DK. 2012. How and how not to correct for CSF-contamination in diffusion MRI. NeuroImage 59:1394–1403. doi:10.1016/j.neuroimage.2011.08.043.

[33] Molina-Romero M, Gómez PA, Sperl JI, Jones DK, Menzel MI, Menze BH. 2016. Tissue microstructure characterisation through relaxometry and diffusion MRI using sparse component analysis. In: Workshop on Breaking the Barriers of Diffusion MRI.

[34] Molina-Romero M, Gómez PA, Sperl JI, Stewart AJ, Jones DK, Menzel MI, Menze BH. 2017. Theory, validation and application of blind source separation to diffusion MRI for tissue characterisation and partial volume correction. ISMRM .

[35] Pasternak O, Sochen N, Gur Y, Intrator N, Assaf Y. 2009. Free Water Elimination and Mapping from Diffusion MRI 730:717–730. doi:10.1002/mrm.22055.

[36] Peled S, Cory DG, Raymond SA, Kirschner DA, Jolesz FA. 1999. Water diffusion, T(2), and compartmentation in frog sciatic nerve. Magnetic resonance in medicine : official journal of the Society of Magnetic Resonance in Medicine / Society of Magnetic Resonance in Medicine 42:911–8.

[37] Pierpaoli C, Jones DK. 2004. Removing CSF Contamination in Brain DT-MRIs by Using a Two-Compartment Tensor Model. International Society for Magnetic Resonance in Medicine Meeting c:1215.

[38] Stanisz GJ, Szafer A, Wright GA, Henkelman RM. 1997. An Analytical Model of Restricted Diffusion in Bovine Optic Nerve. Magnetic resonance in medicine : official journal of the Society of Magnetic Resonance in Medicine / Society of Magnetic Resonance in Medicine 37:103–111.

[39] Stejskal E, Tanner J. 1965. Spin diffusion measurements: spin echoes in the presence of a timedependent field gradient. The journal of chemical physics .

[40] Stoica P, Babu P. 2013. Parameter estimation of exponential signals: A system identification approach. Digital Signal Processing 23:1565–1577. doi:10.1016/j.dsp.2013.05.003.

[41] Szafer a, Zhong J, Gore JC. 1995. Theoretical model for water diffusion in tissues. Magnetic resonance in medicine : official journal of the Society of Magnetic Resonance in Medicine / Society of Magnetic Resonance in Medicine 33:697–712. doi:10.1002/mrm.1910330516.

[42] Vallée E. 2015. Modelling free water in diffusion mri. ISMRM 1215:17365.

[43] Veraart J, Fieremans E, Novikov DS. 2017. Quantifying neuronal microstructure integrity with TE dependent Diffusion Imaging (TEdDI). ISMRM 25th Annual Meeting & Exhibition .

[44] Wang Z, Bovik AC, Sheikh HR, Simoncelli EP. 2004. Image quality assessment: From error visibility to structural similarity. IEEE Transactions on Image Processing 13:600–612. doi: 10.1109/TIP.2003.819861.

[45] Whittall KP, Mackay AL, Graeb DA, Nugent RA, Li DKB, Paty DW. 1997. In vivo measurement of T2 distributions and water contents in normal human brain. Magnetic Resonance in Medicine 37:34–43. doi:10.1002/mrm.1910370107.

[46] Yu X, Hu D, Jindong X. 2014. BLIND SOURCE SEPARATION THEORY AND APPLICATIONS.

[47] Zhang H, Schneider T. 2012. NODDI: Practical in vivo neurite orientation dispersion and density imaging of the human brain. Neuroimage 61:1000–1016. doi:10.1016/j.neuroimage.2012.03.072.

Figures and Tables
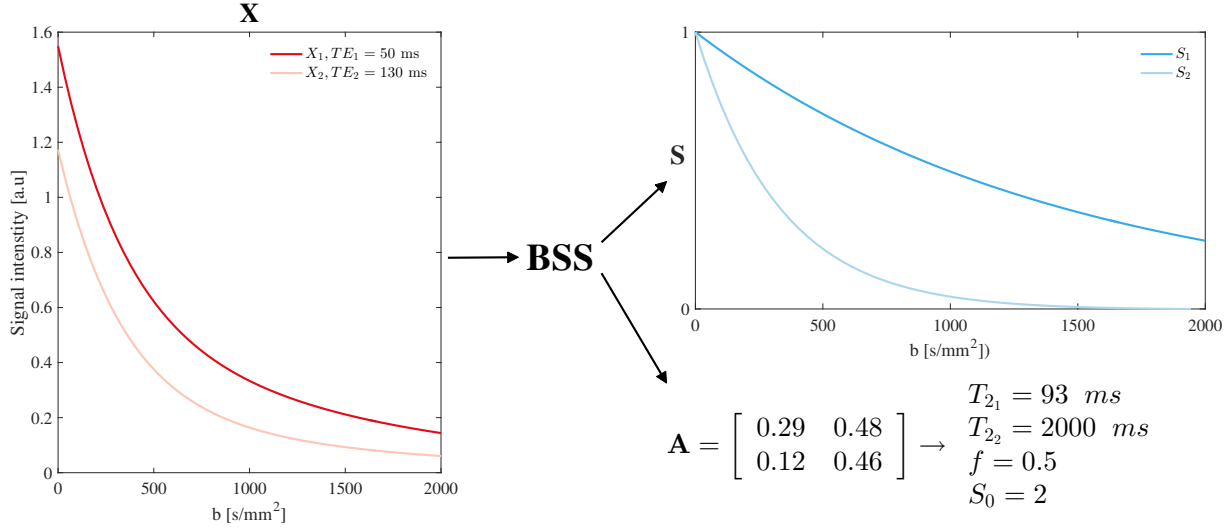
Figure 1: **Factorization of measurements, X, into the sources, S, and mixing matrix, A.**
Example of a blind source separation operation for two monoexponential sources ($M = 2$) and two
TE measurements ($N = 2$). In this illustration, the measurements, **X**, show a bi-exponental decay
profile. BSS is capable of separating these two independent exponential functions, **S**; and calculate
their mixing matrix, **A**. The parameters that determine the level of mixture (T_{2_1}, T_{2_2} and f), plus
the scaling factor S_0, were estimated as described in Eqs. 3 and 4. We showed an exponental case
for simplicity. However, this is not limiting. Any signal can be processed in the same manner.
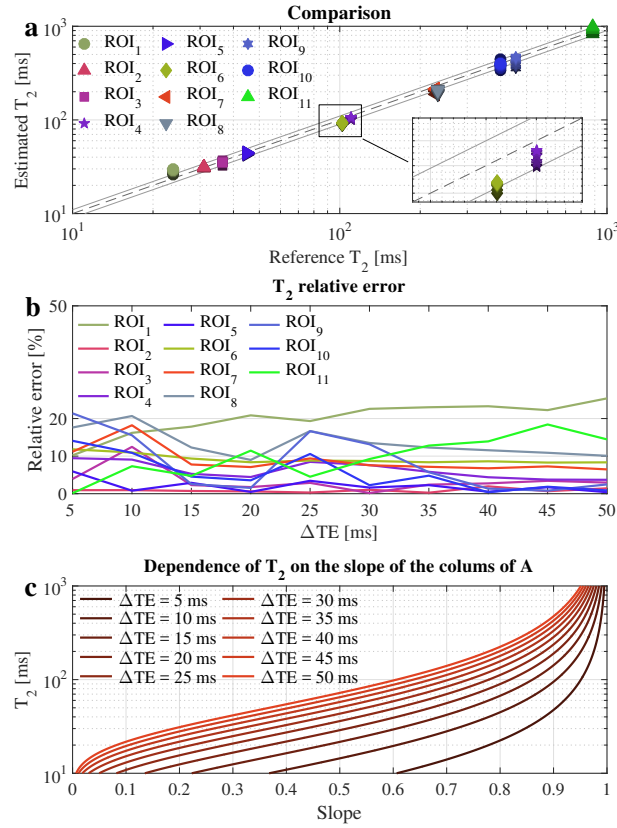
Figure 2: **Evolution of the relative error of the T_2 estimation with ΔTE for one compartment.**

The correlation of T_2 estimated with BSS and the reference is shown in (a), where ΔTE goes from 5 (darker colors) to 50 ms (lighter colors). The dashed line marks the identity while the solid parallel lines are the limits of the 10% error. This plot can be unfold into (b), where error evolution with ΔTE is better seen. Finally, the dependence of T_2 on the direction (slope) of the columns of **A** (Eq. 3) is shown in (c), where one can see how increasing ΔTE improves the dynamic range of the slope of **A**, which results in a better estimation of T_2. Reference and BSS T_2 estimated values agreement increases with ΔTE.
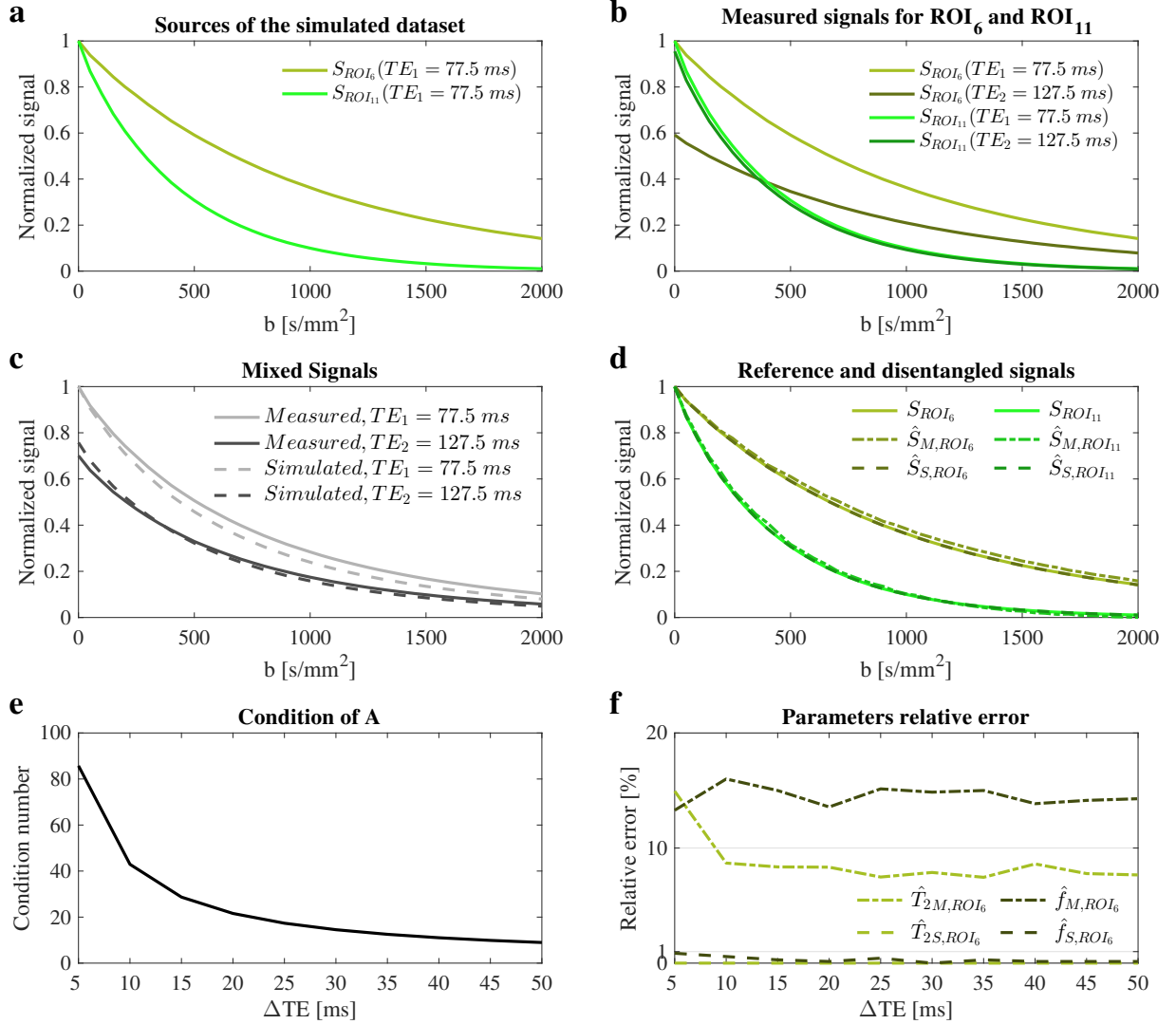
Figure 3: **Separation of two compartments and parameter estimation on phantom.**
The signal sources of the *simulated* dataset are plotted in (a). The *measured* data were generated from the signals in (b). The resulting mixture for both datasets are shown in (c). We used subscripts M and S to refer to estimation of the *measured* and *simulated* datasets respectively. Measurement errors are highlighted by the differences between the *measured* and *simulated* signals (c). BSS disentangled the original sources for both datasets (d). We chose $\Delta TE=50$ ms to minimize the condition of $\mathbf{A}$ and increase the numerical stability of the framework (e). Finally, the relative errors of the estimated parameters $T_{2_{ROI_6}}$ and f_{ROI_6} are plotted in (f) for all possible values of ΔTE. We observed a good agreement between reference signal and those disentangled with BSS.
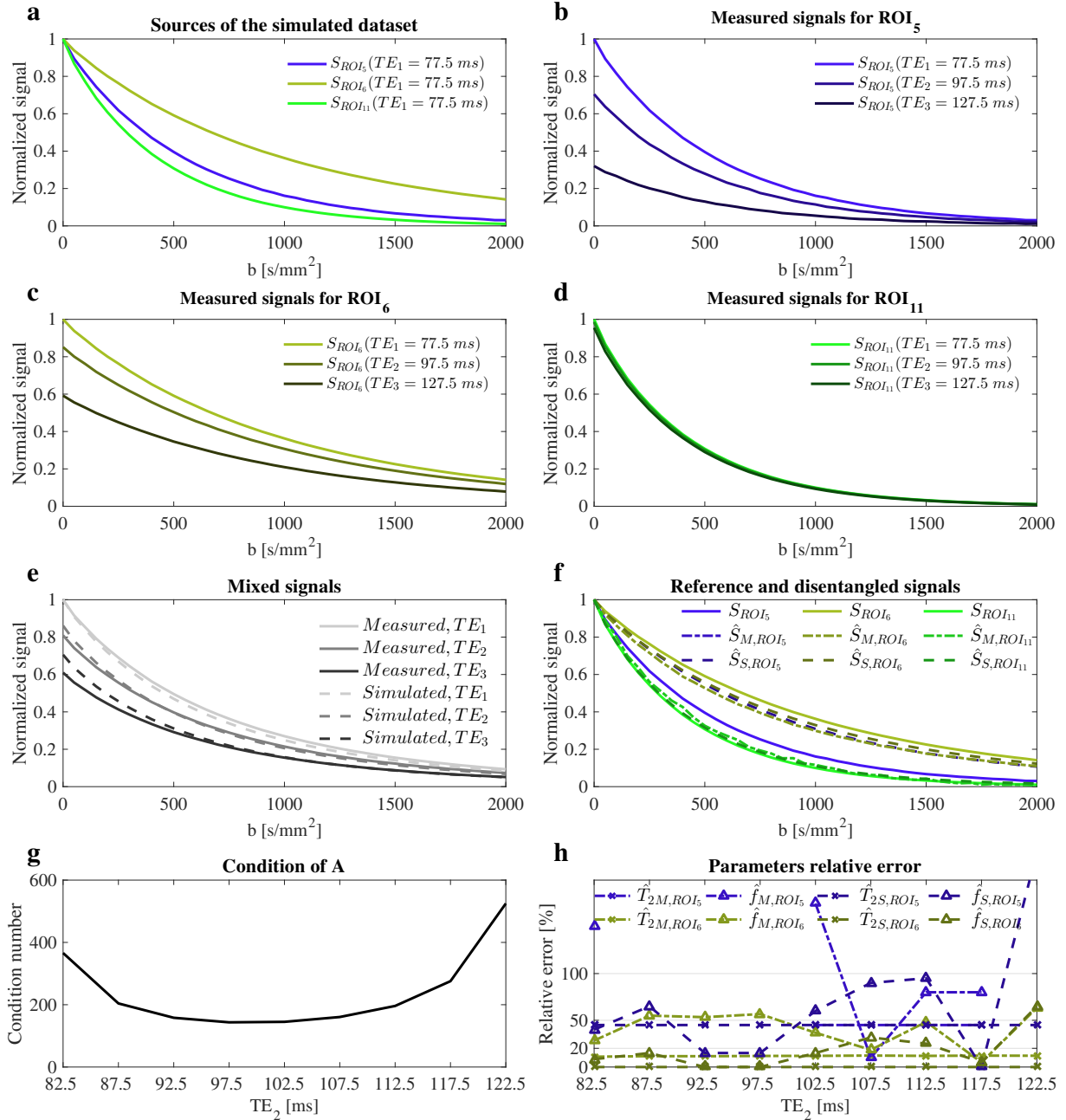
Figure 4: **Separation of three compartments and parameter estimation on phantom data.** The *simulated* dataset was generated from the signal sources in (a). The *measured* dataset were calculated from the measured signals for ROI_5 (b), ROI_6 (c) and ROI_{11} (d). The mixed signals for both datasets (e) show a mismatch due to measuring errors. They were disentangled with BSS (f). We fixed TE_1=77.5 ms and TE_3=127.5 ms, and varied TE_2 to find the minimum condition number of $\mathbf{A}$ (g). Relative errors of the estimated parameters are plotted along the TE_2 (h).
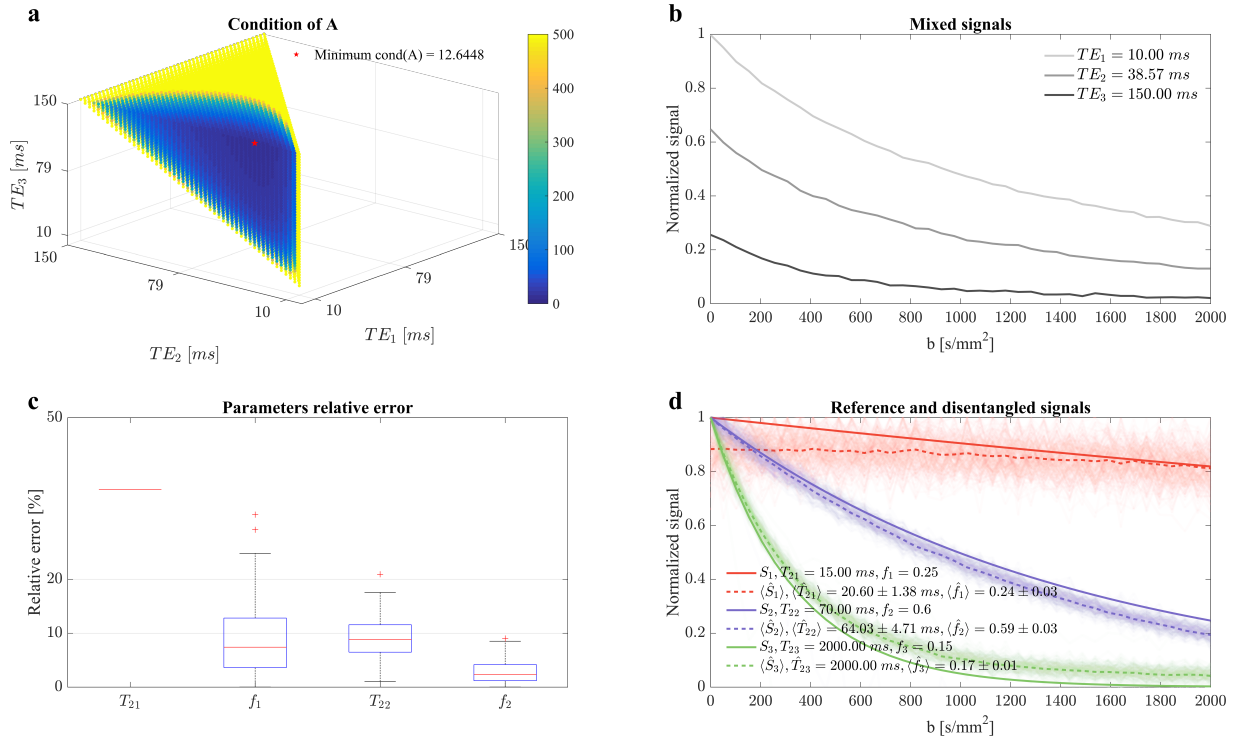
Figure 5: **Simulation of three compartments separation for short TEs**

Distinct signals for three compartments (S_1, S_2 and S_3) (d) were mixed together as in Eq. 2. We used literature T_2 values, and volume fractions for $f_1 = 0.25$ and $f_2 = 0.6$ (b). To maximize the stability of the framework, the TE space for the three measurements was explored to minimize the condition number or **A** (a). The experiment was ran 200 times adding Rician noise, and disentangled with BSS for each execution. Signal sources are represented in (d) with light color lines. The averaged disentangled signal sources are compared (d, dashed) against the reference noise-free sources (d, solid). The statistical distribution of the relative error of the estimated parameter is represented in (c). We observed good stability of the framework for three compartments when short TE values were measured.
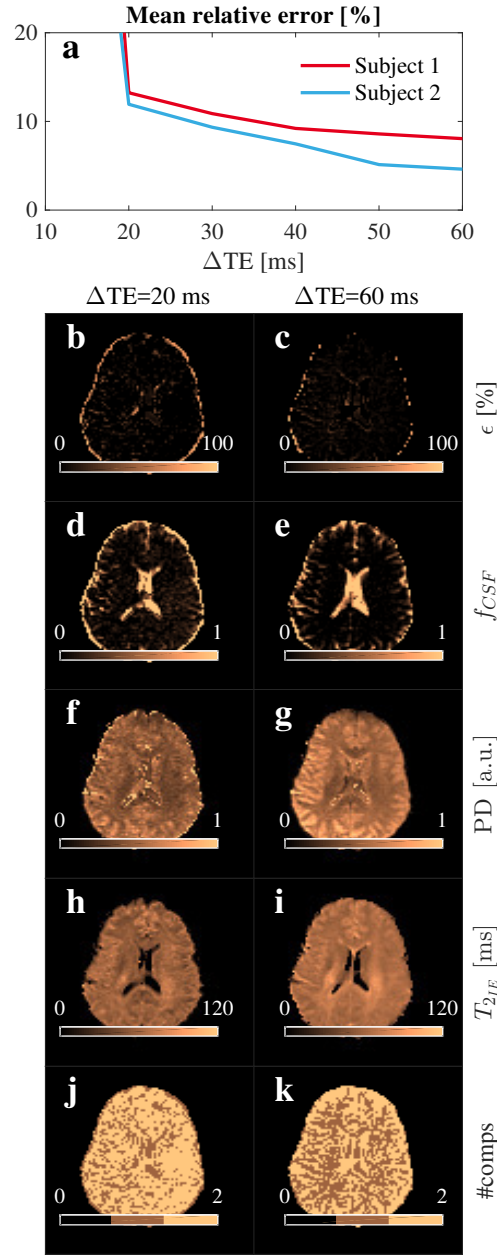
Figure 6: **Relative factorization error of BSS for incremental ΔTE values.**

The evolution of the factorization relative error averaged for the whole brain with ΔTE is shown in (a). As an example of how this error reduction affects the BSS estimation we show in the rows the relative error map (b and c), CSF volume fraction (d and e), PD (f and g), $T_{2_{IE}}$ (h and i) and the number of compartments (j and k) for ΔTEs values of 20 and 60 ms in each column. The mean relative factorization error decreases when ΔTE increases, benefiting the parameter estimation.
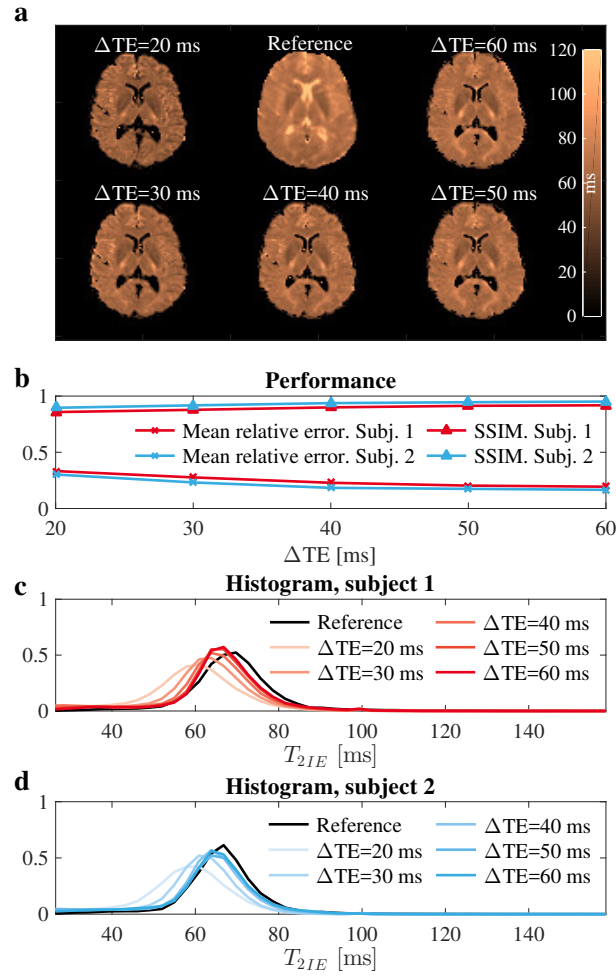
Figure 7: **Comparison of the BSS estimated $T_{2_{IE}}$ against a FLAIR reference.**
The reference (a, upper middle) for subject one is compared to the BSS $T_{2_{IE}}$ estimation for incremental values of ΔTE. The visual comparison was quantified by SSIM (44) and mean relative error (b). Histogram of the BSS estimated $T_{2_{IE}}$ are plotted against the reference (c and d). The high T_2 values in the ventricles for the reference indicate that the suppression of the CSF signal in the FLAIR experiment was not perfect, although they appeared dark in the images (see supplementary Figure S2). This might have induced a positive bias on the reference. Finally, BSS estimation of $T_{2_{IE}}$ for values of ΔTE > 50 ms showed a good agreement with the reference.
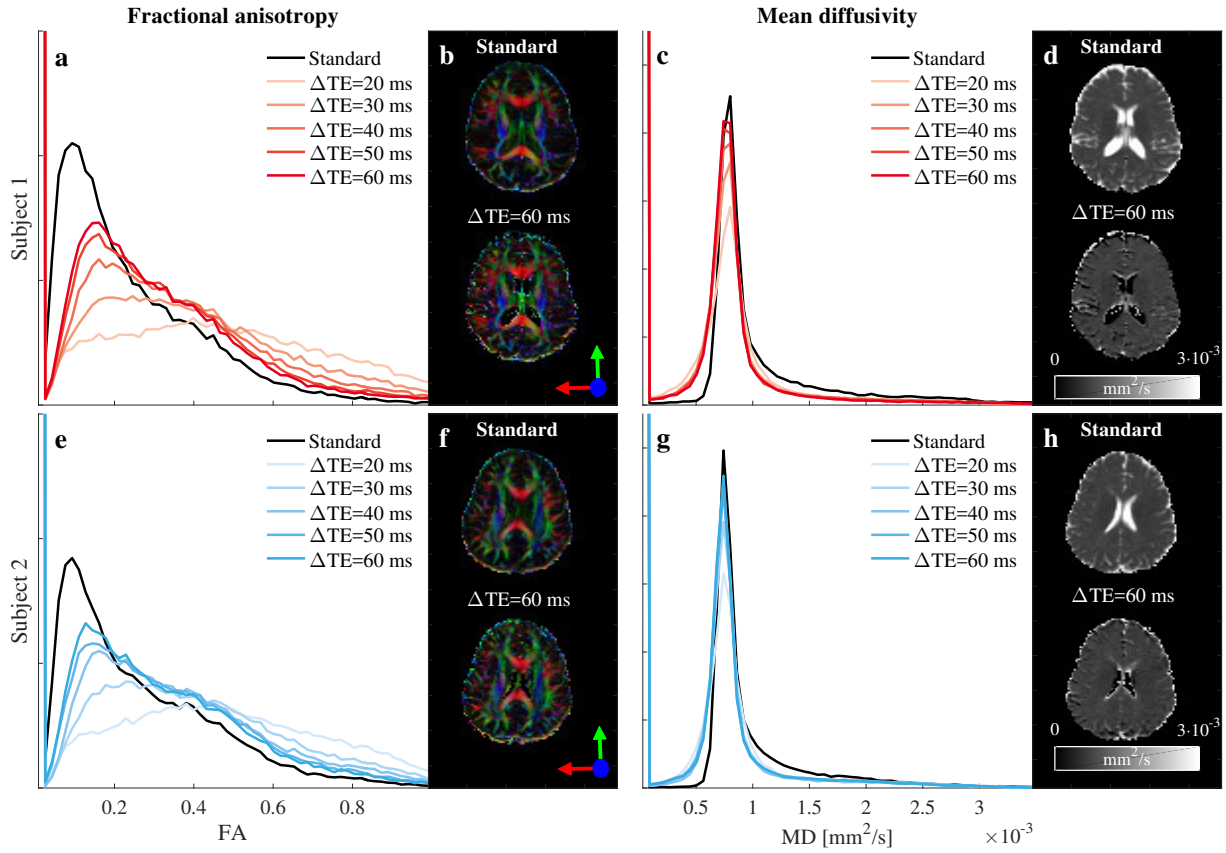
Figure 8: **FA and MD of the BSS disentangled IE signal against the standard estimation.** Comparison of the FA (a and e) and MD(c and g) histograms, for both subjects, calculated from the separated IE signal are plotted against the standard DTI fitting for the short TE measured data. Besides, MD (d and h) and colored FA maps (b and f) are also included for comparison. We observed a CSF correction effect in these metrics.
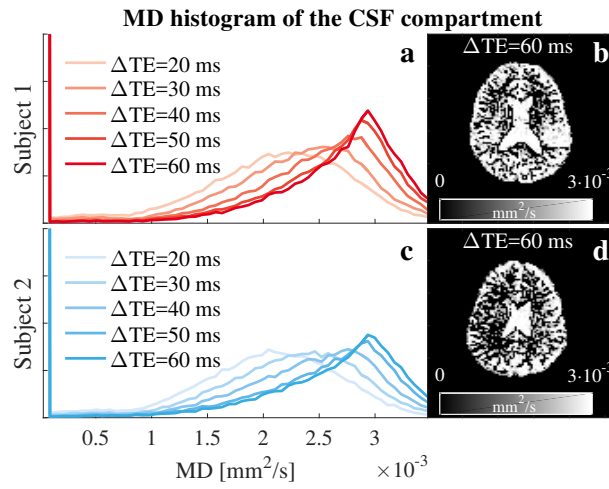
Figure 9: **Evolution of the MD histogram of the BSS disentangled CSF component with ΔTE.**

The MD histograms, calculated from the the DTI fitting on the signal disentangled for the CSF compartment, are plotted in (a and c). MD maps (b and d) are shown for anatomical inspection. CSF MD histograms tends towards $3 \cdot 10^{-3}$ mm^2/s in agreement with literature.

ROI	Agar [%]	Sucrose [%]	$T_{2_{EASI-SM}}[ms]$	$T_{2_{NNLS}}$ [ms]	$T_{2_{BSS}}$ [ms]	Relative error [%]
1	5	15	25.02	23.88 ± 1.92	29.9	25.37
2	5	5	31.59	31.13 ± 2.19	31.6	1.43
3	3	30	37.68	36.50 ± 3.04	35.4	2.95
4	3	15	106.23	110.07 ± 7.93	106.0	3.70
5	3	5	45.40	44.66 ± 2.85	44.5	0.40
6	1	30	95.46	102.19 ± 10.30	93.7	8.34
7	1	15	222.22	228.94 ± 12.15	214.1	6.47
8	1	5	225.19	233.85 ± 13.84	210.3	10.09
9	0	30	457.08	456.37 ± 26.50	467.6	2.47
10	0	15	395.95	397.56 ± 21.17	401.0	0.87
11	0	0.5	876.97	881.23 ± 64.07	1008.6	14.46

Table 1: **Phantom reference values and BSS estimation.**

Each ROI in the phantom was built using the concentration of agar and sucrose here described. Signal decays along the diffusion dimension were compared to each other to ensure their disparity, as required by BSS (see supplementary Figure S1). For reference, T_2 values were characterized using a NNLS fitting. Confidence intervals were taken at half maximum of the NNLS spectral peaks. Besides, a second method, EASI-SM (9) was used to confirm the validity of the fitting. Finally, the $T_{2_{BSS}}$ values were estimated for $\Delta TE = 50$ ms and compared to the NNLS reference.
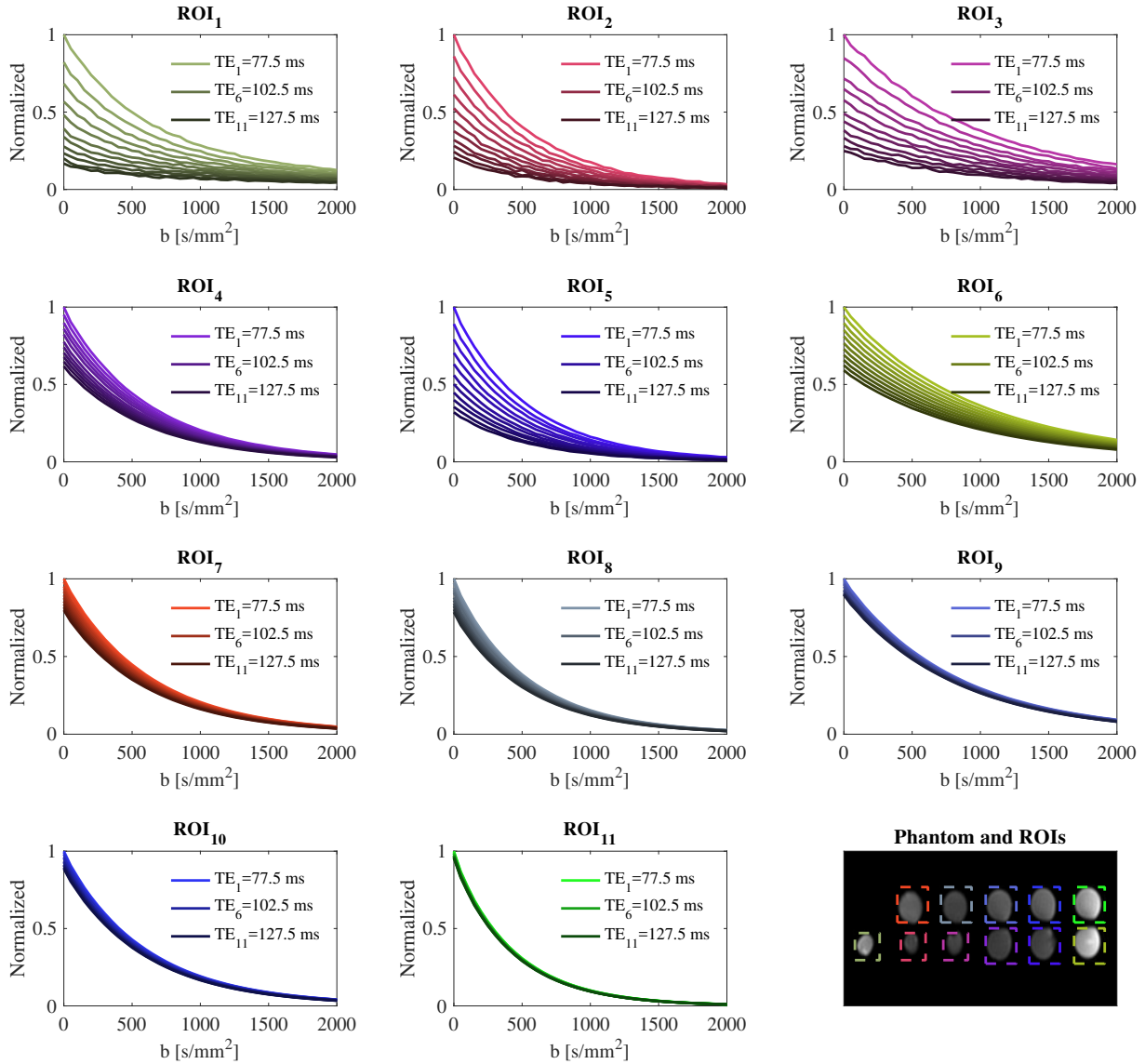
Figure S1: **Normalized diffusion signal decay for all ROIs at each TE.**

For reference, the measured signals for each ROI at all TEs are show. Signals for shorter TEs are plotted in light colors, while longer TEs are represented in dark colors. Eleven TEs were measured from 77.5 to 127.5 ms in 5ms increments. The phantom is shown along the ROIs in the lower right plot. Each ROI has a characteristic diffusion and relaxation signal decay.
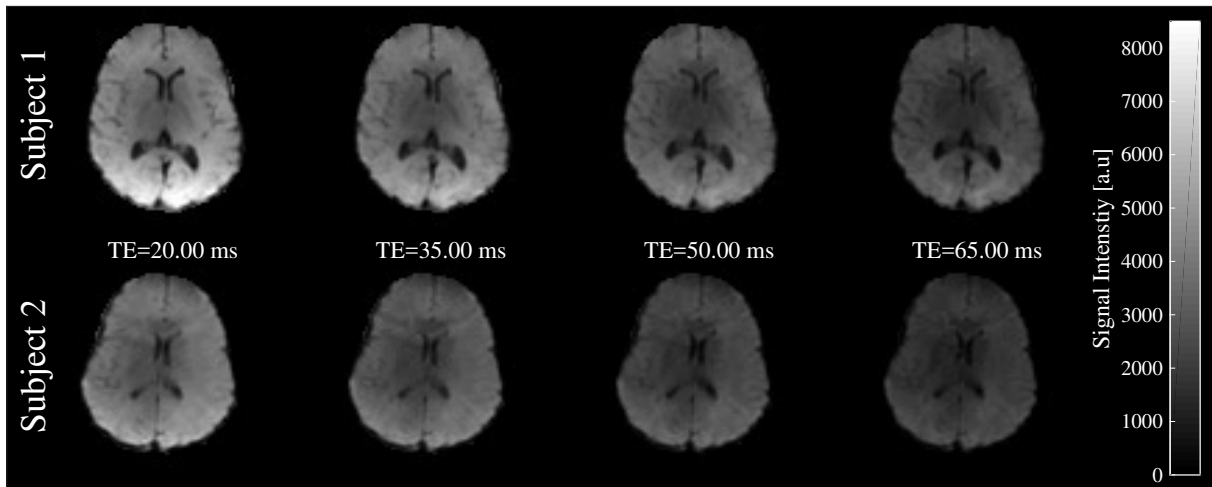
Figure S2: **FLAIR EPI images for both subjects at different echo times.**
We measured FLAIR EPI images for both subjects and TEs from 20 to 260ms with 15 ms increments. We showed the shortest four TEs here for both subjects. The signal intensity in the ventricles is dark, indicating attenuation of the CSF component.

[1] Jan H Ardenkjaer-Larsen, Björn Fridlund, Andreas Gram, Georg Hansson, Lennart Hansson, Mathilde H Lerche, Rolf Servin, Mikkel Thaning, and Klaes Golman. "Increase in signal-to-noise ratio of > 10,000 times in liquid-state NMR." In: *Proceedings of the National Academy of Sciences of the United States of America* 100.18 (2003), pp. 10158–63. ISSN: 0027-8424. DOI: 10.1073/pnas.1733835100.

[2] James T. Arnold. "Magnetic Resonances of Protons in Ethyl Alcohol." In: *Physical Review* 102.1 (1956), pp. 136–150. ISSN: 0031-899X. DOI: 10.1103/PhysRev.102.136.

[3] Yaniv Assaf and Peter J. Basser. "Composite hindered and restricted model of diffusion (CHARMED) MR imaging of the human brain." In: *NeuroImage* 27 (2005), pp. 48–58. ISSN: 10538119. DOI: 10.1016/j.neuroimage.2005.03.042.

[4] Haz Edine Assemlal, David Tschumperlé, Luc Brun, and Kaleem Siddiqi. "Recent advances in diffusion MRI modeling: Angular and radial reconstruction." In: *Medical Image Analysis* 15 (2011), pp. 369–396. ISSN: 13618415. DOI: 10.1016/j.media.2011.02.002.

[5] Jakob Assländer, Steffen J Glaser, and Jürgen Hennig. "Pseudo Steady-State Free Precession for MR-Fingerprinting." In: *Magnetic Resonance in Medicine* 00.February (2016), in press. ISSN: 07403194. DOI: 10.1002/mrm.26202.

[6] Jakob Assländer, Martijn A. Cloos, Florian Knoll, Daniel K. Sodickson, Jürgen Hennig, and Riccardo Lattanzi. "Low rank alternating direction method of multipliers reconstruction for MR fingerprinting." In: *Magnetic Resonance in Medicine* (2017). ISSN: 07403194. DOI: 10.1002/mrm.26639.

[7] P J Basser, J Mattiello, and D LeBihan. "Estimation of the effective self-diffusion tensor from the NMR spin echo." In: *Journal of magnetic resonance. Series B* 103 (1994), pp. 247–254. ISSN: 10641866. DOI: 10.1006/jmrb.1994.1037.

[8] Noam Ben-Eliezer, Daniel K Sodickson, and Kai Tobias Block. "Rapid and accurate T2 mapping from multi-spin-echo data using bloch-simulation-based reconstruction." In: *Magnetic Resonance in Medicine* 817 (2014), pp. 809–817. ISSN: 07403194. DOI: 10.1002/mrm.25156.

[9]   Sampada Bhave, Sajan Goud Lingala, Casey P. Johnson, Vincent A. Magnotta, and Mathews Jacob. "Accelerated whole-brain multi-parameter mapping using blind compressed sensing." In: *Magnetic Resonance in Medicine* 1186 (2015), pp. 1175–1186. ISSN: 15222594. DOI: 10.1002/mrm.25722. URL: http://dx.doi.org/10.1002/mrm.25722.

[10]   Felix Bloch. "Nuclear Induction." In: *Physical Review* 70 (1946), p. 460. ISSN: 0031899X. DOI: 10.1103/PhysRev.70.460.

[11]   K. M. Brindle, I. D. Campbell, and R. J. Simpson. "NMR Methods for Studying Enzyme Kinetics in Cells and Tissue." In: *Biological Magnetic Resonance*. Boston, MA: Springer US, 1987, pp. 81–127. DOI: 10.1007/978-1-4613-1825-5_2.

[12]   Robert W. Brown, Yu-Chung N. Cheng, E. Mark Haacke, Michael R. Thompson, and Ramesh Venkatesan, eds. *Magnetic Resonance Imaging: Physical Principles and Sequence Design, Second Edition*. Chichester, UK: John Wiley & Sons Ltd, 2014, pp. 1–17. DOI: 10.1002/9781118633953.

[13]   Guido Buonincontri and Stephen; Sawiak. "Three-dimensional MR fingerprinting with simultaneous B1 estimation." In: *Magnetic Resonance in Medicine* 00 (2015), pp. 1–9. ISSN: 07403194.

[14]   Guido Buonincontri, Laura Biagi, Pedro A Gómez, Rolf F Schulte, and Michela Tosetti. "Spiral Keyhole Imaging for MR Fingerprinting." In: *Proc Intl Soc Mag Reson Med* (2017).

[15]   Paul T Callaghan. *Principles of Nuclear Magnetic Resonance Microscopy*. 1991. URL: http://cds.cern.ch/record/262334/files/9780198539971{_}TOC.pdf.

[16]   Emmanuel J. Candès, Justin Romberg, and Terence Tao. "Robust uncertainty principles: Exact signal reconstruction from highly incomplete frequency information." In: *IEEE Transactions on Information Theory* 52.2 (2006), pp. 489–509. ISSN: 00189448. DOI: 10.1109/TIT.2005.862083. arXiv: 0409186 [math].

[17]   H. Y. Carr. "Steady-state free precession in nuclear magnetic resonance." In: *Physical Review* 112 (1958), pp. 1693–1701. ISSN: 0031899X. DOI: 10.1103/PhysRev.112.1693.

[18]   Christopher C. Cline, Xiao Chen, Boris Mailhe, Qiu Wang, and Mariappan Nadar. "AIR-MRF: Accelerated iterative reconstruction for magnetic resonance fingerprinting." In: *Proc Intl Soc Mag Reson Med* (2016).

[19]   Martijn A Cloos, F Knoll, T Zhao, K Block, M Bruno, CG Wiggins, and DK Sodickson. "Multiparamatric imaging with heterogenous radiofrequency fields." In: *Nature Communication* (2016), pp. 1–10. ISSN: 2041-1723. DOI: 10.1038/ncomms12445. arXiv: arXiv:1011.1669v3.

[20] Thomas E. Conturo, Erbil Akbudak, Melanie S. Kotys, Maison L. Chen, Steve J. Chun, Raymond M. Hsu, Caitlin C. Sweeney, and Joanne Markham. "Arterial input functions for dynamic susceptibility contrast MRI: Requirements and signal options." In: *Journal of Magnetic Resonance Imaging* 22.6 (2005), pp. 697–703. ISSN: 1053-1807. DOI: 10.1002/jmri.20457.

[21] R Damadian. "Tumor detection by nuclear magnetic resonance." In: *Science* 171.3976 (1971), pp. 1151–3. ISSN: 0036-8075.

[22] Mike Davies, Gilles Puy, Pierre Vandergheynst, and Yves Wiaux. "A Compressed Sensing Framework for Magnetic Resonance Fingerprinting." en. In: *SIAM Journal on Imaging Sciences* 7.4 (2014), pp. 2623–2656. ISSN: 1936-4954. DOI: 10.1137/130947246. arXiv: 1312.2465.

[23] Sean C L Deoni. "Quantitative Relaxometry of the Brain." In: *Top Magn Reson Imaging* 21.2 (2010), pp. 201–113. ISSN: 15378276. DOI: 10.1016/j.pestbp.2011.02.012.Investigations. arXiv: NIHMS150003.

[24] Sean C L Deoni, Brian K. Rutt, and Terry M. Peters. "Rapid combined T1 and T2 mapping using gradient recalled acquisition in the steady state." In: *Magnetic Resonance in Medicine* 49 (2003), pp. 515–526. ISSN: 07403194. DOI: 10.1002/mrm.10407.

[25] Vibhas S. Deshpande, Yiu-Cho Chung, Qiang Zhang, Steven M. Shea, and Debiao Li. "Reduction of Transient Signal Oscillations in True-FISP Using a Linear Flip Angle Series Magnetization Preparation." In: *Magnetic Resonance in Medicine* 49.1 (2003), pp. 151–157. ISSN: 0361803X. DOI: 10.1002/mrm.10337.

[26] Mariya Doneva, Peter Börnert, Holger Eggers, Christian Stehning, Julien Sénégas, and Alfred Mertins. "Compressed sensing reconstruction for magnetic resonance parameter mapping." In: *Magnetic Resonance in Medicine* 64 (2010), pp. 1114–1120. ISSN: 07403194. DOI: 10.1002/mrm.22483.

[27] D.L. L Donoho. "Compressed sensing." In: *IEEE Transactions on Information Theory* 52 (2006), pp. 1289–1306. ISSN: 00189448. DOI: Doi10.1109/Tit.2006.871582. arXiv: 1204.4227v1.

[28] Philipp Ehses, Nicole Seiberlich, Dan Ma, Felix A. Breuer, Peter M. Jakob, Mark A. Griswold, and Vikas Gulani. "IR True-FISP with a golden-ratio-based radial readout: Fast quantification of T1, T2, and proton density." In: *Magnetic Resonance in Medicine* 69 (2013), pp. 71–81. ISSN: 07403194. DOI: 10.1002/mrm.24225.

[29] Carl Ganter. "Off-resonance effects in the transient response of SSFP sequences." In: *Magnetic Resonance in Medicine* 52.2 (2004), pp. 368–375. ISSN: 07403194. DOI: 10.1002/mrm.20173.

[30] Vladimir Golkov et al. "q-Space Deep Learning for Twelve-Fold Shorter and Model-Free Diffusion MRI Scans." In: *MIC-CAI: International Conference on Medical Image Computing and Computer-Assisted Intervention* LNCS 9349 (2015), pp. 37–44.

[31] Klaes Golman, Jan H Ardenkjaer-Larsen, J Stefan Petersson, Sven Mansson, and Ib Leunbach. "Molecular imaging with endogenous substances." In: *Proceedings of the National Academy of Sciences of the United States of America* 100.18 (2003), pp. 10435–9. ISSN: 0027-8424. DOI: 10.1073/pnas.1733836100.

[32] Pedro A. Gómez et al. "Multisite kinetic modeling of 13C metabolic MR using [1-13C]pyruvate." In: *Radiology Research and Practice* 871619 (2014), p. 10. DOI: 10.1155/2014/871619.

[33] Pedro A. Gómez, Tim Sprenger, Marion I. Menzel, and Jonathan I. Sperl. "Fitting the Diffusional Kurtosis Tensor to Rotated Diffusion MR Images." In: *Proc Intl Soc Mag Reson Med*. 2015.

[34] Pedro A. Gómez, Jonathan I. Sperl, Tim Sprenger, Claudia Metzler-Baddeley, Derek K. Jones, Philipp Saemann, Michael Czisch, Marion I. Menzel, and Bjoern H. Menze. "Joint reconstruction of multi-contrast MR images for multiple sclerosis lesion segmentation." In: *Bildverarbeitung für die Medizin 2015* (2015).

[35] Pedro A Gómez, Cagdas Ulas, Jonathan I Sperl, Tim Sprenger, Miguel Molina-Romero, Marion I Menzel, and Bjoern H Menze. "Learning a Spatiotemporal Dictionary for Magnetic Resonance Fingerprinting with Compressed Sensing." In: *MICCAI Patch-MI Workshop* LNCS 9467 (2015), pp. 112–119.

[36] Pedro A. Gómez et al. "Using Diffusion and Structural MRI for the Automated Segmentation of Multiple Sclerosis Lesions." In: *Proc Intl Soc Mag Reson Med*. 2015.

[37] Pedro A Gómez, Guido Bounincontri, Miguel Molina-Romero, Cagdas Ulas, Jonathan I Sperl, Marion I Menzel, and Bjoern H Menze. "3D Magnetic Resonance Fingerprinting with a Clustered Spatiotemporal Dictionary." In: *Proc Intl Soc Mag Reson Med* (2016).

[38] Pedro A. Gómez, Miguel Molina-Romero, Cagdas Ulas, Guido Bounincontri, Jonathan I. Sperl, Derek K. Jones, Marion I. Menzel, and Bjoern H. Menze. "Simultaneous Parameter Mapping, Modality Synthesis, and Anatomical Labeling of the Brain with MR Fingerprinting." In: *MICCAI: International Conference on Medical Image Computing and Computer-Assisted Intervention* LNCS 9902 (2016), pp. 579–586.

[39] Pedro A. Gómez, Guido Buonincontri, Miguel Molina-Romero, Jonathan I Sperl, Marion I Menzel, and Bjoern H Menze. "Accelerated parameter mapping with compressed sensing: an alternative to MR Fingerprinting." In: *Proc Intl Soc Mag Reson Med* (2017).

[40] Pedro A Gomez, Miguel Molina-Romero, Paula Orihuela, Guido Buonincontri, Teresa Rincón-Domínguez, Marion I Menzel, and Bjoern H Menze. "Ultrafast Magnetic Resonance Imaging and Parametric Mapping with Optimal Transient-state Encoding." In: *Nature Biomedical Engineering* (Under Rev (2017).

[41] Mark A. Griswold, Peter M. Jakob, Robin M. Heidemann, Mathias Nittka, Vladimir Jellus, Jianmin Wang, Berthold Kiefer, and Axel Haase. "Generalized autocalibrating partially parallel acquisitions (GRAPPA)." In: *Magnetic Resonance in Medicine* 47.6 (2002), pp. 1202–1210. ISSN: 0740-3194. DOI: 10.1002/mrm.10171. URL: http://www.ncbi.nlm.nih.gov/pubmed/12111967http://doi.wiley.com/10.1002/mrm.10171.

[42] A. Haase, J. Frahm, D. Matthaei, W. Hanicke, and K. D. Merboldt. "FLASH imaging. Rapid NMR imaging using low flip-angle pulses." In: *Journal of Magnetic Resonance* 67.2 (1986), pp. 258–266. ISSN: 00222364. DOI: 10.1016/0022-2364(86)90433-6.

[43] P.E. Hadjidoukas, P. Angelikopoulos, C. Papadimitriou, and P. Koumoutsakos. "Π4U: A high performance computing framework for Bayesian uncertainty quantification of complex models." In: *Journal of Computational Physics* 284 (2015), pp. 1–21. ISSN: 00219991. DOI: 10.1016/j.jcp.2014.12.006.

[44] Brian A. Hargreaves, Shreyas S. Vasanawala, John M. Pauly, and Dwight G. Nishimura. "Characterization and reduction of the transient response in steady-state MR imaging." In: *Magnetic Resonance in Medicine* 46.1 (2001), pp. 149–158. ISSN: 07403194. DOI: 10.1002/mrm.1170.

[45] Jürgen Hennig. "Echoes—how to generate, recognize, use or avoid them in MR-imaging sequences. Part I: Fundamental and not so fundamental properties of spin echoes." In: *Concepts in Magnetic Resonance* 3.3 (1991), pp. 125–143. ISSN: 10437347. DOI: 10.1002/cmr.1820030302.

[46] Junzhou Huang, Chen Chen, and Leon Axel. "Fast multi-contrast MRI reconstruction." In: *Medical image computing and computer-assisted intervention : MICCAI ... International Conference on Medical Image Computing and Computer-Assisted Intervention* 15 (2012), pp. 281–8. DOI: 10.1007/978-3-642-33415-3_35. URL: http://www.ncbi.nlm.nih.gov/pubmed/23285562.

[47]   Jens H Jensen, Joseph A Helpern, Anita Ramani, Hanzhang Lu, and Kyle Kaczynski. "Diffusional kurtosis imaging: the quantification of non-gaussian water diffusion by means of magnetic resonance imaging." In: *Magnetic Resonance in Medicine* 53 (2005), pp. 1432–1440. ISSN: 0740-3194. DOI: 10.1002/mrm.20508.

[48]   Yun Jiang, Dan Ma, Nicole Seiberlich, Vikas Gulani, and Mark A. Griswold. "MR Fingerprinting Using Fast Imaging with Steady State Precession (FISP) with Spiral Readout." In: *MRM* (2014). ISSN: 07403194.

[49]   Konstantinos Kamnitsas, Christian Ledig, Virginia F. J. New-combe, Joanna P. Simpson, Andrew D. Kane, David K. Menon, Daniel Rueckert, and Ben Glocker. "Efficient Multi-Scale 3D CNN with Fully Connected CRF for Accurate Brain Lesion Segmentation." In: *arXiv eprint* (2016). arXiv: 1603.05959. URL: http://arxiv.org/abs/1603.05959.

[50]   Eugen Kubala et al. "Hyperpolarized 13C Metabolic Magnetic Resonance Spectroscopy and Imaging." In: *Journal of Visualized Experiments* 118 (2016), e54751. ISSN: 1940-087X. DOI: 10.3791/54751.

[51]   John Kurhanewicz et al. "Analysis of cancer metabolism by imaging hyperpolarized nuclei: prospects for translation to clinical research." In: *Neoplasia (New York, N.Y.)* 13.2 (2011), pp. 81–97. ISSN: 1476-5586.

[52]   P. C. Lauterbur. "Image formation by induced local interactions. Examples employing nuclear magnetic resonance." In: *Nature* 242 (1973), pp. 190–191. ISSN: 0028-0836. DOI: 10.1038/242190a0.

[53]   D. Le Bihan. "Magnetic resonance imaging of perfusion." In: *Magnetic Resonance in Medicine* 14.2 (1990), pp. 283–292. ISSN: 15222594. DOI: 10.1002/mrm.1910140213.

[54]   Xin Liu, Pedro A Gómez, Tim Sprenger, Ana Beatriz Solana, Florian Wiesinger, Marion I Menzel, Jonathan I Sperl, and Bjoern H Menze. "Fast, Volumetric and Silent Multi-contrast Zero Echo Time Imaging." In: *Proc Intl Soc Mag Reson Med* (2017).

[55]   Michael Lustig, David Donoho, and John M Pauly. "Sparse MRI: The application of compressed sensing for rapid MR imaging." In: *Magnetic Resonance in Medicine* 58 (2007), pp. 1182–1195. ISSN: 0740-3194. DOI: 10.1002/mrm.21391.

[56]   Dan Ma, Vikas Gulani, Nicole Seiberlich, Kecheng Liu, Jeffrey L. Sunshine, Jeffrey L. Duerk, and Mark A. Griswold. "Magnetic resonance fingerprinting." In: *Nature* 495 (2013), pp. 187–192. ISSN: 0028-0836. DOI: 10.1038/nature11971.

[57]   P Mansfield and P K Grannell. "NMR 'diffraction' in solids?"
       In: *Journal of Physics C: Solid State Physics* 6.22 (1973), pp. L422–
       L426. ISSN: 0022-3719. DOI: 10.1088/0022-3719/6/22/007.

[58]   Debra McGivney, Eric Pierre, Dan Ma, Yun Jiang, Haris Say-
       basili, Vikas Gulani, and Mark Griswold. "SVD compression
       for magnetic resonance fingerprinting in the time domain." In:
       IEEE TMI 0062 (2014), pp. 1–13. ISSN: 1558-254X. DOI: 10.1109/
       TMI.2014.2337321.

[59]   Bjoern H. Menze, Andras Jakab, Stefan Bauer, and Others.
       "The Multimodal Brain Tumor Image Segmentation Benchmark
       (BRATS)." In: *IEEE Transactions on Medical Imaging* 34.10 (2015),
       pp. 1993–2024. ISSN: 0278-0062. DOI: 10.1109/TMI.2014.2377694.

[60]   Miguel Molina-Romero, Pedro A Gómez, Jonathan I Sperl, An-
       drew J Stewart, Derek K Jones, Marion I Menzel, and Bjoern
       H Menze. "Theory, validation and application of blind source
       separation to diffusion MRI for tissue characterisation and par-
       tial volume correction." In: *Proc Intl Soc Mag Reson Med* (2017).

[61]   Erik Odeblad and Gunnar Lindström. "Some preliminary ob-
       servations on the proton magnetic resonance in biologic sam-
       ples." In: *Acta Radiologica* 49.434 (1955), pp. 57–61. ISSN: 0284-
       1851. DOI: 10.1080/02841850802133337.

[62]   David Owen, Andrew Melbourne, David Thomas, Enrico De
       Vita, Jonathan Rohrer, and Sebastien Ourselin. "Optimisation
       of Arterial Spin Labelling Using Bayesian Experimental De-
       sign." In: *MICCAI: International Conference on Medical Image
       Computing and Computer-Assisted Intervention* 9902 (2016), pp. 511–
       518. DOI: 10.1007/978-3-319-46720-7.

[63]   Eleftheria Panagiotaki, Torben Schneider, Bernard Siow, Matt
       G. Hall, Mark F. Lythgoe, and Daniel C. Alexander. "Compart-
       ment models of the diffusion MR signal in brain white mat-
       ter: A taxonomy and comparison." In: *NeuroImage* 59 (2012),
       pp. 2241–2254. ISSN: 10538119. DOI: 10.1016/j.neuroimage.
       2011.09.081.

[64]   N J Pelc, R J Herfkens, A Shimakawa, and D R Enzmann.
       "Phase contrast cine magnetic resonance imaging." In: *Mag-
       netic resonance quarterly* 7.4 (1991), pp. 229–54. ISSN: 0899-9422.

[65]   Frederike H. Petzschner, Irene P. Ponce, Martin Blaimer, Pe-
       ter M. Jakob, and Felix A. Breuer. "Fast MR parameter map-
       ping using k-t principal component analysis." In: *Magnetic Res-
       onance in Medicine* 66.3 (2011), pp. 706–716. ISSN: 07403194. DOI:
       10.1002/mrm.22826.

[66] Eric Y. Pierre, Dan Ma, Yong Chen, Chaitra Badve, and Mark A. Griswold. "Multiscale reconstruction for MR fingerprinting." In: *Magnetic Resonance in Medicine* 2492 (2015), pp. 2481–2492. ISSN: 15222594. DOI: 10.1002/mrm.25776.

[67] K P Pruessmann, M Weiger, M B Scheidegger, and P Boesiger. "SENSE: sensitivity encoding for fast MRI." In: *Magnetic Resonance in Medicine* 42 (1999), pp. 952–962. ISSN: 0740-3194. DOI: 10.1002/(SICI)1522-2594(199911)42:5<952::AID-MRM16>3.0.CO;2-S.

[68] E M Purcell, H C Torrey, and R B Pound. "Resonance Absorption by Nuclear Magnetic Moments in a Solid." In: *Phys Rev* (1946), pp. 37–38. ISSN: 0031-899X. DOI: 10.1103/PhysRev.69.37.

[69] Isidor Isaac Rabi, J. R. Zacharias, S. Millman, and P. Kusch. "A New Method of Measuring Nuclear Magnetic Moment." In: *Physical Review* 53 (1938), p. 318. ISSN: 0031-899X. DOI: 10.1103/PhysRev.53.318.

[70] Olaf Ronneberger, Philipp Fischer, and Thomas Brox. "U-Net: Convolutional Networks for Biomedical Image Segmentation." In: *Medical Image Computing and Computer-Assisted Intervention – MICCAI 2015* (2015), pp. 234–241. ISSN: 16113349. DOI: 10.1007/978-3-319-24574-4_28. arXiv: 1505.04597.

[71] Klaus Scheffler. "On the transient phase of balanced SSFP sequences." In: *Magnetic Resonance in Medicine* 49.4 (2003), pp. 781–783. ISSN: 07403194. DOI: 10.1002/mrm.10421.

[72] Jo Schlemper, Jose Caballero, Joseph V. Hajnal, Anthony Price, and Daniel Rueckert. "A Deep Cascade of Convolutional Neural Networks for MR Image Reconstruction." In: *arXiv eprint* (2017). arXiv: 1703.00555.

[73] Peter Schmitt, Mark A Griswold, Peter M Jakob, Markus Kotas, Vikas Gulani, Michael Flentje, and Axel Haase. "Inversion recovery TrueFISP: quantification of T(1), T(2), and spin density." In: *Magnetic resonance in medicine : official journal of the Society of Magnetic Resonance in Medicine / Society of Magnetic Resonance in Medicine* 51 (2004), pp. 661–667. ISSN: 0740-3194. DOI: 10.1002/mrm.20058.

[74] Travis Smith, Gho Zun, Eric C. Wong, and Krishna S. Nayak. "Design and use of variable flip angle schedules in transient balanced SSFP subtractive imaging." In: *Magnetic Resonance in Medicine* 63.2 (2010), pp. 537–542. ISSN: 07403194. DOI: 10.1002/mrm.22255.

[75] M. K Stehling, R Turner, and P Mansfield. "Echo-planar imaging: magnetic resonance imaging in a fraction of a second." In: *Science* 254.5028 (1991), pp. 43–50. ISSN: 0036-8075.

[76] E. O. Stejskal and J. E. Tanner. "Spin diffusion measurements: spin echoes in the presence of a time-dependant field gradient." In: *The Journal of chemical physics* 42.1 (1965), p. 5. ISSN: 0021-9606. DOI: 10.1063/1.1695690.

[77] Tilman J. Sumpf, Andreas Petrovic, Martin Uecker, Florian Knoll, and Jens Frahm. "Fast T2 mapping with improved accuracy using undersampled spin-echo MRI and model-based reconstructions with a generating function." In: *IEEE Transactions on Medical Imaging* 33.12 (2014), pp. 2213–2222. ISSN: 1558254X. DOI: 10.1109/TMI.2014.2333370. arXiv: 1405.3574.

[78] Jonathan I. Tamir, Martin Uecker, Weitian Chen, Peng Lai, Marcus T. Alley, Shreyas S. Vasanawala, and Michael Lustig. "T2 shuffling: Sharp, multicontrast, volumetric fast spin-echo imaging." In: *Magnetic Resonance in Medicine* (2016). ISSN: 07403194. DOI: 10.1002/mrm.26102.

[79] Paul Tofts. *Quantitative MRI of the Brain: Measuring Changes Caused by Disease*. Wiley, 2003, p. 633. ISBN: 0470847212.

[80] David S Tuch. "Q-ball imaging." In: *Magnetic Resonance in Medicine* 52 (2004), pp. 1358–1372. ISSN: 0740-3194. DOI: 10.1002/mrm.20279.

[81] David S. Tuch, Timothy G. Reese, Mette R. Wiegell, Nikos Makris, John W. Belliveau, and Van J. Wedeen. "High angular resolution diffusion imaging reveals intravoxel white matter fiber heterogeneity." In: *Magnetic Resonance in Medicine* 48.4 (2002), pp. 577–582. ISSN: 0740-3194. DOI: 10.1002/mrm.10268.

[82] Martin Uecker, Peng Lai, Mark J. Murphy, Patrick Virtue, Michael Elad, John M. Pauly, Shreyas S. Vasanawala, and Michael Lustig. "ESPIRiT - An eigenvalue approach to autocalibrating parallel MRI: Where SENSE meets GRAPPA." In: *Magnetic Resonance in Medicine* 71 (2014), pp. 990–1001. ISSN: 07403194. DOI: 10.1002/mrm.24751.

[83] Cagdas Ulas, Pedro A. Gomez, Jonathan I. Sperl, Christine Preibisch, and Bjoern H. Menze. "Spatio-temporal MRI Reconstruction by Enforcing Local and Global Regularity via Dynamic Total Variation and Nuclear Norm Minimization." In: *Proceedings of International Symposium on Biomedical Imaging (ISBI)* (2016), pp. 306–309. DOI: 10.1109/ISBI.2016.7493270.

[84] Cagdas Ulas, Pedro A Gomez, Jonathan I Sperl, Christine Preibisch, Marion I Menzel, and Bjoern H Menze. "A Robust Reconstruction Method for Quantitative Perfusion MRI: Application to Brain Dynamic Susceptibility Contrast (DSC) Imaging." In: *Proc Intl Soc Mag Reson Med* (2017).

226   Bibliography

[85]   Cagdas Ulas, Pedro A. Gómez, Felix Krahmer, Jonathan I. Sperl, Marion I. Menzel, and Bjoern H. Menze. "Robust Reconstruction of Accelerated Perfusion MRI Using Local and Nonlocal Constraints." In: *International Workshop on Reconstruction and Analysis of Moving Body Organs* LNCS 10129 (2017), pp. 37–47. DOI: 10.1007/978-3-319-52280-7_4.

[86]   Julia V. Velikina, Andrew L. Alexander, and Alexey Samsonov. "Accelerating MR parameter mapping using sparsity-promoting regularization in parametric dimension." In: *Magnetic Resonance in Medicine* 70 (2013), pp. 1263–1273. ISSN: 07403194. DOI: 10.1002/mrm.24577.

[87]   Isabella Verdinelli and K. Chaloner. "Bayesian Experimental Design : A Review." In: *Statistical Science* 10.3 (1995), pp. 273–304. ISSN: 0883-4237. DOI: 10.1214/ss/1177009939.

[88]   Arno Villringer, Bruce R. Rosen, John W. Belliveau, Jerome L. Ackerman, Randall B. Lauffer, Richard B. Buxton, Yong-Sheng Chao, Van J. Wedeenand, and Thomas J. Brady. "Dynamic imaging with lanthanide chelates in normal brain: Contrast due to magnetic susceptibility effects." In: *Magnetic Resonance in Medicine* 6.2 (1988), pp. 164–174. ISSN: 07403194. DOI: 10.1002/mrm.1910060205.

[89]   Marinus T. Vlaardingerbroek and Jacques A. Boer. *Magnetic Resonance Imaging : Theory and Practice*. Springer Berlin Heidelberg, 2003, p. 500. ISBN: 9783662052525.

[90]   J. B M Warntjes, O. Dahlqvist Leinhard, J. West, and P. Lundberg. "Rapid magnetic resonance quantification on the brain: Optimization for clinical usage." In: *Magnetic Resonance in Medicine* 60 (2008), pp. 320–329. ISSN: 07403194. DOI: 10.1002/mrm.21635.

[91]   M. Weigel, S. Schwenk, V. G. Kiselev, K. Scheffler, and J. Hennig. "Extended phase graphs with anisotropic diffusion." In: *Journal of Magnetic Resonance* 205.2 (2010), pp. 276–285. ISSN: 10907807. DOI: 10.1016/j.jmr.2010.05.011.

[92]   Matthias Weigel. "Extended phase graphs: Dephasing, RF pulses, and echoes - pure and simple." In: *Journal of Magnetic Resonance Imaging* (2014). ISSN: 1522-2586. DOI: 10.1002/jmri.24619.

[93]   Florian Wiesinger, Eliane Weidl, Marion I. Menzel, Martin A. Janich, Oleksandr Khegai, Steffen J. Glaser, Axel Haase, Markus Schwaiger, and Rolf F. Schulte. "IDEAL spiral CSI for dynamic metabolic MR imaging of hyperpolarized [1- 13C]pyruvate." In: *Magnetic Resonance in Medicine* 68.1 (2012), pp. 8–16. ISSN: 07403194. DOI: 10.1002/mrm.23212.

[94] Pauline W. Worters and Brian A. Hargreaves. "Balanced SSFP Transient Imaging using Variable Flip Angles for a Predefined Signal Profile." In: *Magnetic Resonance in Medicine* 64.5 (2011), pp. 1404–1412. DOI: 10.1002/mrm.22541.Balanced.

[95] Lecun Y., Bengio Y., and Hinton G. "Deep learning." In: *Nature* 521.7553 (2015), pp. 436–444. ISSN: 0028-0836. DOI: 10.1038/nature14539. arXiv: arXiv:1312.6184v5.

[96] Yan Yang, Jian Sun, Huibin Li, and Zongben Xu. "Deep ADMM-Net for Compressive Sensing MRI." In: *NIPS - Advances in Neural Information Processing Systems* Nips (2017), pp. 10–18. arXiv: 1705.06869.

[97] Bo Zhao, Wenmiao Lu, T. Kevin Hitchens, Fan Lam, Chien Ho, and Zhi Pei Liang. "Accelerated MR parameter mapping with low-rank and sparsity constraints." In: *Magnetic Resonance in Medicine* 74.2 (2015), pp. 489–498. ISSN: 15222594. DOI: 10.1002/mrm.25421.

[98] Bo Zhao, Kawin Setsompop, Borjan Gagoski, Huihui Ye, Elfar Adalsteinsson, P. Ellen Grant, and Larry L. Wald. "A Model-Based Approach to Accelerated Magnetic Resonance Fingerprinting Time Series Reconstruction." In: *Proc Intl Soc Mag Reson Med* (2016).

[99] Bo Zhao, Kawin Setsompop, Huihui Ye, Stephen Cauley, and Lawrence L Wald. "Maximum Likelihood Reconstruction for Magnetic Resonance Fingerprinting." In: *IEEE Trans Med Imaging* (2016). ISSN: 0278-0062. DOI: 10.1109/TMI.2016.2531640.

[100] Li Zhao, Xue Feng, and Craig H. Meyer. "Direct and accelerated parameter mapping using the unscented Kalman filter." In: *Magnetic Resonance in Medicine* 75 (2016), pp. 1989–1999. ISSN: 07403194. DOI: 10.1002/mrm.25796.